Structural Properties of Biological Integral Feedback Motifs

by

Daniel Myklatun Tveit

Thesis submitted in fulfillment of
the requirements for the degree of

PHILOSOPHIAE DOCTOR
(PhD)

University of
Stavanger

Faculty of Science and Technology
Department of Electrical Engineering and Computer Science
2020

University of Stavanger
N-4036 Stavanger
NORWAY
www.uis.no

ISBN 978-82-7644-951-8
ISSN 1890-1387

PhD Thesis UiS no. 544

Preface

This thesis is submitted as partial fulfillment of the requirements for the degree of *Philosophiae Doctor* at the University of Stavanger, Norway. The research has been carried out at the Department of Electrical Engineering and Computer Science (IDE) in collaboration with the Centre for Organelle Research (CORE), both at the University of Stavanger. A period of ten months (from September 2017 through June 2018) was spent as a visiting research scholar at the Systems Biology and Cancer Metabolism Laboratory, directed by Prof. Fabian V. Filipp, at the University of California, Merced.

The research has resulted in four scientific papers, three of which are published and one is submitted for review. The work and results in these papers are presented as a coherent narrative in this thesis. Thus, the thesis takes a form that is closer to the coherent monograph. The thesis consists of six chapters, where the main part (chapters 3–5) presents the research results in a logical progression. The chapters are written so that the reader can fully understand the work and results without having to carefully read each individual paper. For completeness, the full papers are included at the end of the thesis.

Daniel Myklatun Tveit, June 2020

Abstract

Cells are exposed to a range of external and internal disturbances that may influence the function of cellular processes. The ability of cells to self-regulate and adapt to disturbances enable them to maintain essential variables within narrow limits for proper biological function. This phenomenon is known as homeostasis, and is achieved through certain structural properties of cellular control processes. In particular, negative feedback and integral action play crucial roles in the regulation within cells.

Many cellular processes are tightly regulated, and display so-called perfect adaptation to stepwise perturbations. It has been shown that integral feedback control achieves perfect adaptation in a variety biological systems. These observations have motivated researches to investigate cellular control processes from the perspective of robust control in recent years. It is clear that concepts from control theory, more commonly applied to the automation of engineered systems, are applicable to the analysis and construction of biological control networks.

Whereas cellular control processes have been extensively studied with regards to stepwise perturbations in a regulated variable, less attention has been given to disturbances that affect cellular constituents globally, such as growth-induced dilution, and time-varying perturbations. In this thesis, we aim to take a bottom-up approach to investigate cellular control processes and characterize structural properties that give rise to homeostatic behaviors. In particular, we investigate a class of eight two-component control motifs, described by nonlinear saturation kinetics, to show asymptotic stability and robustness. We go on to show how parameters related to molecular and kinetic mechanisms influence set-point tracking and disturbance rejection properties of the two-component control motifs, and investigate how nonlinearities affect these properties. We also characterize certain constraints and trade-offs associated with the control motifs, and study their performance for time-varying perturbations.

In the last part of the thesis, we investigate disturbances in the form of growth-induced dilution of cellular constituents and stochastic fluctuations.

Especially for cancer cells is it expected that dilution poses a significant challenge for the effective regulation of metabolism, due to increased glycolytic and proliferative activity leading to cell swelling and growth-induced dilution. Based on the reported rewiring of glycolysis in cancer, and differential gene expression data from the Expression Atlas database, we construct a simplified mathematical model of glucose uptake. We show how cancer cells can regulate and maintain an increased uptake and metabolism of glucose during growth. In particular, a nested feedback architecture of the two-component control motifs is crucial to this end. To incorporate the effects of uncertainty and noise, we also present a stochastic version of the glucose uptake model, and show stochastic simulations relate to simulations of the deterministic version.

Acknowledgments

First and foremost I would like to thank my supervisor Tormod Drengstig for accepting me as your PhD student, and introducing me to the ongoing research at the interface of control engineering and biology. I also thank my co-supervisors Peter Ruoff and Kristian Thorsen, for teaching me about chemical kinetics and molecular biology, and introducing me to laboratory work and experimentation.

To all my colleagues and friends at IDE and CORE; thank you for all your help and support. Thank you to my fellow board members of UiSDC and SiN, for working hard to create a good research environment for PhD students and postdocs at UiS and nationally.

A special thanks to Fabian V. Filipp and all the members of the Systems Biology and Cancer Metabolism Laboratory at UCM, for welcoming me and teaching me about cancer cell metabolism, and introducing me to state of the art techniques in quantitative systems biology.

Thank you to my fellow bobcats at UCM for all the great times we had, and for making my visit to California an unforgettable experience.

I would also like to thank my family for all your love and support throughout the PhD program.

Love with your heart. Use your head for everything else.
—Alan Melikdjanian.

List of publications

The main part of this dissertation is made up of the following scientific papers:

- **Paper 1**

  Passivity-based analysis of biochemical networks displaying homeostasis
  Daniel M. Tveit, Kristian Thorsen. *Proceedings of the 58th Conference on Simulation and Modelling (SIMS 58)*, pp. 108–113. Sep. 2017. doi: 10.3384/ecp17138108.

- **Paper 2**

  Tuning of physiological controller motifs
  Kristian Thorsen, Geir B. Risvoll, **Daniel M. Tveit**, Peter Ruoff, Tormod Drengstig. *Proceedings of the 9th EUROSIM Congress on Modelling and Simulation, EUROSIM 2016, and the 57th SIMS Conference on Simulation and Modelling, SIMS 2016*, pp. 31–37. Dec. 2018. doi: 10.3384/ecp1714231.

- **Paper 3**

  Homeostatic controllers compensating for growth and perturbations
  Peter Ruoff, Oleg Agafonov, **Daniel M. Tveit**, Kristian Thorsen, Tormod Drengstig. *PLoS ONE*, vol. 14, no. 8, pp. e0207831. Aug. 2019. doi: 10.1371/journal.pone.0207831.

- **Paper 4**

  Exploring mechanisms of glucose uptake regulation and dilution resistance in growing cancer cells
  Daniel M. Tveit, Gunhild Fjeld, Tormod Drengstig, Fabian V. Filipp, Peter Ruoff, Kristian Thorsen. *bioRxiv*, preprint submitted for review. Jan. 2020. doi: 10.1101/2020.01.02.892729.

List of other imparts

Results from the dissertation have in addition to the scientific papers been communicated to the scientific community at:

(i) **Tuning of physiological controller motifs**
Kristian Thorsen, Geir B. Risvoll, **Daniel M. Tveit**, Peter Ruoff, Tormod Drengstig, *Talk*. The 9th EUROSIM Congress on Modelling and Simulation, EUROSIM 2016, and the 57th SIMS Conference on Simulation and Modelling, SIMS 2016, Oulu, Finland. Sep. 2016.

(ii) **Passivity-based analysis of biochemical networks displaying homeostasis**
Daniel M. Tveit, Kristian Thorsen, *Talk*. The 58th Conference on Simulation and Modelling (SIMS 58), Reykjavik, Iceland. Sep. 2017.

(iii) **Reconciling principles for how to achieve feedback and control in biological systems**
Jordan Ang, **Daniel M. Tveit**, Gunhild Fjeld, Tormod Drengstig, Peter Ruoff, David R. McMillen, Kristian Thorsen, *Talk*. The 18th Conference of the International Study Group for Systems Biology (ISGSB 2018), Tromsø, Norway. Sep. 2018.

(iv) **Regulation of glucose uptake during growth and dilution**
Daniel M. Tveit, *Talk*. Centre for Digital Life Norway Workshop on Control Engineering Concepts in Systems and Synthetic Biology, Stavanger, Norway. May 2019.

Contents

Chapter 1

Introduction

1.1 Cybernetics: The convergence of control engineering and biology

Modern systems and synthetic biology lie at the interface of engineering and biology [38, 164, 3, 200]. Systems biology seeks to understand the complexities of natural biological networks, and importantly, attempts to elucidate the mechanisms of regulation and signaling that govern cellular behavior [79, 82]. Systems biology employs a holistic approach to molecular and cell biology, in the hopes of gaining insights that can only be learned by taking multiple components into account simultaneously [190, 96]. In contrast, synthetic biology seeks to design and construct new biological circuits, with the goal of controlling cellular behavior and engineering new functionalities [79, 36]. Synthetic biology has the potential to address a number of problems facing modern society, with applications in energy, environment, and medicine [36, 82]. Whereas systems biology makes use of concepts from control theory to uncover principles about the function of biochemical reaction networks, and utilize methods from system identification for parameter estimation, synthetic biology makes use of design principles from control theory to guide the construction of optimized and robust biological circuits [190, 38, 164]. These are just a few areas of research at the interface of engineering and biology, and are examples of the ongoing movement for the unification of biology and engineering, referred to as *convergence* [39]. Inspired by the molecular biology revolution of the 1950s–1970s, which enabled a cellular-level understanding of disease state; and the genomic revolution of the 1980s–1990s, which enabled a deeper level of understanding through genome sequencing; it is argued that convergence will be the third revolution, and will further our ability to understand and treat disease [39]. Early indications of convergence

go back to the 1940s and individuals like Norbert Wiener and Arturo Rosenblueth. Influenced by the work of Rosenblueth's colleague, Walter Cannon, they proposed *cybernetics* as a term for the study of control and communication theory in the animal and the machine, which they viewed as a unifying theme in engineering and biology [198, 162, 38]. In contrast to simple interdisciplinary collaborations, the aim of convergence is not only to advance our understanding of biology, but also to push the boundaries of the theoretical foundation of engineering [39]. Evolution has resulted in systems that are highly optimized and fault-tolerant, and could serve as inspiration for innovative solutions to engineering problems [162].

Control theory is aimed at improving the stability, robustness, and performance of physical systems, with applications in mechanical and electrical devices, space and air systems, and chemical processes [36, 155, 44]. An important abstraction used in control theory is the separation of a system into a *process* and a *controller*. In this abstraction, the process represents the basic function of the system, while the controller implements manipulations to improve stability, robustness, and performance of this function [40]. By stability, it is usually meant that a system tends towards a certain steady-state, known as an equilibrium point, as time approaches infinity [92, 160]. Robustness, on the other hand, refers to the ability of the system to resist disturbances [93, 92, 160]. In engineered systems, the presence of model uncertainty, coupled with system perturbations and environmental disturbances, means that a lack of robustness will likely result in a system that is unable to deliver reliable functionality [93, 92, 160]. The principles of stability and robustness also apply to biological systems, and are required for proper biological function under varying conditions [93]. Compared to control engineering, however, the theory for biological robustness remains largely lacking [93].

Negative feedback if often associated with stability and robustness, mainly due to the opposing action this structure produces in response to deviations from its steady-state [92, 198]. For example, a thermostat regulates the heating of a room by turning on a heater if the temperature in the room is below the desired temperature set on the thermostat. If the temperature is greater than the desired room temperature, the thermostat turns off the heater to bring the room temperature down. Hence, the action of the thermostat is negatively related to the deviation of the room temperature from the desired temperature, which is called negative feedback. Note, however, that the thermostat must be designed to respond proportionately,

as a poorly designed thermostat may send the room temperature into violent oscillations [198].

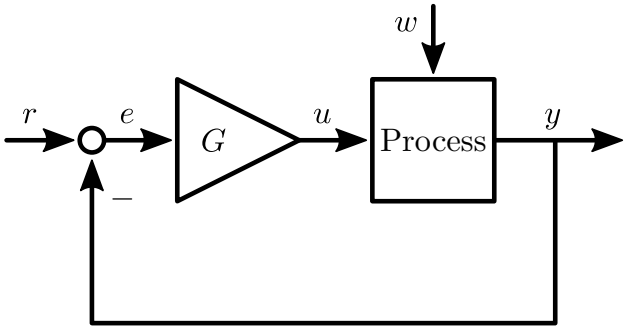

Figure 1.1: Proportional negative feedback. The process output y is fed back and compared to the reference r to produce the regulation error $e = r - y$. The control action u (the process input) is computed as the regulation error multiplied by the controller gain G. The negative feedback connection functions to counteract deviations in process output from the desired reference value, thereby minimizing the impact of the uncontrolled disturbance w.

In negative feedback (e.g. Figure 1.1), the process output y is measured and compared to a reference r, producing the regulation error $e = r - y$. The controller acts on the process through the input u, which is computed based on the regulation error, so that the difference between reference and process output is reduced [36, 155, 92]. Whether the closed-loop system is able to achieve and maintain the reference value is related to stability, whereas robustness is related to the ability of the system to compensate for the unwanted disturbance w. Consider the process of transcription, where y is the concentration of mRNA, u is the concentration of a transcription factor, and w is some unwanted disturbance (e.g. transcription that happens without the transcription factor). Production of mRNA is proportional to the concentration of transcription factor, and degradation of mRNA is proportional to its own concentration. This process is described by the linear differential equation $\dot{y} = -c_1 \cdot y + c_2 \cdot u + w$ [36]. Here, dot notation is used to represent the time derivative. The open-loop (i.e. without feedback) steady-state of this system is given by $y = (c_2 \cdot u + w)/c_1$, which shows that the open-loop output is very much dependent on the disturbance. If we apply the proportional negative feedback in Figure 1.1, $u = G \cdot (r - y)$, the closed-loop steady-state is given by $y = (c_2 \cdot G \cdot r + w)/(c_1 + c_2 \cdot G)$. In this case, if the controller gain G is large enough, the steady-state expression is reduced to $y \approx r$. Hence, the steady-state output of the closed-loop

system with high-gain negative feedback is made largely independent of the disturbance (i.e. the control system is robust to w).

This example demonstrates how biological processes can be described by ordinary differential equations (ODEs). Mathematical models have for the longest time been important for our intuition in many fields of science, including biology, where they are used to aid our understanding of phenomena and predict emergent properties [61]. In biology, detailed large-scale models attempt to incorporate as much as possible of the available data from a system, with the premise that all components and interactions of the system may be needed to reproduce its *quantitative* behavior [61, 48]. Complementary to large-scale models are small-scale models, that seek to model a system using only the essential components and interactions necessary to reproduce its *qualitative* behavior [61, 190, 48]. Although large-scale models are undeniably closer to biological reality than simplified small-scale models, large-scale models suffer from a large number of parameters that are poorly determined, which makes it difficult to differentiate predictions that are dependent on certain parameter choices, and those that are general to the system [61]. On the other hand, small-scale models benefit from a small number of components and parameters, which facilitates interpretation and makes it possible to discern generality of conclusions, and hence, small-scale models are often associated with uncovering principles rather than quantitative predictive power [61].

Systems of ODEs are the natural language for describing biological networks in a mass action approximation, which simply states that a reaction rate is given by a constant multiplied by the product of the reactant concentrations [28, 31]. The mass action approximation holds for a well-mixed reaction compartment, when the number of molecules is great enough that the inherent stochastic fluctuations of chemical reactions become small enough that a deterministic description is sufficient [28, 60]. In general, deterministic models provide a good description for reactions having more than 10^2–10^3 molecules per reactant in all reaction compartments, which holds true for eukaryotic metabolism and signal transduction [28, 169]. Thus, cellular reaction networks can often be investigated by considering deterministic models, which facilitates simulation and analysis efforts.

1.2 Scientific contributions

The scientific contributions of this thesis is made up of three published papers, and one unpublished paper submitted for review. In the thesis we

also expand upon some results, which were not published in the papers, primarily due to space constraints. In addition, the thesis contains results from an as-of-yet unpublished review and perspective on principles and motifs for feedback and homeostatic control in biological systems. A summary of the scientific contributions of the individual papers are provided in the following.

1.2.1 Paper 1: Passivity-based analysis of biochemical networks displaying homeostasis

In Paper 1 (Tveit and Thorsen [186]), we looked at stability and robustness of a class of eight two-component negative feedback motifs. Notably, we considered negative feedback motifs described by nonlinear saturation kinetics. Using a general mathematical framework, a stability analysis of the entire class of eight two-component negative feedback motifs was performed. We described the two-component motifs as negative feedback connections of two subsystems. Using a passivity-based approach, we showed that the two subsystems are output strictly passive and zero-state observable. This implies that the negative feedback connection is asymptotically stable, despite highly nonlinear interactions of saturation kinetics. Furthermore, we showed that the stability result is global. We also showed that robustness to disturbances is ensured, due to the presence of integral feedback, and characterized the condition necessary for perfect adaptation.

1.2.2 Paper 2: Tuning of physiological controller motifs

In Paper 2 (Thorsen et al. [181]), we showed how parameters related to molecular and kinetic mechanisms influence set-point tracking and disturbance rejection properties of the same two-component negative feedback motifs considered in Paper 1. We employed a tuning procedure based on linearization, in a similar way to the tuning of industrial control processes. The tuning procedure enabled us to define a desired dynamical response for the negative feedback motifs, using tuning parameters related to the step response of the systems. These tuning parameters define the response time and overshoot of the step response. We showed analytically and through simulations how *i*) the level of disturbances and *ii*) the values of various rate constants influence set-point tracking and disturbance rejection properties of the negative feedback motifs.

1.2.3 Paper 3: Homeostatic controllers compensating for growth and perturbations

In Paper 3 (Ruoff et al. [147]), we described the performance of selected negative feedback control motifs (including those considered in Papers 1 and 2) in response to different growth laws and time-dependent perturbations. We considered controllers with ideal behavior, in the sense that they for stepwise perturbations show perfect adaptation. We applied growth kinetics that reflect experimentally observed growth laws, ranging from surface-to-volume ratio growth to linear and exponential growth. Our results showed that the kinetic implementation of integral control and the structure of the negative feedback loop are two properties that affect controller performances. Best performance was observed for controllers based on derepression kinetics and controllers with an autocatalytic implementation of integral control, both of which were able to defend exponential growth and perturbations. Controllers with activating signaling using zero-order or bimolecular (antithetic) kinetics for integral control performed less well. Our results provide a guide to what type of feedback structures and integral control kinetics are suitable to oppose dilution by different growth laws and time-dependent perturbations.

1.2.4 Paper 4: Exploring mechanisms of glucose uptake regulation and dilution resistance in growing cancer cells

In Paper 4 (Tveit et al. [185]), we reviewed the literature on cancer cell metabolism and glucose uptake, and employed mathematical modeling to examine control mechanisms in cancer cell metabolism that show robust homeostatic control in the presence of dilution. Using public gene expression data from the Expression Atlas database, we showed that cancer cells, on average, shift towards glucose transporter 1-mediated glucose uptake, predominant expression of the pyruvate kinase M2 isoform, and overexpression of hexokinase 2. Based on this information, we constructed a simplified mathematical model of glucose uptake in cancer, which we used to investigate structural properties of the system. By simulations we found that in a worst-case scenario, in which all components of the protein synthetic machinery of the cell dilute as the cell grows, partial dilution resistance to a linearly increasing cellular volume is achieved. Notably, we found the presence of a nested feedback architecture of the negative feedback motifs studied in Papers 1–3. We showed that negative feedback regulation of

intermediary glycolytic enzymes, in addition to negative feedback from downstream glycolytic metabolites to glucose transporters (i.e. nested feedback), is sufficient in order to achieve homeostatic control during growth. We related our simulation results on dilution resistance to structural properties of the mathematical description, and showed how the two-component negative feedback motifs can be tuned to achieve near-perfect dilution resistance.

1.3 Thesis aims and outline

The main aim of this thesis is to take a bottom-up approach to investigate cellular control processes and to:

- Characterize the structural properties of cellular control processes that give rise to homeostatic behaviors.
- Investigate a class of eight two-component negative feedback motifs, and extend prior analysis to account for highly nonlinear interactions.
- Characterize conditions for ideal and near-ideal behaviors (e.g. perfect adaptation, dilution resistance), and highlight limitations and trade-offs inherent to the negative feedback motifs.
- Show how parameters related to molecular and kinetic mechanisms influence set-point tracking and disturbance rejection properties of the negative feedback motifs.
- Present a model for glucose uptake in cancer, and demonstrate the presence of negative feedback motifs. Show that dilution resistance in the glucose uptake model is achieved by nested feedback regulation, and investigate its behavior subject to disturbances and extrinsic noise.

Before we present the main results, Chapter 2 introduces the negative feedback motifs considered in Papers 1–4 in a historical context, and presents some important concepts in chemical kinetics that will be used throughout the thesis. The chapter is meant to give the reader insight into the approach researchers took to cellular control processes in the latter half of the 20th century, and why a new perspective on cellular control has revitalized the interest of researchers on the topic of feedback mechanisms

in recent years. The results from Paper 1 are presented in Chapter 3, in addition to a short summary on integral feedback motifs in general, based on an unpublished review on the topic. Chapter 4 presents the results from Paper 2, which are expanded upon with some unpublished results that reinforce the main results in the paper. These extended results also relate the results on time-dependent perturbations in Paper 3 to the results in Paper 2. Chapter 5 includes results from both Papers 3 and 4. Because there is significant overlap between the two papers, Chapter 5 focuses primarily on the results of Paper 4. In addition, the chapter includes some extended results on stochastic fluctuations, based on feedback received on the two papers. In Chapter 6 we summarize and discuss the results obtained on stability (Chapter 3), tuning (Chapter 4), and dilution resistance and noise (Chapter 5). We also discuss some limitations inherent to the modeling approach taken in the thesis.

Throughout this thesis, we will use dot notation to represent the time derivative. State variables represent concentrations of compounds, except when variables n_i are used, in which case the state variables represent amounts. For the purpose of demonstration, and because we focus on structural or qualitative properties, parameter values and simulation results are given in arbitrary units (arb. unit). Genes are written in italic, and protein products in normal text.

Chapter 2

Background

In this chapter we look back at the history and discovery of feedback mechanisms in cellular control processes. We start with the discovery of some important phenomena that lead to the understanding of metabolic regulation by negative feedback. We describe the different, and often complementary, negative feedback strategies employed by cells, based on regulation of enzyme synthesis and activity. We go on to introduce some important concepts in chemical kinetics, such as allostery, saturation, and cooperativity, that we will use throughout the thesis. Finally, we take a look at various negative (and some positive) feedback mechanisms by which biochemical oscillations can occur. Oscillations in cellular control processes were extensively studied in the latter half of the 20th century. However, it is only fairly recently that regulatory mechanisms in biological systems have been studied from the perspective of robust control. It is from this new perspective that we investigate cellular control processes in the main part of the thesis. This chapter serves to introduce some central concepts and themes that will set up our investigation of negative feedback motifs in the following chapters.

2.1 Enzyme adaptation

Enzyme adaptation is the phenomenon where microorganisms synthesize enzymes for the metabolism of a particular substrate, only when the substrate is available [13, 111, 188]. The term was coined by Henning Karström in 1938 when he rediscovered the phenomenon, which had first been discovered by Émile Duclaux in the late 1890s [13, 111, 120]. The first clear evidence of enzyme adaptation, however, was given by Frédéric Dienert, a student of Duclaux, as early as 1900 [13, 120, 188, 111]. Dienert studied the "enzyme" galactozymase, today known to be the collection of

enzymes of the Leloir pathway, necessary for the metabolism of galactose in yeast [156, 13, 111]. He found that cells grown on glucose were unable to ferment galactose, whereas cells grown on galactose could ferment both glucose and galactose [188, 13, 111]. Interestingly, when cells were grown on a mixture of glucose and galactose, an inhibitory effect on galactose metabolism was observed; glucose was metabolized first, and after a certain time delay, galactose could be metabolized [188, 13, 111]. Dinert named this inhibitory effect by glucose, the *glucose effect* [120, 111, 188]. Importantly, Dienert also showed that the process of adapting to galactose occurred without cell division, and hence, was not due to the selection of mutants [111, 13].

In the beginning of 1940, Jacques Monod made some interesting observations on the growth of bacteria. He found that cultures grown on certain mixtures of carbohydrates displayed the phenomenon of *diauxie*; that growth consisted of two exponential phases, separated by a complete cessation of growth (Figure 2.1) [119, 120, 188, 111, 13]. It was André Lwoff who directed Monod to the work of Marjory Stephenson and her students, John Yudkin and Ernest Gale, who had published several papers on enzyme adaptation at the time [120, 111]. Monod's diauxie was closely related to enzyme adaptation, and was in fact a case of Dienert's glucose effect [120, 111, 188, 13]. Like Dienert, Monod interpreted the cessation of growth to be an induction period necessary for the bacteria to adapt to a new substrate, having used up the first substrate in the initial exponential phase [111, 188, 13]. Monod and others ruled out the selection of mutants and, like Dinert before them, proved that the adaptation process was a physiological response [111, 13]. Monod proposed that the first carbohydrate to be metabolized was attacked by *constitutive enzymes*, whereas the second carbohydrate was attacked by *adaptive enzymes*, in accordance with the terminology put forth by Karström [111, 188, 13]. This hypothesis explained diauxie, or the glucose effect, by the inhibition of forming adaptive enzymes as long as the first carbohydrate was present [111, 188].

2.2 Control by feedback repression

In order to understand enzyme adaptation, Monod sought it necessary to understand how certain carbohydrates induce the formation of adaptive enzymes, and whether this induction entailed the synthesis of new enzymes, or rather the activation or conversion of existing enzyme precursors [120,

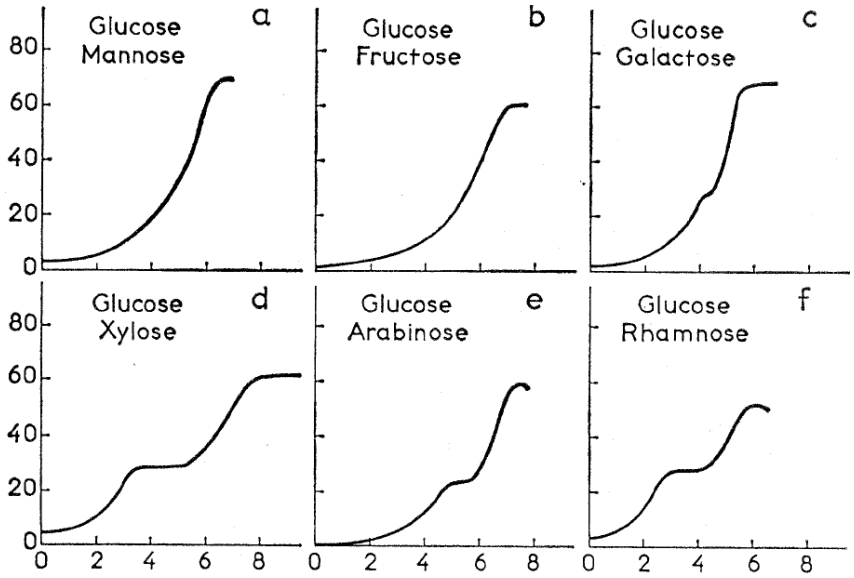

Figure 2.1: Growth of *Escherichia coli* in the presence of different carbohydrate pairs serving as the only carbon source in the medium. Whereas certain mixtures (e.g. glucose and mannose) show a single exponential growth phase, other mixtures (e.g. glucose and xylose) show two exponential phases separated by a complete cessation of growth (diauxie). From Monod [120]. Reprinted with permission from AAAS.

111]. In collaboration with Melvin Cohn, Alvin Pappenheimer, Germaine Cohen-Bazire, and several others[1], Monod was able to establish that enzyme adaptation involved synthesis of enzymes *de novo* [120, 13]. In 1953, Monod and Cohen-Bazire proved that biosynthesis of the enzyme tryptophan synthase is inhibited by the reaction product, tryptophan [120]. This was the first known example of control by *repression*; that a substance, called a *repressor*, inhibits the biosynthesis of a particular enzyme [120, 196, 13]. The term was proposed by Henry Vogel when it was discovered that the enzyme acetylornithinase (acetylornithine deacetylase), involved in the formation of arginine and believed to be induced by its substrate, was instead shown to be repressed by arginine [120, 196]. In the following years, repression was observed in several different organisms with a wide variety of substances [196, 120]. Commonly, the repressors are end products of pathways in which the enzymes they repress occur [196]. And hence, is was understood that enzyme adaptation does not need to entail induction of enzymes by substrates, but

[1]Madeleine Jolit, Anne-Marie Torriani, and David Hogness [120].

could also be explained by repression of enzymes by their end products [196, 120]. Boris Magasanik made the important observation that characteristic of glucose-sensitive enzymes is their repressibility by compounds that can efficiently serve as intermediary metabolites and a source of energy [188, 196]. Therefore, in 1961, he renamed the glucose effect to *catabolite repression*, reasoning that metabolites formed more readily from glucose accumulate in the cell, thereby repressing the formation of glucose-sensitive enzymes that less efficiently produce the same metabolites [188, 13, 120]. Repressors usually have a high specificity for the enzymes they repress, and with often being end products of pathways, have properties important in controlling cellular functions, such as biosynthesis [196, 120].

In 1946, together with Alice Audureau, Monod studied *lactose-negative* bacteria, which is to say bacteria unable to grow on media where lactose is the only carbon source [111, 120]. They showed that an apparently spontaneous mutation allowed the originally lactose-negative bacteria to become *lactose-positive* [120, 111]. Interestingly, the growth curve of these lactose-positive bacteria were typical of diauxie, implying that an adaptive enzyme was involved [111]. Monod and Audureau showed that the lactose-negative and lactose-positive strains did not differ from each other in the presence of the enzyme system necessary to grow on lactose, but rather in the ability to produce this system in the presence of lactose [120, 111]. This implied that the process of enzyme adaptation had a genetic basis, and Monod noted that "the mutation affected a truly genetic property that became evident only in the presence of lactose" [120, 111]. This observation later motivated the *operon model*, in which the expression of a group of *structural genes* is under the control of a single DNA sequence, called the *operator* [120, 111, 83, 84, 13, 17]. The operator is in turn under the influence of a *regulator gene* coding for a protein that can bind to the operator [83, 84, 13, 17]. The affinity of the regulator protein to the operator is influenced by an *effector* that can bind to the regulator protein, thereby controlling the expression of the structural genes [83, 84, 13, 17]. The operon model provided a mechanism by which catabolite repression and activation occurs in prokaryotes, examples of both can be found in *Escherichia coli* (Figure 2.2): The catabolite repressor/activator protein (Cra), encoded by the *cra* gene, activates transcription of genes coding for biosynthetic and oxidative enzymes, while inhibiting transcription of genes coding for glycolytic enzymes [148]. Cra activates transcription by binding to operator regions of target operons where the operator is situated upstream of the RNA polymerase (RNAP) binding site, and inhibits transcription

by binding to operator regions of target operons where the operator is overlapping or downstream of the RNAP binding site [148]. Accumulation of glycolytic catabolites (e.g. due to uptake and catabolism of exogenous glucose) results in binding of the catabolites to the Cra protein, causing it to dissociate from the DNA, thereby reversing the activating effect of Cra in the case of genes coding for biosynthetic and oxidative enzymes, and reversing the inhibiting effect of Cra in the case of genes coding for glycolytic enzymes [148].

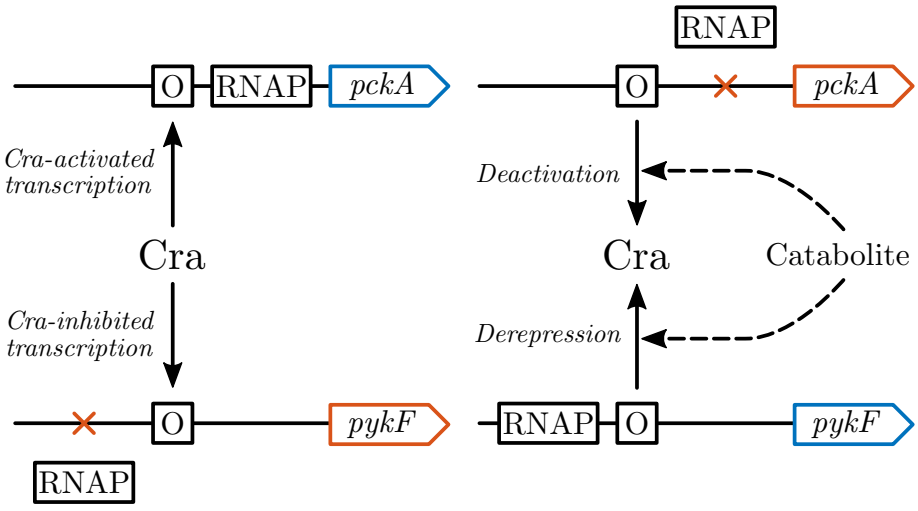

(a) Cra-activated/inhibited transcription. **(b)** Catabolite repression/activation.

Figure 2.2: Cra binds to operator regions (O) of target operons (panel (a)). When the Cra operator is situated upstream of the RNAP binding site, activation of transcription is seen. When the Cra operator is overlapping or downstream of the RNAP binding site, inhibition of transcription is seen. Uptake and catabolism of exogenous sugars result in accumulation of glycolytic catabolites (panel (b)). The catabolites bind to the Cra protein and cause it to dissociate from the DNA. This reverses the activating and inhibiting effects of Cra (catabolite repression and activation, respectively). In *Escherichia coli*, catabolite repression is seen for biosynthetic and oxidative enzymes, such as phosphoenolpyruvate carboxykinase (encoded by the *pckA* gene), and catabolite activation is seen for glycolytic enzymes, such as pyruvate kinase (encoded by the *pykF* gene) [148].

Control by repression is a common regulatory strategy in a wide variety of bacteria and mammalian cells [196, 120, 82, 17]. Much attention has been given to the characterization of cellular control processes utilizing this strategy, and in 1965, the Nobel Prize in Physiology or Medicine was awarded jointly to François Jacob, André Lwoff, and Jacques Monod "for their

discoveries concerning genetic control of enzyme and virus synthesis" [130].

2.3 Control by feedback inhibition

Similar to repression by end products is the phenomenon of *feedback inhibition*, also called *end product inhibition* or *retroinhibition*, in which end products are inhibitors of early enzymatic steps in their own pathways [196, 163, 121, 30]. An important distinction, however, is that feedback inhibition occurs at the level of enzyme action, whereas feedback repression affects enzyme formation [196, 163]. In 1941, Zacharias Dische published a paper in which he described the inhibition of glucose phosphorylation by diphosphoglyceric acid, and how this leads to the automatic regulation of its formation [30]. It was not until 1954, however, that Aaron Novick and Leo Szilard discovered feedback inhibition as a regulatory mechanism in microorganisms, followed by Edwin Umbarger in 1956, and Richard Yates and Arthur Pardee in the same year, who published conclusive evidence that end products inhibit the activity of early enzymes in their own pathway [30, 121, 132, 189, 204]. Later, it has become clear that regulation by feedback inhibition is present in most biosynthetic systems [30, 121, 17, 82].

Monod, together with Jean-Pierre Changeux and François Jacob, found that feedback inhibition entailed a conformational change of the *regulatory enzyme*, i.e. the enzyme subject to feedback inhibition [121, 120]. This conformational change is induced or stabilized by the binding of an *allosteric effector* to an *allosteric site* of the regulatory, or *allosteric*, enzyme [121, 120]. The term allosteric was used to indicate that the effector binds to a regulatory site which is different from the catalytic, or active, site [121, 120, 17]. The allosteric enzyme undergoing a conformational change is called an *allosteric transition* (Figure 2.3), and changes the properties of the active site, thereby changing the kinetic parameters of the enzyme [121, 120, 17]. Since the allosteric site is distinct from the active site, the allosteric effector does not *directly* participate in the reaction catalyzed by the allosteric enzyme. That is to say, the reaction does not depend on the structure or the chemical reactivity of the effector itself, and therefore the effector does not need to bear any particular chemical or metabolic relation to the substrate [121, 120, 17]. The specificity of the allosteric effector is entirely due to the structure of the allosteric enzyme, and hence, allosteric enzymes are signal transducers of allosteric effectors [121, 120, 17]. The *indirect*

nature of allosteric interactions is of extreme biological significance; the precise regulation of cellular metabolism with its overlapping and interlocking metabolic pathways leading to diverse end products would not be possible with only direct interactions between metabolites and enzymes [120, 121]. Such interactions would be severely limited by metabolites possessing the chemical reactivity necessary to be physiologically beneficial, whereas indirect interactions depending exclusively on the structure of the enzyme itself, does not have this limitation [120]. Thus, a clear distinction is made between allosteric interactions and actions of coenzymes, secondary substrates, and substrate analogues, all of which react with the substrate or substitute for the substrate [121].

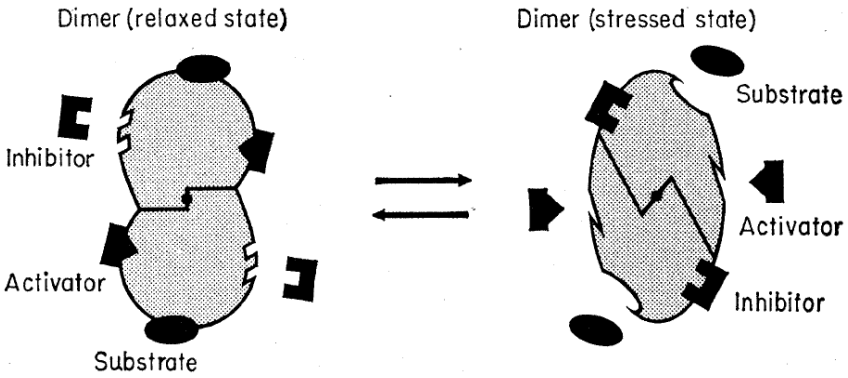

Figure 2.3: In the symmetry model (or allosteric model), Monod, Changeux, and Jeffries Wyman postulated that allosteric proteins could exist in two (or more) conformations; a relaxed state and a stressed (or tense) state [120, 31]. In this model, allosteric effects are mediated by allosteric effectors binding preferentially to one of the conformational states, thereby increasing (for allosteric activators) or decreasing (for allosteric inhibitors) the availability of molecules in the conformation that binds the substrate [31]. From Monod [120]. Reprinted with permission from AAAS.

Control by feedback inhibition is rapid, affecting susceptible enzymes as soon as end products build up in sufficient concentrations [196, 31, 63]. This type of control is said to be part of the *metabolic system* of cells, in which the major activities are the diffusion, interaction, and transformation of small molecules such as metabolites [63, 31]. Interactions between small molecules and macromolecules, such as allosteric interactions, are included in this system, but the synthesis of macromolecules is excluded, concentrations of which are regarded as constant or slowly changing [63, 31]. Different is the *epigenetic system*, in which the major activities are the biosynthesis, diffusion, and interactions of macromolecules [63, 31]. This distinction is

made due to the difference in relaxation time of the two systems, i.e. the time it takes for a system to return to steady-state when subjected to a "small" disturbance [63, 31]. The metabolic and epigenetic systems are said to be operating on different *timescales*. Control by repression is part of the epigenetic system, as it affects the synthesis of new enzyme molecules, but does not affect existing enzyme molecules, whose concentration decrease through degradation and dilution [196, 31, 63]. Interestingly, feedback inhibition and repression frequently appear together in the control of metabolic pathways, as is the case in the glyoxylate cycle of the bacterium *Paracoccus denitrificans* in which succinate (or some derivative of succinate), formed by the cleaving of isocitrate to succinate and glyoxylate by the enzyme isocitrate lyase, represses the formation of isocitrate lyase and simultaneously inhibits its activity (Figure 2.4) [196, 98, 134]. Hence, the coordinated action of feedback inhibition and repression enables an effective response across timescales (metabolic and epigenetic systems), without the limitations of a single negative feedback type (e.g. the response of feedback inhibition is limited to the enzyme molecules already present).

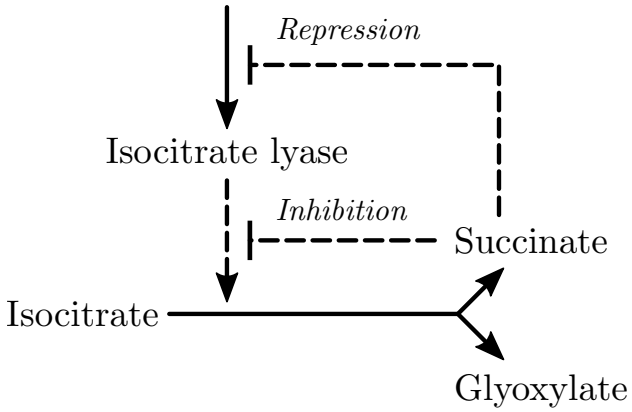

Figure 2.4: The coordinated action of feedback inhibition and repression controlling the cleaving of isocitrate to succinate and glyoxylate by isocitrate lyase in the glyoxylate cycle of the bacterium *Paracoccus denitrificans* [196, 98, 134]. Feedback repression reduces the formation of isocitrate lyase, whereas feedback inhibition reduces the activity of the enzyme [98].

2.4 Saturation and cooperativity

Many allosteric enzymes have a sigmoidal saturation curve, as opposed to the rectangular hyperbola given by the Michaelis–Menten equation [31, 17, 120, 13]. This is called *cooperativity*, because it arises from the "cooperation" of active sites; binding reactions at individual sites affect the likelihood of binding at other sites [31, 17]. The Michaelis–Menten equation describes the reaction rate of an enzyme-catalyzed reaction, assuming steady-state of the enzyme-substrate complex (Briggs–Haldane treatment) [31]

$$v = \frac{V_{\max} \cdot S}{K_{\mathrm{M}} + S} \tag{2.1}$$

where $V_{\max} = k_{\mathrm{cat}} \cdot E_0$ is the limiting rate, k_{cat} is the catalytic constant, or turnover number, and E_0 is the concentration of total enzyme, free and substrate-bound. S is the concentration of substrate, and K_{M} is called the Michaelis constant, which can be defined as the substrate concentration at which $v = 0.5 \cdot V_{\max}$. In contrast, cooperative enzymes have a sigmoidal saturation curve, and it is convenient to describe such enzyme in terms of the Hill equation [31]

$$v = \frac{V_{\max} \cdot S^h}{K_{0.5}^h + S^h} \tag{2.2}$$

where $V_{\max}$, like in the Michaelis–Menten equation, is the limiting reaction rate, $K_{0.5}$ defines the substrate concentration S at which $v = 0.5 \cdot V_{\max}$, and h is the Hill coefficient, an index of the degree of cooperativity. With $h = 1$ (non-cooperative), the Hill equation is the same as the Michaelis–Menten equation, while $h > 1$ corresponds to positive cooperativity [31].

Although many allosteric enzymes are cooperative, it is important to note that they are different properties that should be distinguished [31]. For example, the binding of oxygen to hemoglobin was known to be cooperative for more than 60 years before 2,3-bisphosphoglycerate was demonstrated to be an allosteric effector for hemoglobin (decreasing its oxygen affinity) [31, 16]. Nevertheless, both properties play a crucial role in metabolic regulation, and often appear together [31, 17]. The importance of cooperativity in metabolic regulation is demonstrated by comparing the saturation curves of Michaelis–Menten and Hill kinetics. This is shown in Figure 2.5, where it is seen that an enzyme following Michaelis–Menten kinetics requires a much larger change in substrate concentration to achieve the same change in

activity as an enzyme following Hill kinetics. Because cooperative enzymes are much more sensitive to changes in substrate concentration (near the $K_{0.5}$ value), they are more effective at regulating metabolites within small tolerances [17, 31].

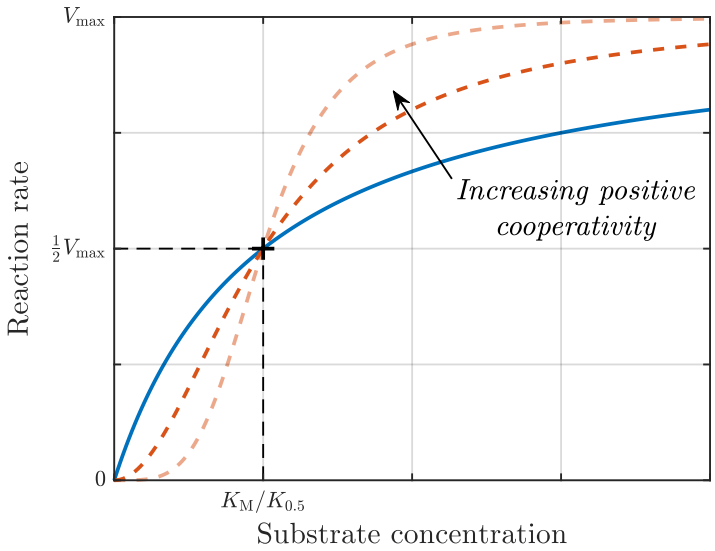

Figure 2.5: Comparison of the saturation curves of Michaelis–Menten kinetics (solid blue line) and Hill kinetics (dashed red lines).

2.5 Dynamical models of cellular processes and the occurrence of oscillations

Feedback inhibition and repression are common control strategies in cells, and although functionally different, work based on the same principle of negative feedback, long familiar to control engineers in the automation of industrial processes [189, 63, 169, 82]. The central importance of negative feedback as a mechanism for control in organisms was first brought to the attention of biologists by Norbert Wiener in 1948 with the publication of his book "Cybernetics: or Control and Communication in the Animal and the Machine" [63, 198]. Wiener reasoned that for humans to effectively perform an action, it is not only essential to have good effectors, but that these effectors are monitored back to the central nervous system and combined with information from other sense organs to produce a properly

proportioned output to the effectors [198]. Such feedback gives a measure by which an action, such as motion, has not yet been accomplished, and it is by this measure the action is regulated [198]. The basis of negative feedback in cellular control processes is the existence of a closed causal circuit of molecular or macromolecular species, resulting in a self-regulating structure [63, 62, 82]. The consequence of such feedback structures can be seen at all levels of organization in an organism, from the the regulation of biosynthetic pathways and control of cell growth, to the regulation of body temperature and maintenance of a blood glucose level within a relatively narrow range [189, 63, 62, 143, 17]. However, qualitative descriptions of cellular control processes do not tell us about their dynamical properties [63, 82, 169]. To investigate these properties, it is necessary to construct dynamical models based on the kinetics of molecular reactions involved in the qualitative descriptions [82, 169].

In his 1963 book, "Temporal Organization in Cells; a Dynamic Theory of Cellular Control Processes," Brian Goodwin proposed a model for metabolic feedback control based on repression [63, 62]. Figure 2.6 shows the system he considered, where mRNA (X) transcribed from DNA (L) is translated by ribosomes (R) to form an enzyme (Y) catalyzing the formation (C) of a metabolite (M) with the ability to repress production of the mRNA [63, 64, 62]. This represents probably the simplest conceivable example of feedback repression, and although necessarily rather approximate, includes essential features of the real system [64, 62]. The dynamical model is given by the system of ODEs [63, 64, 62]

$$\dot{X}(t) = \frac{a}{A + k \cdot Y(t)} - b \tag{2.3}$$

$$\dot{Y}(t) = \alpha \cdot X(t) - \beta \tag{2.4}$$

where X is the concentration of mRNA, whose synthesis is competitively inhibited by the metabolite M[2]. The metabolite belongs to the metabolic system, which operates on a timescale much faster than the epigenetic system, to which the enzyme Y belongs. Therefore, it is assumed that the metabolite is always in steady-state in relation to the enzyme (so that Y can be treated as the repressor for X). The constants a, A, and k are comprised of more elementary constants of reactions involving the metabolite, mRNA,

[2]Under the assumption that mRNA precursors are present in constant concentrations, the expression for competitive inhibition is of the same form as non-competitive inhibition [63].

and enzyme. The parameter b represents the degradation of mRNA, which is assumed to be constant. The expression $\alpha \cdot X$ represents the rate of mRNA-controlled enzyme synthesis, with α being a composite parameter containing the rate constant for enzyme synthesis and amino acid concentrations (assumed to be constant). The degradation rate of the enzyme is assumed to be constant, given by β.

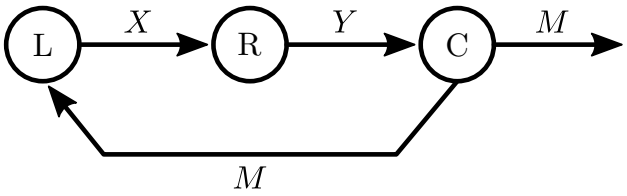

Figure 2.6: In the Goodwin model, mRNA (X) is transcribed from DNA (L) and translated by ribosomes (R) to form an enzyme (Y) catalyzing the formation (C) of a metabolite (M) with the ability to repress production of the mRNA. This forms a negative feedback connection based on repression.

Goodwin was interested in biochemical mechanisms that produce oscillations, as it had become clear that biochemical activities underlying cellular functions do not occur simultaneously at fixed rates. Rather, there is a rhythm to these activities, whereby one after another the activities rise to a maximum and then fall off again [63, 62]. Goodwin worked from the assumption that the occurrence of oscillations in macromolecular concentrations, arising as a consequence of negative feedback, give rise to a time structure in cells [63, 62]. The system in (2.3)–(2.4), known as the Goodwin model, served as an initial mechanism by which oscillations could occur, and in his book, Goodwin went on to study more complex circuits, using the simple Goodwin model as an elementary unit of function [63, 64, 62]. Later, Goodwin also proposed a more general three-variable model in which the degradation terms followed first-order reaction kinetics, regarded to be more realistic than the constant degradation rates in (2.3)–(2.4), but brought about damping in the system such that oscillations would eventually die out [64, 65, 62].

Independently of Goodwin, Manuel Morales and David McKay proposed another mechanism by which oscillations could occur, based on feedback inhibition and cooperativity [124]. This model, strikingly similar to the Goodwin model, differed only in the kinetics of end product feedback and the number of intermediates involved in the pathway [124, 63, 64]. The model proposed by Morales and McKay consisted of a linear pathway in

which the formation of substance S_i from S_{i-1} is catalyzed by enzyme E_{i-1} (Figure 2.7) [124]. The concentration of S_0 is constant, due to replenishment or availability in large amounts, and E_0 is inhibited cooperatively by p molecules of the end product S_n [124]. The model is given by the system of ODEs [124]

$$\dot{S}_1(t) = \frac{k_0 \cdot S_0}{1 + \alpha \cdot S_n(t)^p} - k_1 \cdot S_1(t) \tag{2.5}$$

$$\dot{S}_i(t) = k_{i-1} \cdot S_{i-1}(t) - k_i \cdot S_i(t), \quad i = 2, 3, \ldots, n \tag{2.6}$$

where k_i are first-order rate constants[3], α is the affinity constant of S_n and E_0, and $(1 + \alpha \cdot S_n^p)^{-1}$ is the fraction of active E_0.

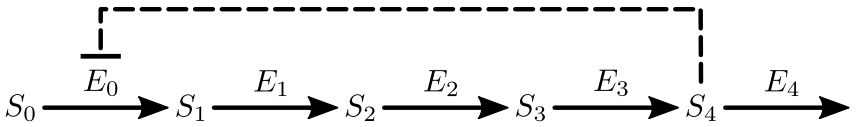

Figure 2.7: The model proposed by Morales and McKay is based on feedback inhibition and cooperativity, and consists of a linear pathway where the formation of substance S_i from S_{i-1} is catalyzed by enzyme E_{i-1}. It is assumed that the concentration of S_0 is constant, due to replenishment or availability in large amounts, and that E_0 is inhibited cooperatively by the end product S_n ($n = 4$ in the figure).

The number of intermediates, together with cooperative feedback inhibition, would prove to be important for the occurrence of sustained oscillations (i.e. limit cycles) [124, 65, 71, 187]. The model proposed by Morales and McKay, although formulated to describe a process different from that of Goodwin's model, served as an extension of the Goodwin model. The same framework was used to model a variety of systems where some form of negative feedback is present, such as the control of tissue growth or feedback regulation of genes for circadian oscillations [71, 62]. These models relied on the generalized Goodwin model [71]

$$\dot{x}_1(t) = f_0(x_n, x_1) - f_1(x_1) \tag{2.7}$$

$$\dot{x}_i(t) = f_{i-1}(x_{i-1}) - f_i(x_i), \quad i = 2, 3, \ldots, n \tag{2.8}$$

where f_0 describes the synthesis of the initial compound x_1, which can depend on the initial compound itself (e.g. autocatalysis), and is inhibited

[3]It is assumed that the reactions driven by enzymes E_i follow Michaelis–Menten kinetics, and that the concentrations of S_i are negligible compared to the corresponding Michaelis constants $K_{\mathrm{M},i}$. These assumptions imply first-order rate constants $k_i = V_{\max,i}/K_{\mathrm{M},i}$ [124].

in some way by the end product x_n. The functions f_i describe the transformation of compound x_i into x_{i+1}, for example by Michaelis–Menten kinetics, first-order kinetics, or by a constant rate.

2.6 Feedback by cross-coupling

There was considerable interest in control mechanisms involving protein synthesis and the regulation of mRNA production at the time, and in particular two questions were considered: One asked under what circumstances stable oscillations could occur, and the other asked what arrangements lead to more than one stable equilibrium point [65, 63, 64]. The latter question was thought to be especially important in relation to the mechanisms of differentiation, which are stable and persistent once induced, and could be explained by mechanisms involving positive feedback [122, 66]. However, over a decade prior, in 1948, Karl-Friedrich Bonhoeffer proposed a set of two-component negative feedback systems in which chemical oscillations could occur [19, 51]. These systems relied on the cross-coupling (cross-catalysis, cross-inhibition) of two simultaneous reactions in order to achieve negative feedback, rather than end product feedback in the Goodwin model [19, 50, 51]. The systems are governed by the ODEs [19]

$$\dot{X}(t) = B_{\mathrm{X}}(t) - Z_{\mathrm{X}}(t) \tag{2.9}$$

$$\dot{Y}(t) = B_{\mathrm{Y}}(t) - Z_{\mathrm{Y}}(t) \tag{2.10}$$

where the chemical species X is coupled to species Y through its synthesis B_{Y} or degradation Z_{Y}, and Y is coupled to X in a similar way (through B_{X} or Z_{X}). However, only certain couplings produce negative feedback. For example, negative feedback is achieved if X activates the synthesis of Y, while Y inhibits the synthesis of X (Figure 2.8) [19]. Interestingly, this is a nearly direct interpretation (albeit simplified) of the mechanism for genetic-metabolic control, proposed by Jacob and Monod[4] (the operon model) [76, 84, 83].

If the inhibitory action of Y in Figure 2.8 is instead activating, positive feedback is obtained [76, 50, 51]. In fact, there are sixteen possible ways to

[4] X is an enzyme produced (B_{X}) from a structural gene under the control of an operator. The enzyme catalyzes the conversion (B_{Y}) of a substrate into the metabolite Y. In turn, the metabolite can increase the affinity of a regulator protein to the operator, which inhibits synthesis of the enzyme [76, 84, 83].

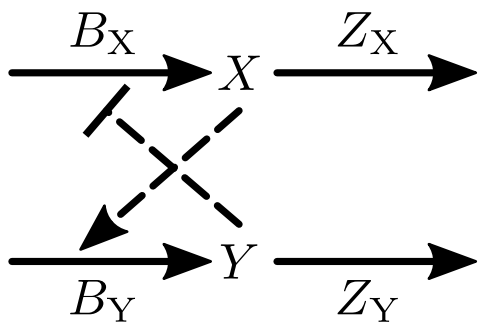

Figure 2.8: Cross-coupling of two simultaneous reactions. Negative feedback is achieved since the inhibition of reaction B_X opposes any change in the concentration of X. For example, if X increases, the synthesis of Y (B_Y) is increased due to activation by X. This increases the level of Y, which in turn increases inhibition of the synthesis of X (B_X).

couple two simultaneous reactions, half of which produce positive feedback, and the other half produce negative feedback [51, 41]. Figure 2.9 shows all of these cross-couplings, indicating the type of feedback formed in each case. The two-component systems can be imagined as simplified versions of larger cross-coupled pathways [76]. This way, the generation and removal reactions of the two components represent net fluxes of combined pathways, and cross-coupling is achieved through activating or inhibitory effects modulating the net fluxes of these combined pathways [76]. In a similar way to how the Goodwin model describes the basic structure of feedback repression, the two-component systems describe the basic structures of interacting pathways or reactions, and how these interactions form positive or negative feedback connections [76, 50, 51].

Biological processes that realize feedback connections, such as the Goodwin model or the two-component systems in Figure 2.9, have been extensively studied from the perspective of oscillations [76, 50, 65, 71, 62, 177]. And as recently as 2017 was the Nobel Prize in Physiology or Medicine awarded jointly to Jeffrey Hall, Michael Rosbash, and Michael Young "for their discoveries of molecular mechanisms controlling the circadian rhythm," a mechanism that relies on negative feedback by repression [131]. However, the existence of periodic solutions often require system parameters to be conveniently chosen, or ideal conditions to be assumed [195, 65, 179, 62]. A much more common property of such systems is the existence of a stable equilibrium point [65, 195, 187, 186]. It is only fairly recently that regulatory mechanisms in biological systems have been comprehen-

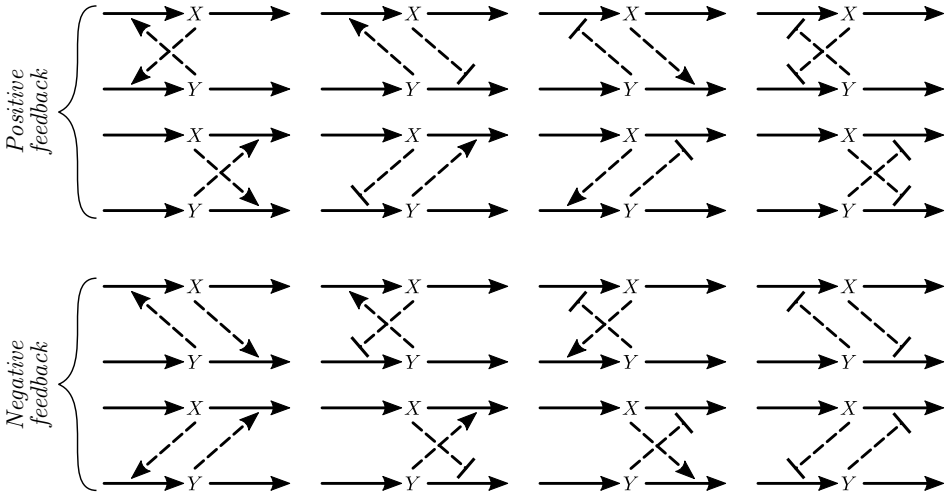

Figure 2.9: There are sixteen possible ways to couple of two simultaneous reactions, half of which produce positive feedback, and the other half produce negative feedback.

sively studied in terms of robust control, in which stability plays a crucial role [152, 205, 45, 129, 41, 21]. The reason for this new focus on robustness of biological control processes is the observation that many physiological processes are tightly regulated and show perfect adaptation to environmental disturbances [129, 41]. The ability of organisms to resist external disturbances is essential for the maintenance of stable internal conditions and the proper function of physiological processes [41, 25]. It is from the perspective of robust control that we will consider the negative feedback structures in Figure 2.9 in this thesis. And although stability can be achieved with positive feedback connections, we will see in the following that negative feedback plays a crucial role in achieving robust perfect adaptation to disturbances [41, 186, 92, 66, 187].

Chapter 3

Homeostatic controller motifs

In this chapter, we will look at so-called *homeostatic controller motifs*, which are variants of the cross-coupled negative feedback structures discussed in the previous chapter. Notably, the homeostatic controller motifs are stable regulatory mechanisms that show robust control, as opposed to the oscillatory behavior of many feedback mechanisms studied in the past. We start by defining a mathematical model for the homeostatic controller motifs. We then use this model to show global asymptotic stability. Because the homeostatic controller motifs are stable, and because they form negative feedback connections with integral action, robustness to disturbances is ensured. However, realizing a constant steady-state for the regulated variable is not always possible, resulting in only partial adaptation to disturbances. We show what condition must be satisfied to achieve near-perfect adaptation. In the last part of this chapter we present some alternative negative feedback motifs in which integral action and robust control are realized.

3.1 Homeostatic controller motifs defined

Homeostasis refers to the ability of organisms and cells to maintain a stable internal environment, even in the presence of disturbances from the external environment. On the cellular level, many chemical species, such as ions, metabolites, and proteins, are tightly regulated [45, 178, 205, 41, 17]. The term homeostasis was coined by Walter Cannon, who defined it as a system subjected to external disturbances, causing system-internal disturbances that are compensated for by bringing automatic adjustments into action, thereby keeping the internal conditions fairly constant [25]. Although

Cannon emphasized that homeostasis does not imply perfect adaptation to disturbances, but rather involves some variability in the steady-state, homeostasis is often associated with the maintenance of constant conditions by negative feedback regulation [125, 25, 143].

Homeostatic controller motifs are variants of the cross-coupled two-component structures discussed in the previous chapter. In the homeostatic controller motifs, the two species are generated and turned over in synthesis and degradation reactions, and are coupled together through reactions that activate or inhibit these synthesis and degradation reactions. Through these coupling reactions, the two species form a negative feedback connection. For the homeostatic controller motifs, a deviation in steady-state of one species, called the *controlled* or *regulated species*, results in an action that opposes the deviation. This compensatory action is mediated through the *compensatory flux*, which is controlled by the second species, called the *controller species*. The compensatory flux represents either the synthesis or degradation reaction of the regulated species. The controller species "measures" the regulated species through the so-called *measurement flux*, which represents the synthesis or degradation of the controller species. The measurement and compensatory fluxes are either activated or inhibited by the regulated and controller species, respectively, giving eight possible combinations that produce negative feedback (Figure 3.1) [41]. These structures are identical to the eight cross-coupled negative feedback structures discussed in the previous chapter (see Figure 2.9), however, the homeostatic controller motifs show robust homeostatic control, as opposed to the oscillatory behavior of the cross-coupled two-component systems discussed so far [41, 51].

Based on whether the compensatory flux represents the synthesis or degradation of the regulated species, the homeostatic controller motifs are classified as inflow or outflow controllers, respectively. Additionally, the way in which the controller species affects the compensatory flux, i.e. by activation or inhibition, decides whether the controller motifs are classified as activating or inhibiting [41]. The complete set of all eight homeostatic controller motifs are shown in Figure 3.1, grouped by inflow and outflow controllers, indicating compensatory (blue) and measurement (red) fluxes, as well as controller type (activating or inhibiting) for each controller.

The homeostatic controller motifs are described by the flux balance

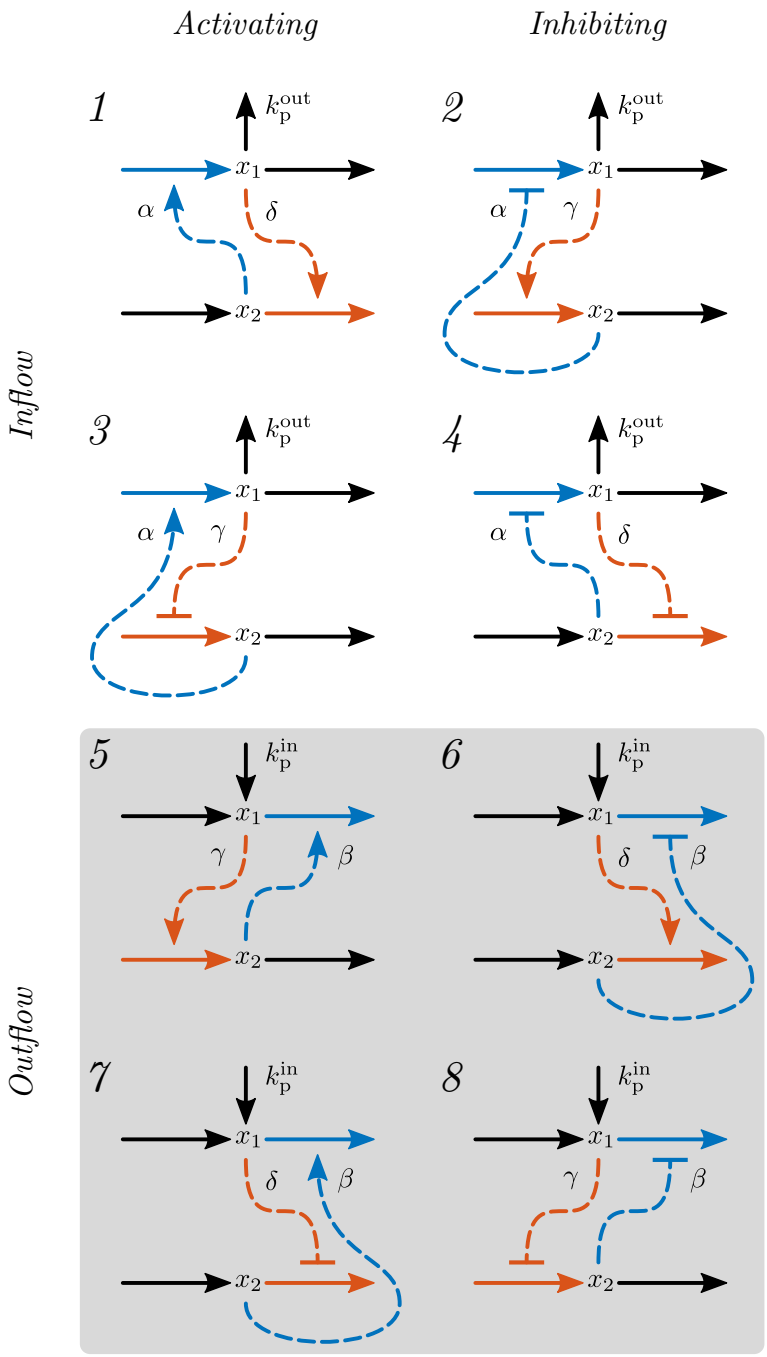

Figure 3.1: (Caption on the following page)

Figure 3.1: Complete set of all eight homeostatic controller motifs, where x_1 represents the regulated species and x_2 represents the controller species. Inflow controllers are shown in the top panel (white background), and outflow controllers in the bottom panel (gray background). Activating controllers are grouped in the left column, and inhibiting controllers are grouped in the right column. The x_2-mediated compensatory fluxes are indicated by blue coloring, while the x_1-mediated measurement fluxes are indicated by red. The type of cross-coupling reactions between x_1 and x_2 are indicated by dashed lines with arrowhead for activation and flat head for inhibition (α, β, γ, and δ). The small vertical arrows indicate perturbations in the regulated species, outflow perturbations ($k_\mathrm{p}^\mathrm{out}$) for inflow controllers, and inflow perturbations (k_p^in) for outflow controllers.

equations

$$\dot{x}_1(t) = \pm j_{\mathrm{b},1}(x_1) \mp j_\mathrm{comp}(x_1, x_2) \pm j_\mathrm{pert}(x_1) \tag{3.1}$$

$$\dot{x}_2(t) = \pm j_{\mathrm{b},2}(x_2) \mp j_\mathrm{meas}(x_1, x_2) \tag{3.2}$$

where x_1 and x_2 are concentrations of the regulated and controller species, respectively, $j_{\mathrm{b},i}$ are fluxes for basal synthesis or degradation of the species, j_comp is the compensatory flux, and j_meas is the measurement flux. The flux j_pert represents an uncontrolled perturbation in the regulated species. Plus-minus signs indicate generation or removal reactions[1] (plus for generation and minus for removal). The basal fluxes ($j_{\mathrm{b},i}$) are not involved in cross-coupling of the two species. Depending on whether these fluxes represent synthesis or degradation, we let $j_{\mathrm{b},i}$ follow either zero-order kinetics or Michaelis–Menten kinetics with respect to x_i

$$j_{\mathrm{b},i}(x_i) = \begin{cases} k_{\mathrm{s},i}, & \text{for synthesis} \\ \frac{k_{\mathrm{d},i} \cdot x_i(t)}{K_{\mathrm{M},i} + x_i(t)}, & \text{for degradation} \end{cases} \tag{3.3}$$

where $k_{\mathrm{s},i}$ is a rate constant for the basal synthesis of x_i, the constant $k_{\mathrm{d},i}$ represents the limiting degradation rate (V_max), and $K_{\mathrm{M},i}$ is the Michaelis constant for the degradation reaction. Note that we consider the synthesis reaction to be enzyme catalyzed, however, it is assumed that the concentration of substrate is constant (e.g. due to replenishment), such that the rate expression is reduced to a constant ($k_{\mathrm{s},i}$).

The compensatory flux j_comp consists of two parts. Like $j_{\mathrm{b},i}$, the first part is given by a zero-order reaction if representing a synthesis reaction,

[1] Note that there is a connection between the various plus-minus signs in the flux balance equations. For example, if $j_{\mathrm{b},1}$ is positive (basal synthesis), then j_comp is negative (outflow controller).

and the Michaelis–Menten equation if representing a degradation reaction. The second part depends on whether the compensatory flux is activated or inhibited by the controller species x_2

$$j_{\text{comp}}(x_1, x_2) = \begin{cases} j_{\text{b},1}(x_1) \cdot f_{\text{act}}(x_2), & \text{for activation} \\ j_{\text{b},1}(x_1) \cdot f_{\text{inh}}(x_2), & \text{for inhibition} \end{cases} \tag{3.4}$$

where $j_{\text{b},1}$ is given by (3.3), and f_{act} and f_{inh} are expressions for activation and inhibition, respectively. We let the activation reaction to be given by allosteric activation (using a special case of mixed activation) [31, 91]

$$f_{\text{act}}(x_i) = \frac{x_i(t)}{K_{\text{A},i} + x_i(t)} \tag{3.5}$$

where the degree of activation is determined by the level of x_i, with activation constant $K_{\text{A},i}$. Similarly, we let the inhibition reaction be given by allosteric inhibition (using a special case of mixed inhibition) [31, 91]

$$f_{\text{inh}}(x_i) = \frac{K_{\text{I},i}}{K_{\text{I},i} + x_i(t)} \tag{3.6}$$

where the level of x_i determines the degree of inhibition, and $K_{\text{I},i}$ is an inhibition constant. Figure 3.2 shows how the activation and inhibition reactions in (3.5) and (3.6) affect the reaction rate of an enzyme catalyzed reaction. Note that both f_{act} and f_{inh} saturates as x_i increases. That is, the relative increase in activation/inhibition is reduced as x_i grows. Furthermore, both f_{act} and f_{inh} take values in the range $[0, 1]$, where 0 represents no activation (or maximum inhibition) and 1 represents maximum activation (or no inhibition)[2].

The measurement flux is given in a similar way to the compensatory flux, but the regulated species and the controller species have swapped roles. The measurement flux is given by

$$j_{\text{meas}}(x_1, x_2) = \begin{cases} j_{\text{b},2}(x_2) \cdot f_{\text{act}}(x_1), & \text{for activation} \\ j_{\text{b},2}(x_2) \cdot f_{\text{inh}}(x_1), & \text{for inhibition} \end{cases} \tag{3.7}$$

[2]Using saturable functions with the same normalized range for both activation and inhibition makes it possible to evaluate activating and inhibiting controller motifs in an objective manner. Several previous works from our group ([41, 182, 176]) and others ([46, 21, 23]) have used linear (non-saturating) activation.

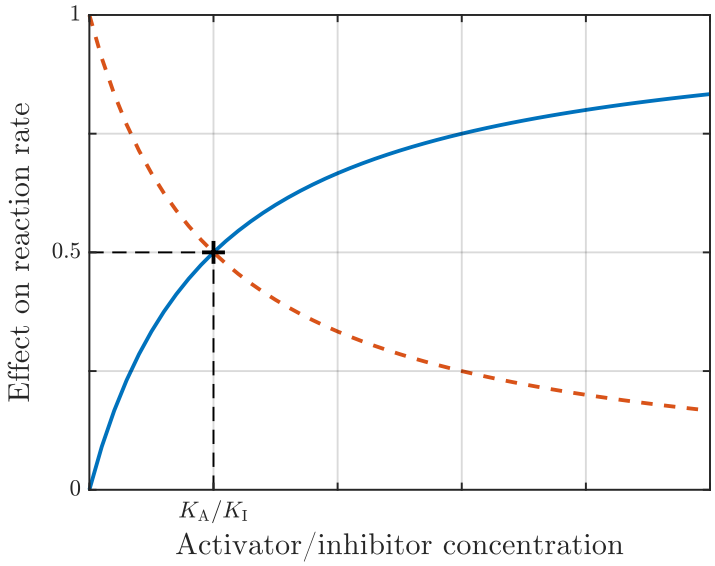

Figure 3.2: Effect of the activation (solid blue line) and inhibition (dashed red line) reactions in (3.5) and (3.6), respectively, on the reaction rate of an enzyme catalyzed reaction. At activator concentration equal to K_A and inhibitor concentration equal to K_I, the limiting rate of the enzyme reaction is half of its maximum value.

where $j_{b,2}$ is given by (3.3), and f_{act} and f_{inh} are given by (3.5) and (3.6), respectively.

Finally, the perturbation flux j_{pert} is given by zero-order kinetics if representing an inflow disturbance, and first-order kinetics if representing an outflow disturbance (with respect to x_1)

$$j_{pert}(x_1) = \begin{cases} k_p^{in}, & \text{for inflow} \\ k_p^{out} \cdot x_1(t), & \text{for outflow} \end{cases} \tag{3.8}$$

where k_p^{in} and k_p^{out} are rate constants for the inflow and outflow disturbance reactions.

We insert the reaction kinetic expressions described above into the flux balance equations in (3.1)–(3.2), and can then express a mathematical model for the homeostatic controller motifs

$$\dot{x}_1(t) = k_{s,1} \cdot \alpha(x_2) - f_{d,1}(x_1) \cdot \beta(x_2) \tag{3.9}$$
$$\dot{x}_2(t) = k_{s,2} \cdot \gamma(x_1) - f_{d,2}(x_2) \cdot \delta(x_1) \tag{3.10}$$

where $k_{\mathrm{s},i}$ are rate constants for the basal synthesis of x_i and $f_{\mathrm{d},i}$ are expressions for the basal degradation of x_i, given by (3.3), and α, β, γ, δ are expressions for activating or inhibiting reactions, given by (3.5) and (3.6).

For now, we disregard the disturbance j_{pert} given by (3.8), and look at the stability of the unperturbed system. However, we will return to the effect of disturbances in our discussion on integral action and robustness in Section 3.4. As shown in Figure 3.1, only one of the expressions α and β, and one of γ and δ, are present for a given controller motif. For example, inflow controller 1 achieves negative feedback using cross-coupling reactions α and δ, while the other two cross-coupling reactions are considered to be constant ($\beta = \gamma = 1$). The reaction associated with the regulated species that is affected by α or β is the compensatory flux (j_{comp}), while the other reaction is the x_1-associated basal flux ($j_{\mathrm{b},1}$). Similarly, the reaction associated with the controller species that is affected by γ or δ is the measurement flux (j_{meas}), while the other reaction is the x_2-associated basal flux ($j_{\mathrm{b},2}$). The mathematical model in (3.9)–(3.10) describes the dynamical behavior of the system shown in Figure 3.3, which is a general description for the homeostatic controller motifs.

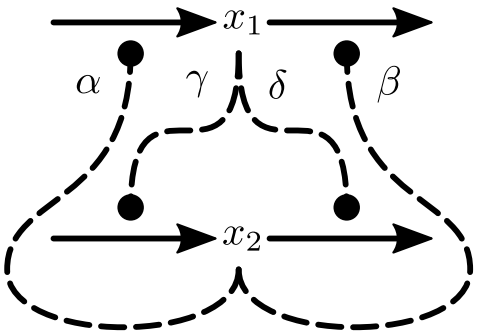

Figure 3.3: General description of the two-component homeostatic controller motifs. The two components are generated and turned over in synthesis and degradation reactions. These reactions are activated or inhibited by the other component through cross-coupling reactions (α, β, γ, δ). For each controller motif, there are only two such cross-coupling reactions, one from the regulated species (x_1) acting on the synthesis or degradation of the controller species (x_2), and one from the controller species acting on the synthesis or degradation of regulated species.

We have chosen to consider saturation kinetics for most of the reactions involved in the homeostatic controller motifs. In this way, we aim to extend prior analyses of the controller motifs to highly nonlinear interactions [41,

182, 176]. And although we have chosen to consider certain expressions for the reactions involved, there are of course other reaction kinetic expressions we could have used. For example, the cross-coupling reactions could follow Hill kinetics (i.e. cooperative activation/inhibition) instead of mixed activation/inhibition. In this chapter, we will consider the homeostatic controller motifs as specified above, however, throughout this thesis we will look at other variants of the homeostatic controller motifs, and try to indicate how general conclusions can be extended to include different reaction kinetic expressions as well.

3.2 Homeostatic controller motifs in cellular control processes

Homeostatic controller motifs have been identified as possible control mechanisms in a wide variety of cellular control processes [41, 178, 81, 2, 185]. For example, in mammalian iron homeostasis, a combination of inflow and outflow controllers have been identified (Figure 3.4a) [41]. At low iron concentrations, iron-responsive element-binding protein 1 and 2 (IRP1 and IRP2) stabilize mRNAs of iron-utilizing proteins by binding to iron-responsive elements, thereby decreasing iron sequestration, and activating the import of iron via transferrin receptors. In turn, as the iron level increases, the F-box protein FBXL5 is stabilized and mediates the proteasomal degradation of IRP2. This forms a negative feedback connection for the import of iron which is similar to inflow controller 1 (see Figure 3.1), where IRP2 (together with IRP1) functions as the controller species, and iron as the regulated species [41]. At high iron concentrations, active IRP levels are low due to the proteasomal degradation of IRP2 and a transformation of IRP1 to an aconitase. Iron is then exported out of the cell by the iron-induced transporter ferroportin, which is regulated by the binding of hepcidin, leading to internalization and degradation of ferroportin. This forms another negative feedback connection, but for the export of iron, which is similar to outflow controller 5, where ferroportin functions as the controller species, and iron as the regulated species [41].

Homeostatic controller motifs have also been identified in the regulatory mechanisms for Na^+/K^+ homeostasis in enterocytes (Figure 3.4b) [178]. Active uptake of glucose via the SGLT1 cotransporter in intestinal epithelial enterocytes imports two Na^+ ions for every glucose molecule, and hence,

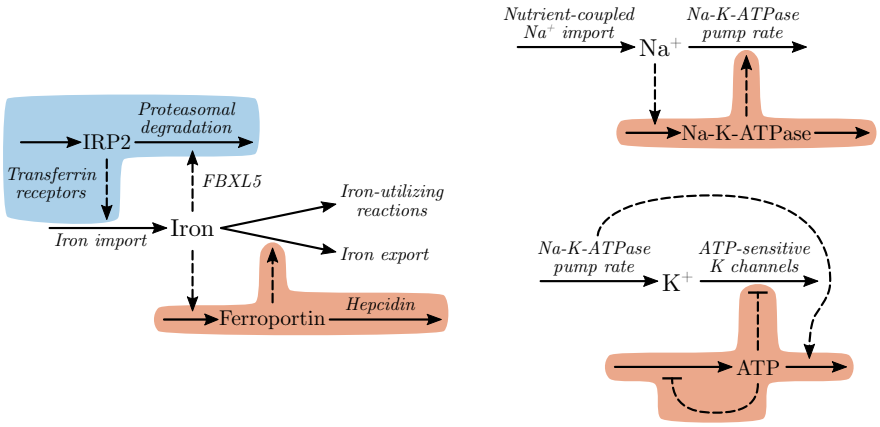

(a) Mammalian iron homeostasis. **(b)** Ionic Na^+/K^+ homeostasis.

Figure 3.4: The combined inflow and outflow controller structure found in mammalian iron homeostasis is shown in panel (a). At low iron concentrations, IRP2 (together with IRP1) activates iron import via the production of transferrin receptors (compensatory flux). As the iron level increases, FBXL5 is stabilized and mediates the proteasomal degradation of IRP2 (measurement flux). This forms a controller for the inflow of iron at low concentrations (blue background). At high iron concentrations, active IRP levels are low due to degradation of IRP2 and a transformation of IRP1 to an aconitase. Iron is then exported out of the cell by the iron-induced (measurement flux) transporter ferroportin (compensatory flux). The binding of hepcidin leads to internalization and degradation of ferroportin, and interestingly, hepcidin has a relatively strong binding affinity for ferroportin, suggesting a possible near zero-order degradation of ferroportin [41]. This forms an outflow controller for iron at high concentrations (red background). Panel (b) shows the mechanism for ionic Na^+/K^+ homeostasis in enterocytes. While Na-K-ATPase exports excess intracellular Na^+ (compensatory flux), it has been suggested that the amount of active Na-K-ATPase is directly controlled by the concentration of intracellular Na^+ (measurement flux). This forms an outflow controller for intracellular Na^+ (top figure, red background). Increased ATP usage by Na-K-ATPase causes a reduction in intracellular ATP (measurement flux), relieving the inhibition of basolateral ATP-sensitive K channels (compensatory flux). This forms an outflow controller regulating the export of K^+ (bottom figure, red background). Intracellular K^+ is considered the regulated species due to the dependency of Na-K-ATPase pump rate on serosal membrane potential [178].

enterocytes require a regulatory mechanism that responds to excess intracellular Na^+ [178]. The Na-K-ATPase membrane protein plays a major role in this regulation by exporting Na^+ ions, coupled to uptake of K^+ ions, thereby maintaining the Na^+ gradient that drives active uptake of glucose [178]. It has been proposed that the amount of active Na-K-ATPase in enterocytes is directly controlled by the concentration of intracellular Na^+, and that this regulation, together with a regulation of basolateral K permeability by intracellular ATP, gives enterocytes the ability to maintain ionic Na^+/K^+ homeostasis [178]. This mechanism establishes a negative feedback connection for the export of Na^+, similar to outflow controller 5, where Na^+ is regulated by adjusting the number of Na-K-ATPase transporter proteins. Increased Na-K-ATPase pump activity during nutrient uptake is accompanied by an increase in the basolateral K permeability, believed to be caused by a reduction in intracellular ATP due to increased ATP usage by Na-K-ATPase, which relieves inhibition of basolateral ATP-sensitive K channels [178]. Thus, another negative feedback connection is formed, where ATP functions as a controller regulating the export of K^+, in a structure similar to outflow controller 6 [178].

3.3 Stability of homeostatic controller motifs

Mathematical models of biochemical networks play an important role in elucidating the mechanisms behind homeostatic behaviors. Of particular interest is the characterization of control theoretic properties such as stability and robustness [43, 41, 42, 186]. These properties imply the inclusion of a subsystem that can recreate and compensate for certain exogenous signals, known as the *internal model principle* (IMP) [161, 176, 92]. In particular, adaptation to constant exogenous signals (stepwise changes) implies the presence of integral feedback [161, 176, 92]. However, in order to establish robustness for the homeostatic controller motifs, we first need to establish stability.

3.3.1 Notes on existence and uniqueness

In the mathematical model for the homeostatic controller motifs, given by (3.9)–(3.10), the system states x_1 and x_2 represent physical concentrations of compounds. Since concentrations are non-negative quantities, a global

result corresponds to non-negative values for the states. To show this, we note that the degradation expressions satisfy $f_{\mathrm{d},i}(0) = 0$ and

$$f_{\mathrm{d},i}(x_i), \alpha(x_i), \beta(x_i), \gamma(x_i), \delta(x_i) \geq 0 \quad \forall\ x_i \geq 0 \tag{3.11}$$

which ensures invariance of the non-negative orthant $\mathbb{R}^2_{\geq 0}$ (first quadrant) [9]. The equilibrium point (x_1^*, x_2^*) is found by setting $\dot{x}_1 = \dot{x}_2 = 0$, and solving for the states. The existence of a non-negative equilibrium point requires a balance between inflow and outflow reactions. We illustrate this point with an analogy to a couple of water tanks with drains at the bottom, arranged such that one tank is drained into the other, shown in Figure 3.5 [195]. The topmost tank is filled by a constant source of water, through a valve whose position is determined by the water level in the bottom tank. For a low water level in the bottom tank, the valve is opened, and for a high water level the valve is closed. This realizes a negative feedback structure similar to the homeostatic controller motifs. If the drain in the topmost tank is too small compared to the drain of the bottom tank, the bottom tank will not fill, resulting in an open valve and a large inflow of water into the top tank. If the drain in the top tank is also too small compared to the inflow of water, the top tank will overflow. For the homeostatic controller motifs, this corresponds to a situation where the regulated species accumulates, while the controller species is removed entirely. In this case, the system parameters have values such that an equilibrium point does not exist. Just like the water tanks need a balance between inflow and outflow to avoid overflowing or emptying, the homeostatic controller motifs need a balance between inflow and outflow reactions of the two species for an equilibrium point to exist.

We assume that a positive equilibrium point for the system in (3.9)–(3.10) exists. Then, it can be shown that the equilibrium point is also unique. We separate the system into a process and a controller, where the process represents the basic function of the system, while the controller implements manipulations to improve stability, robustness, and performance of this function [40]. Hence, the process is given by the differential equation describing the dynamics of the regulated species (x_1), and the controller is given by the differential equation describing the dynamics of the controller species (x_2). This separation is shown in Figure 3.6, where the control action is the process (P) input, and the process output is the controller (C) input.

By characterizing the steady-state input-output relationships for the process and controller, we find the equilibrium point of the closed-loop

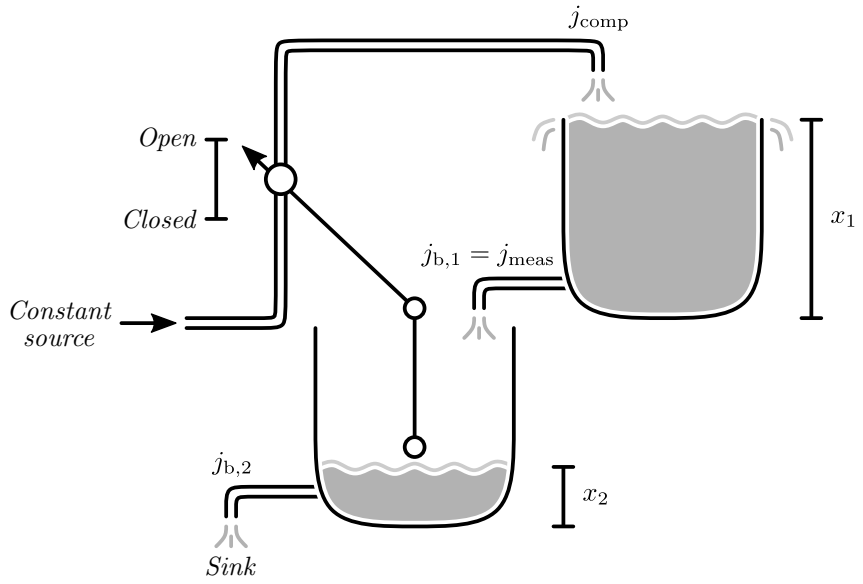

Figure 3.5: A couple of water tanks with drains at the bottom, arranged such that the topmost tank is drained into the bottom tank. The water levels in the top and bottom tanks are represented by the states x_1 and x_2, respectively. The top tank is filled by a constant source, through a valve whose position is determined by the water level in the bottom tank. For a low water level, the valve is in an open position, and for a high water level the valve is in a closed position. Thus, the inflow of water into the top tank is analogous to the compensatory flux (j_{comp}) in the homeostatic controller motifs. The water drained from the top tank into the bottom tank is analogous to the measurement flux, in the special case where the measurement flux happens to be equal to the basal degradation of the regulated species ($j_{\text{b},1} = j_{\text{meas}}$). Finally, the water drained from the bottom tank into the sink is analogous to the basal degradation of the controller species ($j_{\text{b},2}$). For the example illustrated in this figure, the drain hole in the top tank is too small compared to the drain hole in the bottom tank, resulting in the bottom tank being drained. In turn, this leaves the valve in an open position, filling the top tank. Since the drain hole in the top tank is also too small compared to the inflow of water, this results in overflowing of the top tank. This illustrates the balance of system parameters that is necessary for an equilibrium point to exist.

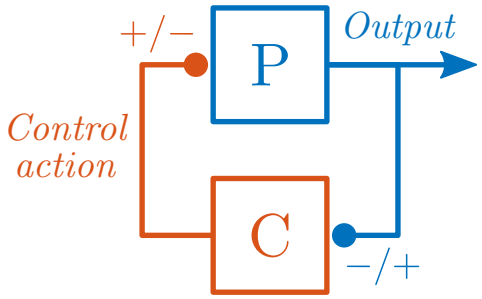

Figure 3.6: Separation of the homeostatic controller motifs into a process (P, blue) and a controller (C, red). The process output is fed into the controller, which produces a control action that is fed back into the process. Negative feedback is realized by having the process output negatively affect the controller output, which in turn positively affects the process output, or by having the process output positively affect the controller output, which in turn negatively affects the process output. The intersection of the steady-state input-output response curves (nullclines) for the process and controller gives the steady-state (equilibrium point) of the closed-loop system.

system as the intersection of these steady-state response curves [6, 82]. Such response curves are known as nullclines, which we will take a closer look at in Chapter 4. Here, we simply note that the nullclines for the homeostatic controller motifs in general take the form

$$x_1^{\text{ss}} = f_{\text{d},1}^{-1}\left(\frac{k_{\text{s},1}\cdot\alpha(x_2^{\text{ss}})}{\beta(x_2^{\text{ss}})}\right) \tag{3.12}$$

$$x_2^{\text{ss}} = f_{\text{d},2}^{-1}\left(\frac{k_{\text{s},2}\cdot\gamma(x_1^{\text{ss}})}{\delta(x_1^{\text{ss}})}\right) \tag{3.13}$$

and, for each individual homeostatic controller motif, it can be verified that these steady-state response curves will only intersect at most in one point for non-negative steady-states. This fact comes from the property that the functions $f_{\text{d},i}$, α, β, γ, and δ are strictly monotone (either strictly increasing or strictly decreasing), and that the homeostatic controller motifs are arranged in a negative feedback connection [6, 82]. Figure 3.7 shows the process and controller nullclines for outflow controller 7, indicating the intersection that represents the equilibrium point for the closed-loop system. The following stability result implies that if a non-negative equilibrium point exists, it must also be unique. Therefore, instead of explicitly showing that the equilibrium point is unique, we will assume that it is, and let uniqueness be implied by the stability result obtained.

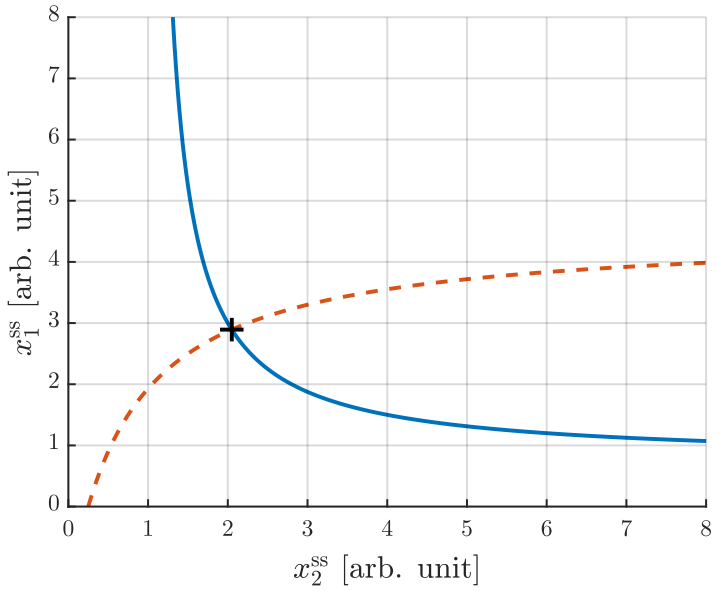

Figure 3.7: Process (solid blue line) and controller (dashed red line) nullclines for outflow controller 7, given by system parameters defined in Section 3.3.3. Since the process nullcline is strictly decreasing and the controller nullcline is strictly increasing, only one intersection of the nullclines is possible (for non-negative steady-states). Therefore, the equilibrium point (x_1^*, x_2^*) must be unique.

3.3.2 Global asymptotic stability

To show stability of the homeostatic controller motifs, we consider the general system in (3.9)–(3.10), and start by performing the change of variables: $z_1 = x_1 - x_1^*$ and $z_2 = x_2 - x_2^*$, where (x_1^*, x_2^*) is the equilibrium point of the system. This way, the equilibrium point is shifted to the origin, giving the system

$$\dot{z}_1(t) = -f_1(z_1) + h_{2,\alpha}(z_2) - g_1(z_1) \cdot h_{2,\beta}(z_2) \tag{3.14}$$
$$\dot{z}_2(t) = -f_2(z_2) + h_{1,\gamma}(z_1) - g_2(z_2) \cdot h_{1,\delta}(z_1) \tag{3.15}$$

where we use the following definitions

$$f_1(z_1) = (f_{\mathrm{d},1}(z_1 + x_1^*) - f_{\mathrm{d},1}(x_1^*)) \cdot \beta(x_2^*) \tag{3.16}$$
$$f_2(z_2) = (f_{\mathrm{d},2}(z_2 + x_2^*) - f_{\mathrm{d},2}(x_2^*)) \cdot \delta(x_1^*) \tag{3.17}$$
$$g_1(z_1) = f_{\mathrm{d},1}(z_1 + x_1^*) \tag{3.18}$$
$$g_2(z_2) = f_{\mathrm{d},2}(z_2 + x_2^*) \tag{3.19}$$

$$h_{1,\gamma}(z_1) = (\gamma(z_1 + x_1^*) - \gamma(x_1^*)) \cdot k_{\mathrm{s},2} \tag{3.20}$$
$$h_{1,\delta}(z_1) = \delta(z_1 + x_1^*) - \delta(x_1^*) \tag{3.21}$$
$$h_{2,\alpha}(z_2) = (\alpha(z_2 + x_2^*) - \alpha(x_2^*)) \cdot k_{\mathrm{s},1} \tag{3.22}$$
$$h_{2,\beta}(z_2) = \beta(z_2 + x_2^*) - \beta(x_2^*) \tag{3.23}$$

and relationships

$$\alpha(x_2^*) = \frac{f_{\mathrm{d},1}(x_1^*) \cdot \beta(x_2^*)}{k_{\mathrm{s},1}} \tag{3.24}$$
$$\delta(x_1^*) = \frac{k_{\mathrm{s},2} \cdot \gamma(x_1^*)}{f_{\mathrm{d},2}(x_2^*)} \tag{3.25}$$

Note that $f_i(0) = 0$ and that f_i are strictly increasing for the interval $[-x_i^*, \infty)$. Additionally, $h_{1,\gamma}(0) = h_{1,\delta}(0) = h_{2,\alpha}(0) = h_{2,\beta}(0) = 0$, and if we define (3.20)–(3.23) to be negative if the corresponding α, β, γ, δ are inhibiting, then (3.20)–(3.23) are also strictly increasing for the interval $[-x_i^*, \infty)$[3]. The functions $g_i \geq 0$ for the same interval. As mentioned before, only one of the functions α and β, and one of the functions γ and δ, are present for a given controller motif (the remaining two are set equal to 1). This means that only one of the functions $h_{2,\alpha}$ and $h_{2,\beta}$, and one of the functions $h_{1,\gamma}$ and $h_{1,\delta}$, are non-zero for a given controller motif. Thus, the shifted system in (3.14)–(3.15) can be reduced to

$$\dot{z}_1(t) = -f_1(z_1) \pm g_1(z_1) \cdot h_2(z_2) \tag{3.26}$$
$$\dot{z}_2(t) = -f_2(z_2) \mp g_2(z_2) \cdot h_1(z_1) \tag{3.27}$$

where $h_1(z_1) = \pm h_{1,\gamma}(z_1) \vee \pm h_{1,\delta}(z_1)$ and $h_2(z_2) = \pm h_{2,\alpha}(z_2) \vee \pm h_{2,\beta}(z_2)$, depending on the particular controller motif. For inhibiting cross-coupling reactions, we define the corresponding functions (3.20)–(3.23) to be negative. Thus, for the system in (3.26)–(3.27) the signs of the last terms are determined from the system in (3.14)–(3.15) (plus for inflow and minus for outflow), with a change of sign if h_i represents inhibition (see Section 3.3.3 for an example). The functions f_i and g_i are given as above, however, for controller motifs that use cross-coupling reactions α or γ, we define the associated $g_i = 1$, so that the reduced system in (3.26)–(3.27) encompasses these controller motifs as well. Note that since all the homeostatic controller

[3]For example, if δ is inhibiting, then $h_{1,\delta}$ is strictly decreasing. However, the negative function $-h_{1,\delta}$ is strictly increasing.

motifs form negative feedback connections, the sign of the last term in (3.26) will always be opposite to the last term of (3.27).

We can now express the system in (3.26)–(3.27) as a negative feedback connection of the two subsystems

$$H_1 : \begin{cases} \dot{z}_1(t) = -f_1(z_1) + g_1(z_1) \cdot u_1(t) \\ y_1(t) = h_1(z_1) \end{cases} \tag{3.28}$$

$$H_2 : \begin{cases} \dot{z}_2(t) = -f_2(z_2) + g_2(z_2) \cdot u_2(t) \\ y_2(t) = h_2(z_2) \end{cases} \tag{3.29}$$

where negative feedback is formed by having

$$u_1 = -y_2,\ u_2 = y_1 \quad \text{or} \quad u_1 = y_2,\ u_2 = -y_1 \tag{3.30}$$

depending on the particular controller motif. This gives a similar separation of the homeostatic controller motifs into a process (H_1) and a controller (H_2) as shown in Figure 3.6.

Next, we consider the two subsystems H_1 and H_2 individually, to show that they are output strictly passive. We use the storage function S_i for subsystem H_i

$$S_i(z_i) = \int_0^{z_i} \frac{h_i(\sigma)}{g_i(\sigma)} \mathrm{d}\sigma \tag{3.31}$$

which has a derivative along trajectories given by

$$\dot{S}_i(z_i) = \frac{h_i(z_i)}{g_i(z_i)} \cdot \dot{z}_i = -f_i(z_i) \cdot \frac{h_i(z_i)}{g_i(z_i)} + u_i \cdot y_i \tag{3.32}$$

where we use that $y_i = h_i(z_i)$. Subsystem H_i is said to be output strictly passive if the following inequality is satisfied [92, 158]

$$\dot{S}_i(z_i) \leq -y_i \cdot \rho_i(y_i) + u_i \cdot y_i \tag{3.33}$$

where $y_i \cdot \rho_i(y_i) > 0 \ \forall \ y_i \neq 0$. A system is said to be passive if the energy stored in the system over a period of time is not greater than the energy supplied to the system over the same period [92, 158]. For (3.33), this means that the input "power" to the system, $u_i \cdot y_i$, is greater than or equal to the rate of change of the stored "energy" in the system, $\dot{S}$. Additionally, (3.33) contains an "excess" of passivity due to the term $-y_i \cdot \rho_i(y_i)$, meaning

that the energy supplied to the system over a period of time will always be greater than the increase in stored energy, unless the output y_i is identically zero [92]. For the homeostatic controller motifs, we choose $y_i \cdot \rho_i(y_i) = p_i \cdot y_i^2$, where p_i is a positive constant. The inequality in (3.33) is then satisfied if

$$0 < p_i \leq \frac{f_i(z_i)}{h_i(z_i) \cdot g_i(z_i)} \tag{3.34}$$

for the interval $[-x_i^*, \infty)$. From the definition of the system in (3.26)–(3.27), it can be seen that the right-hand side expression of (3.34) is positive for this interval, and that it is monotone. Then, (3.34) is satisfied by finding p_i as the lower bound of the right-hand side expression, which is given by [186]

$$\begin{aligned} p_i &= \min_{-x_i^* \leq z_i < \infty} \frac{f_i(z_i)}{h_i(z_i) \cdot g_i(z_i)} \\ &= \min \left\{ \lim_{z_i \to -x_i^{*+}} \frac{f_i(z_i)}{h_i(z_i) \cdot g_i(z_i)}, \lim_{z_i \to \infty} \frac{f_i(z_i)}{h_i(z_i) \cdot g_i(z_i)} \right\} \end{aligned} \tag{3.35}$$

Thus, (3.33) is satisfied, showing that subsystems (3.28) and (3.29) are output strictly passive with storage functions given by (3.31).

It has been shown that a negative feedback connection of two output strictly passive subsystems is asymptotically stable if the subsystems are zero-state detectable [158]. Let us consider the general system

$$H : \begin{cases} \dot{z}(t) = f(z, u) \\ y(t) = h(z, u) \end{cases} \tag{3.36}$$

and set $u = 0$. H is said to be zero-state detectable if the origin is asymptotically stable conditionally to Z, where Z is the largest positively invariant set contained in $\{z \in \mathbb{R}^n \mid y = h(z, 0) = 0\}$ [158]. For the special case when $Z = \{0\}$, the system H is said to be zero-state observable [158, 92]. For subsystems H_1 and H_2 in (3.28) and (3.29), we let $u_1 = u_2 = 0$, and see that

$$y_1 = y_2 = 0 \implies z_1 = z_2 = 0 \tag{3.37}$$

Therefore, subsystems H_1 and H_2 are zero-state observable if the origins of the unforced subsystems, given by system equations $\dot{z}_i = -f_i(z_i)$, are

locally asymptotically stable [92, 158]. Linearization at the origin gives

$$H_1 : -\frac{\partial f_1}{\partial z_1}(z_1)\bigg|_{z_1=0} = -\frac{k_{\mathrm{d},1} \cdot K_{\mathrm{M},1}}{(K_{\mathrm{M},1} + x_1^*)^2} \cdot \beta(x_2^*) < 0 \tag{3.38}$$

$$H_2 : -\frac{\partial f_2}{\partial z_2}(z_2)\bigg|_{z_2=0} = -\frac{k_{\mathrm{d},2} \cdot K_{\mathrm{M},2}}{(K_{\mathrm{M},2} + x_2^*)^2} \cdot \delta(x_1^*) < 0 \tag{3.39}$$

which shows local asymptotic stability.

We now consider the full negative feedback connection of H_1 and H_2. Negative feedback is formed by (3.30), which gives the derivative along trajectories of the combined storage function $S = S_1 + S_2$

$$\dot{S}(z_1, z_2) = \dot{S}_1(z_1) + \dot{S}_2(z_2) \leq -p_1 \cdot y_1^2 - p_2 \cdot y_2^2 \tag{3.40}$$

This implies that S is positive definite[4] [92, 158, 160]

$$S(z_1, z_2) = S_1(z_1) + S_2(z_2) \geq \int_0^T \left(p_1 \cdot y_1^2 + p_2 \cdot y_2^2\right) \mathrm{d}t \tag{3.41}$$

which can also be seen from (3.31) and the fact that if S_1 and S_2 are positive definite, so is S. These properties of the combined storage function shows that all bounded solutions converge to the set $\{(z_1, z_2) \mid y_1 = y_2 = 0\}$ [158]. From (3.37), we know that this set corresponds to the origin. In (3.38) and (3.39), we showed that the origin is locally asymptotically stable by linearization, and hence, we conclude that the homeostatic controller motifs are asymptotically stable [158]. Additionally, if the storage functions S_1 and S_2 are radially unbounded, so is S, and the homeostatic controller motifs are globally asymptotically stable [158]. From the definition of S_1 and S_2 in (3.31), it is seen that S must be radially unbounded.

In the preceding analysis, we showed that a class of eight nonlinear two-component systems, called homeostatic controller motifs, are globally asymptotically stable. This was done by formulating the controller motifs as negative feedback connections of two individual subsystems. By establishing output strict passivity and zero-state observability of these subsystems, global asymptotic stability was shown for the negative feedback connection of the subsystems. At this point, we note that the stability

[4]Positive definiteness is shown by assuming that there is a pair $\bar{z}_1, \bar{z}_2 \neq 0$ such that $S(\bar{z}_1, \bar{z}_2) = 0$, implying that the right-hand side of (3.41) is equal to zero. This leads to a contradiction due to zero-state observability (see (3.37)), which implies that $\bar{z}_1, \bar{z}_2 = 0$ [92].

result obtained does not solely rely on the particular rate expressions chosen for the homeostatic controller motifs. Instead, we see that it is the nature of the expressions, i.e. strictly monotone, that enables us to establish asymptotic stability. Therefore, we could easily perform the same stability analysis on variations of the homeostatic controllers motifs with different reaction kinetic expressions, e.g. cross-coupling reactions using Hill-type kinetics[5]. The clue to the preceding analysis is to describe the controller motifs as negative feedback connections of two output strictly passive subsystems. Then, subject to the zero-state observability condition, the negative feedback connection is asymptotically stable [158]. This demonstrates the potential for passivity theory as a tool to help us understand cellular reaction networks, where individual processes are described in terms of passivity, so that stability properties of the interconnection these processes can be ascertained using fairly simple rules on the interconnection of passive systems [158, 11, 9].

3.3.3 An example

We demonstrate the preceding stability analysis by considering outflow controller 7, shown in Figure 3.8, given by the system of ODEs

$$\dot{x}_1(t) = k_{\mathrm{s},1} - f_{\mathrm{d},1}(x_1)\cdot\beta(x_2) = k_{\mathrm{s},1} - \frac{k_{\mathrm{d},1}\cdot x_1(t)}{K_{\mathrm{M},1}+x_1(t)}\cdot\frac{x_2(t)}{K_{\mathrm{A},2}+x_2(t)} \tag{3.42}$$

$$\dot{x}_2(t) = k_{\mathrm{s},2} - f_{\mathrm{d},2}(x_2)\cdot\delta(x_1) = k_{\mathrm{s},2} - \frac{k_{\mathrm{d},2}\cdot x_2(t)}{K_{\mathrm{M},2}+x_2(t)}\cdot\frac{K_{\mathrm{I},1}}{K_{\mathrm{I},1}+x_1(t)} \tag{3.43}$$

With the change of variables $z_i = x_i - x_i^*$, the equilibrium point is shifted to the origin, which gives the system

$$\begin{aligned}\dot{z}_1(t) &= -\underbrace{\left(f_{\mathrm{d},1}(z_1+x_1^*) - f_{\mathrm{d},1}(x_1^*)\right)\cdot\beta(x_2^*)}_{f_1(z_1)} - \underbrace{f_{\mathrm{d},1}(z_1+x_1^*)}_{g_1(z_1)}\cdot\underbrace{\left(\beta(z_2+x_2^*)-\beta(x_2^*)\right)}_{h_{2,\beta}(z_2)} \\ &= -f_1(z_1) - g_1(z_1)\cdot h_2(z_2)\end{aligned} \tag{3.44}$$

$$\begin{aligned}\dot{z}_2(t) &= -\underbrace{\left(f_{\mathrm{d},2}(z_2+x_2^*) - f_{\mathrm{d},2}(x_2^*)\right)\cdot\delta(x_1^*)}_{f_2(z_2)} + \underbrace{f_{\mathrm{d},2}(z_2+x_2^*)}_{g_2(z_2)}\cdot\underbrace{\left(\delta(x_1^*)-\delta(z_1+x_1^*)\right)}_{-h_{1,\delta}(z_1)} \\ &= -f_2(z_2) + g_2(z_2)\cdot h_1(z_1)\end{aligned} \tag{3.45}$$

[5] A variant of inflow controller 2, the Goodwin model (see (2.3)–(2.4) in Chapter 2), shows oscillations of arbitrary amplitude [63, 65]. However, with degradation of the controller species following Michaelis–Menten kinetics, no stable oscillations can exist, even with Hill-type feedback [65].

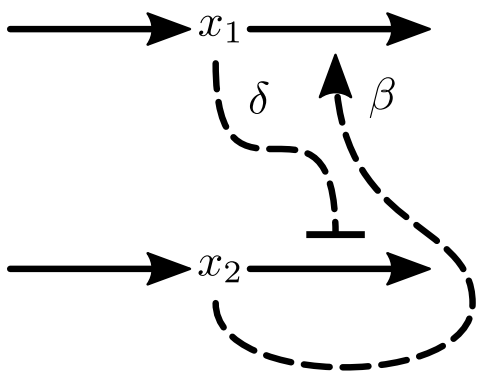

Figure 3.8: Outflow controller 7 with activating and inhibiting cross-coupling reactions β and δ, respectively.

where $h_2(z_2) = h_{2,\beta}(z_2)$ and $h_1(z_1) = -h_{1,\delta}(z_1)$[6]. This system is described by the two subsystems (3.28) and (3.29) in negative feedback connection given by

$$u_1 = -y_2 = -h_2(z_2),\ u_2 = y_1 = h_1(z_1) \tag{3.46}$$

We choose a set of arbitrary parameter values such that the equilibrium point (x_1^*, x_2^*) is non-negative: $k_{\mathrm{s},1} = 1.00$, $k_{\mathrm{d},1} = 3.00$, $K_{\mathrm{M},1} = 1.50$, $k_{\mathrm{s},2} = 1.00$, $k_{\mathrm{d},2} = 4.00$, $K_{\mathrm{M},2} = 0.75$, $K_{\mathrm{I},1} = 1.50$, and $K_{\mathrm{A},2} = 2.00$ (see Figure 3.7 for the intersecting nullclines indicating (x_1^*, x_2^*)). Thereby, the storage function for subsystem H_1 is given by

$$S_1(z_1) = \int_0^{z_1} \frac{h_1(\sigma)}{g_1(\sigma)} \mathrm{d}\sigma = \int_0^{z_1} \left(0.114 - \frac{0.329}{\sigma + 2.893}\right) \mathrm{d}\sigma \tag{3.47}$$

with derivative along trajectories satisfying

$$\dot{S}_1(z_1) \leq -p_1 \cdot y_1^2 + u_1 \cdot y_1 \tag{3.48}$$

where the constant p_1 is determined by

$$0 < p_1 \leq \frac{f_1(z_1)}{h_1(z_1) \cdot g_1(z_1)} = 0.506 + \frac{0.759}{z_1 + 2.893} \tag{3.49}$$

For the interval $[-x_1^*, \infty)$, the right-hand side expression of (3.49) is always greater than or equal to 0.506 (Figure 3.9a), so we choose this value for p_1.

[6]Note that δ is inhibiting, and therefore $h_{1,\delta}$ is negative (see (3.26)–(3.27)).

Similarly, the storage function for subsystem H_2 is given by

$$S_2(z_2) = \int_0^{z_2} \frac{h_2(\sigma)}{g_2(\sigma)} \mathrm{d}\sigma = \int_0^{z_2} \left(0.124 - \frac{0.095}{\sigma + 2.050} - \frac{0.313}{\sigma + 4.050}\right) \mathrm{d}\sigma \tag{3.50}$$

with derivative along trajectories satisfying

$$\dot{S}_2(z_2) \leq -p_2 \cdot y_2^2 + u_2 \cdot y_2 \tag{3.51}$$

where $p_2 = 0.185$, determined by

$$0 < p_2 \leq \frac{f_2(z_2)}{h_2(z_2) \cdot g_2(z_2)} = 0.185 + \frac{0.370}{z_2 + 2.050} \tag{3.52}$$

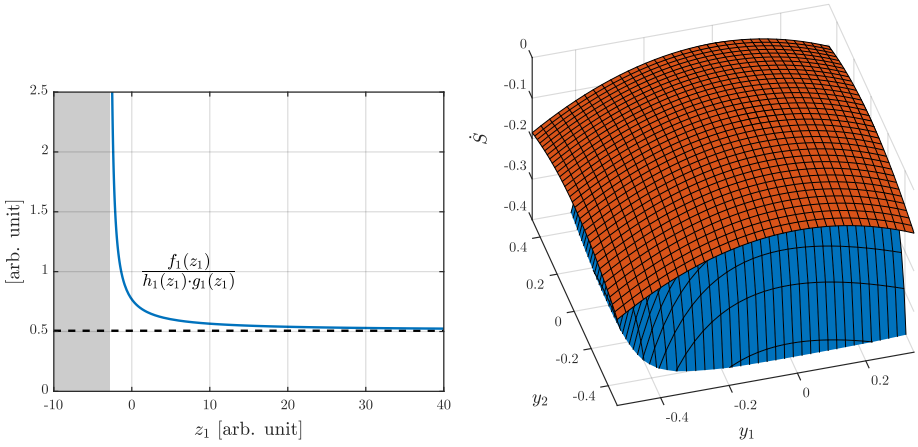

(a) Determination of p_1.

(b) Derivative of S along trajectories.

Figure 3.9: A plot of the right-hand side expression of (3.49) is shown in panel (a). Dashed black line indicates the lower bound of the expression (i.e. the value chosen for p_1). Gray area indicates values of z_1 outside the interval $[-x_1^*, \infty)$. Panel (b) shows that the derivative of S along trajectories ($\dot{S}$, blue) is upper bounded by the quadratic right-hand side expression in (3.53) (red). Note that the surfaces are plotted in terms of y_1 and y_2.

Because S_1 and S_2 are positive definite and radially unbounded (for the interval $[-x_i^*, \infty)$), so is the combined storage function $S = S_1 + S_2$. The derivative of S along trajectories satisfies

$$\dot{S}(z_1, z_2) \leq -0.506 \cdot y_1^2 - 0.185 \cdot y_2^2 \tag{3.53}$$

which shows that $\dot{S}$ is negative definite (Figure 3.9b). The combined storage function S and its derivative along trajectories $\dot{S}$ are shown in Figure 3.10. Because S is positive definite and $\dot{S}$ is negative definite, all bounded solutions converge to the set where the outputs $y_1 = y_2 = 0$. In general, this set could correspond to a number of values (z_1, z_2), however, since the output functions h_i are strictly increasing and satisfy $h_i(0) = 0$, the set corresponds to the origin. This implies that the negative feedback connection of H_1 and H_2 is asymptotically stable if the unforced subsystems are locally asymptotically stable at the origin. We verify this by linearization, according to (3.38) and (3.39)

$$H_1 : -\frac{\partial f_1}{\partial z_1}(z_1)\bigg|_{z_1=0} = -0.118 < 0 \tag{3.54}$$

$$H_2 : -\frac{\partial f_2}{\partial z_2}(z_2)\bigg|_{z_2=0} = -0.131 < 0 \tag{3.55}$$

Thus, the subsystems are zero-state observable, and the negative feedback connection of H_1 and H_2 is asymptotically stable. In addition, because the combined storage function S is radially unbounded, the result is global[7].

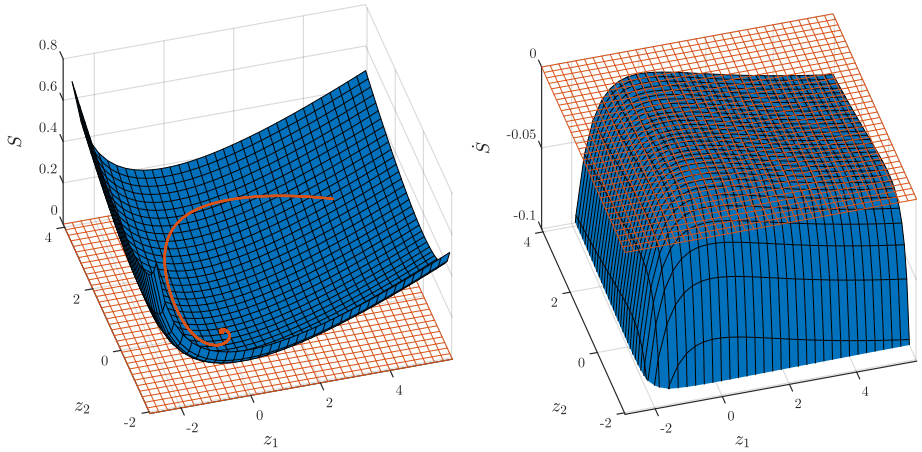

(a) Combined storage function S.

(b) Derivative of S along trajectories.

Figure 3.10: The combined storage function S (panel (a)), and its derivative along trajectories $\dot{S}$ (panel (b)) for the system in (3.44)–(3.45). Since S is positive definite and $\dot{S}$ is negative definite (red grid), all bounded solutions converge to the origin (red line).

[7]Remember that a global result corresponds to non-negative values of the states (x_1 and x_2), since concentrations of substances are non-negative quantities.

3.4 Integral action and robustness

We have shown that the homeostatic controller motifs are globally asymptotically stable due to the formation of a negative feedback connection. However, it is not only important to know that the homeostatic controller motifs tend towards some stable equilibrium point, but also to discern whether the homeostatic controller motifs are able to maintain this equilibrium point in the presence of uncontrolled environmental disturbances. This is because negative feedback and stability alone are not sufficient for robust homeostatic control [41]. It is robustness to disturbances that relate the homeostatic controller motifs to Cannon's definition of homeostasis [25].

Asymptotic regulation is the notion that a regulation error approaches zero, i.e. the output perfectly reaches a desired reference, as time tends to infinity [92]. If asymptotic regulation is achieved in the presence of disturbances, asymptotic disturbance rejection (also called robustness) is achieved [92]. In the case of a constant reference signal, where the goal is to asymptotically regulate the output to a set-point, and a constant disturbance, asymptotic regulation and disturbance rejection can be achieved by integral action [92]. A block diagram of negative feedback with integral action is shown in Figure 3.11. For a process subject to disturbance w, the process output y is to be regulated to a desired set-point r. This is achieved by comparing the process output to the set-point, giving the regulation error $e = r - y$. Based on the regulation error, the controller produces a control action u which acts on the process. For a controller with integral action, the control action is given by the integral of the regulation error. Thus, when the process output deviates from the set-point, the regulation error is non-zero, which produces a change in the control action. Because the feedback of the process output is negative, this change in control action counteracts the deviation in process output from the set-point. Importantly, with integral action, the process output can be maintained exactly at the set-point, since the integrator of the controller functions as a "memory" element that accumulates (i.e. integrates) the regulation error over time, such that the control action corresponding to the desired process output can be maintained, even when the regulation error is zero [142, 42, 155]. In other words, the control action is dependent on the history of past regulation errors, not just the present value, which enables the controller to adapt to uncontrolled changes in the process, such as external disturbances [42, 92].

The mathematical description of an integral controller (with a constant

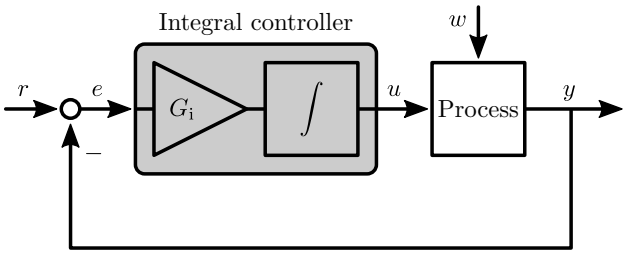

Figure 3.11: Block diagram of a process in negative feedback connection with an integral controller. The process output y is fed back and compared to the set-point r to produce the regulation error $e = r - y$. The regulation error is multiplied by an integral gain G_i and integrated over time to produce the control action u. In the presence of an uncontrolled disturbance w, a deviation in the process output from the set-point will cause a non-zero regulation error. This produces a change in the control action, and since the feedback is negative, this control action functions to counteract the deviation in process output from the set-point.

set-point), called the integral control law, is given by

$$\dot{e}(t) = G_\mathrm{i} \cdot (r - y(t)) \tag{3.56}$$

where G_i is the integral gain, r is the set-point, and y is the process output. Figure 3.11 suggests a constant G_i, however, the integral gain can be variable, often referred to as gain scheduling [41, 92, 155]. For the homeostatic controller motifs, given by the system in (3.9)–(3.10), we use the differential equation for the controller species to show that integral action is included in the negative feedback connection. Depending on the particular controller motif, this differential equation is either given by cross-coupling with the regulated species through reaction γ or reaction δ, corresponding to the two cases where the measurement flux (j_meas) represents an inflow or outflow, respectively. Therefore, integral action has to be shown for the two cases

$$\begin{aligned}
\textbf{case 1:}\ \dot{x}_2(t) &= k_{\mathrm{s},2} \cdot \gamma(x_1) - f_{\mathrm{d},2}(x_2) \\
&= -k_{\mathrm{s},2} \cdot \left(\gamma \left(\gamma^{-1} \left(\frac{f_{\mathrm{d},2}(x_2)}{k_{\mathrm{s},2}} \right) \right) - \gamma(x_1) \right) \\
&= -k_{\mathrm{s},2} \cdot \Big(\gamma(x_1^{\mathrm{set}}) - \gamma(x_1) \Big)
\end{aligned} \tag{3.57}$$

$$\textbf{case 2: } \dot{x}_2(t) = k_{\mathrm{s},2} - f_{\mathrm{d},2}(x_2)\cdot\delta(x_1)$$
$$= f_{\mathrm{d},2}(x_2)\cdot\left(\delta\left(\delta^{-1}\left(\frac{k_{\mathrm{s},2}}{f_{\mathrm{d},2}(x_2)}\right)\right) - \delta(x_1)\right)$$
$$= f_{\mathrm{d},2}(x_2)\cdot\Big(\delta(x_1^{\mathrm{set}}) - \delta(x_1)\Big) \tag{3.58}$$

where $x_1^{\mathrm{set}} = \gamma^{-1}\left(f_{\mathrm{d},2}(x_2)/k_{\mathrm{s},2}\right)$ in (3.57), and $x_1^{\mathrm{set}} = \delta^{-1}\left(k_{\mathrm{s},2}/f_{\mathrm{d},2}(x_2)\right)$ in (3.58). Because γ and δ can represent activation or inhibition, there are four possible expression for x_1^{set} [145]. Additionally, the integral gain is different for the two cases: In (3.57) the integral gain is constant $G_{\mathrm{i}} = -k_{\mathrm{s},2}$, whereas in (3.58) the integral gain is variable $G_{\mathrm{i}} = f_{\mathrm{d},2}(x_2)$. Table 3.1 lists the expressions associated with integral action for all the homeostatic controller motifs.

Controller Motif	G_{i}	x_1^{set}	x_1^{meas}
1 and 6	$f_{\mathrm{d},2}(x_2)$	$\frac{K_{\mathrm{A},1}\cdot k_{\mathrm{s},2}}{f_{\mathrm{d},2}(x_2)-k_{\mathrm{s},2}}$	$\frac{x_1}{K_{\mathrm{A},1}+x_1}$
2 and 5	$-k_{\mathrm{s},2}$	$\frac{K_{\mathrm{A},1}\cdot f_{\mathrm{d},2}(x_2)}{k_{\mathrm{s},2}-f_{\mathrm{d},2}(x_2)}$	$\frac{x_1}{K_{\mathrm{A},1}+x_1}$
3 and 8	$-k_{\mathrm{s},2}$	$\frac{K_{\mathrm{I},1}\cdot\left(k_{\mathrm{s},2}-f_{\mathrm{d},2}(x_2)\right)}{f_{\mathrm{d},2}(x_2)}$	$\frac{K_{\mathrm{I},1}}{K_{\mathrm{I},1}+x_1}$
4 and 7	$f_{\mathrm{d},2}(x_2)$	$\frac{K_{\mathrm{I},1}\cdot\left(f_{\mathrm{d},2}(x_2)-k_{\mathrm{s},2}\right)}{k_{\mathrm{s},2}}$	$\frac{K_{\mathrm{I},1}}{K_{\mathrm{I},1}+x_1}$

Table 3.1: There are four possible ways in which the homeostatic controller motifs realize integral action. The table lists all expressions for integral gain G_{i}, set-point x_1^{set}, and measurement x_1^{meas} (γ or δ, which can be activating or inhibiting).

It is seen from the expressions for x_1^{set} in Table 3.1 that the set-point for the regulated species (x_1) is dependent on the level of the controller species (x_2). However, in the special case where $K_{\mathrm{M},2} = 0$, we have zero-order degradation of the controller species ($f_{\mathrm{d},2}(x_2) = k_{\mathrm{d},2}$), and the set-point is constant. In this case, since the homeostatic controller motifs are globally asymptotically stable, and since (3.57) and (3.58) show that the controller motifs also include integral action, robustness to all constant parameter perturbations that do not destroy the stability of the closed-loop system is ensured [92]. The homeostatic controller motifs have a globally asymptotically stable equilibrium point, and hence, all trajectories converge to this equilibrium point. At this point all signals must be constant. For the integral controller to have a constant output, the regulation error $e = r - y$

must be zero. Thus, the inclusion of integral action forces the regulation error to zero at the equilibrium. Parameter perturbations may change the equilibrium, but the condition $e = 0$ at the equilibrium point is maintained. Therefore, as long as the perturbed homeostatic controller motifs remain globally asymptotically stable, asymptotic disturbance rejection is achieved [92]. This holds true as long as the compensatory flux (j_{comp}) does not reach its upper limit, at which point capacity related breakdown occurs [41].

If we now reintroduce the perturbation flux, given in (3.8), to the homeostatic controller motifs (see the flux balance equations in (3.1)–(3.2)), we can study how uncontrolled disturbances in the regulated species are compensated for. For zero-order degradation of the controller species ($K_{\text{M},2} = 0$), the set-point remains unchanged for constant perturbations (stepwise changes in $k_{\text{p}}^{\text{in/out}}$) in the regulated species, such that x_1 is always regulated back to its pre-perturbed value. Perturbations in x_1 are effectively "absorbed" by x_2, thereby maintaining a constant steady-state level for the regulated species [4]. If the removal of the controller species follows the Michaelis–Menten equation, and we assume that the enzyme driving the reaction is saturated with substrate (i.e. $K_{\text{M},2} \ll x_2$), the degradation rate can be approximated by zero-order [41, 6]. However, in the case where such an approximation can not be made ($K_{\text{M},2} \not\ll x_2$), the regulation error will still go to zero, but as shown in Table 3.1, the set-point is now dependent on the level of x_2. Thus, perturbations in x_1 will change the value of x_1^{set} through changes in the level of x_2, meaning that the controller species is not able to fully absorb perturbations in the regulated species, resulting in only partial adaptation to disturbances. Although partial adaptation may seem less desirable than perfect adaptation[8], it still represents better regulation compared to no adaptation to disturbances (Figure 3.12). In addition, it is likely that mechanisms for zero-order removal in biological systems rely on saturation, rather than true zero-order kinetics, so that near-perfect adaptation is likely the best achievable response [6].

Also note, that in the case of zero-order degradation of the controller species ($K_{\text{M},2} = 0$), the expressions for x_1^{set} are given entirely by reaction kinetic parameters associated with the synthesis and degradation of the controller species. Therefore, the process of tuning the homeostatic controller motifs for a desired set-point is achieved by manipulating reactions

[8] It has been demonstrated that a variable set-point may be a relaxing condition for the controller, reducing the necessary control action, and representing a saving in energy expenditure [145].

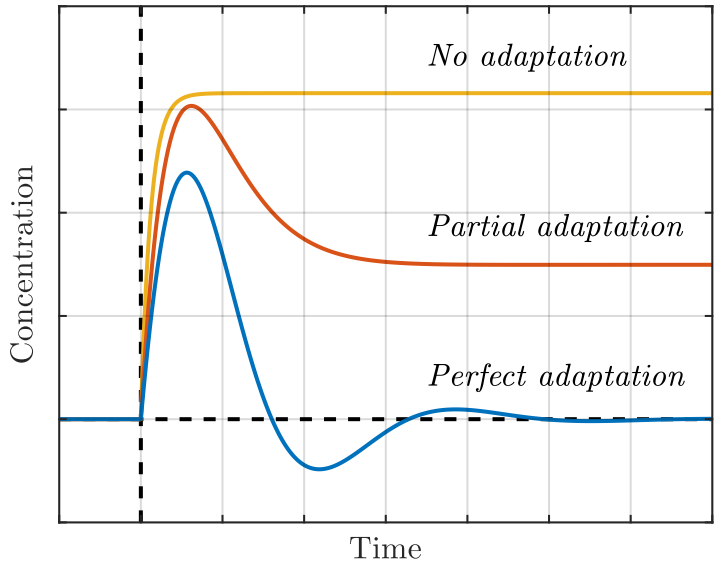

Figure 3.12: The different adaptation responses shown by the homeostatic controller motifs to constant disturbances. At one extreme, the regulated species is completely decoupled from the controller species, and there is no adaptation to perturbations in the regulated species (yellow line). At the other extreme, the degradation of the controller species is zero-order ($K_{\mathrm{M},2} = 0$), and the homeostatic controller motifs show perfect adaptation (blue line). In-between these extremes, the homeostatic controller motifs show partial adaptation (red line), corresponding to unsaturated Michaelis–Menten kinetics ($K_{\mathrm{M},2} \not\ll x_2$).

associated with the controller species only, a property which could see the homeostatic controller motifs as useful building blocks in synthetic biological networks [180, 176, 6]. For now, we leave the tuning of homeostatic controller motifs to Chapter 4.

3.4.1 Integral control motifs

Aside from zero-order degradation, or saturated removal, of the controller species, there are other reaction kinetic mechanisms that have been shown to realize integral action [42, 21, 142]. A variant of the homeostatic controller motifs, where the controller species is removed in a first-order reaction, has been shown to to achieve integral action through autocatalytic generation of the controller species [42]. Figure 3.13 shows an example of such a control motif, where inflow controller 1 is augmented into an autocatalytic

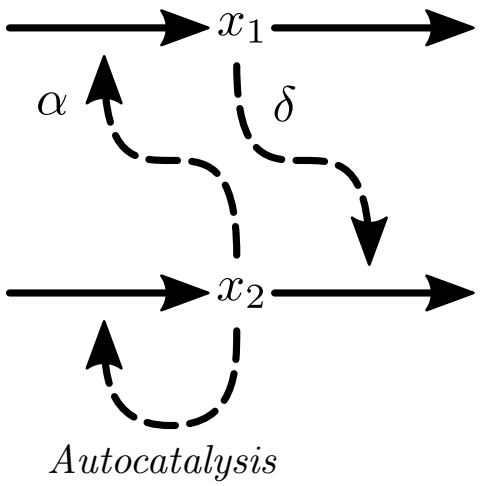

Figure 3.13: A variant of inflow controller 1, where the controller species x_2 is generated autocatalytically. Autocatalytic controllers achieve integral action by matching the reaction orders for synthesis and degradation of the controller species, with respect to the controller species. This way, perfect adaptation is achieved without requiring zero-order degradation of the controller species.

controller. This system is given by the ODEs [42]

$$\dot{x}_1(t) = k_{\mathrm{s},1} \cdot \alpha(x_2) - f_{\mathrm{d},1}(x_1) \tag{3.59}$$

$$\dot{x}_2(t) = k_{\mathrm{s},2} \cdot x_2 - k_{\mathrm{d},2} \cdot x_2 \cdot \delta(x_1) \tag{3.60}$$

where the synthesis of x_2 is activated by itself (autocatalysis), and the degradation is first-order ($f_{\mathrm{d},2}(x_2) = k_{\mathrm{d},2} \cdot x_2$). To see that the controller species implements integral action, we rewrite (3.60) into

$$\begin{aligned}
\dot{x}_2(t) &= k_{\mathrm{s},2} \cdot x_2 - k_{\mathrm{d},2} \cdot x_2 \cdot \delta(x_1) \\
&= k_{\mathrm{d},2} \cdot x_2 \cdot \left(\delta\left(\delta^{-1}\left(\frac{k_{\mathrm{s},2}}{k_{\mathrm{d},2}} \right) \right) - \delta(x_1) \right) \\
&= k_{\mathrm{d},2} \cdot x_2 \cdot \Big(\delta(x_1^{\mathrm{set}}) - \delta(x_1) \Big)
\end{aligned} \tag{3.61}$$

where it is seen that the set-point $x_1^{\mathrm{set}} = \delta^{-1}(k_{\mathrm{s},2}/k_{\mathrm{d},2})$ is constant. In comparison to the homeostatic controller motifs, the autocatalytic controllers achieve perfect adaptation without requiring zero-order removal of the controller species [42]. Notably, the autocatalytic controllers can also achieve perfect adaptation for other reaction kinetic expressions for the degradation of x_2, as long as the autocatalytic generation of x_2 is identical

(up to multiplication by a positive constant) [42, 49]. It is apparent that the autocatalytic controllers achieve integral action by matching the expressions for synthesis and degradation of the controller species, with respect to the controller species[9] (i.e. the reaction orders with respect to x_2) [49].

In terms of stability, the autocatalytic controllers have been demonstrated to be asymptotically stable, however, they can not be globally asymptotically stable [42, 176]. This is due to the fact that trajectories on the line $x_2 = 0$ will never escape it. Depending on the particular autocatalytic controller motif, it can be shown that x_1 either grows to infinity, reaches a positive steady-state, or depletes completely, for trajectories staring on $x_2 = 0$. This may pose difficulties for autocatalytic controllers with low molecular counts, where the presence of biochemical noise could potentially bring the controller species to zero [23].

Another way to realize integral action is the use of two controller species that "annihilate" each other, in a so-called antithetic integral feedback controller [21]. The antithetic controller has been shown to regulate the output species of undefined reaction networks consisting of unimolecular and bimolecular reactions, as shown in Figure 3.14. The reaction network being controlled (the cloud in Figure 3.14) and the antithetic controller are both described by mass-action kinetics. The antithetic controller consists of two controller species, x_2 and x_3, and four reactions: One *reference reaction* generating x_2 at a constant rate, one *measurement reaction* generating x_3 via the network output species x_1, one *comparison reaction* that annihilates the controller species x_2 and x_3 in a bimolecular reaction, and one *actuation reaction* that affects the controlled reaction network via the controller species x_2 [21, 22]. The antithetic controller regulates the network output species x_1 to a steady-state determined by the rate constants for the production of the controller species, and notably, achieves robust perfect adaptation in a stochastic setting (the system converges to a unique stationary distribution) [21]. To see how integral action is achieved, we take a look at the controller species of the (deterministic) antithetic controller, given by the ODEs [21, 142]

$$\dot{x}_2(t) = \mu - \eta \cdot x_2(t) \cdot x_3(t) \tag{3.62}$$

$$\dot{x}_3(t) = \theta \cdot x_1(t) - \eta \cdot x_2(t) \cdot x_3(t) \tag{3.63}$$

[9] This is also true for the homeostatic controller motifs, where the synthesis and degradation of the controller species are zero-order with respect to the controller species. In this sense, the autocatalytic controllers are generalizations of the homeostatic controller motifs.

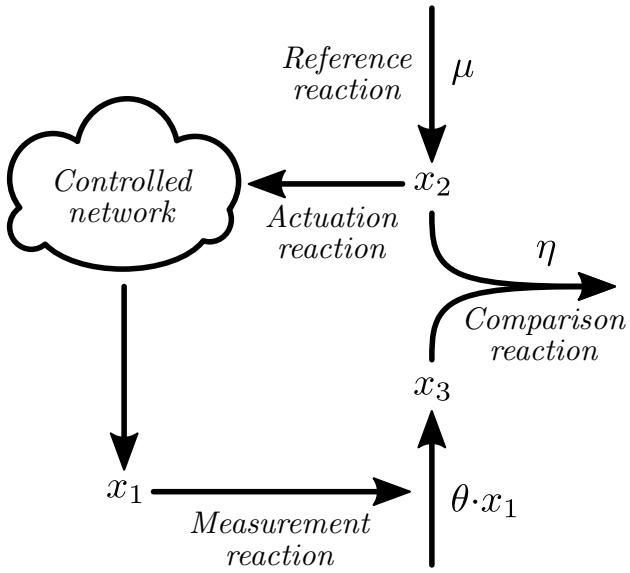

Figure 3.14: The antithetic controller consists of two controller species x_2 and x_3 that annihilate each other in a so-called comparison reaction. A reference reaction generating x_2 at a constant rate (partly) defines the set-point of the controller. The actuation reaction affects some undefined reaction network (the cloud), with the goal of controlling the network output x_1, via the controller species x_2. The output species is sensed in a measurement reaction activating the generation of the controller species x_3. The antithetic controller implements integral action with the hidden variable $\chi = x_2 - x_3$, and defines a set-point for the network output species by the rate constants for the production of the controller spices.

where μ is the constant production rate of x_2, both controller species are annihilated in the comparison reaction $\eta \cdot x_2 \cdot x_3$, and $\theta \cdot x_1$ is the measurement reaction producing x_3. Then, the hidden variable $\chi = x_2 - x_3$ is given by

$$\dot{\chi}(t) = \dot{x}_2(t) - \dot{x}_3(t) = \theta \cdot \left(\frac{\mu}{\theta} - x_1(t) \right) \tag{3.64}$$

which has the same form as the integral control law (see (3.56)) [21, 142].

It has been shown that the antithetic controller is the minimal implementation that achieves robust perfect adaptation using mass-action kinetics, with only two controller species and one annihilation reaction[10] [8]. A

[10] Although the homeostatic controller motifs only consist of one controller species, they are not described using mass-action kinetics.

benefit of the antithetic controller is that tuning is done by manipulating production rates only, whereas tuning of the homeostatic controller motifs entails manipulation of degradation rates as well [181]. It is often easier to manipulate production rates [5].

Enzyme reactions catalyzed by "one-way enzymes," or coupled to thermodynamically favorable reactions, may be practically irreversible [31, 17]. However, we would expect that elementary reaction steps are reversible [31, 91]. For the comparison reaction in the antithetic controller, this does not pose a problem, but for the reference, measurement, and actuation reactions, reversibility could lead to disruption of the integral control law in (3.64), resulting in only partial adaptation to disturbances.

Interestingly, if the reaction network controlled by the antithetic controller is a single species x_1 being generated and turned over, it is possible to construct eight negative feedback connections, analogous to the homeostatic controller motifs [147]. This way, the antithetic controller configurations can be defined as inflow or outflow controllers, depending on whether the actuation reaction is affecting the synthesis or degradation of the regulated species x_1, respectively. Thus, the antithetic controller configurations can be used in a similar way to the homeostatic controller motifs, where inflow controllers primarily compensate for outflow perturbations, and outflow controllers primarily compensate for inflow perturbations [41]. In addition, the antithetic controller configurations can be defined as activating or inhibiting, depending on whether the actuation reaction is activating or inhibiting. It should be noted, that the mechanism for inhibition is not described by a simple elementary reaction step, leaving only two possible configurations (one inflow and one outflow configuration) in accordance with the original description of the antithetic controller by Briat et al. [21]. The complete set of antithetic controller configurations are shown in Figure 3.15.

The various reaction kinetic mechanisms for realizing integral control discussed so far (homeostatic controller motifs, autocatalytic controllers, and the antithetic controller) are collectively referred to as *integral control motifs* (ICMs) [142]. Functionally, these ICMs implement negative feedback with integral action in different ways, but the objective is always the same; an integral controller that works to counteract deviations in the regulated variable from a desired set-point [41, 42, 21, 142]. In this way, ICMs are effective mechanisms for mitigating the effects of unknowns in biological systems, such as uncontrolled variations in the external environment or unforeseen interactions within the system, and provide the ability to fine

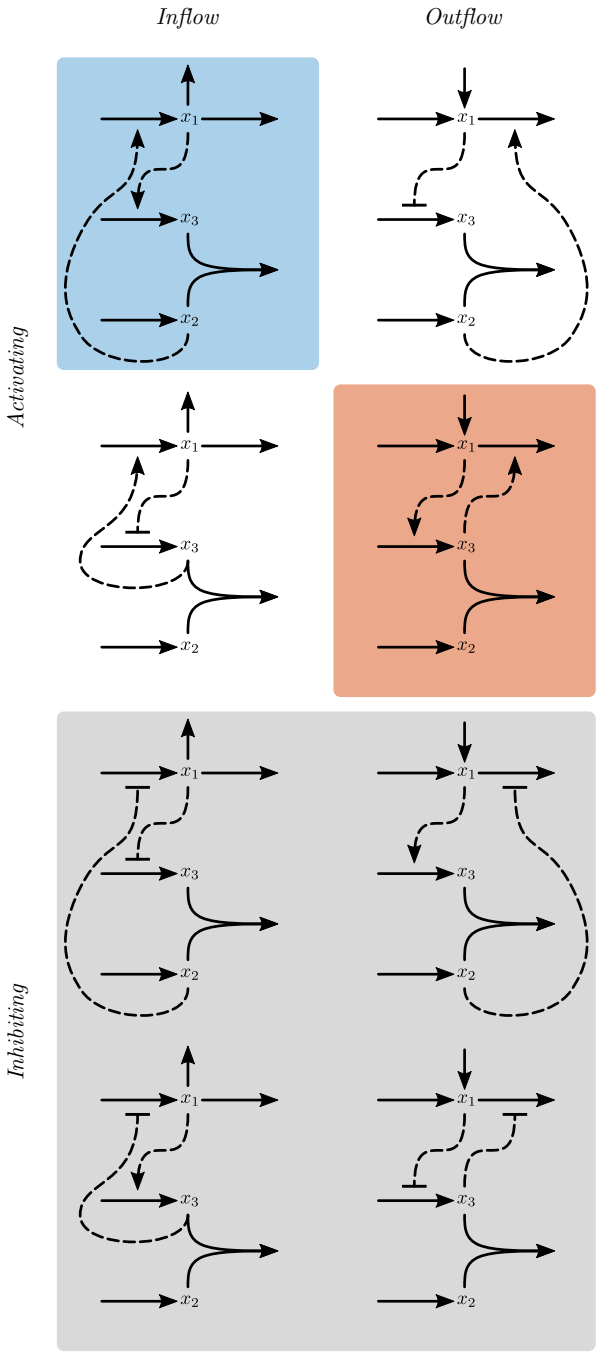

Figure 3.15: (Caption on the following page)

Figure 3.15: Complete set of all eight antithetic controller configurations regulating a single species x_1 being generated and turned over. Like the homeostatic controller motifs, these antithetic controller configurations can be classified as inflow (left column) or outflow (right column) controllers, depending on whether the actuation reaction affects the synthesis or degradation of the regulated species, respectively. Furthermore, whether the actuation reaction is activating (top panel) or inhibiting (bottom panel), the antithetic controller configurations are classified as activating or inhibiting. For a pure mass-action kinetics description, however, there are only two possible configurations, one inflow (blue) and one outflow (red), both of which are activating.

tune central parameters of the control system [142, 6, 181]. Even for wide-ranging and unavoidable effects such as molecule dilution during cell growth and division, general design principles for ICMs that perform well despite the presence of dilution have been proposed [142]. We will take a closer look at the homeostatic controller motifs in the presence of dilution and environmental stochasticity in Chapter 5.

Chapter 4

Tuning of homeostatic controller motifs

In this chapter, we show how parameters related to molecular and kinetic mechanisms influence set-point tracking and disturbance rejection properties of the homeostatic controller motifs. We use a tuning procedure based on linearization, which enables us to define a desired dynamical response for the homeostatic controller motifs. We linearize the controller motifs around a working point, and identify tuning parameters that relate system parameters to the step response[1] of the systems. We verify the tuning procedure by simulations, and look at some constraints that limit the achievable steady-state behaviors of the homeostatic controller motifs. We also investigate trade-offs in relation to time-varying inputs, and how this ultimately affects the tuning procedure. In the final part of this chapter, we investigate how nonlinearities in the homeostatic controller motifs influence the tuned response.

4.1 Tuning by linearization

Implementing control mechanisms, such as the homeostatic controller motifs, in living cells is an attractive prospect that could aid in the design of cellular processes that are robust in the presence of changing and uncertain environments, and could facilitate optimization or creation of novel reaction networks [79, 6, 180, 181]. Aside from the practicalities of implementation in living cells, great difficulties are faced with quantitatively tuning the parameters of such control mechanisms in order to achieve some desired function [79]. The ability to quantitatively tune individual components in a biological network is central to synthetic biology, and is required for the

[1] The (dynamical) output response of a system to a step change in its input.

engineering of complex reaction networks, where connected components must be matched in terms of input and output levels, and internal dynamics must be tuned to guarantee stability and robustness [5]. Such a tuning procedure can be facilitated by concepts from control theory, and in particular, the characterization of set-point tracking and disturbance rejection properties provide a theoretical foundation that can guide us in achieving desired dynamical and steady-state behaviors [181, 6].

The dynamical properties of a two-component biochemical system (second-order system) around a working point can be described in terms of the undamped natural frequency ω_{n} and the damping ratio ζ [181, 155, 72]. To illustrate this, we consider the homeostatic controller motifs shown in Figure 4.1. As shown in Chapter 3, the homeostatic controller motifs consist of two components, a regulated species x_1, and a controller species x_2, that form a negative feedback connection through cross-coupling [41, 186]. In order to describe the dynamical behaviors of the homeostatic controller motifs in terms of the tuning parameters ω_{n} and ζ, we need to linearize the nonlinear system equations for the controller motifs (see (3.9)–(3.10) in Chapter 3) around a working point. It is natural that this working point coincides with the set-point for the controller motifs.

We use outflow controller 5 as an example to show how the tuning parameters ω_{n} and ζ relate to reaction kinetic parameters of the homeostatic controller motifs. Outflow controller 5 is given by the system of nonlinear ODEs

$$\begin{aligned}\dot{x}_1(t) &= j_{\mathrm{b},1}(x_1) - j_{\mathrm{comp}}(x_1, x_2) = k_{\mathrm{s},1} - f_{\mathrm{d},1}(x_1) \cdot \beta(x_2) \\ &= k_{\mathrm{s},1} - k_{\mathrm{d},1} \cdot x_1(t) \cdot \frac{x_2(t)}{K_{\mathrm{A},2} + x_2(t)}\end{aligned} \tag{4.1}$$

$$\begin{aligned}\dot{x}_2(t) &= j_{\mathrm{meas}}(x_1, x_2) - j_{\mathrm{b},2}(x_2) = k_{\mathrm{s},2} \cdot \gamma(x_1) - f_{\mathrm{d},2}(x_2) \\ &= k_{\mathrm{s},2} \cdot x_1(t) - \frac{k_{\mathrm{d},2} \cdot x_2(t)}{K_{\mathrm{M},2} + x_2(t)}\end{aligned} \tag{4.2}$$

where $k_{\mathrm{s},i}$ are basal rates of production of x_i, the functions $f_{\mathrm{d},i}$ describe the degradation or removal of x_i, and β and γ describe the cross-coupling between the two components. For this example we let the removal of x_1 follow first-order kinetics ($f_{\mathrm{d},1}(x_1) = k_{\mathrm{d},1} \cdot x_1$), activated by x_2 in a way that saturates ($\beta(x_2) = x_2/(K_{\mathrm{A},2} + x_2)$). The generation of x_2 is activated by x_1 in a way that does not saturate ($\gamma(x_1) = x_1$), and the removal of x_2 follows Michaelis–Menten kinetics. In order to investigate the disturbance rejection

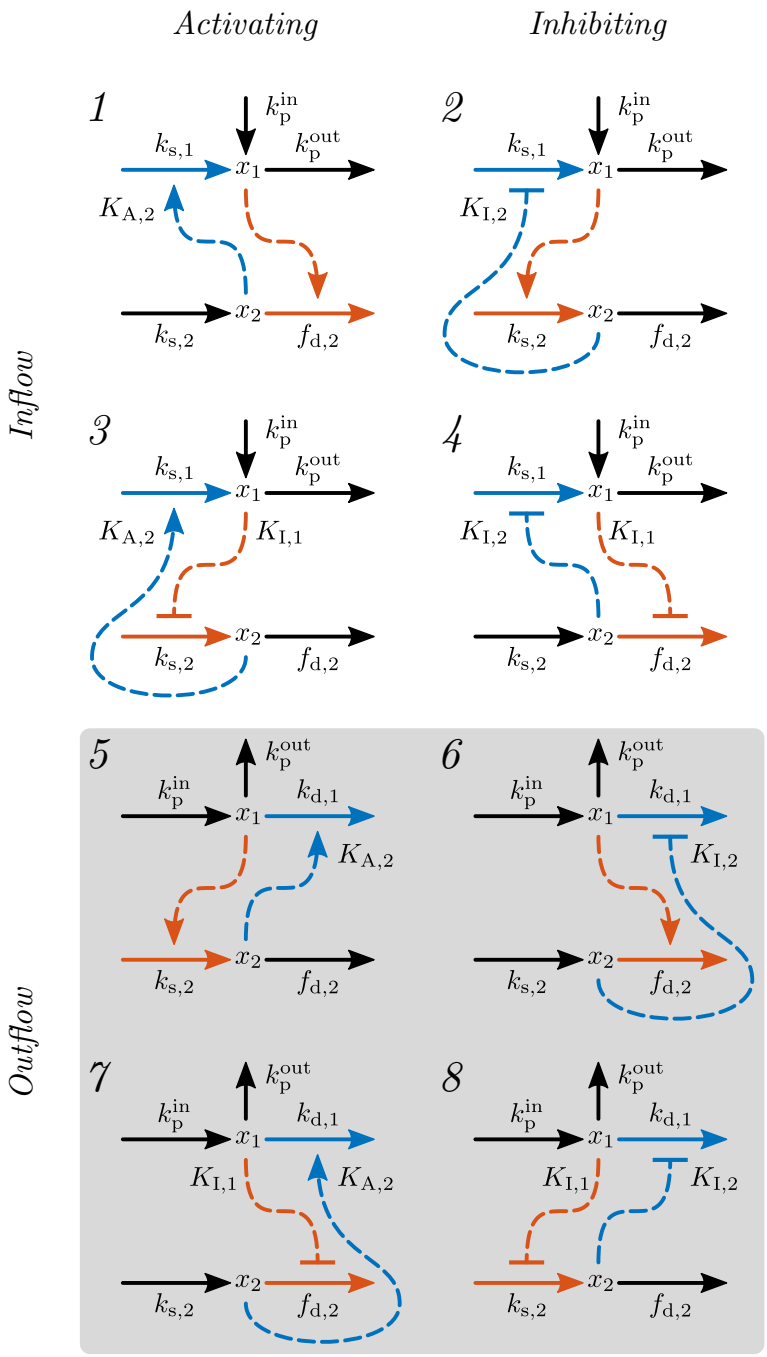

Figure 4.1: (Caption on the following page)

Figure 4.1: Complete set of all eight homeostatic controller motifs with inflow (k_p^in) and outflow ($k_\mathrm{p}^\mathrm{out}$) disturbances. The x_2-mediated compensatory flux is shown in blue, based on which the controllers are grouped into inflow (top, white background) and outflow (bottom, gray background) controllers. If the compensatory flux is activated by x_2, the controllers are classified as activating (left column), and if the compensatory flux is inhibited by x_2, the controllers are classified as inhibiting (right column). The measurement flux is shown in red. Note that we use a slightly different variant of the controller motifs than previously. Namely, we let the degradation of x_1 be first-order ($f_{\mathrm{d},1}(x_1) = k_{\mathrm{d},1} \cdot x_1$), and use a non-saturating expression for the x_1-activated measurement flux ($f_\mathrm{act}(x_1) = x_1$).

properties of this system, we include disturbances in the dynamical model (see perturbation flux in (3.8) in Chapter 3). We add an inflow perturbation in the form of a small uncontrolled deviation in the basal synthesis of the regulated species x_1, such that $k_\mathrm{p}^\mathrm{in} = k_{\mathrm{s},1} + \Delta k_{\mathrm{s},1}$ ($k_\mathrm{p}^\mathrm{out}$ is defined similarly for inflow controllers). We also add an outflow perturbation in the form of an uncontrolled first-order removal reaction of x_1. Hence, the dynamical model for controller motif 5 used in this example is given by

$$\dot{x}_1(t) = k_\mathrm{p}^\mathrm{in} - k_\mathrm{p}^\mathrm{out} \cdot x_1(t) - k_{\mathrm{d},1} \cdot x_1(t) \cdot \frac{x_2(t)}{K_{\mathrm{A},2} + x_2(t)} \tag{4.3}$$

$$\dot{x}_2(t) = k_{\mathrm{s},2} \cdot x_1(t) - \frac{k_{\mathrm{d},2} \cdot x_2(t)}{K_{\mathrm{M},2} + x_2(t)} \tag{4.4}$$

where k_p^in and $k_\mathrm{p}^\mathrm{out}$ represent parameters with uncontrolled elements that give rise to inflow and outflow disturbances.

As shown in Chapter 3, a constant set-point for the regulated species, x_1^set, is found by assuming zero-order removal of the controller species, that is, $f_{\mathrm{d},2}(x_2) = k_{\mathrm{d},2}$. This is achieved by assuming $K_{\mathrm{M},2} = 0$ (or $K_{\mathrm{M},2} \ll x_2$), which implies that the enzyme responsible for the removal of x_2 is saturated with substrate [6]. Because these ideal conditions are assumed, the set-point is called *ideal* or *theoretical*, and is given by the ratio of rate constants for the degradation and synthesis of the controller species $x_1^\mathrm{set} = k_{\mathrm{d},2}/k_{\mathrm{s},2}$. Using this set-point, we rearrange (4.4) into the integral control law

$$\begin{aligned}\dot{x}_2(t) &= -k_{s,2} \cdot \left(\gamma \left(\gamma^{-1} \left(\frac{f_{\mathrm{d},2}(x_2)}{k_{\mathrm{s},2}} \right) \right) - \gamma(x_1) \right) \\ &= \underbrace{-k_{\mathrm{s},2} \cdot \frac{x_2(t)}{K_{\mathrm{M},2} + x_2(t)}}_{G_\mathrm{i}} \cdot \Bigg(\underbrace{\frac{k_{\mathrm{d},2}}{k_{\mathrm{s},2}}}_{x_1^\mathrm{set}} - \underbrace{x_1(t) \cdot \frac{K_{\mathrm{M},2} + x_2(t)}{x_2(t)}}_{x_1^\mathrm{meas}} \Bigg)\end{aligned} \tag{4.5}$$

which shows the expressions for integral gain G_{i}, set-point x_1^{set}, and measurement x_1^{meas}.

In order to identify the tuning parameters ω_{n} and ζ, the dynamical model (4.3)–(4.4) is linearized around a working point (x^*, u^*), where $x^* = [x_1^*, x_2^*]^{\mathsf{T}}$ is the steady-state solution (equilibrium point) of the system. To have this working point coincide with the ideal set-point for x_1, we set $K_{\mathrm{M},2} = 0$, which guarantees that system trajectories pass through x_1^{set}. The second part of the working point, $u^* = [u_1^*, u_2^*]^{\mathsf{T}}$, is a vector of system input values corresponding to the steady-state x^*. We use these system inputs to characterize set-point tracking and disturbance rejection properties of the linearized system. To identify set-point tracking properties, we need to make a change in the set-point $x_1^{\mathrm{set}} = k_{\mathrm{d},2}/k_{\mathrm{s},2}$, and observe the consequent system response. Since the set-point is given by the ratio of two rate constants, either of these parameters can be used to make changes in the set-point. We choose $k_{\mathrm{d},2}$ to be the parameter that changes the set-point, such that $u_1 = k_{\mathrm{d},2}$, and u_1^* is the value of $k_{\mathrm{d},2}$ before a set-point change is made. To investigate disturbance rejection properties, it is natural to look at the system's response to changes in $k_{\mathrm{p}}^{\mathrm{in}}$. This is due to the fact that controller motif 5 is an outflow controller that maintains homeostasis through the removal of x_1, and hence, is primarily suited to compensate for perturbations that increase x_1 [41]. Therefore, we use $u_2 = k_{\mathrm{p}}^{\mathrm{in}}$ as the disturbance input, where u_2^* is the pre-perturbed value of $k_{\mathrm{p}}^{\mathrm{in}}$, i.e. the basal synthesis of x_1 ($k_{\mathrm{s},1}$). The linearized model is then given by [43]

$$\Delta\dot{x}(t) = \frac{\partial f}{\partial x}(x^*, u^*) \cdot \Delta x(t) + \frac{\partial f}{\partial u}(x^*, u^*) \cdot \Delta u(t) = A \cdot \Delta x(t) + B \cdot \Delta u(t) \tag{4.6}$$

where $\Delta x = [\Delta x_1, \Delta x_2]^{\mathsf{T}}$ is a vector of deviations from steady-state values x^*, and $\Delta u = [\Delta u_1, \Delta u_2]^{\mathsf{T}}$ is a vector of deviations in system inputs, with pre-perturbed values u^*. $f = [f_1, f_2]^{\mathsf{T}}$ is a vector of the right-hand side expressions of the system equations in (4.3)–(4.4). The matrix A is the system matrix, and B is the input matrix. We are investigating set-point tracking and disturbance rejection properties of the linearized model, and therefore are only interested in the regulated variable x_1 as our output. Hence, the system output is given by $\Delta y = C \cdot \Delta x$, where $C = [1, 0]$ is the output matrix. By applying the Laplace transform to the linearized model in (4.6), we find the transfer function matrix H, which describes the connection between small changes in system inputs Δu and the resulting

changes in system output Δy [43]

$$H(s) = \frac{\mathcal{L}\{\Delta y(t)\}}{\mathcal{L}\{\Delta u(t)\}} = \frac{\Delta y(s)}{\Delta u(s)} = C(sI - A)^{-1}B \tag{4.7}$$

where $\mathcal{L}$ represents the Laplace transform, s is the complex-valued variable introduced by the Laplace transform, and I is the identity matrix.

The elements of H are transfer functions characterizing the linearized system from the input $k_{\mathrm{d},2}$ to the output, and from $k_{\mathrm{p}}^{\mathrm{in}}$ to the output. First, we take a look at the set-point tracking properties of the linearized system, that is, the element of H that describes the relationship between set-point and output, given by

$$\begin{aligned} M(s) &= \frac{\Delta x_1(s)}{\Delta k_{\mathrm{d},2}(s)} = \frac{\Delta y(s)}{\Delta u_1(s)} = \frac{K \cdot \omega_{\mathrm{n}}^2}{s^2 + 2 \cdot \zeta \cdot \omega_{\mathrm{n}} \cdot s + \omega_{\mathrm{n}}^2} \\ &= \frac{\frac{\left(\left(k_{\mathrm{p}}^{\mathrm{out}} + k_{\mathrm{d},1}\right) \cdot k_{\mathrm{d},2} - k_{\mathrm{p}}^{\mathrm{in}} \cdot k_{\mathrm{s},2}\right)^2}{K_{\mathrm{A},2} \cdot k_{\mathrm{d},1} \cdot k_{\mathrm{s},2} \cdot k_{\mathrm{d},2}}}{s^2 + \frac{k_{\mathrm{p}}^{\mathrm{in}} \cdot k_{\mathrm{s},2}}{k_{\mathrm{d},2}} \cdot s + \frac{\left(\left(k_{\mathrm{p}}^{\mathrm{out}} + k_{\mathrm{d},1}\right) \cdot k_{\mathrm{d},2} - k_{\mathrm{p}}^{\mathrm{in}} \cdot k_{\mathrm{s},2}\right)^2}{K_{\mathrm{A},2} \cdot k_{\mathrm{d},1} \cdot k_{\mathrm{d},2}}} \end{aligned} \tag{4.8}$$

By rearranging the expression for the set-point into $k_{\mathrm{d},2} = x_1^{\mathrm{set}} \cdot k_{\mathrm{s},2}$, we can express the tuning parameters ω_{n} and ζ in terms of the set-point

$$\omega_{\mathrm{n}} = \frac{\sqrt{k_{\mathrm{s},2}} \cdot \left(\left(k_{\mathrm{p}}^{\mathrm{out}} + k_{\mathrm{d},1}\right) \cdot x_1^{\mathrm{set}} - k_{\mathrm{p}}^{\mathrm{in}}\right)}{\sqrt{K_{\mathrm{A},2} \cdot k_{\mathrm{d},1} \cdot x_1^{\mathrm{set}}}} \tag{4.9}$$

$$\zeta = \frac{k_{\mathrm{p}}^{\mathrm{in}} \cdot \sqrt{K_{\mathrm{A},2} \cdot k_{\mathrm{d},1}}}{2 \cdot \sqrt{k_{\mathrm{s},2} \cdot x_1^{\mathrm{set}}} \cdot \left(\left(k_{\mathrm{p}}^{\mathrm{out}} + k_{\mathrm{d},1}\right) \cdot x_1^{\mathrm{set}} - k_{\mathrm{p}}^{\mathrm{in}}\right)} \tag{4.10}$$

The transfer function gain is given by $K = 1/k_{\mathrm{s},2}$, due to the fact that we are manipulating $k_{\mathrm{d},2}$ as a proxy for changing the set-point. We see that there is a close relationship between the expressions for ω_{n} and ζ, and hence, it is not possible to specify both tuning parameters independently.

The other element of the transfer function matrix H in (4.7) describes the relationship between the disturbance input $k_{\mathrm{p}}^{\mathrm{in}}$ and the output. This is the transfer function used to characterize the disturbance rejection properties of the linearized system, given by

$$\begin{aligned} N(s) &= \frac{\Delta x_1(s)}{\Delta k_{\mathrm{p}}^{\mathrm{in}}(s)} = \frac{\Delta y(s)}{\Delta u_2(s)} \\ &= \frac{s}{s^2 + \frac{k_{\mathrm{p}}^{\mathrm{in}} \cdot k_{\mathrm{s},2}}{k_{\mathrm{d},2}} \cdot s + \frac{\left(\left(k_{\mathrm{p}}^{\mathrm{out}} + k_{\mathrm{d},1}\right) \cdot k_{\mathrm{d},2} - k_{\mathrm{p}}^{\mathrm{in}} \cdot k_{\mathrm{s},2}\right)^2}{K_{\mathrm{A},2} \cdot k_{\mathrm{d},1} \cdot k_{\mathrm{d},2}}} \end{aligned} \tag{4.11}$$

Importantly, this transfer function has a zero at the origin, meaning that $N(0) = 0$, and that the steady-state contribution of a constant disturbance input $k_{\mathrm{p}}^{\mathrm{in}}$ to the system output is zero. This implies robust perfect adaptation to a step change in the disturbance [43].

We linearize all eight homeostatic controller motifs (see Figure 4.1), assuming ideal conditions, and identify the set-point x_1^{set}, undamped natural frequency ω_{n}, and damping ratio ζ for each controller. The expressions for these tuning parameters are summarized in Table 4.1.

		Set-point x_1^{set}	Undamped natural frequency ω_{n}	Damping ratio ζ
Inflow controllers	1	$\frac{\boldsymbol{k_{s,2}}}{k_{\mathrm{d},2}}$	$\frac{\sqrt{k_{\mathrm{d},2}}\left(k_{\mathrm{p}}^{\mathrm{in}}-k_{\mathrm{p}}^{\mathrm{out}}x_1^{\mathrm{set}}+k_{\mathrm{s},1}\right)}{\sqrt{K_{\mathrm{A},2}k_{\mathrm{s},1}}}$	$\frac{k_{\mathrm{p}}^{\mathrm{out}}\sqrt{K_{\mathrm{A},2}k_{\mathrm{s},1}}}{2\sqrt{k_{\mathrm{d},2}}\left(k_{\mathrm{p}}^{\mathrm{in}}-k_{\mathrm{p}}^{\mathrm{out}}x_1^{\mathrm{set}}+k_{\mathrm{s},1}\right)}$
	2	$\frac{\boldsymbol{k_{d,2}}}{k_{\mathrm{s},2}}$	$\frac{\sqrt{k_{\mathrm{s},2}}\left(k_{\mathrm{p}}^{\mathrm{out}}x_1^{\mathrm{set}}-k_{\mathrm{p}}^{\mathrm{in}}\right)}{\sqrt{K_{\mathrm{I},2}k_{\mathrm{s},1}}}$	$\frac{k_{\mathrm{p}}^{\mathrm{out}}\sqrt{K_{\mathrm{I},2}k_{\mathrm{s},1}}}{2\sqrt{k_{\mathrm{s},2}}\left(k_{\mathrm{p}}^{\mathrm{out}}x_1^{\mathrm{set}}-k_{\mathrm{p}}^{\mathrm{in}}\right)}$
	3	$\frac{\left(\boldsymbol{k_{s,2}}-k_{\mathrm{d},2}\right)K_{\mathrm{I},1}}{k_{\mathrm{d},2}}$	$\frac{\sqrt{k_{\mathrm{d},2}}\left(k_{\mathrm{p}}^{\mathrm{in}}-k_{\mathrm{p}}^{\mathrm{out}}x_1^{\mathrm{set}}+k_{\mathrm{s},1}\right)}{\sqrt{\left(K_{\mathrm{I},1}+x_1^{\mathrm{set}}\right)K_{\mathrm{A},2}k_{\mathrm{s},1}}}$	$\frac{k_{\mathrm{p}}^{\mathrm{out}}\sqrt{\left(K_{\mathrm{I},1}+x_1^{\mathrm{set}}\right)K_{\mathrm{A},2}k_{\mathrm{s},1}}}{2\sqrt{k_{\mathrm{d},2}}\left(k_{\mathrm{p}}^{\mathrm{in}}-k_{\mathrm{p}}^{\mathrm{out}}x_1^{\mathrm{set}}+k_{\mathrm{s},1}\right)}$
	4	$\frac{\left(\boldsymbol{k_{d,2}}-k_{\mathrm{s},2}\right)K_{\mathrm{I},1}}{k_{\mathrm{s},2}}$	$\frac{\sqrt{k_{\mathrm{s},2}}\left(k_{\mathrm{p}}^{\mathrm{out}}x_1^{\mathrm{set}}-k_{\mathrm{p}}^{\mathrm{in}}\right)}{\sqrt{\left(K_{\mathrm{I},1}+x_1^{\mathrm{set}}\right)K_{\mathrm{I},2}k_{\mathrm{s},1}}}$	$\frac{k_{\mathrm{p}}^{\mathrm{out}}\sqrt{\left(K_{\mathrm{I},1}+x_1^{\mathrm{set}}\right)K_{\mathrm{I},2}k_{\mathrm{s},1}}}{2\sqrt{k_{\mathrm{s},2}}\left(k_{\mathrm{p}}^{\mathrm{out}}x_1^{\mathrm{set}}-k_{\mathrm{p}}^{\mathrm{in}}\right)}$
Outflow controllers	5	$\frac{\boldsymbol{k_{d,2}}}{k_{\mathrm{s},2}}$	$\frac{\sqrt{k_{\mathrm{s},2}}\left(\left(k_{\mathrm{p}}^{\mathrm{out}}+k_{\mathrm{d},1}\right)x_1^{\mathrm{set}}-k_{\mathrm{p}}^{\mathrm{in}}\right)}{\sqrt{K_{\mathrm{A},2}k_{\mathrm{d},1}x_1^{\mathrm{set}}}}$	$\frac{k_{\mathrm{p}}^{\mathrm{in}}\sqrt{K_{\mathrm{A},2}k_{\mathrm{d},1}}}{2\sqrt{k_{\mathrm{s},2}x_1^{\mathrm{set}}\left(\left(k_{\mathrm{p}}^{\mathrm{out}}+k_{\mathrm{d},1}\right)x_1^{\mathrm{set}}-k_{\mathrm{p}}^{\mathrm{in}}\right)}}$
	6	$\frac{\boldsymbol{k_{s,2}}}{k_{\mathrm{d},2}}$	$\frac{\sqrt{k_{\mathrm{d},2}}\left(k_{\mathrm{p}}^{\mathrm{in}}-k_{\mathrm{p}}^{\mathrm{out}}x_1^{\mathrm{set}}\right)}{\sqrt{K_{\mathrm{I},2}k_{\mathrm{d},1}x_1^{\mathrm{set}}}}$	$\frac{k_{\mathrm{p}}^{\mathrm{in}}\sqrt{K_{\mathrm{I},2}k_{\mathrm{d},1}}}{2\sqrt{k_{\mathrm{d},2}x_1^{\mathrm{set}}}\left(k_{\mathrm{p}}^{\mathrm{in}}-k_{\mathrm{p}}^{\mathrm{out}}x_1^{\mathrm{set}}\right)}$
	7	$\frac{\left(\boldsymbol{k_{d,2}}-k_{\mathrm{s},2}\right)K_{\mathrm{I},1}}{k_{\mathrm{s},2}}$	$\frac{\sqrt{k_{\mathrm{s},2}}\left(\left(k_{\mathrm{p}}^{\mathrm{out}}+k_{\mathrm{d},1}\right)x_1^{\mathrm{set}}-k_{\mathrm{p}}^{\mathrm{in}}\right)}{\sqrt{\left(K_{\mathrm{I},1}+x_1^{\mathrm{set}}\right)K_{\mathrm{A},2}k_{\mathrm{d},1}x_1^{\mathrm{set}}}}$	$\frac{k_{\mathrm{p}}^{\mathrm{in}}\sqrt{\left(K_{\mathrm{I},1}+x_1^{\mathrm{set}}\right)K_{\mathrm{A},2}k_{\mathrm{d},1}}}{2\sqrt{k_{\mathrm{s},2}x_1^{\mathrm{set}}}\left(\left(k_{\mathrm{p}}^{\mathrm{out}}+k_{\mathrm{d},1}\right)x_1^{\mathrm{set}}-k_{\mathrm{p}}^{\mathrm{in}}\right)}$
	8	$\frac{\left(\boldsymbol{k_{s,2}}-k_{\mathrm{d},2}\right)K_{\mathrm{I},1}}{k_{\mathrm{d},2}}$	$\frac{\sqrt{k_{\mathrm{d},2}}\left(k_{\mathrm{p}}^{\mathrm{in}}-k_{\mathrm{p}}^{\mathrm{out}}x_1^{\mathrm{set}}\right)}{\sqrt{\left(K_{\mathrm{I},1}+x_1^{\mathrm{set}}\right)K_{\mathrm{I},2}k_{\mathrm{d},1}x_1^{\mathrm{set}}}}$	$\frac{k_{\mathrm{p}}^{\mathrm{in}}\sqrt{\left(K_{\mathrm{I},1}+x_1^{\mathrm{set}}\right)K_{\mathrm{I},2}k_{\mathrm{d},1}}}{2\sqrt{k_{\mathrm{d},2}x_1^{\mathrm{set}}}\left(k_{\mathrm{p}}^{\mathrm{in}}-k_{\mathrm{p}}^{\mathrm{out}}x_1^{\mathrm{set}}\right)}$

Table 4.1: Expressions for the tuning parameters of all eight homeostatic controller motifs in Figure 4.1, assuming ideal conditions (zero order degradation of the controller species, $K_{\mathrm{M},2} = 0$). Bold text indicates parameters used as proxies for changing the corresponding set-points. The disturbance input (u_2) for each controller is determined by the controller structure, $k_{\mathrm{p}}^{\mathrm{out}}$ for inflow controllers and $k_{\mathrm{p}}^{\mathrm{in}}$ for outflow controllers.

4.1.1 Tuning procedure

Tuning the homeostatic controller motifs for a desired response, that is, to achieve certain values for the tuning parameters x_1^{set}, ω_{n}, and ζ, is done by

manipulating values of the reaction kinetic parameters in the expressions in Table 4.1. In the following, we demonstrate this tuning procedure, focusing on manipulation of the rate constants for generation and removal of the controller species, $k_{\mathrm{s},2}$ and $k_{\mathrm{d},2}$, respectively, and the constant associated with the compensatory flux ($k_{\mathrm{s},1}$ for inflow controllers, and $k_{\mathrm{d},1}$ for outflow controllers). We elect to focus on these parameters as it is more conceivable that they are possible to tune from the perspective of synthetic biology, and offer a greater tunable range than the parameters associated with saturation ($K_{\mathrm{M},i}$, $K_{\mathrm{A},i}$, and $K_{\mathrm{I},i}$) [5].

We start by considering the operational range of the controller motifs. Although it is the job of the controller species to "absorb" perturbations in the regulated species, we do not want the level of the controller species to be unbounded. Therefore, we define an operational range for the compensatory flux, and a corresponding operational range for the level of the controller species. As an example, we let the maximum compensatory flux be $j_{\mathrm{comp}}^{\mathrm{max}} = 10.00$. The maximum compensatory flux is achieved when the controller species is at its maximum value, x_2^{max}, for activating controllers (controller motifs 1, 3, 5, and 7), and at its minimum value, x_2^{min}, for inhibiting controllers (controller motifs 2, 4, 6, and 8) [41]. We let the operational range of the controller species be given by $x_2^{\mathrm{max}} = 15.00$ and $x_2^{\mathrm{min}} = 0$ for this example. Furthermore, the reaction kinetic constants for activation and inhibition are chosen to avoid saturation in the operational range: $K_{\mathrm{A},2} = 2.00$, $K_{\mathrm{I},1} = 0.10$, and $K_{\mathrm{I},2} = 1.00$. We let the working point for inflow and outflow perturbations be given by $k_{\mathrm{p}}^{\mathrm{in}} = 2.00$ and $k_{\mathrm{p}}^{\mathrm{out}} = 5.00$ for inflow controllers, and $k_{\mathrm{p}}^{\mathrm{in}} = 5.00$ and $k_{\mathrm{p}}^{\mathrm{out}} = 2.00$ for outflow controllers[2]. If we specify the desired set-point $x_1^{\mathrm{set}} = 1.00$, the tuning procedure is reduced to finding the parameters $k_{\mathrm{s/d},1}$ ($k_{\mathrm{s},1}$ for inflow controllers and $k_{\mathrm{d},1}$ for outflow controllers), $k_{\mathrm{s},2}$, and $k_{\mathrm{d},2}$, such that a certain value for ζ (or ω_{n}, but not both) is achieved.

We tune the controller motifs for two different dynamical responses to a step change in set-point. One response is critically damped, corresponding to $\zeta = 1.00$ and no overshoot, and one underdamped response, corresponding to $\zeta = 0.20$ and 50% overshoot [155, 72]. A strongly underdamped system overshoots when adapting to a step change in set-point, but has considerably better disturbance rejection properties than a critically damped

[2]The difference in perturbation working point for inflow and outflow controllers is due to the fact that the two controller structures are suited to primarily compensate for different types of perturbations (outflow perturbations for inflow controllers, and inflow perturbations for outflow controllers) [41].

system. Tuning for better disturbance rejection properties may be more compelling for many biological systems. For outflow controller 5, given by (4.3)–(4.4), the compensatory flux is given by

$$j_{\text{comp}}(x_1, x_2) = k_{\text{d},1} \cdot x_1(t) \cdot \frac{x_2(t)}{K_{\text{A},2} + x_2(t)} \tag{4.12}$$

By setting $j_{\text{comp}} = j_{\text{comp}}^{\max} = 10.00$ and inserting $x_2 = x_2^{\max} = 15.00$, $x_1 = x_1^{\text{set}} = 1.00$, and $K_{\text{A},2} = 2.00$, we find that $k_{\text{d},1} = 11.33$. Using the expressions for set-point and damping ratio for controller motif 5 in Table 4.1, we find that $k_{\text{s},2} = 2.04$ and $k_{\text{d},2} = 2.04$ for $\zeta = 1.00$, and $k_{\text{s},2} = 51.00$ and $k_{\text{d},2} = 51.00$ for $\zeta = 0.20$. These values correspond to integral controller gains of $G_{\text{i}} = -2.04$ and $G_{\text{i}} = -51.00$ (see (4.5) with $K_{\text{M},2} = 0$), and response times[3] of $T_{\text{r}} \approx 0.8$ ($\omega_{\text{n}} = 2.50$) and $T_{\text{r}} \approx 0.1$ ($\omega_n = 12.50$), respectively [155, 72]. The same tuning procedure is performed for the complete set of homeostatic controller motifs in Figure 4.1. Table 4.2 lists the resulting values for the reaction kinetic parameters for each individual controller, tuned for the two different dynamical responses ($\zeta = 1.00$ and $\zeta = 0.20$). In particular, we note the same absolute values of G_{i} for all activating controllers (controller motifs 1, 3, 5, and 7), and all inhibiting controllers (controller motifs 2, 4, 6, and 8), respectively, indicating that the controllers are indeed tuned for the same response. We also note the opposite sign of G_{i} for inflow and outflow controllers of the same type (activating or inhibiting). This is due to the difference in function of inflow and outflow controllers (inflow controllers regulate x_1 by generation of the species, whereas outflow controllers regulate x_1 by its removal) [41].

Figure 4.2 shows simulation results of the *nonlinear* homeostatic controller motifs, using the parameter values for critically damped and underdamped responses in Table 4.2 (i.e. we are not simulating the linearized controller motifs). Looking at disturbance rejection properties, we see that controller responses cluster into two groups, one with activating controllers (controller motifs 1, 3, 5, and 7), and one with inhibiting controllers (controller motifs 2, 4, 6, and 8), where the activating controllers show a slower adaptation to perturbations than the inhibiting controllers. These differences in dynamical responses of equally tuned controllers is attributed to the fact that linearization is only a good approximation of the nonlinear systems close to the working point. And hence, for a relatively large change in set-point

[3]The time it takes for the step response to reach 63% of its steady-state value (from the initial steady-state value) [72].

		$k_{s,1}$	$k_{d,1}$	$k_{s,2}$	$k_{d,2}$	G_i
Critically damped ($\zeta = 1.00$)						
Inflow controllers	1	11.33	–	2.04	2.04	**2.04**
	2	10.00	–	6.94	6.94	**-6.94**
	3	11.33	–	24.68	2.24	**2.04**
	4	10.00	–	7.64	84.03	**-6.94**
Outflow controllers	5	–	11.33	2.04	2.04	**-2.04**
	6	–	10.00	6.94	6.94	**6.94**
	7	–	11.33	2.24	24.68	**-2.04**
	8	–	10.00	84.03	7.64	**6.94**
Underdamped ($\zeta = 0.20$)						
Inflow controllers	1	11.33	–	51.00	51.00	**51.00**
	2	10.00	–	173.61	173.61	**-173.61**
	3	11.33	–	617.10	56.10	**51.00**
	4	10.00	–	190.97	2100.69	**-173.61**
Outflow controllers	5	–	11.33	51.00	51.00	**-51.00**
	6	–	10.00	173.61	173.61	**173.61**
	7	–	11.33	56.10	617.10	**-51.00**
	8	–	10.00	2100.69	190.97	**173.61**

Table 4.2: Parameter values for all eight homeostatic controller motifs, tuned for critically damped ($\zeta = 1.00$) and underdamped ($\zeta = 0.20$) responses. Unspecified values are given by the working point value of the corresponding disturbance input for each controller (k_p^{out} for inflow controllers and k_p^{in} for outflow controllers). Bold text indicates the resulting integral gain.

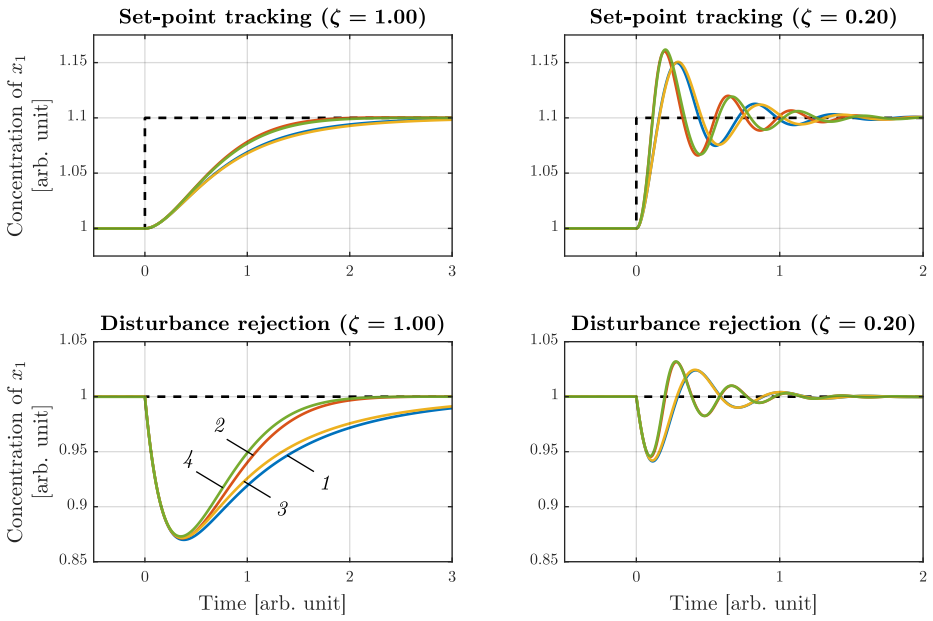

(a) Inflow controllers.

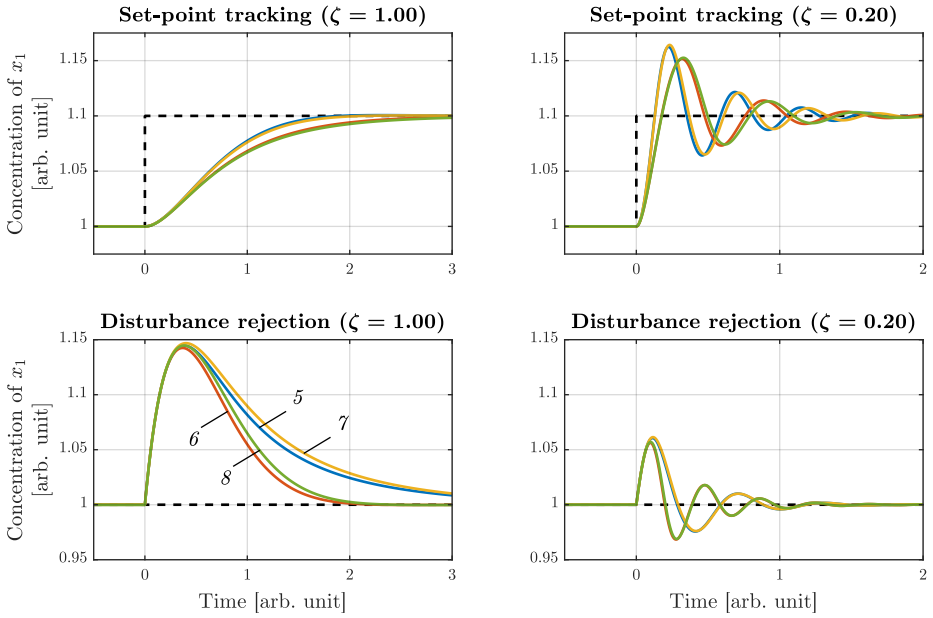

(b) Outflow controllers.

Figure 4.2: (Caption on the following page)

Figure 4.2: Simulation results of the homeostatic controller motifs in Figure 4.1 for the two different dynamical responses specified in Table 4.2. The inflow controllers (1, 2, 3, 4; colored blue, red, yellow, green, respectively) are shown in panel (a), and the outflow controllers (5, 6, 7, 8; colored blue, red, yellow, green, respectively) are shown in panel (b). Dashed black lines indicate the set-point for x_1. Controllers tuned for a critically damped response ($\zeta = 1.00$) are shown in the left column, and controllers tuned for a underdamped response ($\zeta = 0.20$) are shown in the right column. To investigate set-point tracking properties, a 10% increase in x_1^{set} is made at $t = 0$ (from $x_1^{\text{set}} = 1.00$ to $x_1^{\text{set}} = 1.10$). For disturbance rejection, a 20% increase is made in the disturbance input ($k_{\text{p}}^{\text{out}}$ for inflow controllers and k_{p}^{in} for outflow controllers) at $t = 0$ (from $k_{\text{p}}^{\text{in/out}} = 5.00$ to $k_{\text{p}}^{\text{in/out}} = 6.00$).

(10%) or disturbance (20%), differences in the responses of equally tuned controller motifs are expected. Overall, however, the controller motifs show very similar responses, with set-point tracking and disturbance rejection properties in accordance with the specified tuning parameters.

The tuning procedure used in this chapter relies on linearization of the homeostatic controller motifs, in a similar way to the tuning of industrial control processes. Of course, the controller motifs are nonlinear, meaning that the tuning procedure can only guarantee a certain dynamical response locally to the working point. However, linearization allows us to relate the nonlinear homeostatic controller motifs to well-known concepts in linear control analysis. From a synthetic biology point of view, such a tuning procedure provides a basis for the determination of system parameters, and gives insight into the relationship between parameter values and the dynamical response of the system. Additionally, by performing the same tuning procedure for several different working points, it is possible to characterize the dynamical behavior of the controller motifs over a range of inputs and steady-states, in a way similar to gain scheduling.

4.2 Constraints and trade-offs

In tuning the homeostatic controller motifs for a desired behavior, we are faced with certain constraints and trade-offs, some of which we can control (i.e. those related to the controller species), and others we have to work around (i.e. those related to the regulated species). Steady-state constraints arise from the fact that certain steady-state values are not attainable for a given set of system parameter values. Steady-state constraints define the tunable range of the homeostatic controller motifs. On the other

hand, trade-offs are related to the differential amplification of frequency components of an input signal during transmission through the system. The presence of time-varying exogenous signals may restrict the type of response we can tune the homeostatic controller motifs for in practice.

4.2.1 Steady-state constraints

In mathematical models of homeostatic controller motifs, the state variables represent concentrations of species, which are non-negative quantities by definition. And hence, we are faced with a constraint imposed by the nature of the system itself: We may only tune the system for a set-point constrained by $x_1^{\text{set}} > 0$. Similarly, we also encounter constraints due to saturation effects. Often, these constraints are difficult or even impossible to circumvent, and as a result, any tuning is limited by these constraints.

As discussed in Chapter 3, it is useful to separate the homeostatic controller motifs into a negative feedback connection of a process and a controller. In this abstraction, the process represents the generation and removal of the regulated species x_1, whereas the controller represents the generation and removal of the controller species x_2. This is illustrated by the block diagram in Figure 4.3. To investigate constraints associated with this system, we consider the process and controller components individually, and look at their steady-state input-output response curves. For the process, we characterize the steady-state output x_1^{ss} for a range of steady-state values of the control action (x_2^{ss}) and disturbance input ($k_{\text{p}}^{\text{in/out}}$). Similarly, we characterize the steady-state controller output x_2^{ss} for a range of steady-state controller inputs (x_1^{ss}). These steady-state input-output relationships are known as the process and controller nullclines, or in a biological context, dose-response curves, from which we can determine the steady-state of the closed-loop system, given as the intersection of the process and controller nullclines [6, 82].

Figure 4.4 shows a general sketch of the process (P) and controller (C) nullclines for a two-component system (such as the homeostatic controller motifs) in negative feedback connection. The nullclines experience upper and lower saturation limits, as is generally the case for biological systems [6]. Disturbances can alter the shape and position of the process nullcline, and hence, to guarantee an achievable set-point in the presence of disturbances, the set-point must be defined within the saturation limits of the process nullcline experiencing high (P_{high}) and low (P_{low}) expected disturbance

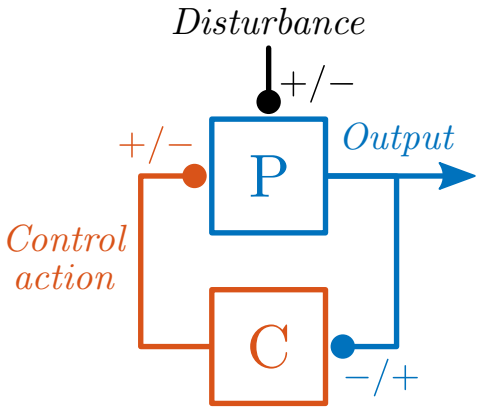

Figure 4.3: Separation of the homeostatic controller motifs into a process (P, blue) and a controller (C, red). The process output is fed into the controller, which produces a control action that is fed back into the process. Negative feedback is realized by having the process output negatively affect the controller output, which in turn positively affects the process output, or by having the process output positively affect the controller output, which in turn negatively affects the process output. The intersection of the steady-state input-output response curves (nullclines) for the process and controller gives the steady-state (equilibrium point) of the closed-loop system. Disturbances can alter the shape and position of the process nullcline, potentially affecting the closed-loop steady-state.

levels. From these process nullclines, it is seen that the saturation limits constraint achievable set-point values to the range $[P_{\min}, P_{\max}]$. As these constraints are imposed by the process, it is impossible to change them without altering the process itself, and thus, it is not simply a matter of tuning the controller [6].

Another important constraint is imposed by the controller, which we have already discussed before, namely zero-order degradation of the controller species. The degradation of the controller species is approximately zero-order when the enzyme responsible for the removal of the controller species is saturated with substrate, i.e. $K_{\mathrm{M},2} \ll x_2$. Naturally, we should tune the system for a steady-state such that this constraint holds, in order to achieve near-perfect adaptation [41, 6]. Importantly, this constraint governs the shape of the controller nullcline within the operational range of the controller species ($[x_2^{\min}, x_2^{\max}]$), which determines the deviation in steady-state of the regulated species ($[x_1^{\min}, x_1^{\max}]$) in the presence of disturbances [41, 6]. For a perfect integrator ($K_{\mathrm{M},2} = 0$), the controller nullcline is completely flat, such that no deviation in x_1^{ss} is seen [6]. Additionally, the saturation limits

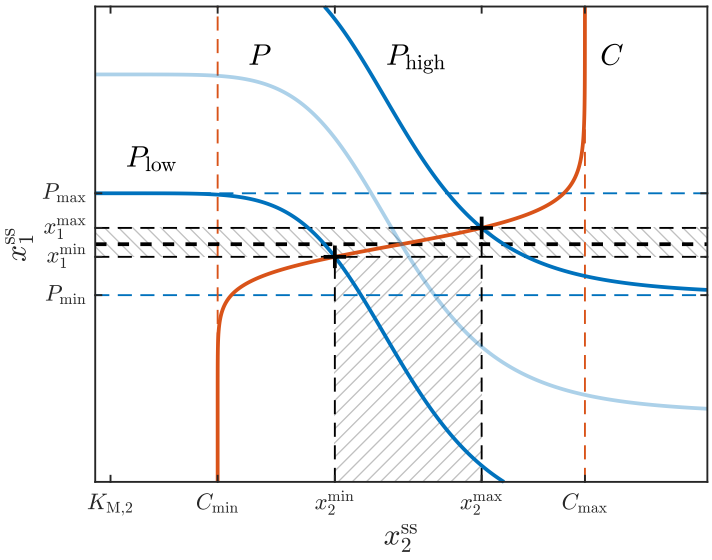

Figure 4.4: A sketch of general process (P, blue) and controller (C, red) nullclines for a two-component system experiencing upper and lower saturation limits. The presence of disturbances can alter the shape and position of the process nullcline, such that the range of achievable steady-states for the regulated species, x_1^{ss}, is given by the saturation limits of the process nullcline experiencing high (P_{high}) and low (P_{low}) expected disturbance levels ($[P_{\mathrm{min}}, P_{\mathrm{max}}]$). Similarly, saturation limits of the controller nullcline put constraints on the range of possible steady-state values for the controller species x_2^{ss} ($[C_{\mathrm{min}}, C_{\mathrm{max}}]$). The shape of the controller nullcline determines the deviation in x_1^{ss} for various disturbance levels ($[x_1^{\mathrm{min}}, x_1^{\mathrm{max}}]$). For the homeostatic controller motifs, a small deviation in x_1^{ss} is achieved when $K_{\mathrm{M},2} \ll x_2$, imposing yet another constraint on x_2^{ss}. Note that no deviation in x_1^{ss} is seen for a completely flat controller nullcline (dashed black line, thick).

of the controller nullcline put constraints on the operational range of the controller species ($[C_{\mathrm{min}}, C_{\mathrm{max}}]$), which if too narrow, could limit the range of disturbances the controller can compensate for. The constraints imposed by the controller are indicated in Figure 4.4.

To demonstrate this procedure for evaluating steady-state constraints (nullcline analysis), we again consider outflow controller 5. We find the process and controller nullclines by setting (4.3) and (4.4) to zero, and solving for the steady-states. The nullclines are given by

$$x_1^{ss} = P(k_{\mathrm{p}}^{\mathrm{in}}, x_2^{\mathrm{ss}}) = \frac{k_{\mathrm{p}}^{\mathrm{in}}}{k_{\mathrm{p}}^{\mathrm{out}} + k_{\mathrm{d},1} \cdot \beta(x_2^{\mathrm{ss}})} = \frac{k_{\mathrm{p}}^{\mathrm{in}}}{k_{\mathrm{p}}^{\mathrm{out}} + k_{\mathrm{d},1} \cdot \frac{x_2^{\mathrm{ss}}}{K_{\mathrm{A},2}+x_2^{\mathrm{ss}}}} \tag{4.13}$$

$$x_2^{\mathrm{ss}} = C(x_1^{\mathrm{ss}}) = f_{\mathrm{d},2}^{-1}\left(k_{\mathrm{s},2} \cdot \gamma(x_1^{\mathrm{ss}})\right) = \frac{k_{\mathrm{s},2} \cdot K_{\mathrm{M},2} \cdot x_1^{\mathrm{ss}}}{k_{\mathrm{d},2} - k_{\mathrm{s},2} \cdot x_1^{\mathrm{ss}}} \tag{4.14}$$

where P is the process nullcline, C is the controller nullcline, and $k_{\mathrm{p}}^{\mathrm{in}}$ is a steady-state inflow perturbation. We consider $k_{\mathrm{p}}^{\mathrm{out}}$ to be constant, since outflow controllers primarily compensate for inflow disturbances [41]. Figure 4.5 shows an example of the process and controller nullclines for outflow controller 5, where the process nullcline is given for various steady-state disturbance levels. The controller nullcline is given for various values of $K_{\mathrm{M},2}$, with the lowest value such that the degradation of the controller species is close to zero-order. This produces a relatively flat controller nullcline, and the intersections of the process nullclines with the controller nullcline show little variation in the steady-state value of the regulated species (x_1^{ss}). This shows that the controller nullcline is tuned to give good disturbance rejection over a range of expected disturbance levels[4]. Note that the process and controller nullclines in Figure 4.5 do not share the sigmoidal shape of the nullclines in Figure 4.4, and thus permit a larger range of steady-state values for both the process and controller species. However, we are still constrained by the lower saturation limit of the process nullcline ($P_{\min}$).

4.2.2 Trade-offs for time-varying inputs

In the preceding analysis and tuning of the homeostatic controller motifs, we looked at step responses to characterize set-point tracking and disturbance rejection properties. As discussed in Chapter 3, the inclusion of integral action in the homeostatic controller motifs is crucial for asymptotic regulation and disturbance rejection in the presence of constant exogenous signals, i.e. constant disturbance and reference (set-point). However, we should also consider the performance of the homeostatic controller motifs for time-varying exogenous signals. To investigate how the controller motifs respond to time-varying signals, we evaluate their response to sinusoidal[5] input signals of various frequencies [105, 93]. This gives the frequency response of the controller motifs, which tells us how various frequency

[4] However, we cannot say anything about the dynamical disturbance rejection properties of the controller motifs based on nullclines alone.

[5] Time-varying signals can be represented (or synthesized) by everlasting sinusoids, such that slowly varying signals are made up of low frequency sinusoids, while fast signals also contain high frequency sinusoids [105, 93].

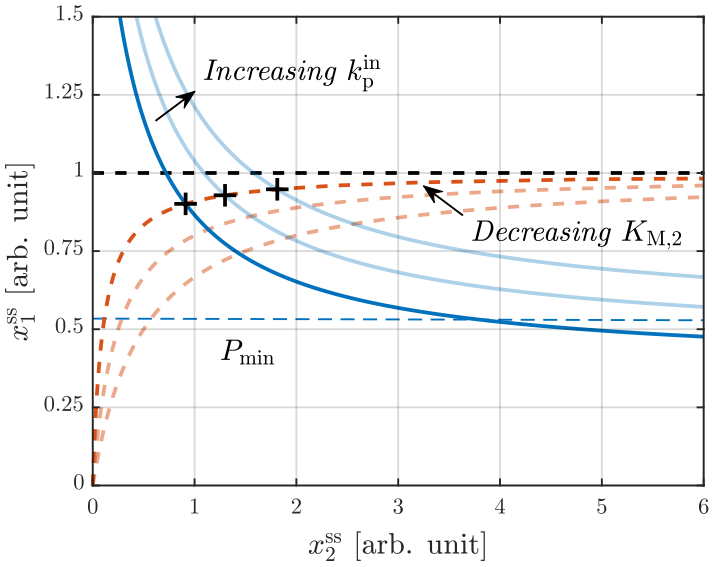

Figure 4.5: Process (solid blue lines) and controller (dashed red lines) nullclines for outflow controller 5, using parameters for a critically damped response ($\zeta = 1.00$ in Table 4.2) with $k_p^{in} = \{5.00, 6.00, 7.00\}$ and $K_{M,2} = \{0.10, 0.25, 0.50\}$. Achievable steady-state values for the regulated species x_1^{ss} are constrained by the lower saturation limit of the high disturbance process nullcline (P_{min}). For the lowest value of $K_{M,2}$, the controller nullcline is relatively flat, such that intersections of the process nullclines with the controller nullcline show little variation in steady-state of the regulated species x_1^{ss} (black crosses). In comparison, a completely flat controller nullcline (dashed black line) shows no deviation in x_1^{ss}.

components (sinusoids) are modified during transmission of an input signal through the system [105]. For input signals of a certain frequency, it is only necessary that the controller motifs have good set-point tracking and disturbance rejection properties at this frequency [93]. In most cases, however, input signals are not limited to single frequencies (or constant values), and therefore it is crucial to achieve good set-point tracking and disturbance rejection properties over a range of frequencies [93].

A large bandwidth (large range of frequencies) enables the homeostatic controller motifs to respond quickly to set-point changes and attenuate disturbances over a large frequency range. Let us consider the transfer functions for the linearized outflow controller 5, given by (4.8) and (4.11). The transfer function M in (4.8) describes the relationship between a change in set-point (using the parameter $k_{d,2}$) and the resulting output response (the regulated species x_1). Hence, the frequency response of M describes

the relationship between sinusoidal fluctuations in the set-point and the resulting fluctuations in the output, for different frequencies. On the other hand, the transfer function N in (4.11) describes the relationship between a change in disturbance input $k_{\mathrm{p}}^{\mathrm{in}}$ and the output response. Therefore, the frequency response of N describes the resulting output fluctuations in response to sinusoidal fluctuations in $k_{\mathrm{p}}^{\mathrm{in}}$, for different frequencies. For outflow controller 5, the integral gain is given in (4.5), and assuming ideal conditions ($K_{\mathrm{M},2} = 0$), the expression is reduced to $G_{\mathrm{i}} = -k_{\mathrm{s},2}$. We tune outflow controller 5 for three different responses $\zeta = \{1.00, 0.50, 0.20\}$, corresponding to integral gains $G_{\mathrm{i}} = \{-2.04, -8.16, -51.00\}$. Because the transfer function gain $K = 1/k_{\mathrm{s},2}$ (see (4.8)) is different for the different responses, we normalize the transfer functions to describe the relationship between changes in x_1^{set} and the output (as opposed to changes in $k_{\mathrm{d},2}$ and the output). Figure 4.6 shows the Bode magnitude plots[6] of M and N, along with corresponding step responses.

From the plots in Figure 4.6 it is seen that an increased integral gain $|G_{\mathrm{i}}|$ (absolute value) results in a faster step response, but also brings about oscillations and overshoot [182]. From the Bode magnitude plots of M, we see the that increased $|G_{\mathrm{i}}|$ results in a larger bandwidth, that is, a larger range of frequencies for the input signal for which the system has a desirable response (unity gain). However, we also see the emergence of a resonant peak, mid-frequencies for which the system produces an undesirable amplification [93]. This is also illustrated by the Bode magnitude plots of N, where low frequency disturbances are severely attenuated (and the zero frequency is completely attenuated, implying perfect adaptation to constant disturbances [43]), but less so are mid-frequencies at the resonant peak. Hence, the controller species is not able to compensate for disturbances fluctuating at these mid-frequencies. This demonstrates an important trade-off encountered in tuning: The more robustness realized at lower frequencies, the less robustness and more fragility is created at other frequencies [93]. Of course, a well tuned system is robust to disturbances of frequencies commonly encountered, while fragile to disturbances of frequencies that are uncommon or unnatural. Therefore, the presence of time-varying input disturbances may limit the values of G_{i} that can be chosen in practice, thereby limiting the response time we may tune the system for.

[6] A plot of the gain a sinusoidal input experiences during transmission through the system, as a function of frequency [105].

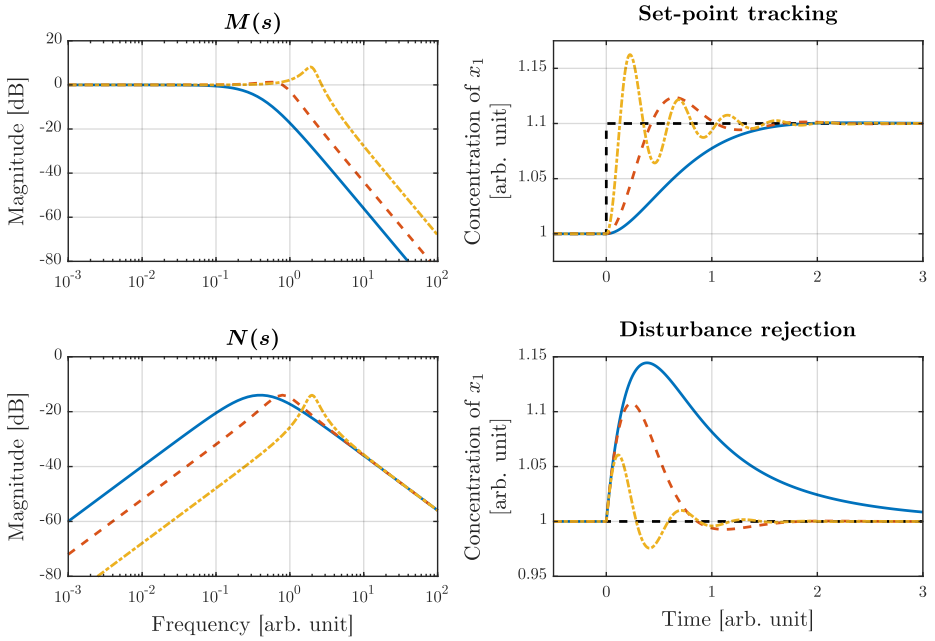

Figure 4.6: Bode magnitude plots of the transfer functions M and N in (4.8) and (4.11), respectively, with corresponding step responses (M is normalized as described in the main text). Outflow controller 5 is tuned for three different responses $\zeta = \{1.00, 0.50, 0.20\}$, corresponding to integral gains $G_\mathrm{i} = \{-2.04, -8.16, -51.00\}$ (solid blue line, dashed red line, and dash-dotted yellow line, respectively). Increased (absolute value) integral gain results in a faster response to step changes in set-point and disturbance input (larger bandwidth), however, it also brings about more overshoot and oscillations. These oscillations are reflected in the Bode magnitude plots as a resonant peak, mid-frequencies for which the system produces an undesired amplification. The frequency response of N illustrates an important trade-off in tuning: Realizing better disturbance rejection properties for low frequencies results in more fragility at higher frequencies [93].

4.3 The impact of nonlinearities

It is important to note that the homeostatic controller motifs are nonlinear, meaning that a tuning procedure based on linearization can only guarantee a certain dynamical response locally to the working point. As we have already seen, relatively large disturbance inputs have an influence on the dynamical properties of the homeostatic controller motifs (Figure 4.2). The relationship between (constant and time-varying) disturbance inputs and the dynamical properties of the homeostatic controller motifs are investigated in the last part of this chapter.

4.3.1 Constant disturbance inputs

An important aspect of the expression for the tuning parameters ω_n and ζ in Table 4.1, is that they depend on the parameters for inflow and outflow disturbances (k_p^{in} and k_p^{out}). To visualize this dependency, Figure 4.7 shows simulation results of inflow controller 3 for different working point values of the outflow disturbance $k_p^{out} = \{3.00, 5.00, 7.00\}$ (yellow, left), and outflow controller 6 for different working point values of the inflow disturbance $k_p^{in} = \{5.00, 7.00, 9.00\}$ (red, right). The simulation results show dynamical responses to step changes in set-point and disturbance input, for each of the different working point values given for k_p^{in} and k_p^{out}. It is seen that increasing the working point value of k_p^{out} for inflow controller 3 results in slower dynamics with a more damped response. On the other hand, increasing the working point value of k_p^{in} for outflow controller 6 results in faster dynamics with a less damped response. These simulation results demonstrate that changes in the perturbations k_p^{in} and k_p^{out} influence the dynamical response of the nonlinear controller motifs, implying that the linearized models (with a static working point) do not fully capture the nonlinear dynamics of the homeostatic controller motifs.

The effect of various perturbation values on the tuning parameters ω_n and ζ are shown in Figure 4.8. Comparing the activating controllers (controller motifs 1, 3, 5, and 7) to inhibiting controllers (controller motifs 2, 4, 6, and 8), we see that the tuning parameters are altered in different ways as the perturbation increases. Looking at activating controllers (red, left), we see that an increase in perturbation results in a decreased undamped natural frequency (ω_n) and an increased damping ratio (ζ). On the other hand, inhibiting controllers (blue, right) show an increase in undamped natural frequency and a decrease in damping ratio as the perturbation increases. Interestingly, the activating controllers are upper bounded (in terms of perturbation magnitude) by the capacity related breakdown[7] that occurs when $\omega_n \to 0$ (alternatively, $\zeta \to \infty$). On the other hand, inhibiting controllers are lower bounded by a similar capacity related breakdown. Depending on the use case, it may be more desirable to choose one controller type over the other. For example, a controller whose dynamical response becomes more damped with increasing disturbance (activating controller) may be more desirable over a controller whose response becomes faster, and more unstable, with increasing disturbance (inhibiting controller).

[7] Capacity related breakdown occurs when the compensatory flux (j_{comp}) reaches its upper limit, corresponding to the largest disturbance that can be compensated for [41].

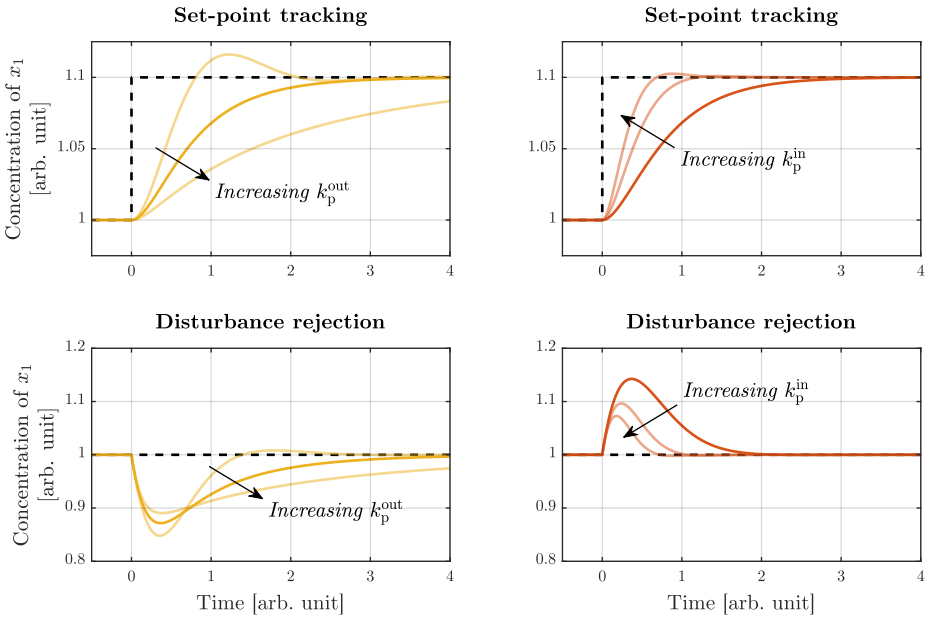

Figure 4.7: Simulation results of set-point tracking and disturbance rejection properties of inflow controller 3 (yellow, left) and outflow controller 6 (red, right). For inflow controller 3, three different trajectories are simulated using the outflow perturbation values $k_p^{out} = \{3.00, 5.00, 7.00\}$, and for outflow controller 6, three different trajectories are simulated using the inflow perturbation values $k_p^{in} = \{5.00, 7.00, 9.00\}$. The controllers are simulated for a 10% increase in set-point at $t = 0$, and an increase in perturbation values (k_p^{out} for inflow controller 3 and k_p^{in} for outflow controller 6) by 1.00 at $t = 0$. Highlighted lines indicate dynamical responses corresponding to Figure 4.2 (with the appropriate colors), and dashed black lines indicate the set-point for x_1.

4.3.2 Time-varying disturbance inputs

In many control problems, it is required that all solutions of the closed-loop system "forget" their initial conditions and converge to some steady-state solution, which is determined only by the input of the system [136]. The input can be, for example, a reference signal (asymptotic regulation) or a disturbance (asymptotic disturbance rejection). For asymptotically stable linear systems excited by inputs, all solutions converge to each other regardless of initial conditions, such that after transients, the dynamics of the system are determined only by the input [136]. It is this property, called *convergent dynamics*, that enables us to find the frequency response functions of the linearized homeostatic controller motifs. Global asymptotic stability of a nonlinear system with zero input does not generally guarantee

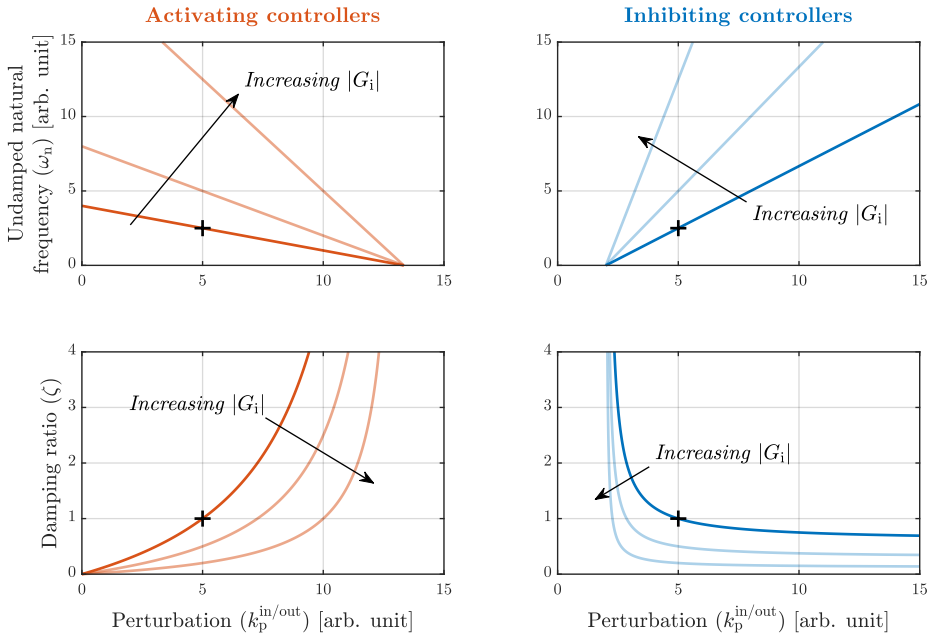

Figure 4.8: The effect of various perturbation values on the tuning parameters ω_n and ζ given in Table 4.1. Black crosses show controllers tuned for a critically damped response ($\zeta = 1.00$ in Table 4.2) at $k_p^{in/out} = 5.00$. The tuning parameters are then plotted for various perturbation values (highlighted lines). Plots for controllers with higher integral gain $|G_i|$ (absolute value) are also shown. Based on the controller type (activating or inhibiting), we see two distinct behaviors: For activating controllers, increasing the perturbation value results in an increasingly damped response, and for inhibiting controllers, increasing the perturbation value results in a less damped response.

that all solutions of the system with *nonzero* input converge [136]. In fact, there are several examples of nonlinear globally asymptotically stable systems that, when excited by a periodic input, have coexisting periodic solutions [136]. Thus, extending frequency response functions to the nonlinear case is not straightforward. It is clear that for nonlinear systems, convergent dynamics require additional conditions. Let us again consider outflow controller 5, and rewrite the system equations in (4.3)–(4.4) using vector notation

$$\dot{z}(t) = F(z, w) \tag{4.15}$$

where $z = [z_1, z_2]^\mathsf{T}$ are the system states with equilibrium point shifted to the origin ($z_i = x_i - x_i^*$, see Chapter 3), F is a vector of the (nonlinear) right-hand side expressions with $F(0, 0) = 0$, and w represents deviations in

$k_{\mathrm{p}}^{\mathrm{in}}$ around its working point value (i.e. the same situation described by N in (4.11) for the linearized system). We consider $k_{\mathrm{p}}^{\mathrm{out}}$ to be constant. We let $K_{\mathrm{M},2} = 0$ (i.e. perfect adaptation), and use parameters for a critically damped response ($\zeta = 1.00$ in Table 4.2).

The system in (4.15) is locally exponentially convergent (solutions exponentially converge to each other) if the matrix $\partial F/\partial z(0,0)$ is Hurwitz[8] (see Theorem 2.41 in Pavlov et al. [136]). Then, there exists a positive definite matrix $P = P^{\mathsf{T}} > 0$ such that

$$J(0,0) = P \cdot \frac{\partial F}{\partial z}(0,0) + \frac{\partial F}{\partial z}^{\mathsf{T}}(0,0) \cdot P < 0 \tag{4.16}$$

where $J(z,w) = P \cdot \partial F/\partial z(z,w) + \partial F/\partial z^{\mathsf{T}}(z,w) \cdot P$. Since $J(0,0)$ is negative definite, $J(z,w)$ is negative definite for all small z and w. A neighborhood of the origin $z = 0$ can be chosen such that $J(z,w) < -Q$ for some $Q > 0$, all z in the neighborhood, and all $|w|$ bounded by some positive value [136]. It can then be shown that for every $|w(t)| \leq \bar{r}$ ($\bar{r} > 0$) there exists a steady-state solution that lies in the neighborhood for all time, and that any two solutions starting in the neighborhood exponentially converge to each other [136]. Note that the use of "steady-state" in this case does not necessarily imply that $\dot{z} = 0$, but rather that all solutions "forget" their initial conditions and converge to some unique solution determined only by the input, which can be called a steady-state solution [136].

From our discussion on stability in Chapter 3, we know that the homeostatic controller motifs have a globally asymptotically stable equilibrium point for zero disturbance input. This implies that the matrix $\partial F/\partial z(0,0)$ is Hurwitz for outflow controller 5. The level surface of the quadratic function $W(z) = z^{\mathsf{T}} \cdot P \cdot z$ where $J(z,w) < -Q$ is satisfied defines the neighborhood of the origin where the system in (4.15) is locally exponentially convergent. It is then possible to choose $\bar{r}$ such that the neighborhood is invariant for any disturbance input satisfying $|w(t)| \leq \bar{r}$ [136]. This neighborhood is shown for outflow controller 5 in Figure 4.9a. Any solution stating in this neighborhood, excited by a sinusoidal disturbance with amplitude $a \leq \bar{r}$, will converge to each other (Figure 4.9b).

The dynamical properties shown in Figure 4.9b are similar to that of asymptotically stable linear systems. In fact, the convergence property is an extension of stability properties of asymptotically stable linear time-invariant (LTI) systems to the nonlinear case [136, 137]. For a periodic

[8] A matrix is said to be Hurwitz when all eigenvalues satisfy $\mathrm{Re}(\lambda_i) < 0$ [92].

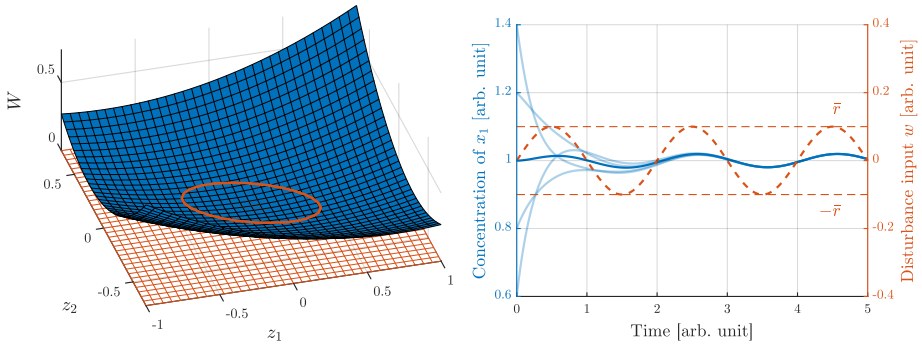

(a) Convergence region estimate.

(b) Converging trajectories.

Figure 4.9: Estimate of the convergence region for outflow controller 5 (red ellipsis, panel (a)), tuned for a critically damped response ($\zeta = 1.00$ in Table 4.2). All solutions starting in the convergence region exponentially converge to the same steady-state solution (solid blue lines, panel (b)). This is true for any sinusoidal disturbance input with amplitude $a \leq \bar{r}$ (dashed red line).

input, the steady-state solution of uniformly convergent[9] systems is also periodic, with the same period as the input [136, 137]. This enables us to numerically find the nonlinear frequency response function for (4.15) by simulating the system with disturbance input $w(t) = a \cdot \sin(\omega \cdot t)$, over a range of excitation amplitudes a and frequencies ω [137, 136]. The nonlinear Bode magnitude plot for outflow controller 5, tuned for a critically damped response with excitation amplitude $a = \bar{r}$ is shown in Figure 4.10 (highlighted solid blue line). In comparison to the Bode magnitude plot of the linearized version of outflow controller 5 (dashed red line), we see virtually identical responses. However, for $K_{\mathrm{M},2} > 0$, we see discrepancies at low frequencies, showing that only partial adaptation is achieved in this case. For nonlinear convergent systems we may observe a non-proportional change in amplitude of the steady-state solution with respect to a change in the excitation amplitude [137]. However, we saw no appreciable difference in the nonlinear Bode magnitude plot of outflow controller 5 for excitation amplitudes $a < \bar{r}$ compared to $a = \bar{r}$.

It is evident from the Bode magnitude plots in Figure 4.10 that the transfer function N in (4.11) provides a good approximation to the nonlinear system, at least for the estimated convergence region shown in Figure 4.9a with excitation amplitudes $a \leq \bar{r}$ (see Figure 4.9b). This result demonstrates

[9] Exponentially convergent is a stronger sense of the convergence property than uniformly convergent [136, 135].

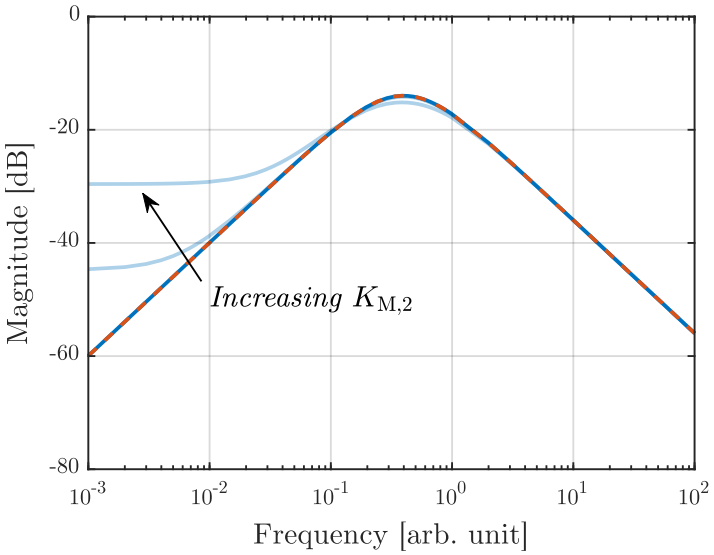

Figure 4.10: Bode magnitude plots for the disturbance sensitivity of the nonlinear (solid blue lines) and linearized (dashed red line) versions of outflow controller 5, tuned for a critically damped response ($\zeta = 1.00$ in Table 4.2) with excitation amplitude $a = \bar{r}$. Nonlinear Bode magnitude plots are shown for $K_{M,2} = \{0, 0.01, 0.10\}$. It is apparent that the linearized version (N in (4.11)) provides a good approximation of the nonlinear system, for the convergence region in Figure 4.9a and excitation amplitudes $a \leq \bar{r}$ (see Figure 4.9b). However, for increasing $K_{M,2}$, discrepancies appear, particularly for low frequencies.

that the tuning procedure presented for the homeostatic controller motifs, despite relying on linearization, provides a set of system parameters that produces the desired dynamical response in a reasonably large neighborhood of the working point, and that the desired response also holds for time-varying input signals. However, it is likely that our estimate for the convergence region is rather conservative, which leaves $\bar{r}$ fairly low. This could be due to a suboptimal choice for the matrix P, or the fact that the estimation procedure is based on quadratic Lyapunov functions analysis, which is conservative by itself when applied to nonlinear systems [136]. It is possible that a better estimate for the convergence region could be made using the combined storage function presented in Chapter 3. Nevertheless, the results in Figure 4.10 give us a sense of how well the linearized homeostatic controller motifs approximate the nonlinear systems for time-varying disturbance inputs.

Chapter 5

Dilution resistance and noise

In this chapter, we take a look at the homeostatic controller motifs under non-ideal conditions. In particular, we consider some practical aspects in living cells that may impact the performance of homeostatic mechanisms. Namely, we will look at dilution of cellular constituents and stochastic fluctuations in chemically reacting systems. Especially for cancer cells is it expected that dilution poses a significant challenge for the effective regulation of metabolism, due to increased glycolytic and proliferative activity leading to cell swelling and growth-induced dilution. We start with a brief recount of how mathematical modeling based on reaction rate equations account for growth-induced dilution. We then review the literature to give an overview of the rewiring of glycolysis in cancer. We focus on the various signaling pathways involved in the regulation of glucose uptake in cancer, and show that differential gene expression of cancer and normal cells corroborate the reported rewiring in cancer. It is based on this information that we construct a mathematical model of glucose uptake in cancer, which we study in the presence of growth-induced dilution and extrinsic noise in the final parts of this chapter.

5.1 Dilution of cellular constituents

In growing cells, dilution globally affects the concentrations of cellular constituents [79, 104]. The protective mechanisms that maintain homeostasis also need to be in place during growth, meaning that homeostatic mechanisms need the ability to compensate for growth-induced dilution, in addition to perturbations of the type considered in Chapter 4 [147]. For the homeostatic controller motifs, growth-induced dilution means that both the regulated species and the controller species dilute as the cell grows. In addition, the enzymes driving the synthesis and degradation reactions of

these species are subject to dilution. Assuming that the cellular volume increases exponentially, the effect of dilution is a first-order removal term in the reaction rate equations of all cellular constituents [6, 4, 142]. The rate constant, k_{dil}, for this first-order removal term is related to the cell volume doubling time (τ_2) by $k_{\text{dil}} = \ln(2)/\tau_2$ [6, 4]. As we have already seen in Chapter 4, homeostatic inflow controllers are capable of fully compensating for such first-order outflow perturbations in the regulated species. However, because dilution affects all cellular constituents, a first-order removal term is also added to the controller species. Such a perturbation in the controller species interferes with the ability of the homeostatic controller motifs to achieve robust regulation. In fact, dilution leads to "leaky" integral action, with the consequence that the adaptation property is diminished [142]. Dilution of the enzymes generating and turning over the controller species will affect the V_{max} value of these reactions (recall that $V_{\text{max}} = k_{\text{cat}} \cdot E_0$). As we have seen in Chapter 3, these parameters define the set-point for the controller motifs, and changes in these parameter values lead to changes in the set-point. With a doubling time (τ_2) of 20–30 min for *Escherichia coli*, the rate of dilution becomes large enough to dominate the rate of proteolysis and poses a significant challenge for transcriptional regulation [4, 6, 79]. In mammalian cells, doubling can take hours to days, and hence, the effect of growth-induced dilution is less severe in these cells [79].

Aside from dilution of cellular constituents due to growth and division, dilution can also result from osmotic swelling [104, 73]. The membrane of animal cells is highly permeable to water, and any imbalance of intracellular and extracellular osmolarity results in movement of water across the cell membrane [104]. The transport of nutrients, such as amino acids and glucose, into the cell can lead to increased cellular volume [104, 73]. Especially Na^+-coupled transport processes can generate large chemical gradients across the cell membrane, giving rise to an osmotic water shift into the cell [104, 73]. A wide variety of metabolic pathways produce osmotically active substances, such as the degradation of proteins to amino acids or glycogen to glucose phosphate, which may lead to cell swelling [104]. The accumulation of lactate, e.g. during muscle exercise, develops intracellular acidosis and can lead to cell swelling [104].

It is well established that cell swelling and shrinkage affect important cellular functions, in part by dilution and concentration of cellular compounds [104, 29, 138, 73]. Such changes in concentration can markedly influence the function of intracellular proteins, and cell swelling/shrinkage affects the expression of a wide variety of genes [104, 110]. It has been

Figure 5.1: Most proteins and mRNAs are size dependent, meaning that their concentrations remain fairly constant during growth. Moreover, the size of organelles (e.g. nucleus, nucleolus, mitochondria, vacuole) often scale with cell size. By contrast, the amount of genomic DNA remains constant during growth, which is also true for some proteins and mRNAs [153, 149].

demonstrated that dilution poses a significant challenge to enzyme reactions in solitary vesicles, showing that there is a considerable impact on the dynamical and steady-state behaviors of such reactions [110]. In fact, a large enough rate of dilution can effectively stop enzyme reactions [110]. Dilution can also be exploited by cells. For example, in the budding yeast *Saccharomyces cerevisiae*, the concentration of a cell cycle activator is maintained at a constant level during growth relative to a growth diluted inhibitor, providing a measurement of cell volume and a molecular mechanism for cell size control [154, 153]. Although most proteins are maintained at fairly constant concentrations in growing cells, owing to mRNA amounts and number of ribosomes increasing with cell size, some do not (Figure 5.1) [153, 149]. In order to understand how cell size differentially affects the concentration of certain proteins, it is necessary to understand how cells coordinate biosynthesis to keep most macromolecules at constant concentrations [153].

5.2 Reaction rate equation models in a changing volume

To describe changes in the concentrations of cellular constituents during growth, we start by considering some compound (P) in a growing cell (Figure 5.2a). We let n_{P} denote the amount (i.e. moles) of the compound, such that the concentration is $c_{\mathrm{P}}(t) = n_{\mathrm{P}}(t)/V(t)$, where V denotes the cellular volume. Using the product rule, we express the change in concentration of

the compound as

$$n_{\mathrm{P}}(t) = c_{\mathrm{P}}(t) \cdot V(t) \tag{5.1}$$

$$\dot{n}_{\mathrm{P}}(t) = \dot{c}_{\mathrm{P}}(t) \cdot V(t) + c_{\mathrm{P}}(t) \cdot \dot{V}(t) \tag{5.2}$$

$$\dot{c}_{\mathrm{P}}(t) = \frac{\dot{n}_{\mathrm{P}}(t)}{V(t)} - c_{\mathrm{P}}(t) \cdot \frac{\dot{V}(t)}{V(t)} \tag{5.3}$$

where the first term on the right-hand side of (5.3) is identical to the time derivative of c_{P} in a constant volume, while the second term represents the dilution of c_{P}, which we will call the *dilution term* [147, 110].

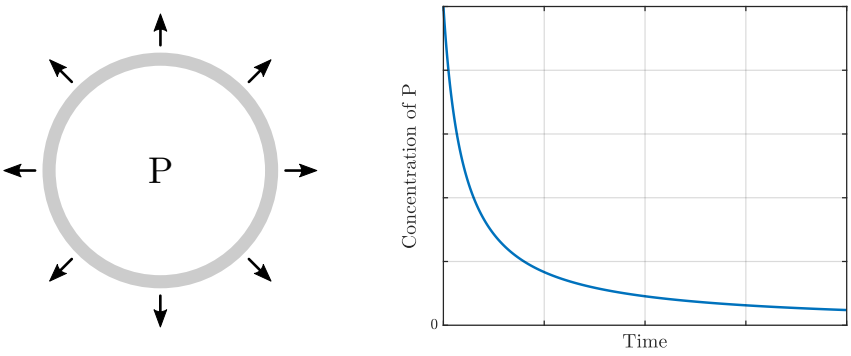

(a) Growth-induced dilution. **(b)** Dilution of P.

Figure 5.2: For a constant amount of some compound P ($\dot{n}_{\mathrm{P}}(t) = 0$) in a growing cell (panel (a)), the concentration c_{P} will dilute according to $-c_{\mathrm{P}} \cdot \dot{V}/V$. For the linear growth equation $V(t) = V_0 + k_{\mathrm{V}} \cdot t$, where V_0 is the initial cell volume and k_{V} is a constant growth rate, the concentration of P decays exponentially (panel (b)).

We use (5.3) as a "template" for formulating reaction rate equations for cellular constituents in a growing cell. As an example, we consider the formation of a product by an enzyme reaction in a growing cell (Figure 5.3a). The reaction rate is described by the Michaelis–Menten equation

$$v = \frac{k_{\mathrm{cat}} \cdot c_{\mathrm{E}} \cdot c_{\mathrm{S}}}{K_{\mathrm{M}} + c_{\mathrm{S}}} \tag{5.4}$$

where v is the reaction rate, k_{cat} is the catalytic constant (or turnover number), K_{M} is the Michaelis constant, c_{E} is the (total) concentration of enzyme, and c_{S} is the concentration of substrate [31]. By inserting (5.4) into (5.3), we get the differential equation describing the formation of a

product by an enzyme reaction in a growing cell [110]

$$\dot{c}_{\mathrm{P}}(t) = \frac{k_{\mathrm{cat}} \cdot c_{\mathrm{E}}(t) \cdot c_{\mathrm{S}}(t)}{K_{\mathrm{M}} + c_{\mathrm{S}}(t)} - c_{\mathrm{P}}(t) \cdot \frac{\dot{V}(t)}{V(t)} \tag{5.5}$$

where c_{P} denotes the concentration of the product. It is important to note that dilution affects the concentrations of all constituents of the enzyme reaction, i.e. product, enzyme, and substrate, not just the concentration of product. This is indicated by the time-dependencies introduced in (5.5), which come from the relationship $c_{\mathrm{E/S}}(t) = n_{\mathrm{E/S}}(t)/V(t)$, where V is time-dependent in a growing cell, even if $n_{\mathrm{E/S}}$ may be constant.

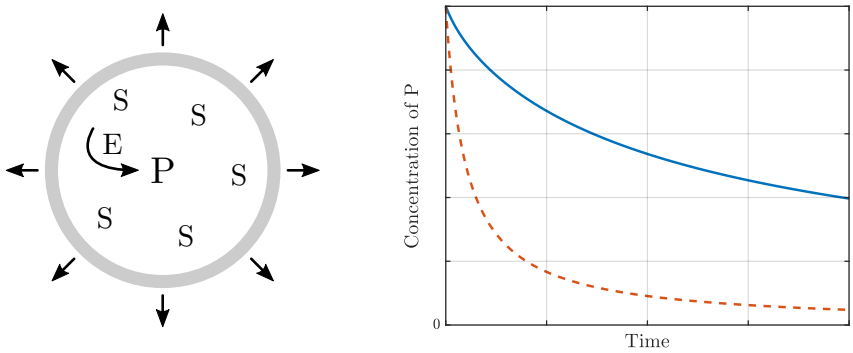

(a) Cell-internal generation. **(b)** Dilution of P.

Figure 5.3: For an enzyme reaction in a growing cell (panel (a)), all constituents of the reaction (substrate, enzyme, and product) are affected by dilution. Linear cell growth results in a slowdown of the enzyme reaction (due to dilution of enzyme and substrate concentrations), and dilution of the product concentration (panel (b), solid blue line). However, because the enzyme reaction is not completely stopped, the rate of dilution of c_{P} is significantly reduced in comparison to the case in Figure 5.2 (dashed red line). Unless c_{E} and c_{S} are replenished, the enzyme reaction will eventually stop, and c_{P} will dilute completely.

Whereas the case in Figure 5.3 considers a compound being produced internally in a growing cell, another important case to consider is when the compound is being generated by a transporter-based process (Figure 5.4a). In this case, we express the transporter as a surface concentration at the cell surface. Assuming that the transporter reaction can be approximated by the Michaelis–Menten equation (which is often true if the intracellular

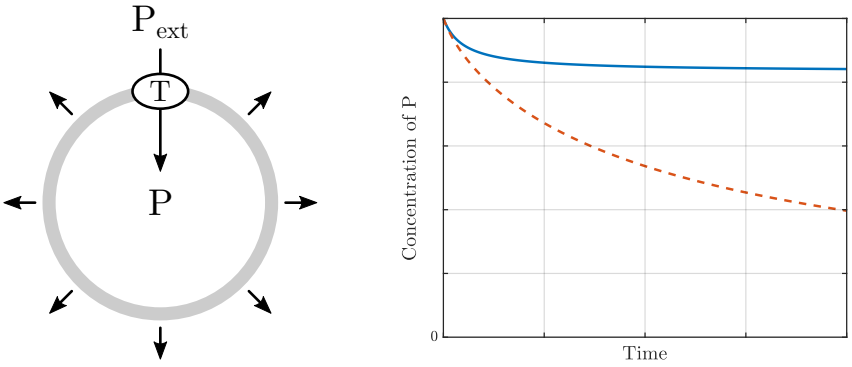

(a) Transporter-based generation. **(b)** Dilution of P.

Figure 5.4: For transporter-based generation of P in a growing cell (panel (a)), the extracellular concentration of P can be considered constant. In comparison to internally generated P (panel (b), dashed red line), transporter-based generation of P results in a steady-state concentration (solid blue line). Note that it is also possible to achieve a steady-state for internally generated P if we let the intracellular concentration of substrate be constant.

concentration of P is low [171, 165]), the system is given by

$$\dot{c}_{\mathrm{P}}(t) = \frac{k_{\mathrm{cat}} \cdot c_{\mathrm{T}}(t) \cdot c_{\mathrm{P,ext}}(t)}{K_{\mathrm{M}} + c_{\mathrm{P,ext}}(t)} \cdot \frac{A(t)}{V(t)} - c_{\mathrm{P}}(t) \cdot \frac{\dot{V}(t)}{V(t)} \tag{5.6}$$

$$\dot{c}_{\mathrm{T}}(t) = -c_{\mathrm{T}}(t) \cdot \frac{\dot{A}(t)}{A(t)} \tag{5.7}$$

where c_{T} is the surface concentration of the transporter, $c_{\mathrm{P,ext}}$ is the extracellular concentration of P, and A is the surface area of the cell. Note that the import of P is multiplied by the conversion factor A/V. This is because the transporter is localized in the cell membrane, such that the import of P is a flux with respect to the surface area, which has to be converted into a flux with respect to the cell volume. Notably, the intracellular concentration of P and the surface concentration of T are subject to different dilution terms. For a spherical cell, the equation

$$\frac{\dot{A}(t)}{A(t)} = \frac{2}{3} \cdot \frac{\dot{V}(t)}{V(t)} \tag{5.8}$$

expresses the relationship between surface area and volume growth [185]. An important difference between the cases in Figure 5.3 and Figure 5.4 is that the external concentration of substrate can often be regarded as constant,

whereas this may not be true for the internal substrate concentration. Since the extracellular concentration of P in Figure 5.4 is not subject to dilution, and because the dilution term vanishes as the cellular volume becomes large (for linear growth), intracellular P reaches a steady-state concentration[1]. Note, however, that this steady-state is not robust to perturbations in c_{P} [147].

5.3 Dilution resistance in growing cancer cells

Cancer cells show an increased uptake of glucose and a high rate of glycolysis and lactic acid fermentation, even in the presence of oxygen, and a more glycolytic phenotype is persistent with a more aggressive cancer cell type [57, 37, 150]. This is known as the *Warburg effect*, or *aerobic glycolysis*, and is necessary in order to meet the increased demands of rapid proliferation [191, 57]. Cancer cells have functional mitochondria, and oxidative phosphorylation can occur at rates similar to that seen in normal cells [74]. This is in contrast to most normal cells that maintain a high rate of glycolysis at the expense of oxidative phosphorylation; a phenomenon known as the *Crabtree effect* [74]. However, in the hypoxic tumor microenvironment, cancer cells naturally show a decreased reliance on oxidative phosphorylation [80, 74]. The increased glycolytic flux in cancer supplies biosynthetic pathways with precursors, meets the increased bioenergetic demand of proliferation, and contributes to tumor invasion through the excretion of lactate and consequent acidification of the tumor microenvironment [191, 74, 68, 35, 57].

The growth mode of cancer cells relies on a balanced production of cellular components to avoid molecular crowding and solvent capacity constraints [194, 193]. The cell represents a tiny reagent reservoir and is reliant on a balanced influx and efflux of compounds to support growth rates corresponding to that seen in cancer. Thus, as the cell expands, its constituents need to increase at the same rate to meet the growth requirements, meaning a proportional increase in nucleic acids, polysaccharides, proteins, and lipids [67]. Aside from biomass formation for the purpose of growth, increased metabolic activity also affects the cell volume through uptake of nutrients, creation of osmotically active substances, developing intracellular acidosis, and depletion of available ATP [104, 52, 128]. In fact, increased

[1] This is also the case for the enzyme reaction in Figure 5.3 if the intracellular substrate concentration can be considered constant [147].

cellular volume appears to be required for proliferation, and hypertonic shrinkage inhibits cell proliferation, whereas slight osmotic swelling has the opposite effect [104]. In contrast, differentiation is followed by cell shrinkage in a number of cells [104]. It is clear that control mechanisms employed by cancer cells to maintain a highly glycolytic phenotype must be robust to dilution.

5.3.1 Rewiring of glycolysis in cancer

The mechanisms that reprogram metabolism in cancer are often cancer-specific; nevertheless, there are common hallmarks, notably a shift towards protein isoforms that promote biosynthesis and proliferation [74, 191]. In the first step of glycolysis, glucose is transported into the cell. The GLUT (gene symbol *SLC2A*) family of glucose transporters are membrane-spanning proteins facilitating the transport of sugars across biological membranes along the concentration gradient [26, 89]. GLUT1 is one of 14 currently identified GLUT proteins expressed in humans, and is expressed in almost every tissue [175, 15, 174, 55]. Together with its high affinity for glucose, this gives GLUT1 a clear role in the basal glucose uptake of most tissues [15, 174, 26]. Elevated expression of GLUT1 has been reported in most cancers, and the expression level correlates reciprocally with the survival of cancer patients [55, 57, 68]. Hypoxia-inducible factor-1 (HIF-1), a dimer of HIF-1α and HIF-1β, is one of the factors responsible for upregulating GLUT1 in tumor cells [157, 55, 74, 57, 207]. HIF-1β is constitutively expressed, whereas HIF-1α is regulated through oxygen-dependent and oxygen-independent mechanisms [157]. GLUT1 expression is upregulated through hypoxia-response elements on the GLUT1 promoter that bind HIF-1 [55]. HIF-1α has increased levels in most cancers, which provides a mechanism by which cancer cells overexpress GLUT1 [55, 157, 57]. Other factors known to cause overexpression and translocation of GLUT1 to the cell membrane in cancer include the oncoprotein c-Myc, the protein kinase Akt/PKB, and oncogenic KRAS and BRAF [55, 74, 57, 207].

Glycolysis consists of several reversible reactions and three (essentially) irreversible reactions (Figure 5.5). Because they are irreversible, these three reactions represent committed steps of glycolysis, and the enzymes that drive these reactions are gatekeepers of glycolysis and have a key role in regulating the glycolytic flux [74]. In the first irreversible reaction of glycolysis, glucose is phosphorylated to glucose 6-phosphate (G6P) by hexokinase, coupled to the dephosphorylation of ATP, thereby trapping

glucose inside the cell[2] [139, 115, 17]. Hexokinase 2 (HK2) is one of four isoforms of hexokinase found in mammalian tissue [115]. HK2 has a very high affinity for glucose, with a Michaelis constant (K_{M} value) of 0.02–0.03 mM [139, 115]. Overexpression of HK2 in cancer occurs through multiple mechanisms, and includes the involvement of HIF-1, c-Myc, and Akt/PKB [74, 157, 207]. To support increased glucose uptake, HK2 is bound to the outer mitochondrial membrane protein voltage-dependent anion channel (VDAC) [139, 115, 74]. VDAC supplies HK2 with ATP by recruiting help from ATP synthase and the adenine nucleotide translocator, resulting in a mechanism that rapidly converts glucose to G6P [115]. HK2 is product inhibited by G6P, however, it is likely that this inhibition is minimal due to rapid utilization of G6P in cancer cells, and diminished (or possibly saturated) inhibition experienced by mitochondrial bound HK2 [74, 139, 24, 127, 114]. In addition, the binding of HK2 to the outer mitochondrial membrane via VDAC helps prevent apoptosis in cancer cells [115, 139].

The second irreversible reaction of glycolysis is catalyzed by phosphofructokinase 1 (PFK1), and is the phosphorylation of fructose 6-phosphate (F6P) to fructose 1,6-bisphosphate (F1,6BP) with the concomitant dephosphorylation of ATP [123, 74, 17]. PFK1 is a tetrameric enzyme that exists in liver (PFKL), muscle (PFKM), and platelet (PFKP) isoforms in mammalian cells [95, 123, 74]. PFK1 expression is upregulated in cancer cells, and increased expression of the PFKP isoform is a characteristic feature of cancer [123, 95]. Krüppel-like factor 4 (KLF4), which has elevated levels in certain cancer types, has been shown to activate transcription of the *PFKP* gene by directly binding to its promoter [123]. In addition, PFK1 is allosterically activated by fructose 2,6-bisphosphate (F2,6BP), which shows increased generation associated with overexpression of the phosphofructokinase 2 (PFK2) isoform PFKFB3 in cancer [74, 157].

The third irreversible reaction of glycolysis is the conversion of phosphoenolpyruvate (PEP) to pyruvate by the transfer of a phosphoryl group to ADP [74, 17]. Cancer cells control this reaction by expressing the low-affinity M2 isoform of pyruvate kinase (PKM2) [191, 74]. The PKM2 tetramer is allosterically regulated by various metabolites and responds to nutritional and stress signals, whereas the normal M1 isoform of pyruvate kinase (PKM1) is a constitutively active tetramer [74, 47]. The regulation of PKM2 enables cancer cells to dictate the flow of carbon into biosynthetic

[2] G6P is not transported out of the cell, and cannot pass through the cell membrane [17].

pathways and adapt to varying conditions of nutrient availability and anabolic demands [191, 74, 47]. Additionally, PKM2 is regulated between its metabolically active tetrameric form and metabolically inactive dimeric form, where the PKM2 dimer is imported into the nucleus and stimulates transcription of glycolytic genes [47]. Interestingly, PKM2 expression is under direct control of c-Myc and HIF-1, in a positive feedback connection that promotes the Warburg effect in cancer [47, 112].

In addition to the key regulatory enzymes of glycolysis described above, other important glycolytic enzymes are upregulated in cancer. For example, of the lactate dehydrogenases (LDHs), LDHA is the predominantly expressed isozyme in cancer [74]. Both HIF-1 and c-Myc increase the expression of LDHA, which has a high affinity for pyruvate, and favors the conversion of pyruvate to lactate [74, 157, 207]. Enolase 1 (ENO1) is induced in cancer cells through HIF-1α overexpression [55, 157]. Aldolase A (ALDOA), which is also induced by HIF-1α overexpression, is the predominant aldolase isoform expressed in hepatoma and gastric cancer tissues, and favors the cleaving of F1,6BP [10, 74, 157]. Taken together, the glycolytic isoforms expressed in cancer show a concerted effort to increase glycolytic activity and promote production of biosynthetic precursors. The diagram of glycolysis shown in Figure 5.5 highlights some of the key isoforms that are commonly overexpressed in cancer, along with some key factors responsible for overexpression.

5.3.2 Regulation of glucose uptake in cancer

We now focus our attention to glucose uptake and the initial steps of glycolysis, and discuss the control mechanisms that regulate glucose uptake in cancer. Although key glycolytic enzymes are upregulated in cancer, they are still involved in metabolic regulation and respond to signals such as nutritional and oxidative stress, however, this regulation changes to favor proliferation [191, 74, 47, 206]. Regulation of nutrient transporters by the availability of nutrients is a phenomenon observed in bacteria and yeast, and similarly, an inhibitory effect of glucose on GLUT1 mRNA and protein expression has been observed in several mammalian cell lines [97, 27]. To study the effect of glucose on GLUT1 expression, cells have been subjected to glucose deprivation experiments, with the common result that GLUT1 content at the cell surface is increased [97, 69, 70, 170, 18, 184]. This is achieved by different mechanisms, including increased GLUT1 mRNA

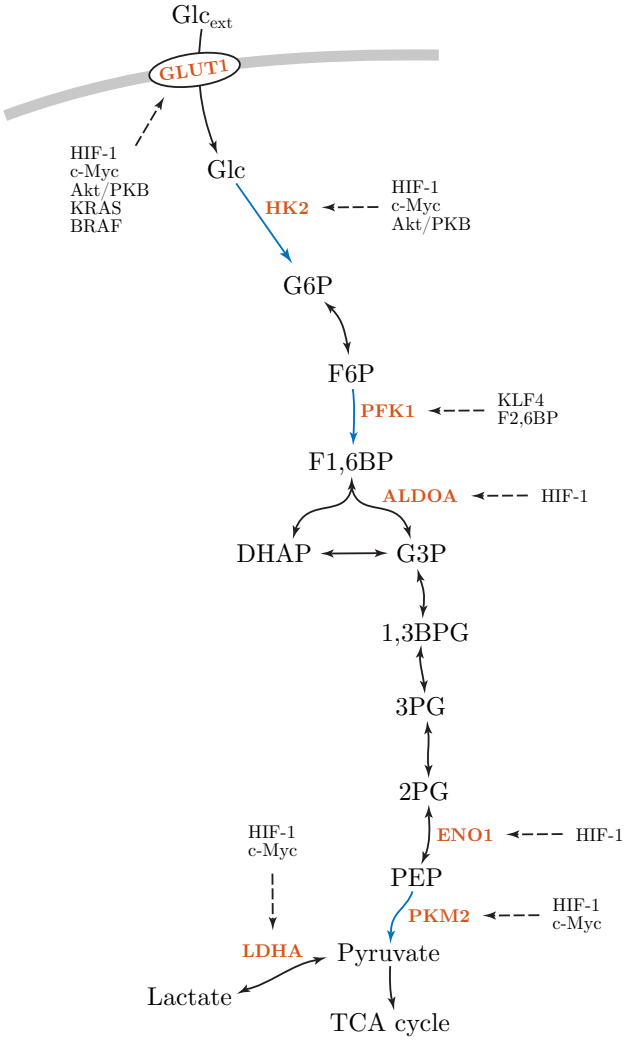

Figure 5.5: Diagram of glycolysis with some of the commonly overexpressed protein isoforms in cancer highlighted in red. Dashed lines show some key factors responsible for overexpression. Reactions highlighted in blue indicate the committed steps of glycolysis. See main text for details. Abbreviations used for glycolytic metabolites: Extracellular glucose (Glc_{ext}), glucose (Glc), glucose 6-phosphate (G6P), fructose 6-phosphate (F6P), fructose 1,6-bisphosphate (F1,6BP), dihydroxyacetone phosphate (DHAP), glyceraldehyde 3-phosphate (G3P), 1,3-bisphosphoglycerate (1,3BPG), 3-phosphoglycerate (3PG), 2-phosphoglycerate (2PG), phosphoenolpyruvate (PEP), tricarboxylic acid cycle (TCA cycle).

transcription and stability, increased protein synthesis or decreased protein degradation, and translocation of the transporter to the cell membrane [97].

Extracellular glucose supply directly affects the levels of intracellular glucose and early glycolytic metabolites [88, 69]. Thus, it is possible that GLUT1 content at the cell surface is regulated in some way by the intracellular level of glucose or G6P, as has been previously suggested [113, 69]. In fact, comparisons of mammary tumors and normal mammary tissue in mice have shown that an increased GLUT1 level correlates with a decreased level of intracellular glucose and increased glycolytic activity [206]. It is possible that this glucose-dependent regulation of GLUT1 functions via AMP-activated protein kinase (AMPK) [86]. AMPK is comprised of one catalytic α-subunit, and two regulatory subunits, β and γ [86, 32]. Glucose-induced regulation of AMPK activity happen in a few different ways: An abundance of glucose will quickly be phosphorylated to G6P by HK2. G6P is then used to supply glycolysis, lowering the AMP/ATP and ADP/ATP ratios, keeping AMPK from being activated by the binding of AMP and ADP [86]. High glucose levels and increased biomass generation reduce the NAD^+/NADH ratio, which indirectly inhibits AMPK through silent information regulator T1 (SIRT1) and liver kinase B1 (LKB1) [86, 146, 192, 74]. Downstream of G6P, the accumulation of diacylglycerol (DAG) and glycogen both lead to inhibition of AMPK. DAG inhibits AMPK by activating protein kinase C (PKC), which in turn induces the inhibitory phosphorylation of the AMPK α-subunit, while glycogen inhibits AMPK by binding to the β-subunit [86]. In addition, activation of protein phosphatase 2A (PP2A) as a result of high glucose levels inhibits AMPK [86, 54, 90].

AMPK in turn has been shown to affect GLUT1 expression [12, 86]. A mechanism by which this happens is by increasing the degradation of thioredoxin-interacting protein (TXNIP) [201]. TXNIP can bind directly to GLUT1 and induce internalization, as well as reduce the GLUT1 mRNA level [201]. Another suggested mechanism is that downstream of AMPK, p38 mitogen-activated protein kinase (p38 MAPK) activation leads to enhancement of GLUT1-mediated glucose transport [203]. A suggested nuclear sensor of G6P is the transcription factor complex MondoA-Mlx, which induces the *TXNIP* gene [34, 166, 167]. Because TXNIP is a potent negative regulator of GLUT1 activity, this forms a negative feedback connection in which elevated G6P levels restrict GLUT1-mediated glucose uptake through TXNIP [201, 34, 166, 167].

Another important aspect of glucose uptake is the regulation of HK2, as it drives the first committed step of glycolysis and maintains a high glucose concentration gradient across the cell membrane, which drives the facilitated diffusion of glucose by GLUT1 [74, 171, 165]. Activators of the HK2 promoter include glucose, insulin, glucagon, p53, cAMP, and hypoxic conditions [139, 106, 115]. Interestingly, it is glucose rather than downstream glycolytic metabolites that activates the HK2 promoter [116, 144, 139, 106, 115]. Together with the fact that HK2 phosphorylates glucose to G6P in a reaction that is essentially irreversible, a negative feedback connection between glucose and HK2 is formed [115, 41].

These control mechanisms are summarized in Figure 5.6a. Here, glucose uptake is regulated by pathways that inhibit GLUT1-mediated glucose uptake via AMPK, and intracellular glucose forms a negative feedback connection with HK2. The mechanisms that affect AMPK depend on the production of G6P, and therefore, G6P represents the potential for these mechanisms to ultimately affect GLUT1-mediated glucose uptake. Before we can construct a mathematical model of the system in Figure 5.6a, activating and inhibiting pathways need to be translated into reactions that can be described by reaction kinetic equations. To this end, parallel pathways with similar overall effects are grouped together, shown in Figure 5.6b. These combined pathways are then turned into activating or inhibiting reactions affecting generation or removal reactions of the remaining species, shown in Figure 5.6c. The conversion of the system in Figure 5.6b to the system in Figure 5.6c preserves the effect one compound has on another, however, this conversion is not unique. For example, a negative (or diminishing) effect of G6P on GLUT1 content at the cell surface could also be achieved if G6P activates the degradation or internalization of GLUT1 [41]. Additionally, the activating and inhibiting reactions in Figure 5.6c do not need to represent the same molecular mechanisms. For example, the generation of G6P is driven by the phosphorylation of glucose by HK2, whereas intracellular glucose induces HK2 generation by activating the HK2 promoter. We use the system in Figure 5.6c as a simplified representation of glucose uptake in cancer, and as a basis for our mathematical model. Notably, this model reveals the presence of negative feedback structures, similar to the homeostatic controller motifs, in a nested configuration. This is a commonly occurring regulatory architecture in metabolic networks [82].

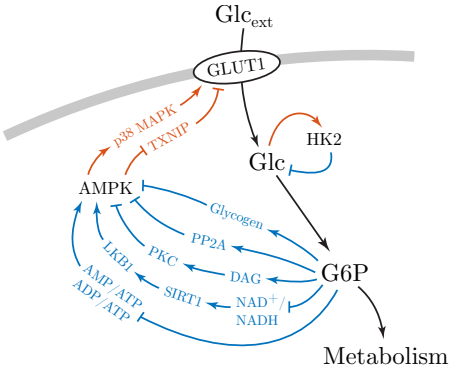

(a) Regulation of glucose uptake in cancer.

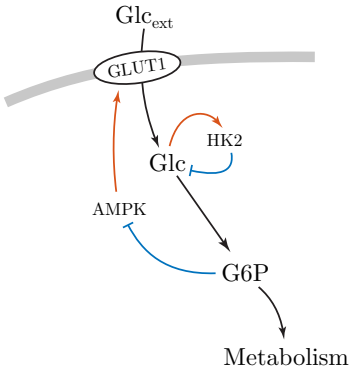

(b) Simplified model.

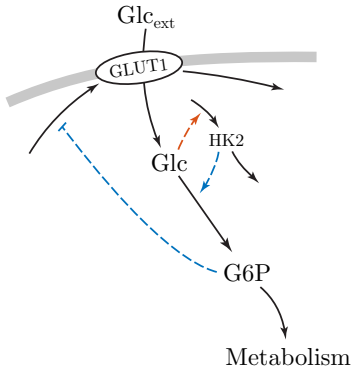

(c) Mathematical model.

Figure 5.6: The regulation of glucose uptake in cancer is summarized in panel (a). Line marker-ends indicate the effect one species has on another, arrowhead for positive/activating and flat head for negative/inhibiting. Colored pathways indicate the overall effect of that pathway, red for positive and blue for negative. For example, HK2 negatively affects glucose since it phosphorylates glucose to G6P, and AMPK positively affects GLUT1, since it increases the degradation of TXNIP, which induces internalization of GLUT1. Black lines represent the flow of glucose metabolism. Panel (b) shows colored pathways grouped together based on similar overall effects. Panel (c) shows the same, but translated into a form where activating and inhibiting effects act on reactions generating and turning over the species. This allows for the system to be described by a simplified mathematical model using reaction kinetic equations.

5.3.3 Modeling glucose uptake in cancer

Expression Atlas was used to collect differential gene expression data comparing cancer cells with normal (i.e. non-cancerous) cells, across a variety of tissues and cell types. Expression Atlas is an open science resource that provides information on gene and protein expression in animal and plant samples of different cell types, organism parts, developmental stages, diseases, and other conditions [141]. Expression Atlas contains thousands of selected microarray and RNA-sequencing datasets that are manually curated, annotated, checked for high quality, and processed using standardized analysis methods [141]. For genes of interest, users can view baseline expression in tissues, and differential expression for biologically meaningful pairwise comparisons [141].

Differential expression data for the *SLC2A* gene family, *HK1-3*, *GCK*, *PFKM*, *PFKP*, *PKM*, and *PKLR* genes in human was gathered from the Expression Atlas database. We curated the data to ensure only experiments comparing cancer cells with corresponding normal cells were included. Differential gene expression experiments with drug treatments were removed. Average $\log_2$-fold changes for the key genes associated with glucose uptake and glycolysis are shown in Figure 5.7. The differential gene expression data largely corroborates the reported rewiring of glycolysis in cancer discussed in Section 5.3.1. Namely, a shift towards glucose uptake mediated by GLUT1 (*SLC2A1* gene), predominant expression of the PKM2 (PKM1 and PKM2 are different splicing products of the *PKM* gene [74]) isoform, and overexpression of HK2. We also found a slight upregulation of the *PFKP* gene in cancer, consistent with previous studies [123]. Hence, the model proposed in Figure 5.6c appears to include the key components of glucose uptake in cancer, and provides a good basis for mathematical modeling.

The results in Figure 5.7 also shows an increased *HK3* transcript abundance in cancer. This is not surprising, since it has been shown that HK3 is upregulated by hypoxia, partially through HIF-dependent signaling [202]. Whereas HK2 bind to the outer mitochondrial membrane, HK3 does not [115, 202]. A consequence of mitochondrial bound HK2 is the prevention of cell death by inhibiting formation of the mitochondrial permeability transition pore (MPTP) complex [115, 202]. On the other hand, HK3 overexpression promotes cell survival in response to oxidative stress, decreases the production of reactive oxygen species (ROS), preserves mitochondrial membrane potential, and promotes mitochondrial biogenesis [202]. Therefore, it is likely that HK2 and HK3 serve different, but complementary,

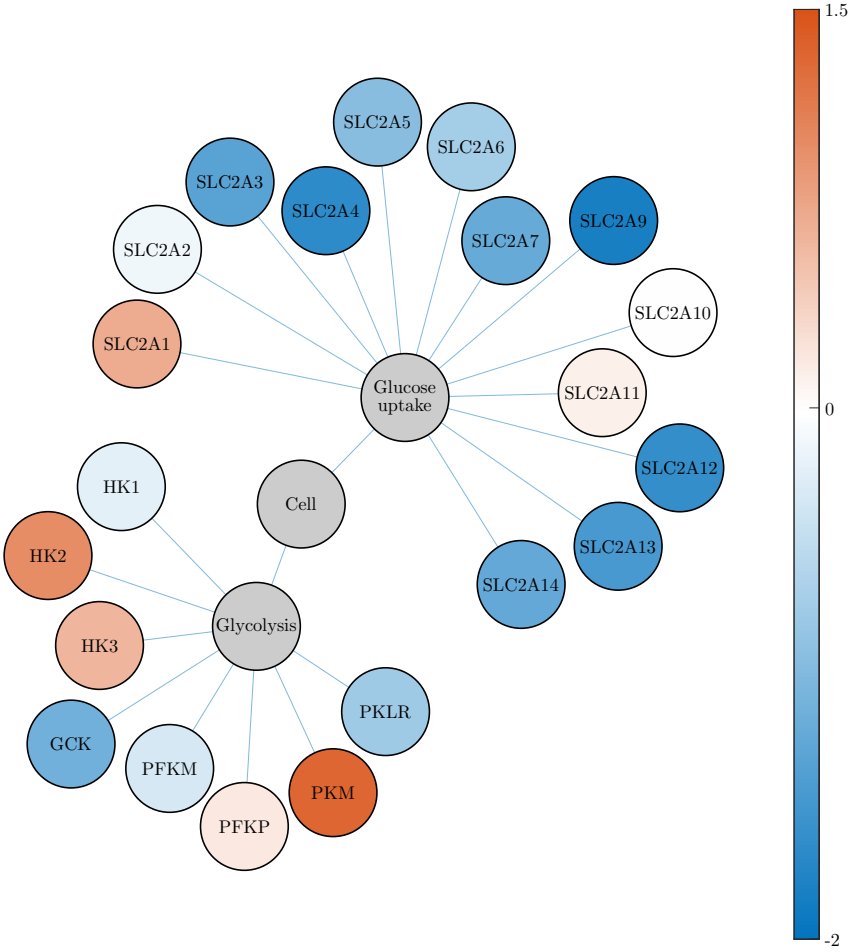

Figure 5.7: Differential expression data for the *SLC2A* gene family, *HK1-3*, *GCK*, *PFKM*, *PFKP*, *PKM*, and *PKLR* genes in human was gathered from the Expression Atlas database. Results are given as the average $\log_2$-fold change of several experiments. Upregulation in cancer cells is indicated by red, and downregulation by blue. White indicates no change.

roles in maintaining a highly glycolytic phenotype and promoting cancer cell survival. Notably, inhibition of glucose or G6P binding to the regulatory half of HK3 (N-terminal domain) impairs catalysis in the catalytic half (C-terminal domain), suggesting a cooperative effect of glucose binding in the regulatory half to subsequent binding in the catalytic half [202]. Hence, HK3 interacts with glucose in a similar way to that of HK2 shown in Figure 5.6. As a result, we will only consider HK2 in the following mathematical modeling, but note that HK2 can be thought of as a pool of both HK2 and HK3.

Our model of glucose uptake in cancer is shown in Figure 5.8. Assuming low intracellular concentration of glucose due to rapid conversion by HK2, facilitated diffusion of glucose by GLUT1 can be approximated by the Michaelis–Menten equation [165, 171]. We model the phosphorylation of glucose to G6P by the Michaelis–Menten equation, and the sink reaction to metabolism by a first-order reaction with rate constant $k_{\text{metabolism}}$. GLUT1 is assumed to be generated and turned over in reactions driven by enzymes E_1 and E_2, respectively. We assume the production of GLUT1 is proportional to the concentration of E_1, and that the degradation of GLUT1 by E_2 is given by a Michaelis–Menten-type process.

The feedback inhibition from G6P to GLUT1 production is based on the many pathways that regulate GLUT1-mediated glucose uptake via AMPK, summarized in Figure 5.6a. With this feedback, a reduction in G6P level will reduce inhibition of GLUT1 production, thereby increasing GLUT1-mediated glucose uptake, and providing a mechanism for regulating the glycolytic flux. We model the feedback by allosteric inhibition (using a special case of mixed inhibition) of the reaction producing GLUT1 [31, 91].

The activation of HK2 synthesis by intracellular glucose forms a negative feedback connection together with the phosphorylation of glucose to G6P [41]. Activation of HK2 synthesis is modeled by allosteric activation[3] (using a special case of mixed activation) [31, 91]. We assume the synthesis and degradation of HK2 are driven by enzymes E_3 and E_4, respectively, where the synthesis is proportional to the level of E_3, and the degradation by E_4 follows a Michaelis–Menten-type process. The enzymes responsible for generating and removing GLUT1 and HK2 ($E_i,\ i = 1, 2, 3, 4$) are

[3]Note that we are simply using the expression for allosteric activation to model saturation in HK2 promoter activation by glucose. In this sense, the transcriptional and translational machinery are represented by the "enzyme" synthesizing HK2. In fact, a similar abstraction is made for all the enzymes E_i ($i = 1, 2, 3, 4$).

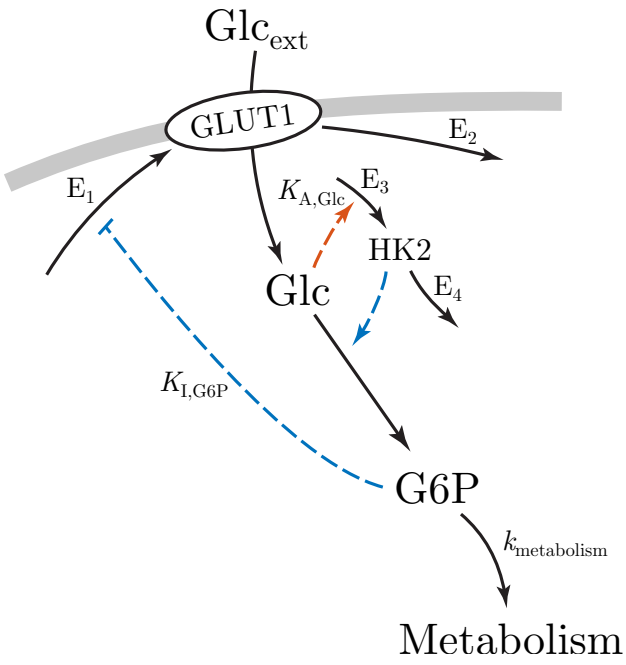

Figure 5.8: Our model for glucose uptake in cancer. GLUT1 transports extracellular glucose into the cell, which is then phosphorylated to G6P by HK2. The sink reaction to metabolism is modeled by a first-order reaction with rate constant $k_{\text{metabolism}}$. GLUT1 and HK2 are assumed to be generated and turned over in reactions driven by the enzymes E_i $(i = 1, 2, 3, 4)$. Feedback inhibition from G6P to GLUT1 production is modeled by allosteric inhibition with inhibition constant $K_{\text{I,G6P}}$, and activation of HK2 synthesis by intracellular glucose is modeled by allosteric activation with activation constant $K_{\text{A,Glc}}$.

assumed to be present in constant amounts only, meaning that their concentrations simply dilute with increasing volume. We believe this represents a *worst-case* scenario in which dilution resistance can be achieved, where all components of the protein synthetic machinery of the cell dilute as the cell grows.

The glucose uptake model in Figure 5.8 is given by the flux balance equations

$$\dot{c}_{\text{Glc}}(t) = j_{\text{GLUT1}}(t) \cdot \frac{A(t)}{V(t)} - j_{\text{HK2}}(t) - c_{\text{Glc}}(t) \cdot \frac{\dot{V}(t)}{V(t)} \tag{5.9}$$

$$\dot{c}_{\text{G6P}}(t) = j_{\text{HK2}}(t) - j_{\text{met}}(t) - c_{\text{G6P}}(t) \cdot \frac{\dot{V}(t)}{V(t)} \tag{5.10}$$

$$\dot{c}_{\mathrm{GLUT1}}(t) = j_{\mathrm{E},1}(t) \cdot \frac{V(t)}{A(t)} - j_{\mathrm{E},2}(t) \cdot \frac{V(t)}{A(t)} - c_{\mathrm{GLUT1}}(t) \cdot \frac{\dot{A}(t)}{A(t)} \tag{5.11}$$

$$\dot{c}_{\mathrm{HK2}}(t) = j_{\mathrm{E},3}(t) - j_{\mathrm{E},4}(t) - c_{\mathrm{HK2}}(t) \cdot \frac{\dot{V}(t)}{V(t)} \tag{5.12}$$

where c_{Glc}, c_{G6P}, and c_{HK2} are concentrations in the cellular volume V, whereas c_{GLUT1} is a concentration at the cell surface A. As a consequence, the import of glucose (j_{GLUT1}) is converted by the factor A/V to a flux given with respect to the cellular volume. Similarly, the generation and degradation of GLUT1 ($j_{\mathrm{E},1}$ and $j_{\mathrm{E},2}$) are converted by the factor V/A to fluxes with respect to the cell surface area, since the enzymes generating and turning over GLUT1 are situated inside the cell. Because we are considering a growing cell, the dilution term from (5.3) must be added to the reaction rate equations. The flux expressions in (5.9)–(5.12) are given by

$$j_{\mathrm{GLUT1}}(t) = \frac{k_{\mathrm{cat,GLUT1}} \cdot c_{\mathrm{GLUT1}}(t) \cdot c_{\mathrm{Glc,ext}}(t)}{K_{\mathrm{M,GLUT1}} + c_{\mathrm{Glc,ext}}(t)} \tag{5.13}$$

$$j_{\mathrm{HK2}}(t) = \frac{k_{\mathrm{cat,HK2}} \cdot c_{\mathrm{HK2}}(t) \cdot c_{\mathrm{Glc}}(t)}{K_{\mathrm{M,HK2}} + c_{\mathrm{Glc}}(t)} \tag{5.14}$$

$$j_{\mathrm{met}}(t) = k_{\mathrm{metabolism}} \cdot c_{\mathrm{G6P}}(t) \tag{5.15}$$

$$j_{\mathrm{E},1}(t) = k_{\mathrm{cat},1} \cdot c_{\mathrm{E},1}(t) \cdot \frac{K_{\mathrm{I,G6P}}}{K_{\mathrm{I,G6P}} + c_{\mathrm{G6P}}(t)} \tag{5.16}$$

$$j_{\mathrm{E},2}(t) = \frac{k_{\mathrm{cat},2} \cdot c_{\mathrm{E},2}(t) \cdot c_{\mathrm{GLUT1}}(t)}{K_{\mathrm{M},2} + c_{\mathrm{GLUT1}}(t)} \tag{5.17}$$

$$j_{\mathrm{E},3}(t) = k_{\mathrm{cat},3} \cdot c_{\mathrm{E},3}(t) \cdot \frac{c_{\mathrm{Glc}}(t)}{K_{\mathrm{A,Glc}} + c_{\mathrm{Glc}}(t)} \tag{5.18}$$

$$j_{\mathrm{E},4}(t) = \frac{k_{\mathrm{cat},4} \cdot c_{\mathrm{E},4}(t) \cdot c_{\mathrm{HK2}}(t)}{K_{\mathrm{M},4} + c_{\mathrm{HK2}}(t)} \tag{5.19}$$

The enzymes E_i ($i = 1, 2, 3, 4$) are not assumed to be generated and turned over, and their concentrations simply dilute as the volume increases. These concentrations are given by $c_{\mathrm{E},i}(t) = n_{\mathrm{E},i}/V(t)$, where $n_{\mathrm{E},i}$ (the amount of E_i) are constant quantities. $K_{\mathrm{I,G6P}}$ is the inhibition constant for the allosteric inhibition of GLUT1 production by G6P, and $K_{\mathrm{A,Glc}}$ is the activation constant for the allosteric activation of HK2 synthesis by intracellular glucose.

We assume a spherical cell and simulate the system (5.9)–(5.12) in four phases (Figure 5.9): In the first phase (white area, $t = [0, 400]$), the volume

is constant. In the second phase (light gray area, $t = [400, 800]$), the volume is increased linearly. In the third phase (dark gray area, $t = [800, 1200]$), while the volume is still increasing, the extracellular glucose concentration is increased 4-fold (at $t = 800$). Finally, in the last phase (white area, $t = [1200, 1600]$), the volume increase is stopped. The simulation results are shown in Figure 5.9, with initial values and parameters provided in Table 5.1. The bottom right plot shows the increase in volume (solid black line) and surface area (dashed black line) during the simulation.

In the first phase (white area), the system has settled at steady-state, producing a constant glycolytic flux (represented by the phosphorylation of glucose to G6P, j_{HK2}). In the second phase (light gray area), despite growth-induced dilution, a constant glycolytic flux is maintained. This shows that the system is able to achieve dilution resistance under linear growth. Note, however, that without active regulation of the HK2 level (negative feedback between glucose and HK2), dilution resistance is not possible (see Paper 4 for more details). Hence, a nested feedback architecture appears to be significant in achieving robustness to global effects such as dilution. In comparison to steady-state values associated with constant volume (dashed black lines in intracellular glucose and G6P plots), we see a shift in the new steady-state values of the system during growth. Notably, there is a (slight) reduction in the glycolytic flux, together with an increased level of intracellular glucose, and a reduced G6P level. This suggests that glucose is no longer being converted into G6P as efficiently, which is evident from the reduction in HK2 level. It is important to note that the simulation results show concentrations of species, and that molecular amounts scale with cell size. This scaling is achieved by increasing the *concentration* of GLUT1 at the cell surface, made possible by the differential dilution experienced by species in the cellular volume and at the cell surface, expressed by the relationship in (5.8).

To investigate how dilution causes offsets in the steady-state values of the system, we increased the extracellular glucose concentration at the start of the third phase (dark gray area). Interestingly, the control mechanisms attempt to bring the system back to steady-state values associated with growth, and not to steady-state values associated with constant volume. If the latter were true, we would not expect to see the regulatory action in Figure 5.9 bringing intracellular glucose and G6P levels away from steady-state values associated with constant volume (dashed black lines). This suggests that the growth-induced offsets may be caused by set-point changes, rather than breakdown of regulation. Finally, in the last phase,

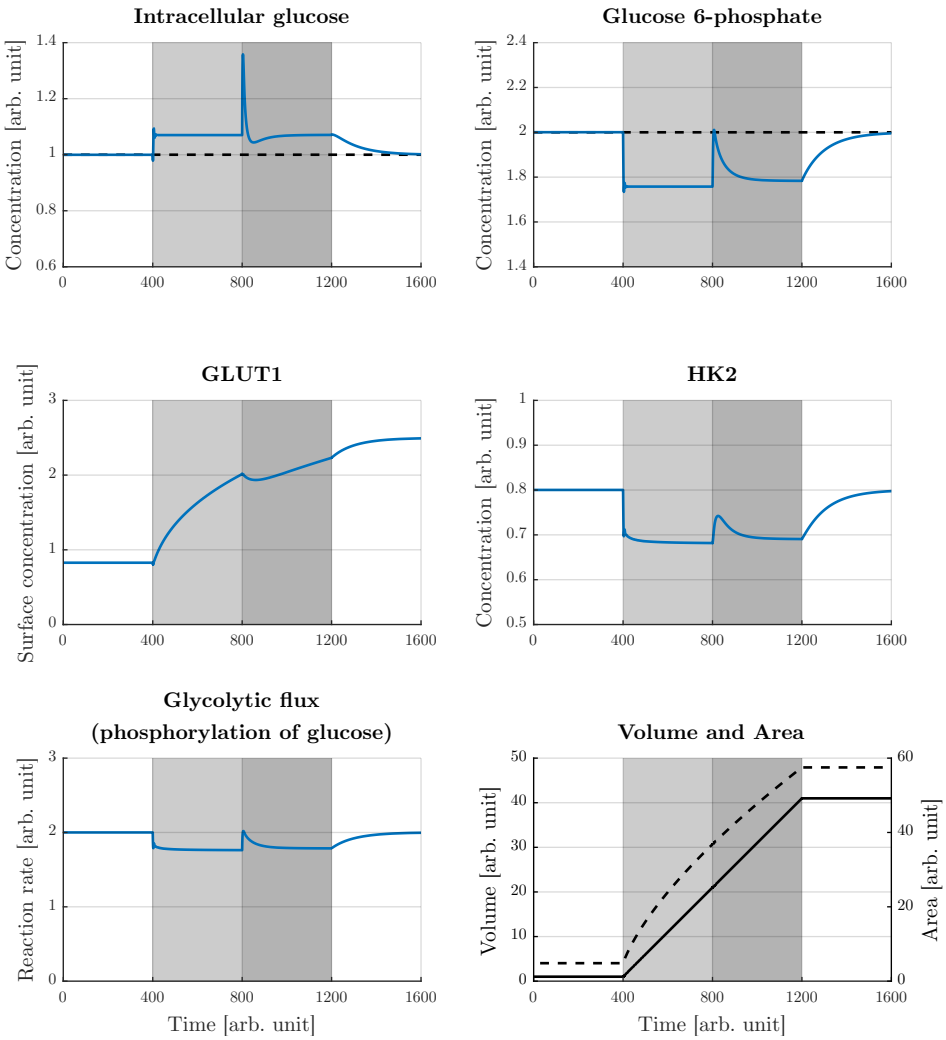

Figure 5.9: Simulation results of the glucose uptake model. The bottom right plot shows volume (solid black line) and surface area (dashed black line) during the simulation. A spherical cell is assumed. Initially, the cellular volume is kept constant, and the system has settled at steady-state (white area, $t = [0, 400]$). In the second phase (light gray area, $t = [400, 800]$), the cellular volume increases linearly. During growth, steady-state metabolite levels are shifted compared to steady-state values associated with constant volume (dashed black lines in intracellular glucose and G6P plots). At the start of the third phase (dark gray area, $t = [800, 1200]$), as the volume is still increasing, the concentration of extracellular glucose is increased 4-fold. Finally, the first phase is repeated, and the volume is kept constant (white area, $t = [1200, 1600]$). Initial values and parameters are given in Table 5.1.

Initial Values	
c_{Glc}	0.9997
c_{G6P}	2.0004
c_{GLUT1}	0.8273
c_{HK2}	0.8002
Parameters/expressions	
$V(t)$	$1.0000 + \dot{V}(t) \cdot t$
$\dot{V}(t)$	$\begin{cases} 0.0500, & 400 \leq t < 1200 \\ 0, & \text{otherwise} \end{cases}$
$c_{\text{Glc,ext}}(t)$	$\begin{cases} 5.0000, & t < 800 \\ 20.000, & t \geq 800 \end{cases}$
$k_{\text{cat,GLUT1}}$	0.6000
$K_{\text{M,GLUT1}}$	1.0000
$k_{\text{cat,HK2}}$	5.0000
$K_{\text{M,HK2}}$	1.0000
$k_{\text{metabolism}}$	1.0000
$k_{\text{cat,1}}$	6.0000
$n_{\text{E,1}}$	1.0000
$k_{\text{cat,2}}$	2.0000
$K_{\text{M,2}}$	0.0001
$n_{\text{E,2}}$	1.0000
$k_{\text{cat,3}}$	2.0000
$n_{\text{E,3}}$	1.0000
$k_{\text{cat,4}}$	1.0000
$K_{\text{M,4}}$	0.0001
$n_{\text{E,4}}$	1.0000
$K_{\text{I,G6P}}$	1.0000
$K_{\text{A,Glc}}$	1.0000

Table 5.1: Initial values and parameters for the simulation of the glucose uptake model in Figure 5.9.

volume growth is stopped, but the cellular volume has now grown much larger than initially (white area). In this phase, metabolite levels, together with the glycolytic flux, return back to steady-state values associated with constant volume. Thus, the growth-induced offsets must be dependent on the rate of volume increase, and not the total volume.

The simulation results in Figure 5.9 demonstrate that the glucose uptake model (Figure 5.8, (5.9)–(5.12)) is able to achieve dilution resistance during linear growth, and that dilution resistance is achieved by the formation of a nested negative feedback structure. In fact, it appears that dilution resistance in linear pathways require that intermediary enzymes are regulated by negative feedback in a nested configuration, or that the generation and removal reactions of theses enzymes already show dilution resistance. Either way, our results demonstrate the need for regulation of intermediary enzymatic steps in linear pathways in order to achieve dilution resistance. Our simulation results also show the presence of growth-induced offsets in steady-state values of the system, and that these offsets appears to be caused by set-point changes that are dependent on the growth rate. Interestingly, investigations into ICMs have shown that growth-induced offsets become negligible if the kinetics of the controller species behave on a timescale much faster than cell growth [147, 142, 6, 4, 8]. In the following, we take a closer look at how growth-induced offsets can be minimized for the glucose uptake model, and how this leads to near-perfect dilution resistance.

5.3.4 Realizing dilution resistance with homeostatic controller motifs

While ICMs cannot achieve perfect adaptation in the presence of dilution, and their performance deteriorate with increasing dilution rate, it has been shown that near-perfect adaptation can still be achieved by increasing the rates of the controller reactions [142, 147]. ICMs with controller reactions much faster than the rate of dilution are called *quasi-ICMs*, and characteristically show small or negligible growth-induced offsets [142]. To illustrate how quasi-ICMs achieve dilution resistance, we take a closer look at the feedback inhibition by G6P to GLUT1-mediated glucose uptake in Figure 5.8. The interaction between G6P and GLUT1 forms a structure similar to that of the homeostatic controller motifs (inflow controller 3) [41]. As shown in Chapter 3, this constitutes a negative feedback connection with integral action. Comparing an ideal integral controller, shown in Figure 5.10,

with the feedback inhibition in Figure 5.8, we see that the output feedback (y) corresponds to the inhibition of GLUT1 production by G6P (blue in Figure 5.10 and Figure 5.8); the integral controller block corresponds to the GLUT1 level; process input (u) corresponds to GLUT1-mediated glucose uptake (red in Figure 5.10); and the process block corresponds to the level of G6P. The disturbance input (w) corresponds to perturbations made in extracellular glucose and cellular volume.

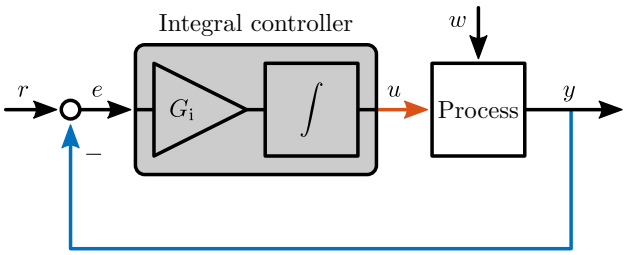

Figure 5.10: Block diagram of a process in negative feedback connection with an integral controller. The process output y is fed back (blue output feedback) and compared to the set-point r to produce the regulation error $e = r - y$. The regulation error is multiplied by an integral gain G_i and integrated over time to produce the control action u (red process input). In the presence of an uncontrolled disturbance w, a deviation in the process output from the set-point will cause a non-zero regulation error. This produces a change in the control action, and since the feedback is negative, this control action functions to contract the deviation in process output from the set-point.

By rewriting (5.11), we can show that GLUT1 functions as an integral controller for G6P

$$\dot{c}_{\mathrm{GLUT1}}(t) = j_{\mathrm{E},1}(t) \cdot \frac{V(t)}{A(t)} - j_{\mathrm{E},2}(t) \cdot \frac{V(t)}{A(t)} - c_{\mathrm{GLUT1}}(t) \cdot \frac{\dot{A}(t)}{A(t)} \tag{5.20}$$

$$\approx G_\mathrm{i}(t) \cdot \left(c_{\mathrm{G6P,set}} - \dot{A}(t) \cdot o_{\mathrm{G6P}}(t) - c_{\mathrm{G6P}}(t) \right) \tag{5.21}$$

where we assume zero-order degradation of GLUT1 ($K_{\mathrm{M},2} \ll c_{\mathrm{GLUT1}}$) [41]. The following definitions are made

$$G_\mathrm{i}(t) = \frac{1}{A(t)} \cdot \frac{k_{\mathrm{cat},2} \cdot n_{\mathrm{E},2}}{K_{\mathrm{I,G6P}} + c_{\mathrm{G6P}}(t)} \tag{5.22}$$

$$c_{\mathrm{G6P,set}} = \frac{k_{\mathrm{cat},1} \cdot n_{\mathrm{E},1} - k_{\mathrm{cat},2} \cdot n_{\mathrm{E},2}}{k_{\mathrm{cat},2} \cdot n_{\mathrm{E},2}} \cdot K_{\mathrm{I,G6P}} \tag{5.23}$$

$$o_{\mathrm{G6P}}(t) = \frac{K_{\mathrm{I,G6P}} + c_{\mathrm{G6P}}(t)}{k_{\mathrm{cat},2} \cdot n_{\mathrm{E},2}} \cdot c_{\mathrm{GLUT1}}(t) \tag{5.24}$$

In the case without growth, $\dot{A} = 0$, (5.21) is reduced to the same form as the integral control law (see (3.56) in Chapter 3). And since the set-point for G6P level, $c_{\mathrm{G6P,set}}$, is given entirely by parameters associated with GLUT1 generation and removal, perfect adaptation to perturbations in G6P is realized, as the set-point remains unchanged for such perturbations [6]. However, in the case with growth, the additional term $\dot{A} \cdot o_{\mathrm{G6P}}$ is introduced in the integral control law, which causes a growth-induced offset in G6P level. By comparing the above equations to the simulation results shown in Figure 5.9, we can make a couple of observations: First, the growth-induced offset is indeed dependent on the growth rate of the cell ($\dot{A}$, or indirectly, $\dot{V}$), like our simulation results suggested. Second, (5.21) shows that the offset can be interpreted as a change in set-point of the controller, i.e. the set-point during growth is given by $c^*_{\mathrm{G6P,set}} = c_{\mathrm{G6P,set}} - \dot{A}(t) \cdot o_{\mathrm{G6P}}(t)$. An alternative interpretation is that the growth associated offset results in an inaccuracy in the measurement of G6P level. However, because the offset appears as an additional term in (5.21), this interpretation differs somewhat from previous uses of controller accuracy in the context of homeostatic controller motifs[4] [41, 145].

If the reaction rates for the generation and removal of GLUT1 behave on a timescale much faster than the rate of dilution, o_{G6P} is small, and the growth associated offset ($\dot{A} \cdot o_{\mathrm{G6P}}$) becomes negligible [147, 142]. For example, increasing $k_{\mathrm{cat},2}$ lowers the value of o_{G6P} (see (5.24)). If $k_{\mathrm{cat},1}$ is also increased such that $c_{\mathrm{G6P,set}}$ remains unchanged (see (5.23)), the impact of dilution can be arbitrarily reduced, resulting in a so-called quasi-ICM [147, 142]. Tuning the reaction rate parameters of the controller species in this manner is a way of increasing the "aggressiveness" of the integral controller [147]. A way that GLUT1 and HK2 activity can be regulated, is through translocation between biological membranes and the cytosol, indicating that the activity of these species can respond quickly, and that regulation of glucose uptake in cancer may achieve dilution resistance through the formation of quasi-ICMs [97, 201, 87]. Similar to GLUT1, it is possible to show that HK2 functions as an integral controller for the level of intracellular glucose (see Paper 4).

In our model for glucose uptake in cancer (Figure 5.8, (5.9)–(5.12)), enzymes responsible for generating and removing the controller species

[4]In the context of homeostatic controller motifs, accuracy usually refers to the discrepancy between set-point and actual steady-state value of the regulated species that appears if the removal of the controller species is not zero-order (see Figure 3.12 in Chapter 3) [41, 145].

($\mathrm{E}_i,\ i = 1, 2, 3, 4$) are present in constant amounts only, meaning that their concentrations simply dilute with increasing volume. As mentioned before, we view this as a worst-case scenario in which regulation in the presence of dilution is possible. In this scenario, we found that dilution resistance to a linearly increasing volume is possible. However, because most protein and mRNA concentrations are independent of cell size, it is likely that the concentrations $c_{\mathrm{E},i}$ should be considered constant [153, 149]. In this case, it has been shown that dilution resistance can be achieved for an exponentially increasing cellular volume [147, 142]. Note, however, that capacity limits or exhaustion of the controller species may lead to breakdown and loss of regulation entirely [147]. It is clear that to ensure robustness of the homeostatic controller motifs to perturbations that affect the system locally (i.e. perturbations in the regulated species) as well as globally (i.e. dilution), it is necessary to satisfy two conditions; *i*) the degradation of the controller species must be (close to) zero-order ($K_{\mathrm{M},2} \ll x_2$), and *ii*) the controller reactions must be much faster than the rate of dilution.

5.4 Stochastic fluctuations in reaction networks

Although continuous-state deterministic models of chemically reacting systems, such as the reaction rate equations for the homeostatic controller motifs, are undeniably useful for describing and studying such systems (as we have seen so far), it is clear that time-evolution of chemically reacting systems are neither continuous nor deterministic [58, 199]. Molecular populations can only change by discrete integer amounts, implying that chemically reacting systems are fundamentally discrete. Moreover, although the time-evolution of a chemically reacting system of classical molecules[5] is deterministic in the position-momentum phase space, it is not deterministic in the subspace of population numbers, as implied by reaction rate equations [58]. Continuous-state deterministic models fail to capture these aspects, and as a consequence, the "missing detail" manifests itself as an apparent unpredictability of the underlying system [199].

Due to the stochastic nature of chemical reactions, the dynamics within cells are often noisy [8]. This stochasticity is more pronounced in reactions involving low molecular counts, like gene transcription, where quantities such as DNA transcripts and transcription factors participate in low copy numbers [8, 168]. The randomness in intracellular reactions can lead to

[5]Classical in the sense that molecular motions are governed by classical mechanics.

significant cell-to-cell heterogeneities, in which genetically identical cells exposed to homogeneous environments can show remarkable phenotypic differences [8, 168, 107, 199]. This is demonstrated by the bistable genetic toggle switch, which is comprised of two repressors and two constitutive promoters arranged in a mutually inhibiting feedback connection (Figure 5.11a) [56, 79]. Stochasticity lets the system flip between two stable states, whereas the deterministic version will always stay in one of the stable states[6], determined by initial conditions (assuming no external input) [56, 79]. Bistable mechanisms similar to the genetic toggle switch can be exploited by cells to select one of two phenotypic traits at random, even in uniform genetic and environmental conditions, which can have selective advantages [199]. The genetic toggle switch is given by the deterministic model [56, 79]

$$\dot{R}_1(t) = \frac{\alpha_1}{1 + R_2(t)^{\beta}} - R_1(t) \tag{5.25}$$

$$\dot{R}_2(t) = \frac{\alpha_2}{1 + R_1(t)^{\gamma}} - R_2(t) \tag{5.26}$$

where R_1 and R_2 are concentrations of the repressors, α_1 and α_2 are the effective rates of synthesis of R_1 and R_2, respectively, and β and γ denote the cooperativity of repression of their respective promoter. For the deterministic model, simulation trajectories are generated using a standard ODE solver. In the stochastic model, each reaction is modeled as a discrete event that occurs with a certain propensity, and sample paths can be generated using a stochastic simulation algorithm [79, 58]. A comparison of deterministic and stochastic simulations of the genetic toggle switch is shown in Figure 5.11b.

5.4.1 Intrinsic noise

Because reactions occur when molecules collide according to random processes, chemically reacting systems experience *intrinsic* noise [58, 199]. In biochemical systems, intrinsic noise has many sources, including randomness in DNA binding events, mRNA transcription and degradation processes, translation and protein degradation, and other protein-protein and protein-metabolite interactions [199, 168, 107]. If we consider a population of cells,

[6] With the exact initial conditions, the deterministic system can theoretically stay in one additional unstable state. But in practice, like a pendulum balanced in the upwards direction, this state cannot be maintained for long [56].

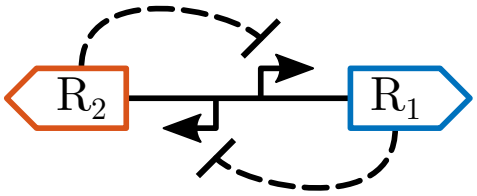

(a) Bistable genetic toggle switch.

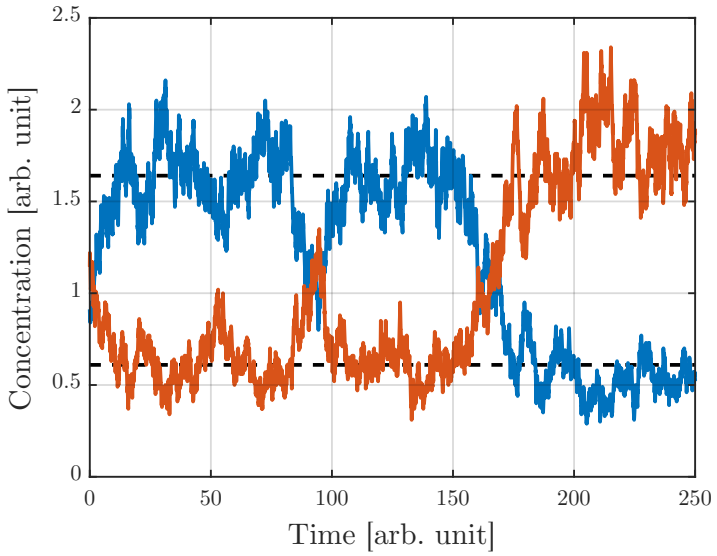

(b) Simulation of the bistable genetic toggle switch.

Figure 5.11: The bistable genetic toggle switch consist of two repressors and two constitutive promoters in a mutually inhibiting feedback connection (panel (a)). A stochastic simulation of the genetic toggle switch shows a switching behavior between a state with mostly repressor 1 (blue) being transcribed, and another state with mostly repressor 2 (red) being transcribed (panel (b)). By contrast, deterministic simulations will always settle at one of the two steady-states indicated by the dashed black lines, depending on initial conditions. Sample paths are generated using parameter values $\alpha_1 = \alpha_2 = 2.25$, and $\beta = \gamma = 2.00$.

the amount of protein produced from a particular gene will vary from cell to cell and over time, even if the cells start out in exactly the same state [168]. This is due to the fact that reaction events leading to transcription and translation of the gene occur at different times and in different orders, in the different cells [168].

One way to approach modeling and simulation of stochastic systems is to consider the differential equations for the statistical moments (e.g. mean and variance) of the state variables [20, 21]. This method brings the problem back to deterministic differential equations (statistical moments evolve according to deterministic dynamics [21]). However, except for linear systems and special cases of nonlinear systems, we encounter the so-called *moment closure problem*, whereby the differential equations for moments of a given order contain terms involving higher order moments [20, 21]. The result is that an infinite set of deterministic differential equations is needed to determine even the first two moments [20, 21].

Another approach is to define the states of a chemically reacting system, assuming it is well stirred, as the current number of molecules of each species, which are quantities that change discretely through reactions between the different species [59, 199]. In doing so, we must accept that the states cannot evolve according to a deterministic process. The reason is that molecular counts alone do not specify the positions and momenta of every single molecule, and hence, the timings of reaction events are essentially unpredictable [59, 58, 199]. This stochastic chemical kinetics approach implies that molecular populations evolve according to a *Markov jump process*, whereby any population change happens discretely and after a random time, where the change and time only depend on the previous state of the system [60, 199]. Furthermore, by deriving a time-evolution equation for the Markov jump process, we get the *chemical master equation* (CME), which is a deterministic differential equation for the probability function describing the distribution of molecular counts for the different species, given some initial condition [60, 59, 58]. As in the deterministic case, some simple reaction network models are analytically tractable, and an explicit solution for the time-evolution of the probability function for the system states can be found [60, 199]. However, the class of solvable models is small, and in practice, exact solution of the CME is rarely obtained [60, 199].

In order to deal with intractable reaction network models, we can turn to numerical simulation of the system [199]. The *stochastic simulation*

algorithm (SSA, also known as the Gillespie algorithm) produces exact[7] realizations of the underlying Markov jump process, and multiple runs of the algorithm can be used to approximate the time-evolution of the probability function for the system states, in what is equivalent to Monte Carlo simulations of the CME[8] [58, 60, 199, 208]. Like the CME, the SSA correctly accounts for the inherent fluctuations and correlations that are ignored in the deterministic case, and unlike procedures for numerically solving deterministic reaction rate equations, the SSA never approximates infinitesimal time increments by finite time steps [58]. The sample paths for the genetic toggle switch shown in Figure 5.11b were generated using the SSA.

The SSA can be computationally expensive, even for single runs, if the reaction network of interest contains many fast-acting reactions or large numbers of molecules [199, 101, 126]. In this case, it becomes infeasible to approximate the CME by Monte Carlo simulations [126, 101]. Instead, an approximation of the underlying Markov jump process can be used, such as the *chemical Langevin equation* (CLE) [60, 199]. This approach is based on approximating the dynamics of the Markov jump process by a system of stochastic differential equations (SDEs) [60, 199]. Realizations of the system of SDEs can then be generated using numerical integration schemes similar to those used for ODEs (such as the Euler–Maruyama method [77]), which significantly reduces simulation time compared to the SSA [199]. However, whereas the underlying Markov jump processes is discrete-state, the CLE is a continuous-state approximation, which necessarily introduces approximation errors [60, 199]. Nevertheless, the CLE is reasonably accurate, except in the case of systems with very low molecular counts [60, 199]. In fact, large molecular populations[9] for the reactant species greatly facilitates the validity of the continuous approximation underlying the CLE [60]. However, it is important to keep in mind that the discrepancy between an "approximate" and "exact" model will typically be substantially less than the discrepancy between the "exact" model and

[7] The SSA is "exact" in the sense that it, like the CME, is an exact consequence of the fundamental premise of stochastic chemical kinetics [58, 60].

[8] Another strategy for dealing with intractable reaction kinetic models is to numerically solve the CME, thereby directly computing the system probability function [208, 126, 101].

[9] In reality, it is not the size of the system in itself that determines the validity of the CLE, but the existence of a *domain of macroscopically infinitesimal time intervals*, which is defined such that during any time interval in that domain, no propensity function will suffer a noticeable change in its value, yet every reaction channel can be expected to fire many more times than once [60].

the real biological process [199]. Note that the CLE is derived from the same fundamental premise that give rise to the CME, and so the CLE also accounts for the inherent fluctuations of the chemical system, even though similar SDE formulations are often used to account for *extrinsic* noise sources [60]. Indeed, it is straightforward to add various sources of extrinsic uncertainty, such as randomly time-varying parameters or input perturbations, with a CLE model [199]. We take a look at extrinsic sources of noise in the following.

5.4.2 Extrinsic noise

There are several sources of extrinsic noise that should be incorporated into a mathematical model if we aim to most accurately represent a biological process. For example, randomness in initial conditions can lead to different behaviors, even if the system evolves according to a deterministic process (e.g. the genetic toggle switch in Figure 5.11) [199]. There can also be uncertainty in system parameters, or parameters that are randomly time-varying due to some part of the system not being explicitly modeled [199]. The former can be dealt with by running different simulations of the system with parameter values from a specified probability distribution, while the latter can be dealt with by associating a diffusion process with the parameters (i.e. an SDE model) [199]. Noise in one cellular component can influence the whole system in some unpredictable way [107]. For example, intrinsic noise in some unmodeled part of the system can manifest itself as extrinsic noise in the model [168, 199]. Thus, extrinsic noise sources arise independently, either from other cellular processes or from environmental fluctuations, but affect the system of interest [168, 107]. A particular system of interest will in general experience both intrinsic and extrinsic sources of noise [168].

It is difficult to ascertain the relative magnitude of intrinsic and extrinsic noise sources. However, a well-known rule-of-thumb in chemical kinetics is that the relative magnitude of intrinsic noise scales as the inverse square root of the reactant populations[10] ($1/\sqrt{N}$ for a single reaction, where N is the number of molecules) [60, 28]. Thus, in eukaryotic metabolism and signal transduction, it is likely that intrinsic noise becomes negligible [28, 169]. If we disregard intrinsic noise (due to large reactant populations), the

[10]In fact, this rule-of-thumb emerges as a direct consequence of the same fundamental premise that gave rise to the CME and CLE, and gives a direct logical linking to deterministic reaction rate equations in the thermodynamic limit [60].

system of interest can be modeled by deterministic reaction rate equations with added noise terms representing extrinsic noise [60, 28, 36, 75]. These noise terms then function as random inflow and outflow perturbations, for example due to unmodeled sink and source reactions in metabolic pathways, or fluctuations in extracellular nutrient supply [36]. It is useful to describe extrinsic noise in terms of a white noise process, based on a great variety of physical phenomena (such as noise due to low copy number-induced dynamics) that are met in many experimental situations [75, 1, 36]. White noise is a random variable with zero mean that is independent in time, and is called so because of its constant spectrum, meaning that all frequency components have the same weight [75, 77]. It is therefore expected that homeostatic controller motifs subject to white extrinsic noise will show a shift in the noise spectrum of the regulated species towards the resonant peak observed in Chapter 4 [36]. In this way, the analysis of deterministic systems in terms of their frequency response can still be useful in understanding the behavior of their stochastic counterparts.

Without detailed knowledge of how the random perturbations representing extrinsic noise are distributed, we let the white noise random variable be normally distributed[11]. Extrinsic noise is then given by the Wiener process, which is a random variable $W(t)$ that depends continuously on $t \in [0, T]$ and has the following properties [77, 75]:

(i) $W(0) = 0$ (with probability 1).

(ii) For $0 \leq s < t \leq T$, the random variable given by the increment $W(t) - W(s)$ (white noise) is normally distributed with zero mean and variance $t - s$.

(iii) For $0 \leq s < t < u < v \leq T$, the increments $W(t) - W(s)$ and $W(v) - W(u)$ are independent (i.e. white noise is independent in time).

Then, the time-evolution of the random variable X, subject to extrinsic noise, can be modeled by the scalar stochastic differential (Itô) equation (SDE) [75, 77]

$$\mathrm{d}X(t) = a(X)\mathrm{d}t + b(X)\mathrm{d}W(t) \tag{5.27}$$

[11] Gaussian white noise emerges from the CLE approximation [1, 60].

where a and b are deterministic functions, called the drift coefficient and diffusion coefficient, respectively, and W is the Wiener process[12] (the increment $\mathrm{d}W(t)$ is white noise). White noise represents the only stochastic element in this equation, and hence if $b = 0$, the noise term vanishes, and the SDE is reduced to an ODE [77, 75]. The SDE in (5.27) can be simulated using readily available numerical methods, such as the Euler–Maruyama method [77, 78].

Taking a look at our model for glucose uptake in cancer, given by the deterministic reaction rate equations in (5.9)–(5.12), the large molecular populations of the species involved justifies the use of a deterministic model, as intrinsic noise becomes negligible [60, 28]. However, in constructing the model, we combined and simplified many of the signaling reactions that form negative feedback, in order to investigate the structural properties of the system (see Figure 5.6). In addition, we only considered the primary components of glucose uptake in cancer, as determined by the differential gene expression results shown in Figure 5.7. These are typical sources of model uncertainty and extrinsic noise [199]. Whereas simplifying the underlying system may result in uncertainty in system parameters, by disregarding the downregulated components of glucose uptake (such as GLUT2-14), we risk leaving out background reactions that affect the system. To alleviate these concerns, we present a stochastic model for glucose uptake in cancer according to the SDE in (5.27)

$$\mathrm{d}c_{\mathrm{Glc}}(t) = f_{\mathrm{Glc}}(t)\mathrm{d}t + g_{\mathrm{Glc}}(t)\mathrm{d}W_1(t) \tag{5.28}$$

$$\mathrm{d}c_{\mathrm{G6P}}(t) = f_{\mathrm{G6P}}(t)\mathrm{d}t + g_{\mathrm{G6P}}(t)\mathrm{d}W_2(t) \tag{5.29}$$

$$\mathrm{d}c_{\mathrm{GLUT1}}(t) = f_{\mathrm{GLUT1}}(t)\mathrm{d}t + g_{\mathrm{GLUT1}}(t)\mathrm{d}W_3(t) \tag{5.30}$$

$$\mathrm{d}c_{\mathrm{HK2}}(t) = f_{\mathrm{HK2}}(t)\mathrm{d}t + g_{\mathrm{HK2}}(t)\mathrm{d}W_4(t) \tag{5.31}$$

where f_i ($i = \mathrm{Glc}, \mathrm{G6P}, \mathrm{GLUT1}, \mathrm{HK2}$) are the right-hand side expressions of (5.9)–(5.12), respectively. The functions g_i ($i = \mathrm{Glc}, \mathrm{G6P}, \mathrm{GLUT1}, \mathrm{HK2}$) are diffusion coefficients which, in the absence of detailed knowledge of how extrinsic noise affects the system, are set to be proportional to the system states; $g_i(t) = \sigma_i \cdot c_i(t)$, where σ_i are constants that take a similar role to the perturbation constants used in Chapter 4 ($k_{\mathrm{p}}^{\mathrm{in}}$ and $k_{\mathrm{p}}^{\mathrm{out}}$). W_i ($i = 1, 2, 3, 4$) are independent Wiener processes. Then, the system (5.28)–(5.31) can be written using vector notation, which takes the form of (5.27), where X is

[12] Note that we do not write $\mathrm{d}W(t)/\mathrm{d}t$, because the paths of the Wiener process are nowhere differentiable [75, 77].

now a vector of the states, a is a vector of drift coefficients, b is a diagonal matrix of diffusion coefficients, and W is a vector of Wiener processes (where $\mathrm{d}W(t) = [\mathrm{d}W_1(t), \ldots, \mathrm{d}W_4(t)]^\mathsf{T}$) [133].

Figure 5.12 shows the mean of 100 sample paths generated from the stochastic glucose uptake model (solid blue lines), along with a simulation of the deterministic version of the model (dashed red lines). Dark blue and light blue shaded areas indicate one and two standard deviations of the sample paths. The bottom right plot of cellular volume (solid black line) and surface area (dashed black line) is the same for all simulations. A spherical cell is assumed. Initial values and parameters are identical to the simulation of the deterministic glucose uptake model in Figure 5.9 (values given in Table 5.1), except that the third phase (dark gray area in Figure 5.9) is omitted. Sample paths are generated with random initial conditions, uniformly distributed ($\pm 50\%$) around the values given in Table 5.1 (not shown in Figure 5.12). We used the SDETools toolbox for MATLAB to generate sample paths, using the Euler–Maruyama method [78].

Simulations of the deterministic and stochastic versions of the glucose uptake model start at steady-state (in the mean) with a constant cellular volume in the first phase (white area, $t = [0, 400]$). In the second phase (light gray area, $t = [400, 800]$), the cellular volume starts to grow linearly. Finally, in the third phase (white area, $t = [800, 1200]$), volume growth is stopped, but the cellular volume has now grown much larger than in the initial phase. Looking at the mean trajectory of the stochastic glucose uptake model, we see good consistency with the deterministic model. An interesting observation is that standard deviations increase as the cellular volume grows. A possible explanation for this behavior is that the noise terms scale proportionally with the states ($g_i(t) = \sigma_i \cdot c_i(t)$), however, simulations with constant diffusion coefficients ($g_i(t) = \sigma_i$) display a similar behavior, albeit less pronounced (simulations not shown). Hence, it appears that this behavior is a structural property of the system. It is likely that extrinsic noise, e.g. from unmodeled cellular reactions, scales in some way with cell size [149, 154]. And therefore, increased variance with increasing cell size is an expected behavior. However, a result of this behavior is that, for the regulated species (intracellular glucose and G6P), we end up with a situation where mean trajectories are regulated to constant values, while standard deviations continue to grow with increasing cell size. It is possible that this could pose a limitation on cell growth, or that additional mechanisms must be in place to minimize the effect of extrinsic noise in larger cells.

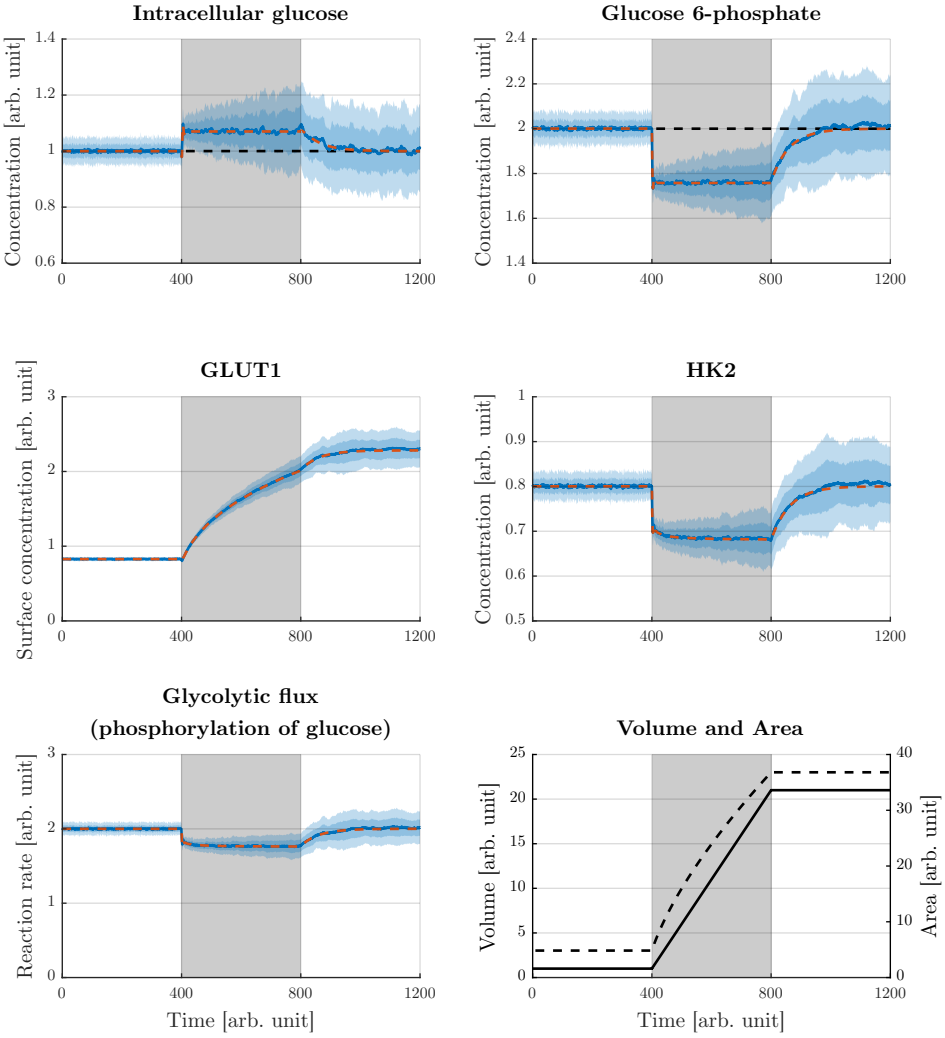

Figure 5.12: Simulation results of the stochastic and deterministic versions of the glucose uptake model. Solid blue lines show the mean trajectory of 100 sample paths generated from the SDEs (5.28)–(5.31). Dark blue and light blue shaded areas show one and two standard deviations of the sample paths. Dashed red lines show a simulation of the ODEs (5.9)–(5.12). Bottom right plot of cellular volume (solid black line) and surface area (dashed black line) is the same for all simulations (spherical cell assumed). Cellular volume is constant in the first phase of the simulations (white area, $t = [0, 400]$). In the second phase (light gray area, $t = [400, 800]$), cellular volume starts to grow linearly. Small offsets can be seen in the regulated species during growth (dashed black lines in intracellular glucose and G6P plots). Growth is stopped in the last phase (white area, $t = [800, 1200]$). Initial values and parameters are given in Table 5.1 (third phase omitted). Sample paths are generated with random initial values ($\pm 50\%$).

Despite the fact that noise terms can drastically change the behavior of the associated deterministic system (e.g. it is possible to construct an unstable deterministic system that can be made stable by the introduction of a noise term [94]), we see that the stability properties of the homeostatic controller motifs (see Chapter 3) are maintained in the stochastic versions[13] (i.e. asymptotic stability in the mean is preserved). Additionally, we see that standard deviations converge to constant values for constant cellular volume. If the joint probability distribution of the states of a stochastic system converges to a unique stationary distribution regardless of initial conditions, it is said to be ergodic [21]. Ergodicity has been shown for the stochastic antithetic integral controller in a constant volume, and hence, it is possible that ergodicity can be shown for stochastic versions of the homeostatic controller motifs as well [21].

Regarding the general question of qualitative behavior and stability of SDE models, there exists methods that use generalizations to stochastic systems of Lyapunov's direct method [94, 103, 183, 118]. Showing stability properties, such as ergodicity, may be facilitated by stability results learned from the associated deterministic system. If the system of interest can be approximated by a stochastic process taking the form of (5.27), we can make use of the well-developed theory on Itô diffusions [94, 103, 183, 118]. Notably, the CLE takes the form of (5.27) [60, 94, 199]. Therefore, in some cases, it is possible to to model intrinsic and extrinsic noise as separate noise terms in a system SDEs [107]. This is a convenient way to include various noise sources, with the benefit that stochastic Lyapunov function approaches can be used. When appropriate, this approach enables us to circumvent certain difficulties encountered with stochastic systems, such as the moment closure problem, to give a qualitative description of their behavior [21].

[13] Note that we have not shown this in general for the homeostatic controller motifs, but our simulations in Figure 5.12 indicate this to be true, at least for the system parameters chosen.

Chapter 6

Discussion and concluding remarks

Cellular processes and biological motifs, or arrangements of biochemical reactions, that can show and explain the mechanisms behind oscillations were extensively studied in the latter half of the 20th century. However, it is only fairly recently that regulatory mechanisms in biological systems have been studied from the perspective of robust control. It is from this new perspective that we have taken a bottom-up approach to cellular control processes in this thesis. In broad strokes, the work in this thesis considers the structural properties of a class of integral feedback structures, called homeostatic controller motifs, and extends upon prior analysis of these structures to encompass a range of non-ideal conditions. In this final chapter we summarize and discuss the results obtained on stability (Chapter 3), tuning (Chapter 4), and dilution resistance and noise (Chapter 5). We also discuss some limitations inherent to the modeling approach used in our work and in this thesis.

6.1 On stability

In Chapter 3, we looked at stability properties of the homeostatic controller motifs. We considered the situation in which most reactions of the homeostatic controller motifs are described by saturation kinetics. In this case, we were able to show that the homeostatic controller motifs are globally asymptotically stable, despite highly nonlinear interactions. This stability result greatly reinforces prior studies into the homeostatic controller motifs, that have investigate robustness and the presence of integral action [43, 129, 41, 176]. Prior stability analyses of the homeostatic

controller motifs have only considered autocatalytic variants with linear cross coupling, or been limited to linearization and local results [42, 176].

We employed a passivity-based approach in which we described the homeostatic controller motifs as negative feedback connections of two individual subsystems. We established output strict passivity and zero-state observability for the subsystems, and showed that this implies global asymptotic stability for the negative feedback connection. Note that the stability result obtained does not solely rely on the particular rate expressions chosen for the homeostatic controller motifs. Instead, it is the nature of the expressions, i.e. strictly monotone, that enables us to establish asymptotic stability. Therefore, we could easily perform the same stability analysis on variations of the homeostatic controllers motifs with different reaction kinetic expressions (e.g. cross-coupling reactions using Hill-type kinetics). Still, the stability analysis only considered activation/inhibition expressions that change the limiting rate ($V_{\max}$) of enzyme reactions. Such expressions arise for special cases of mixed activation/inhibition (e.g. pure noncompetitive inhibition), but a more common behavior is that activation/inhibition changes both $V_{\max}$ and K_{M} values of enzyme reactions [31, 30, 5]. Hence, the measurement (j_{meas}) and compensatory (j_{comp}) fluxes are likely more complicated expressions in which activation/inhibition is not a simple multiplication by the functions $f_{\mathrm{act}}/f_{\mathrm{inh}}$. It would be interesting to extend the stability analysis to include more complex expressions.

Using the stability result obtained for the homeostatic controller motifs, we showed that integral action ensures asymptotic disturbance rejection to constant disturbances. This holds true as long as the compensatory flux (j_{comp}) does not reach its upper limit, at which point capacity related breakdown occurs [41]. However, perfect adaptation to disturbances in the regulated species relies on zero-order degradation of the controller species. It is likely that mechanisms for zero-order removal in biological systems rely on saturation, rather than true zero-order kinetics, so that near-perfect adaptation is likely the best achievable response [6]. Nevertheless, partial adaptation to disturbances represents better regulation than no adaptation, and in many cases living organisms are not concerned with perfect regulation, but rather with the presence of some level of regulation.

In the final part of Chapter 3, we related the homeostatic controller motifs to other reaction kinetic mechanisms, or motifs, that achieve integral control. These mechanisms are collectively known as ICMs. Functionally, ICMs implement negative feedback with integral action in different ways, but the objective is always the same; an integral controller that works to

counteract deviations in the regulated variable from a desired set-point [41, 42, 21, 142]. In this way, ICMs are effective mechanisms for mitigating the effects of unknowns in biological systems, such as uncontrolled variations in the external environment or unforeseen interactions within the system, and provide the ability to fine tune central parameters of the control system [142, 6, 181].

We believe that our application of passivity theory to biological processes only scratches the surface of passivity theory as a tool to help us understand cellular reaction networks. Passivity is defined as an input-output property, and is particularly useful in stability analysis of interconnected systems [11, 158, 92]. By characterizing the individual processes within cells in terms of passivity, it is possible to describe large nonlinear cellular networks as interconnections subsystems, and ascertain stability properties of the network using fairly simple rules on the interconnection of passive systems [158, 11, 9]. For example, the parallel connection of two passive systems, or the feedback connection of two passive system, are both passive [158, 92]. And the shortage of passivity in one system can be compensated for by the excess of passivity in another system [11, 158, 151]. It would be interesting to approach the analysis of large reaction networks from a passivity-based perspective.

6.2 On tuning

In Chapter 4, we showed how parameters related to molecular and kinetic mechanisms influence set-point tracking and disturbance rejection properties of the homeostatic controller motifs. We used a tuning procedure based on linearization, which enabled us to describe the dynamical behavior of the homeostatic controller motifs in terms of the undamped natural frequency (ω_{n}) and the damping ratio (ζ). By specifying these tuning parameters, along with the set-point (x_1^{set}), the tuning procedure involved calculating the rate constants associated with the controller species and the compensatory flux, based on transfer functions for set-point tracking and disturbance rejection of the linearized controller motifs. We elected to focus on these rate constants as it is more conceivable that they are possible to tune from the perspective of synthetic biology, and offer a greater tunable range than the parameters associated with saturation ($K_{\mathrm{M},i}$, $K_{\mathrm{A},i}$, and $K_{\mathrm{I},i}$) [5]. For example, the rate constant for the synthesis of a protein, acting as the controller species, can in practice be modified by altering the promoter

of the gene coding for the protein. One way to do this is a fixed tuning of the promoter itself, e.g. the copper-dependent promoter of the *CUP1* gene of *Saccharomyces cerevisiae* can be modified by mutations to show a wide range of induction ratios [172]. Another possibility is to use a dual mode promoter, a type of promoter whose regulation of protein production depends on two activators. One activator would be the regulated species, and the other would be a chemical compound that can be meticulously added to the growth medium to achieve a certain level of gene transcription and production of the controller species. One such promoter, controlled by testosterone and IPTG, has demonstrated the ability to tune the promoter's output curve over a wide range [117].

We verified the tuning procedure by simulations, where the *nonlinear* homeostatic controller motifs were shown to produce the expected dynamical behaviors. We used nullcline analysis to characterize constraints associated with the steady-state behavior of the homeostatic controller motifs, and looked at trade-offs associated with time-varying inputs. The tuning procedure used relies on linearization of the homeostatic controller motifs, in a similar way to the tuning of industrial control processes. Of course, the controller motifs are nonlinear, meaning that the tuning procedure can only guarantee a certain dynamical response locally to the working point. However, linearization allows us to relate the nonlinear homeostatic controller motifs to well-known concepts in linear control analysis. From a synthetic biology point of view, such a tuning procedure provides a basis for the determination of system parameters, and gives insight into the relationship between parameter values and the dynamical response of the system. Additionally, by performing the same tuning procedure for several different working points, it is possible to characterize the dynamical behavior of the controller motifs over a range of inputs and steady-states, in a way similar to gain scheduling.

In the final part of Chapter 4, we investigated the mismatch between the nonlinear dynamics of the controller motifs and the linearization used in the tuning procedure. In particular, we observed a significant change in set-point tracking and disturbance rejection properties with increasing disturbance magnitude. To elucidate this relationship, we showed how the tuning parameters (ω_{n} and ζ) change with increasing perturbation ($k_{\mathrm{p}}^{\mathrm{in/out}}$). Importantly, we found that the homeostatic controller motifs are divided into two groups based on how the tuning parameters are altered, determined by the controller type (activating or inhibiting). For time-varying disturbance inputs we were able to show that the Bode magnitude

plot for the linearized outflow controller 5 provides a good approximation to the nonlinear controller motif, at least for the estimated convergence region indicated in Figure 4.9a with excitation amplitudes $a \leq \bar{r}$ (see Figure 4.9b). However, it is likely that our estimate for the convergence region is rather conservative, which leaves $\bar{r}$ fairly low. This could be due to a suboptimal choice for the matrix P, or the fact that the estimation procedure is based on quadratic Lyapunov functions analysis, which is conservative by itself when applied to nonlinear systems [136]. It is possible that a better estimate for the convergence region could be made using the combined storage function presented in Chapter 3.

There is a great effort going on in both academia and industry to genetically manipulate organisms to create useful bioproducts. One of the landmark studies published in Science in 2015 was the implementation of the complete biosynthesis of opioids in yeast [53, 159]. Opioids like morphine are the primary drugs used for treatment of severe pain and pain management, and production depends on the cultivation of opium poppies. While the implementation of opioid biosynthesis in yeast is a tremendous achievement, it still requires an improvement in overall yield by a factor of $\sim 7 \times 10^6$ to compete with poppies [53]. Great improvements are expected, but this will require an intricate tuning of the different parts of the biosynthetic pathway.

6.3 On dilution resistance and noise

In Chapter 5 we investigated the homeostatic controller motifs under non-ideal conditions. In particular, we considered some practical aspects in living cells that may impact the performance of homeostatic mechanisms. Namely, we looked at dilution of cellular constituents and stochastic fluctuations in chemically reacting systems. We reasoned that increased glycolytic and proliferative activity in cancer cells lead to cell swelling and growth-induced dilution. This causes dilution of cellular constituents, which can markedly influence cellular reactions and the function of proteins, and hence, control mechanisms used by cancer cells to maintain a highly glycolytic phenotype must be robust to dilution. We reviewed the literature to give an overview of the rewiring of glycolysis in cancer, and looked at the various signaling pathways involved in the regulation of glucose uptake in cancer. Using public gene expression data from the Expression Atlas database, we showed that cancer cells, on average, shift towards GLUT1-mediated glucose uptake,

predominant expression of the PKM2 isoform, and overexpression of HK2. With this information we constructed a simplified mathematical model of glucose uptake in cancer, in order to investigate structural properties of the system. By simulations we found that in a worst-case scenario, in which enzymes for the generation and removal of the controller species are subject to dilution, partial dilution resistance to a linearly increasing cellular volume is achieved, and that a nested feedback architecture of homeostatic controller motifs appears significant to this end. In fact, in Paper 4, we showed that negative feedback regulation of intermediary glycolytic enzymes, in addition to negative feedback from downstream glycolytic metabolites to glucose transporters (i.e. nested feedback), is sufficient in order to achieve homeostatic control during growth.

To investigate why only partial dilution resistance was achieved, we performed simulations to show that growth-induced offsets in the regulation of glucose uptake appear to be caused by set-point changes, rather than breakdown of regulation, and that these growth-induced offsets are dependent on the rate of volume increase, not the total volume. Based on previous investigations into ICMs subject to dilution, we wanted to relate our observations on dilution resistance to the mathematical description of the system. We found that the growth-induced offsets can be represented by offset terms in the integral control law for the controller species, and that these offset terms are indeed dependent on the growth rate. We also showed how the growth-induced offsets can be minimized by increasing the rate constants associated with the controller species, such that near-perfect dilution resistance is achieved. Interestingly, a way in which GLUT1 and HK2 activity is regulated, is through translocation between biological membranes and the cytosol, indicating that the activity of these species can respond quickly, and that regulation of glucose uptake in cancer may achieve dilution resistance through the formation of quasi-ICMs [97, 201, 87]. It is clear that to ensure robustness of the homeostatic controller motifs to perturbations that affect the system locally (i.e. perturbations in the regulated species) as well as globally (i.e. dilution), it is necessary to satisfy two conditions; *i*) the degradation of the controller species must be (close to) zero-order ($K_{\mathrm{M},2} \ll x_2$), and *ii*) the controller reactions must be much faster than the rate of dilution.

While in many cases a chemically reacting system can be treated as a continuous-state deterministic process, in other cases, particularly when the number of reactant molecules becomes low, reactions may be better described as discrete-state stochastic processes [58, 59]. For the glucose

uptake model, we reasoned that the large molecular populations of the species involved justified the use of a deterministic model. However, a general problem of simple conceptual models, like the glucose uptake model, is the unavoidable fact that some information is left out of the model. This can be a source of model uncertainty and extrinsic noise [199]. In an attempt to include the effects of uncertainty and noise in the model, we presented a stochastic version of the glucose uptake model. By simulations we found good agreement with the deterministic model in the mean. We also found that increased cellular volume resulted in increased variance of the system states. It is likely that noise, e.g. from unmodeled cellular reactions, scales in some way with cell size [149, 154]. However, a result of this behavior is that mean trajectories for the regulated species are regulated to constant values, while standard deviations continue to grow with increasing cell size. It is possible that this could pose a limitation on cell growth, or that additional mechanisms must be in place to minimize the effect of extrinsic noise in larger cells.

Despite the fact that noise can drastically change the behavior of a deterministic system (e.g. it is possible to construct an unstable deterministic system that can be made stable by the introduction of a noise term [94]), the stability properties of the homeostatic controller motifs were largely preserved in the stochastic versions (i.e. asymptotic stability in the mean is preserved). We also found that standard deviations converge to constant values for constant cellular volume. If the joint probability distribution of the states of a stochastic system converges to a unique stationary distribution regardless of initial conditions, it is said to be ergodic [21]. Ergodicity has been shown for the stochastic antithetic integral controller in a constant volume, and hence, it is possible that ergodicity can be shown for stochastic versions of the homeostatic controller motifs as well [21].

Regarding the general question of qualitative behavior and stability of SDE models, there exists methods that use generalizations to stochastic systems of Lyapunov's direct method [94, 103, 183, 118]. It is possible that the stability result obtained in Chapter 3 could facilitate stability analysis of stochastic versions of the homeostatic controller motifs. These stochastic controller motifs would be based on SDEs, and could include noise terms for both intrinsic and extrinsic noise [107]. This way, a more rigorous investigation of stochastic homeostatic controller motifs could be done.

We also mentioned some results on the performance of homeostatic controller motifs for different types of volume increase. This is an important

consideration, since cellular volume increase is not limited to linear growth, e.g. both linear and exponential volume increase has been observed in *Escherichia coli* [102, 197]. In Paper 3, we investigated the performance of selected negative feedback controllers in response to dilution under different growth laws. Based on a previous study (Fjeld et al. [49]), we chose to look at four integral feedback mechanism: A motif 1 (inflow controller 1) zero-order controller, a motif 2 (inflow controller 2) zero-order controller, a motif 1 variant of the antithetic controller, and a motif 1 autocatalytic variant. Table 6.1 gives an overview of the controller performances for linear and exponential volume increases, and provides a guide to what type of feedback structures and integral control kinetics are suitable to oppose dilution by different growth laws. Note that in Paper 3 we did not consider dilution of the generation and removal reactions for the controller species, and hence, dilution resistance to exponential growth was possible.

Controller type	**Linear volume increase**	**Exponential volume increase**
Motif 1, zero-order	perfect resistance	partial resistance
Motif 1, antithetic	perfect resistance	partial resistance
Motif 1, autocatalytic	perfect resistance	perfect resistance
Motif 2, zero-order	perfect resistance	partial resistance

Table 6.1: Summary of controller performances in linearly and exponentially increasing volumes. Perfect resistance means that there is no offset in the steady-state value of the regulated species during growth, whereas partial resistance means that there is an offset, but that a steady-state is maintained (i.e. no breakdown). See Paper 3 for details.

Notably, we found that the autocatalytic controller performed well, even with an exponential growth law. The occurrence of autocatalysis and positive feedback loops are becoming more and more recognized in signaling and homeostatic regulation [14, 7]. For example, in cortisol homeostasis, ACTH signaling from the brain-pituitary system to the cortisol producing adrenals occurs by autocatalysis/positive feedback [140]. In blood sugar homeostasis, insulin secretion is activated by several positive feedback/autocatalytic signaling pathways to ensure an effective regulation in glucose concentration [173, 108, 85]. These examples indicate the importance of additional "helper kinetics" (such as autocatalysis/positive feedback) to obtain homeostatic regulation with optimal response and precision properties. For synthetic biology this means that knowledge about controller

structure and their inherent kinetics are important aspects in the design and implementation of artificial regulatory units when trying to oppose the dilution effects of growth or other time-dependent perturbations.

We should note that our review of cancer metabolism and glucose uptake in Chapter 5 is not exhaustive, but meant to give and overview of key aspects. In particular, we only mentioned some of the factors involved in the rewiring of glycolysis in cancer. One potentially important factor that we did not include is the mammalian target of rapamycin (mTOR), which acts as a central activator of the Warburg effect under normoxic conditions [207, 48]. mTOR is downstream of Akt/PKB in the PI3K-Akt-mTOR pathway, which plays a crucial role in the regulation of aerobic glycolysis and tumor growth [207, 35]. In tumorigenesis, overproduction or mutation of growth factors lead to activation of the PI3K-Akt-mTOR pathway and the downstream targets HIF-1α and c-Myc [207, 35]. Additionally, for the regulation of GLUT1-mediated glucose uptake, we primarily focused on feedback mechanisms that involve the main energy sensor of the cell (AMPK) [207, 48]. Naturally, other control mechanisms may contribute to the regulation of glucose uptake in cancer, without the involvement of AMPK.

Further exploration of glucose uptake in cancer using the glucose uptake model in Chapter 5 would likely require expanding the model, possibly incorporating spatial aspects, and that experimental data be collected. A possible experiment setup uses confocal microscopy to capture 3D images of living cells expressing HK2 tagged with yellow fluorescent protein (YFP) and GLUT1 tagged with green fluorescent protein (GFP) [87]. Then, intracellular glucose can be measured with a genetically-encoded glucose biosensor (FLIPglu-600µM) [87, 88]. This way, intracellular concentrations can be measured, together with spatial information.

6.4 Limitations of simplified small-scale models

In this thesis we have investigated the structural properties of a class of integral feedback mechanisms called homeostatic controller motifs. Most of our modeling efforts are based on *qualitative* descriptions, with the consequence that simulation results are given in arbitrary units, and that parameter values are chosen arbitrarily for the purpose of demonstration. Therefore, we do not expect that the simulation results provide any *quantitative* predictive power. In the study of structural properties, we are more

concerned with the range of possible behaviors a system can display (e.g. adaptation to disturbances), and under what conditions these behaviors are maintained (e.g. in the presence of dilution). Investigations of simplified small-scale models aim to form an intuitive understanding of processes, and to uncover principles of function [61, 82]. This is facilitated by the small number components and parameters in small-scale models. However, complex large-scale models are undeniably closer to biological reality than simplified small-scale models [61, 82]. And although large-scale models may suffer from a large number of parameters that are poorly determined, it is important to remember that the qualitative nature of complex systems can be drastically altered by seemingly insignificant quantitative differences [61, 82].

The work in this thesis is based on ODE/SDE modeling, which assumes that the cellular volume is well-mixed and homogeneous. There are situations where these assumptions are not appropriate, for instance when dealing with transport and diffusion of metabolites between cellular compartments [33, 147]. Spatial aspects can be dealt with using ODEs in compartmentalized models (e.g. our glucose uptake model), however, it is often more appropriate to construct spatial models using partial differential equations (PDEs) [33]. Such models have been successfully used to study mechanisms for gradient sensing and adaptation to spatial disturbances [109, 99, 100, 48].

Finally, we must not lose sight of the fact that models are not only measured by their correctness (in terms of quantitative predictive power), but also by their ability to help us understand how and why a system behaves in a certain way. In this thesis, we have taken a bottom-up approach to modeling, in which systems are built up gradually from essential components and interactions. Hence, the results in this thesis can serve as a foundation to build more complex models, in which the knowledge acquired (e.g. conditions for stability, adaptation, dilution resistance) can guide model construction. In this way, construction of complex large-scale models can be approached with some knowledge of what interactions are conducive to certain behaviors, and what interactions are destructive. This highlights an important complementary relation between small-scale and large-scale models.

Bibliography

[1] **Adamer MF, Harrington HA, Gaffney EA, Woolley TE**. Coloured noise from stochastic inflows in reaction–diffusion systems. *Bulletin of Mathematical Biology*, 82: 44. 2020. doi: 10.1007/s11538-020-00719-w.

[2] **Agafonov O, Selstø CH, Thorsen K, Xu XM, Drengstig T, Ruoff P**. The organization of controller motifs leading to robust plant iron homeostasis. *PLoS ONE*, 11: e0147120. 2016. doi: 10.1371/journal.pone.0147120.

[3] **Andrianantoandro E, Basu S, Karig DK, Weiss R**. Synthetic biology: New engineering rules for an emerging discipline. *Molecular Systems Biology*, 2: 2006.0028. 2006. doi: 10.1038/msb4100073.

[4] **Ang J, Bagh S, Ingalls BP, McMillen DR**. Considerations for using integral feedback control to construct a perfectly adapting synthetic gene network. *Journal of Theoretical Biology*, 266: 723–738. 2010. doi: 10.1016/j.jtbi.2010.07.034.

[5] **Ang J, Harris E, Hussey BJ, Kil R, McMillen DR**. Tuning response curves for synthetic biology. *ACS Synthetic Biology*, 2: 547–567. 2013. doi: 10.1021/sb4000564.

[6] **Ang J, McMillen DR**. Physical constraints on biological integral control design for homeostasis and sensory adaptation. *Biophysical Journal*, 104: 505–515. 2013. doi: 10.1016/j.bpj.2012.12.015.

[7] **Angeli D, Ferrell JE, Sontag ED**. Detection of multistability, bifurcations, and hysteresis in a large class of biological positive-feedback systems. *Proceedings of the National Academy of Sciences of the United States of America*, 101: 1822–1827. 2004. doi: 10.1073/pnas.0308265100.

[8] **Aoki SK, Lillacci G, Gupta A, Baumschlager A, Schweingruber D, Khammash M**. A universal biomolecular integral feedback controller for robust perfect adaptation. *Nature*, 570: 533–537. 2019. doi: 10.1038/s41586-019-1321-1.

[9] **Arcak M, Sontag ED**. Diagonal stability of a class of cyclic systems and its connection with the secant criterion. *Automatica: a journal of IFAC, the International Federation of Automatic Control*, 42: 1531–1537. 2006. doi: 10.1016/j.automatica.2006.04.009.

[10] **Asaka M, Kimura T, Meguro T, Kato M, Kudo M, Miyazaki T, Alpert E**. Alteration of aldolase isozymes in serum and tissues of patients with cancer and other diseases. *Journal of Clinical Laboratory Analysis*, 8: 144–148. 1994. doi: 10.1002/jcla.1860080306.

[11] **Bao J, Lee PL**. *Process Control: The Passive Systems Approach*. Advances in Industrial Control. London, England: Springer. 2007. ISBN: 978-1-84628-892-0.

[12] **Barnes K, Ingram JC, Porras OH, Barros LF, Hudson ER, Fryer LGD, Foufelle F, Carling D, Hardie DG, Baldwin SA**. Activation of GLUT1 by metabolic and osmotic stress: Potential involvement of AMP-activated protein kinase (AMPK). *Journal of Cell Science*, 115: 2433–2442. 2002.

[13] **Barnett JA**. A history of research on yeasts 7: Enzymic adaptation and regulation. *Yeast*, 21: 703–746. 2004. doi: 10.1002/yea.1113.

[14] **Becskei A, Séraphin B, Serrano L**. Positive feedback in eukaryotic gene networks: Cell differentiation by graded to binary response conversion. *The EMBO Journal*, 20: 2528–2535. 2001. doi: 10.1093/emboj/20.10.2528.

[15] **Bell GI, Kayano T, Buse JB, Burant CF, Takeda J, Lin D, Fukumoto H, Seino S**. Molecular biology of mammalian glucose transporters. *Diabetes Care*, 13: 198–208. 1990. doi: 10.2337/diacare.13.3.198.

[16] **Benesch R, Benesch RE**. The effect of organic phosphates from the human erythrocyte on the allosteric properties of hemoglobin. *Biochemical and Biophysical Research Communications*, 26: 162–167. 1967. doi: 10.1016/0006-291X(67)90228-8.

[17] **Berg JM, Tymoczko JL, Gatto GJ, Stryer L**. *Biochemistry*. New York, NY, USA: W. H. Freeman and Company, eighth edn. 2015. ISBN: 978-1-4641-2610-9.

[18] **Boado RJ, Pardridge WM**. Glucose deprivation causes posttranscriptional enhancement of brain capillary endothelial glucose transporter gene expression via GLUT1 mRNA stabilization. *Journal of Neurochemistry*, 60: 2290–2296. 1993. doi: 10.1111/j.1471-4159.1993.tb03516.x.

[19] **Bonhoeffer KF**. Über periodische chemische Reaktionen I. *Zeitschrift für Elektrochemie und angewandte physikalische Chemie*, 52: 24–29. 1948.

[20] **Bover DCC**. Moment equation methods for nonlinear stochastic systems. *Journal of Mathematical Analysis and Applications*, 65: 306–320. 1978. doi: 10.1016/0022-247X(78)90182-8.

[21] **Briat C, Gupta A, Khammash M**. Antithetic integral feedback ensures robust perfect adaptation in noisy biomolecular networks. *Cell Systems*, 2: 15–26. 2016. doi: 10.1016/j.cels.2016.01.004.

[22] **Briat C, Gupta A, Khammash M**. Antithetic proportional-integral feedback for reduced variance and improved control performance of stochastic reaction networks. *Journal of The Royal Society Interface*, 15: 20180079. 2018. doi: 10.1098/rsif.2018.0079.

[23] **Briat C, Zechner C, Khammash M**. Design of a synthetic integral feedback circuit: Dynamic analysis and DNA implementation. *ACS Synthetic Biology*, 5: 1108–1116. 2016. doi: 10.1021/acssynbio.6b00014.

[24] **Bustamante E, Pedersen PL**. High aerobic glycolysis of rat hepatoma cells in culture: Role of mitochondrial hexokinase. *Proceedings of the National Academy of Sciences of the United States of America*, 74: 3735–3739. 1977. doi: 10.1073/pnas.74.9.3735.

[25] **Cannon WB**. Organization for physiological homeostasis. *Physiological Reviews*, 9: 399–431. 1929. doi: 10.1152/physrev.1929.9.3.399.

[26] **Carruthers A, DeZutter J, Ganguly A, Devaskar SU**. Will the original glucose transporter isoform please stand up! *American Journal of Physiology-Endocrinology and Metabolism*, 297: E836–E848. 2009. doi: 10.1152/ajpendo.00496.2009.

[27] **Celenza JL, Marshall-Carlson L, Carlson M**. The yeast SNF3 gene encodes a glucose transporter homologous to the mammalian protein. *Proceedings of the National Academy of Sciences of the United States of America*, 85: 2130–2134. 1988. doi: 10.1073/pnas.85.7.2130.

[28] **Chen WW, Niepel M, Sorger PK**. Classic and contemporary approaches to modeling biochemical reactions. *Genes & Development*, 24: 1861–1875. 2010. doi: 10.1101/gad.1945410.

[29] **Clegg JS, Jackson SA, Fendl K**. Effects of reduced cell volume and water content on glycolysis in L-929 cells. *Journal of Cellular Physiology*, 142: 386–391. 1990. doi: 10.1002/jcp.1041420223.

[30] **Cohen GN**. Regulation of enzyme activity in microorganisms. *Annual Review of Microbiology*, 19: 105–126. 1965. doi: 10.1146/annurev.mi.19.100165.000541.

[31] **Cornish-Bowden A**. *Fundamentals of Enzyme Kinetics*. Weinheim, Germany: Wiley-Blackwell, fourth edn. 2012. ISBN: 978-3-527-33074-4.

[32] **Davies SP, Hawley SA, Woods A, Carling D, Haystead TAJ, Hardie DG**. Purification of the AMP-activated protein kinase on ATP-γ-Sepharose and analysis of its subunit structure. *European Journal of Biochemistry*, 223: 351–357. 1994. doi: 10.1111/j.1432-1033.1994.tb19001.x.

[33] **de Jong H**. Modeling and simulation of genetic regulatory systems: A literature review. *Journal of Computational Biology*, 9: 67–103. 2002. doi: 10.1089/10665270252833208.

[34] **de Padua MC, Delodi G, Vučetić M, Durivault J, Vial V, Bayer P, Noleto GR, Mazure NM, Ždralević M, Pouysségur J**. Disrupting glucose-6-phosphate isomerase fully suppresses the "Warburg effect" and activates OXPHOS with minimal impact on tumor growth except in hypoxia. *Oncotarget*, 8: 87623–87637. 2017. doi: 10.18632/oncotarget.21007.

[35] **DeBerardinis RJ, Lum JJ, Hatzivassiliou G, Thompson CB**. The biology of cancer: Metabolic reprogramming fuels cell growth and proliferation. *Cell Metabolism*, 7: 11–20. 2008. doi: 10.1016/j.cmet.2007.10.002.

[36] **Del Vecchio D, Dy AJ, Qian Y**. Control theory meets synthetic biology. *Journal of the Royal Society Interface*, 13: 20160380. 2016. doi: 10.1098/rsif.2016.0380.

[37] **Di Chiro G, Hatazawa J, Katz DA, Rizzoli HV, De Michele DJ**. Glucose utilization by intracranial meningiomas as an index of tumor aggressivity and probability of recurrence: A PET study. *Radiology*, 164: 521–526. 1987. doi: 10.1148/radiology.164.2.3496626.

[38] **Doyle FJ**. Control and biology [president's message]. *IEEE Control Systems*, 36: 8–10. 2016. doi: 10.1109/MCS.2016.2536118.

[39] **Doyle FJ**. Reflections on the convergence paradigm [president's message]. *IEEE Control Systems*, 36: 8–10. 2016. doi: 10.1109/MCS.2016.2584389.

[40] **Doyle J, Csete M**. Motifs, control, and stability. *PLoS Biology*, 3: e392. 2005. doi: 10.1371/journal.pbio.0030392.

[41] **Drengstig T, Jolma IW, Ni XY, Thorsen K, Xu XM, Ruoff P**. A basic set of homeostatic controller motifs. *Biophysical Journal*, 103: 2000–2010. 2012. doi: 10.1016/j.bpj.2012.09.033.

[42] **Drengstig T, Ni XY, Thorsen K, Jolma IW, Ruoff P**. Robust adaptation and homeostasis by autocatalysis. *The Journal of Physical Chemistry B*, 116: 5355–5363. 2012. doi: 10.1021/jp3004568.

[43] **Drengstig T, Ueda HR, Ruoff P**. Predicting perfect adaptation motifs in reaction kinetic networks. *The Journal of Physical Chemistry B*, 112: 16752–16758. 2008. doi: 10.1021/jp806818c.

[44] **Egeland O, Gravdahl JT**. *Modeling and Simulation for Automatic Control*. Trondheim, Norway: Marine Cybernetics. 2002. ISBN: 82-92356-01-0.

[45] **El-Samad H, Goff JP, Khammash M**. Calcium homeostasis and parturient hypocalcemia: An integral feedback perspective. *Journal of Theoretical Biology*, 214: 17–29. 2002. doi: 10.1006/jtbi.2001.2422.

[46] **Ferrell JE**. Perfect and near-perfect adaptation in cell signaling. *Cell Systems*, 2: 62–67. 2016. doi: 10.1016/j.cels.2016.02.006.

[47] **Filipp FV**. Cancer metabolism meets systems biology: Pyruvate kinase isoform PKM2 is a metabolic master regulator. *Journal of Carcinogenesis*, 12: 14. 2013. doi: 10.4103/1477-3163.115423.

[48] **Fjeld G**. *A Systems Biology Approach to Cellular Homeostasis, Volume Changes and Regulation of Metabolism*. PhD Thesis, University of Stavanger, Stavanger, Norway. 2020. ISBN: 978-82-7644-916-7.

[49] **Fjeld G, Thorsen K, Drengstig T, Ruoff P**. Performance of homeostatic controller motifs dealing with perturbations of rapid growth and depletion. *The Journal of Physical Chemistry B*, 121: 6097–6107. 2017. doi: 10.1021/acs.jpcb.7b01989.

[50] **Franck UF**. Chemical oscillations. *Angewandte Chemie International Edition in English*, 17: 1–15. 1978. doi: 10.1002/anie.197800013.

[51] **Franck UF**. Feedback kinetics in physicochemical oscillators. *Berichte der Bunsengesellschaft für physikalische Chemie*, 84: 334–341. 1980. doi: 10.1002/bbpc.19800840407.

[52] **Furlong TJ, Spring KR**. Mechanisms underlying volume regulatory decrease by Necturus gallbladder epithelium. *American Journal of Physiology-Cell Physiology*, 258: C1016–C1024. 1990. doi: 10.1152/ajpcell.1990.258.6.C1016.

[53] **Galanie S, Thodey K, Trenchard IJ, Interrante MF, Smolke CD**. Complete biosynthesis of opioids in yeast. *Science*, 349: 1095–1100. 2015. doi: 10.1126/science.aac9373.

[54] **Galbo T, Perry RJ, Nishimura E, Samuel VT, Quistorff B, Shulman GI**. PP2A inhibition results in hepatic insulin resistance despite Akt2 activation. *Aging*, 5: 770–781. 2013. doi: 10.18632/aging.100611.

[55] **Ganapathy V, Thangaraju M, Prasad PD**. Nutrient transporters in cancer: Relevance to Warburg hypothesis and beyond. *Pharmacology & Therapeutics*, 121: 29–40. 2009. doi: 10.1016/j.pharmthera.2008.09.005.

[56] **Gardner TS, Cantor CR, Collins JJ**. Construction of a genetic toggle switch in *Escherichia coli*. *Nature*, 403: 339–342. 2000. doi: 10.1038/35002131.

[57] **Gatenby RA, Gillies RJ**. Why do cancers have high aerobic glycolysis? *Nature Reviews Cancer*, 4: 891–899. 2004. doi: 10.1038/nrc1478.

[58] **Gillespie DT**. Exact stochastic simulation of coupled chemical reactions. *The Journal of Physical Chemistry*, 81: 2340–2361. 1977. doi: 10.1021/j100540a008.

[59] **Gillespie DT**. A rigorous derivation of the chemical master equation. *Physica A: Statistical Mechanics and its Applications*, 188: 404–425. 1992. doi: 10.1016/0378-4371(92)90283-V.

[60] **Gillespie DT**. The chemical Langevin equation. *The Journal of Chemical Physics*, 113: 297–306. 2000. doi: 10.1063/1.481811.

[61] **Gómez-Schiavon M, El-Samad H**. Complexity-aware simple modeling. *Current Opinion in Microbiology*, 45: 47–52. 2018. doi: 10.1016/j.mib.2018.01.004.

[62] **Gonze D, Ruoff P**. The Goodwin oscillator and its legacy. *Acta Biotheoretica*. 2020. doi: 10.1007/s10441-020-09379-8.

[63] **Goodwin BC**. *Temporal Organization in Cells; a Dynamic Theory of Cellular Control Processes*. London, England: Academic Press. 1963.

[64] **Goodwin BC**. Oscillatory behavior in enzymatic control processes. *Advances in Enzyme Regulation*, 3: 425–438. 1965. doi: 10.1016/0065-2571(65)90067-1.

[65] **Griffith JS**. Mathematics of cellular control processes I. Negative feedback to one gene. *Journal of Theoretical Biology*, 20: 202–208. 1968. doi: 10.1016/0022-5193(68)90189-6.

[66] **Griffith JS**. Mathematics of cellular control processes II. Positive feedback to one gene. *Journal of Theoretical Biology*, 20: 209–216. 1968. doi: 10.1016/0022-5193(68)90190-2.

[67] **Guertin DA, Sabatini DM**. Cell growth. In: *The Molecular Basis of Cancer*, edited by Mendelsohn J, Howley PM, Israel MA, Gray JW, Thompson CB, 169–175. Philadelphia, PA, USA: Saunders, third edn. 2008. ISBN: 978-1-4160-3703-3.

[68] **Hanahan D, Weinberg RA**. Hallmarks of cancer: The next generation. *Cell*, 144: 646–674. 2011. doi: 10.1016/j.cell.2011.02.013.

[69] **Haspel HC, Mynarcik DC, Ortiz PA, Honkanen RA, Rosenfeld MG**. Glucose deprivation induces the selective accumulation of hexose transporter protein GLUT-1 in the plasma membrane of normal rat kidney cells. *Molecular Endocrinology*, 5: 61–72. 1991. doi: 10.1210/mend-5-1-61.

[70] **Haspel HC, Wilk EW, Birnbaum MJ, Cushman SW, Rosen OM**. Glucose deprivation and hexose transporter polypeptides of murine fibroblasts. *The Journal of Biological Chemistry*, 261: 6778–6789. 1986.

[71] **Hastings S, Tyson J, Webster D**. Existence of periodic solutions for negative feedback cellular control systems. *Journal of Differential Equations*, 25: 39–64. 1977. doi: 10.1016/0022-0396(77)90179-6.

[72] **Haugen F**. *Dynamiske systemer: modellering, analyse og simulering*. Trondheim, Norway: Tapir Akademisk Forlag, third edn. 2007. ISBN: 978-82-519-2260-9.

[73] **Häussinger D, Newsome W, vom Dahl S, Stoll B, Noe B, Schreiber R, Wettstein M, Lang F**. Control of liver cell function by the hydration state. *Biochemical Society Transactions*, 22: 497–502. 1994. doi: 10.1042/bst0220497.

[74] **Hay N**. Reprogramming glucose metabolism in cancer: Can it be exploited for cancer therapy? *Nature Reviews Cancer*, 16: 635–649. 2016. doi: 10.1038/nrc.2016.77.

[75] **Henderson D, Plaschko P**. *Stochastic Differential Equations in Science and Engineering*. Toh Tuck Link, Singapore: World Scientific Publishing. 2006. ISBN: 981-256-296-6.

[76] **Higgins J**. The theory of oscillating reactions. *Industrial and Engineering Chemistry*, 59: 18–62. 1967. doi: 10.1021/ie50689a006.

[77] **Higham DJ**. An algorithmic introduction to numerical simulation of stochastic differential equations. *SIAM Review*, 43: 525–546. 2001. doi: 10.1137/S0036144500378302.

[78] **Horchler AD**. SDETools: A MATLAB toolbox for the numerical solution of stochastic differential equations (SDEs). 2011. URL: `https://github.com/horchler/SDETools`.

[79] **Hsiao V, Swaminathan A, Murray RM**. Control theory for synthetic biology: Recent advances in system characterization, control design, and controller implementation for synthetic biology. *IEEE Control Systems*, 38: 32–62. 2018. doi: 10.1109/MCS.2018.2810459.

[80] **Hsu PP, Sabatini DM**. Cancer cell metabolism: Warburg and beyond. *Cell*, 134: 703–707. 2008. doi: 10.1016/j.cell.2008.08.021.

[81] **Huang Y, Drengstig T, Ruoff P**. Integrating fluctuating nitrate uptake and assimilation to robust homeostasis. *Plant, Cell & Environment*, 35: 917–928. 2012. doi: 10.1111/j.1365-3040.2011.02462.x.

[82] **Ingalls BP**. *Mathematical Modeling in Systems Biology: An Introduction*. Cambridge, MA, USA: The MIT Press. 2013. ISBN: 978-0-262-01888-3.

[83] **Jacob F, Monod J**. Genetic regulatory mechanisms in the synthesis of proteins. *Journal of Molecular Biology*, 3: 318–356. 1961. doi: 10.1016/S0022-2836(61)80072-7.

[84] **Jacob F, Monod J**. On the regulation of gene activity. *Cold Spring Harbor Symposia on Quantitative Biology*, 26: 193–211. 1961. doi: 10.1101/SQB.1961.026.01.024.

[85] **Jacques-Silva MC, Correa-Medina M, Cabrera O, Rodriguez-Diaz R, Makeeva N, Fachado A, Diez J, Berman DM, Kenyon NS, Ricordi C, Pileggi A, Molano RD, Berggren PO, Caicedo A**. ATP-gated $P2X_3$ receptors constitute a positive autocrine signal for insulin release in the human pancreatic β cell. *Proceedings of the National Academy of Sciences of the United States of America*, 107: 6465–6470. 2010. doi: 10.1073/pnas.0908935107.

[86] **Jeon SM**. Regulation and function of AMPK in physiology and diseases. *Experimental & Molecular Medicine*, 48: e245. 2016. doi: 10.1038/emm.2016.81.

[87] **John S, Weiss JN, Ribalet B**. Subcellular localization of hexokinases I and II directs the metabolic fate of glucose. *PLoS ONE*, 6: e17674. 2011. doi: 10.1371/journal.pone.0017674.

[88] **John SA, Ottolia M, Weiss JN, Ribalet B**. Dynamic modulation of intracellular glucose imaged in single cells using a FRET-based glucose nanosensor. *Pflügers Archiv - European Journal of Physiology*, 456: 307–322. 2008. doi: 10.1007/s00424-007-0395-z.

[89] **Joost HG, Bell GI, Best JD, Birnbaum MJ, Charron MJ, Chen YT, Doege H, James DE, Lodish HF, Moley KH, Moley JF, Mueckler M, Rogers S, Schürmann A, Seino S, Thorens B**. Nomenclature of the GLUT/SLC2A family of sugar/polyol transport facilitators. *American Journal of Physiology-Endocrinology and Metabolism*, 282: E974–E976. 2002. doi: 10.1152/ajpendo.00407.2001.

[90] **Kabashima T, Kawaguchi T, Wadzinski BE, Uyeda K**. Xylulose 5-phosphate mediates glucose-induced lipogenesis by xylulose 5-phosphate-activated protein phosphatase in rat liver. *Proceedings of the National Academy of Sciences of the United States of America*, 100: 5107–5112. 2003. doi: 10.1073/pnas.0730817100.

[91] **Keener J, Sneyd J**. *Mathematical Physiology I: Cellular Physiology*. No. 8/I in Interdisciplinary Applied Mathematics. New York, NY, USA: Springer, second edn. 2009. ISBN: 978-0-387-75846-6.

[92] **Khalil HK**. *Nonlinear Systems*. Upper Saddle River, NJ, USA: Prentice Hall, third edn. 2002. ISBN: 0-13-067389-7.

[93] **Khammash M**. An engineering viewpoint on biological robustness. *BMC Biology*, 14: 22. 2016. doi: 10.1186/s12915-016-0241-x.

[94] **Khasminskii R**. *Stochastic Stability of Differential Equations*. No. 66 in Stochastic Modelling and Applied Probability. Berlin, Germany: Springer, second edn. 2012. ISBN: 978-3-642-23279-4.

[95] **Kim NH, Cha YH, Lee J, Lee SH, Yang JH, Yun JS, Cho ES, Zhang X, Nam M, Kim N, Yuk YS, Cha SY, Lee Y, Ryu JK, Park S, Cheong JH, Kang SW, Kim SY, Hwang GS, Yook JI, Kim HS**. Snail reprograms glucose metabolism by repressing phosphofructokinase PFKP allowing cancer cell survival under metabolic stress. *Nature Communications*, 8: 14374. 2017. doi: 10.1038/ncomms14374.

[96] **Kitano H**. Systems biology: A brief overview. *Science*, 295: 1662–1664. 2002. doi: 10.1126/science.1069492.

[97] **Klip A, Tsakiridis T, Marette A, Ortiz PA**. Regulation of expression of glucose transporters by glucose: A review of studies in vivo and in cell cultures. *The FASEB Journal*, 8: 43–53. 1994. doi: 10.1096/fasebj.8.1.8299889.

[98] **Kornberg HL, Collins JF, Bigley D**. The influence of growth substrates on metabolic pathways in *micrococcus denitrificans*. *Biochimica et Biophysica Acta*, 39: 9–24. 1960. doi: 10.1016/0006-3002(60)90117-7.

[99] **Krishnan J**. Signal processing through a generalized module of adaptation and spatial sensing. *Journal of Theoretical Biology*, 259: 31–43. 2009. doi: 10.1016/j.jtbi.2009.02.015.

[100] **Krishnan J, Floros I**. Adaptive information processing of network modules to dynamic and spatial stimuli. *BMC Systems Biology*, 13: 32. 2019. doi: 10.1186/s12918-019-0703-1.

[101] **Kryven I, Röblitz S, Schütte C**. Solution of the chemical master equation by radial basis functions approximation with interface tracking. *BMC Systems Biology*, 9: 67. 2015. doi: 10.1186/s12918-015-0210-y.

[102] **Kubitschek HE**. Cell volume increase in Escherichia coli after shifts to richer media. *Journal of Bacteriology*, 172: 94–101. 1990. doi: 10.1128/jb.172.1.94-101.1990.

[103] **Kushner HJ**. *Stochastic Stability and Control*. New York, NY, USA: Academic Press. 1967.

[104] **Lang F, Busch GL, Ritter M, Völkl H, Waldegger S, Gulbins E, Häussinger D**. Functional significance of cell volume regulatory mechanisms. *Physiological Reviews*, 78: 247–306. 1998. doi: 10.1152/physrev.1998.78.1.247.

[105] **Lathi BP**. *Linear Systems and Signals*. The Oxford Series in Electrical and Computer Engineering. New York, NY, USA: Oxford University Press, second edn. 2010. ISBN: 978-0-19-539256-2.

[106] **Lee MG, Pedersen PL**. Glucose metabolism in cancer: Importance of transcription factor-DNA interactions within a short segment of the proximal region og the type II hexokinase promoter. *The Journal of Biological Chemistry*, 278: 41047–41058. 2003. doi: 10.1074/jbc.M307031200.

[107] **Lei X, Tian W, Zhu H, Chen T, Ao P**. Biological sources of intrinsic and extrinsic noise in *cI* expression of lysogenic phage lambda. *Scientific Reports*, 5: 13597. 2015. doi: 10.1038/srep13597.

[108] **Leibiger IB, Leibiger B, Berggren PO**. Insulin feedback action on pancreatic β-cell function. *FEBS Letters*, 532: 1–6. 2002. doi: 10.1016/S0014-5793(02)03627-X.

[109] **Levchenko A, Iglesias PA**. Models of eukaryotic gradient sensing: Application to chemotaxis of amoebae and neutrophils. *Biophysical Journal*, 82: 50–63. 2002. doi: 10.1016/S0006-3495(02)75373-3.

[110] **Lizana L, Bauer B, Orwar O**. Controlling the rates of biochemical reactions and signaling networks by shape and volume changes. *Proceedings of the National Academy of Sciences of the United States of America*, 105: 4099–4104. 2008. doi: 10.1073/pnas.0709932105.

[111] **Loison L**. Monod before Monod: Enzymatic adaptation, Lwoff, and the legacy of general biology. *History and Philosophy of the Life Sciences*, 35: 167–192. 2013.

[112] **Luo W, Hu H, Chang R, Zhong J, Knabel M, O'Meally R, Cole RN, Pandey A, Semenza GL**. Pyruvate kinase M2 is a PHD3-stimulated coactivator for hypoxia-inducible factor 1. *Cell*, 145: 732–744. 2011. doi: 10.1016/j.cell.2011.03.054.

[113] **Macheda ML, Rogers S, Best JD**. Molecular and cellular regulation of glucose transporter (GLUT) proteins in cancer. *Journal of Cellular Physiology*, 202: 654–662. 2005. doi: 10.1002/jcp.20166.

[114] **Marín-Hernández A, Rodríguez-Enríquez S, Vital-González PA, Flores-Rodríguez FL, Macías-Silva M, Sosa-Garrocho M, Moreno-Sánchez R**. Determining and understanding the control of glycolysis in fast-growth tumor cells. Flux control by an over-expressed but strongly product-inhibited hexokinase. *The FEBS Journal*, 273: 1975–1988. 2006. doi: 10.1111/j.1742-4658.2006.05214.x.

[115] **Mathupala SP, Ko YH, Pedersen PL**. Hexokinase II: Cancer's double-edged sword acting as both facilitator and gatekeeper of malignancy when bound to mitochondria. *Oncogene*, 25: 4777–4786. 2006. doi: 10.1038/sj.onc.1209603.

[116] **Mathupala SP, Rempel A, Pedersen PL**. Glucose catabolism in cancer cells. Isolation, sequence, and activity of the promoter for type II hexokinase. *The Journal of Biological Chemistry*, 270: 16918–16925. 1995. doi: 10.1074/jbc.270.28.16918.

[117] **Mazumder M, McMillen DR**. Design and characterization of a dual-mode promoter with activation and repression capability for tuning gene expression in yeast. *Nucleic Acids Research*, 42: 9514–9522. 2014. doi: 10.1093/nar/gku651.

[118] **Meyn SP, Tweedie RL**. Stability of Markovian processes III: Foster-Lyapunov criteria for continuous-time processes. *Advances in Applied Probability*, 25: 518–548. 1993. doi: 10.2307/1427522.

[119] **Monod J**. The growth of bacterial cultures. *Annual Review of Microbiology*, 3: 371–394. 1949. doi: 10.1146/annurev.mi.03.100149.002103.

[120] **Monod J**. From enzymatic adaptation to allosteric transitions. *Science*, 154: 475–483. 1966. doi: 10.1126/science.154.3748.475.

[121] **Monod J, Changeux JP, Jacob F**. Allosteric proteins and cellular control systems. *Journal of Molecular Biology*, 6: 306–329. 1963. doi: 10.1016/S0022-2836(63)80091-1.

[122] **Monod J, Jacob F**. General conclusions: Teleonomic mechanisms in cellular metabolism, growth, and differentiation. *Cold Spring Harbor Symposia on Quantitative Biology*, 26: 389–401. 1961. doi: 10.1101/SQB.1961.026.01.048.

[123] **Moon JS, Kim HE, Koh E, Park SH, Jin WJ, Park BW, Park SW, Kim KS**. Krüppel-like factor 4 (KLF4) activates the transcription of the gene for the platelet isoform of phosphofructokinase (PFKP) in breast cancer. *The Journal of Biological Chemistry*, 286: 23808–23816. 2011. doi: 10.1074/jbc.M111.236737.

[124] **Morales M, McKay D**. Biochemical oscillations in "controlled" systems. *Biophysical Journal*, 7: 621–625. 1967. doi: 10.1016/S0006-3495(67)86611-6.

[125] **Mrosovsky N**. *Rheostasis: The Physiology of Change*. New York, NY, USA: Oxford University Press. 1990. ISBN: 0-19-506184-5.

[126] **Munsky B, Khammash M**. The finite state projection algorithm for the solution of the chemical master equation. *The Journal of Chemical Physics*, 124: 044104. 2006. doi: 10.1063/1.2145882.

[127] **Nakashima RA, Paggi MG, Scott LJ, Pedersen PL**. Purification and characterization of a bindable form of mitochondrial bound hexokinase from the highly glycolytic AS-30D rat hepatoma cell line. *Cancer Research*, 48: 913–919. 1988.

[128] **Natarajan R, Gonzales N, Xu L, Nadler JL**. Vascular smooth muscle cells exhibit increased growth in response to elevated glucose. *Biochemical and Biophysical Research Communications*, 187: 552–560. 1992. doi: 10.1016/S0006-291X(05)81529-3.

[129] **Ni XY, Drengstig T, Ruoff P**. The control of the controller: Molecular mechanisms for robust perfect adaptation and temperature compensation. *Biophysical Journal*, 97: 1244–1253. 2009. doi: 10.1016/j.bpj.2009.06.030.

[130] **Nobel Media AB**. Summary: The Nobel Prize in physiology or medicine 1965. URL: `https://www.nobelprize.org/prizes/medicine/1965/summary/` (Accessed 2020-02-29).

[131] **Nobel Media AB**. Press release: The Nobel Prize in physiology or medicine 2017. URL: `https://www.nobelprize.org/prizes/medicine/2017/press-release/` (Accessed 2020-03-01).

[132] **Novick A, Szilard L**. Experiments with the chemostat on the rates of amino acid synthesis in bacteria. In: *Dynamics of Growth Processes*, edited by Boell EJ, 21–32. Princeton, NJ, USA: Princeton University Press. 1954.

[133] **Øksendal B**. *Stochastic Differential Equations: An Introduction with Applications*. Universitext. Berlin, Germany: Springer, fifth edn. 1998. ISBN: 978-3-540-63720-2.

[134] **Ozaki H, Shiio I**. Regulation of the TCA and glyoxylate cycles in *Brevibacterium flavum*: I. Inhibition of isocitrate lyase and isocitrate dehydrogenase by organic acids related to the TCA and glyoxylate cycles. *The Journal of Biochemistry*, 64: 355–363. 1968. doi: 10.1093/oxfordjournals.jbchem.a128902.

[135] **Pavlov A, Pogromsky A, van de Wouw N, Nijmeijer H**. Convergent dynamics, a tribute to Boris Pavlovich Demidovich. *Systems & Control Letters*, 52: 257–261. 2004. doi: 10.1016/j.sysconle.2004.02.003.

[136] **Pavlov A, van de Wouw N, Nijmeijer H**. *Uniform Output Regulation of Nonlinear Systems: A Convergent Dynamics Approach*. Systems and Control: Foundations & Applications. Boston, MA, USA: Birkhäuser. 2006. ISBN: 978-0-8176-4445-1.

[137] **Pavlov A, van de Wouw N, Nijmeijer H**. Frequency response functions and Bode plots for nonlinear convergent systems. In: *Proceedings of the 45th IEEE Conference on Decision and Control*, 3765–3770. Piscataway, NJ, USA: IEEE. 2007. doi: 10.1109/CDC.2006.377669.

[138] **Peak M, al-Habori M, Agius L**. Regulation of glycogen synthesis and glycolysis by insulin, pH and cell volume. Interactions between swelling and alkalinization in mediating the effects of insulin. *Biochemical Journal*, 282: 797–805. 1992. doi: 10.1042/bj2820797.

[139] **Pedersen PL, Mathupala S, Rempel A, Geschwind J, Ko YH**. Mitochondrial bound type II hexokinase: A key player in the growth and survival of many cancers and an ideal prospect for therapeutic intervention. *Biochimica et Biophysica Acta (BBA) - Bioenergetics*, 1555: 14–20. 2002. doi: 10.1016/S0005-2728(02)00248-7.

[140] **Peters A, Conrad M, Hubold C, Schweiger U, Fischer B, Fehm HL**. The principle of homeostasis in the hypothalamus-pituitary-adrenal system: New insight from positive feedback. *American Journal of Physiology-Regulatory, Integrative and Comparative Physiology*, 293: R83–R98. 2007. doi: 10.1152/ajpregu.00907.2006.

[141] **Petryszak R, Keays M, Tang YA, Fonseca NA, Barrera E, Burdett T, Füllgrabe A, Fuentes AMP, Jupp S, Koskinen S, Mannion O, Huerta L, Megy K, Snow C, Williams E, Barzine M, Hastings E, Weisser H, Wright J, Jaiswal P, Huber W, Choudhary J, Parkinson HE, Brazma A**. Expression Atlas update—an integrated database of gene and protein expression in humans, animals and plants. *Nucleic Acids Research*, 44: D746–D752. 2016. doi: 10.1093/nar/gkv1045.

[142] **Qian Y, Del Vecchio D**. Realizing 'integral control' in living cells: How to overcome leaky integration due to dilution? *Journal of the Royal Society Interface*, 15: 20170902. 2018. doi: 10.1098/rsif.2017.0902.

[143] **Reece JB, Urry LA, Cain ML, Wasserman SA, Minorsky PV, Jackson RB**. *Campbell Biology*. Boston, MA, USA: Pearson, ninth edn. 2011. ISBN: 978-0-321-73975-9.

[144] **Rempel A, Mathupala SP, Pedersen PL**. Glucose catabolism in cancer cells: Regulation of the type II hexokinase promoter by glucose and cyclic AMP. *FEBS Letters*, 385: 233–237. 1996. doi: 10.1016/0014-5793(96)00399-7.

[145] **Risvoll GB, Thorsen K, Ruoff P, Drengstig T**. Variable setpoint as a relaxing component in physiological control. *Physiological Reports*, 5: e13408. 2017. doi: 10.14814/phy2.13408.

[146] **Ruderman NB, Xu XJ, Nelson L, Cacicedo JM, Saha AK, Lan F, Ido Y**. AMPK and SIRT1: A long-standing partnership? *American Journal of Physiology-Endocrinology and Metabolism*, 298: E751–E760. 2010. doi: 10.1152/ajpendo.00745.2009.

[147] **Ruoff P, Agafonov O, Tveit DM, Thorsen K, Drengstig T**. Homeostatic controllers compensating for growth and perturbations. *PLoS ONE*, 14: e0207831. 2019. doi: 10.1371/journal.pone.0207831.

[148] **Saier MH, Ramseier TM**. The catabolite repressor/activator (Cra) protein of enteric bacteria. *Journal of Bacteriology*, 178: 3411–3417. 1996. doi: 10.1128/jb.178.12.3411-3417.1996.

[149] **Saint M, Bertaux F, Tang W, Sun XM, Game L, Köferle A, Bähler J, Shahrezaei V, Marguerat S**. Single-cell imaging and RNA sequencing reveal patterns of gene expression heterogeneity during fission yeast growth and adaptation. *Nature Microbiology*, 4: 480–491. 2019. doi: 10.1038/s41564-018-0330-4.

[150] **Sánchez-Aragó M, Chamorro M, Cuezva JM**. Selection of cancer cells with repressed mitochondria triggers colon cancer progression. *Carcinogenesis*, 31: 567–576. 2010. doi: 10.1093/carcin/bgq012.

[151] **Sastry S**. *Nonlinear Systems: Analysis, Stability, and Control*. No. 10 in Interdisciplinary Applied Mathematics. New York, NY, USA: Springer. 1999. ISBN: 0-387-98513-1.

[152] **Saunders PT, Koeslag JH, Wessels JA**. Integral rein control in physiology. *Journal of Theoretical Biology*, 194: 163–173. 1998. doi: 10.1006/jtbi.1998.0746.

[153] **Schmoller KM, Skotheim JM**. The biosynthetic basis of cell size control. *Trends in Cell Biology*, 25: 793–802. 2015. doi: 10.1016/j.tcb.2015.10.006.

[154] **Schmoller KM, Turner JJ, Kõivomägi M, Skotheim JM**. Dilution of the cell cycle inhibitor Whi5 controls budding-yeast cell size. *Nature*, 526: 268–272. 2015. doi: 10.1038/nature14908.

[155] **Seborg DE, Edgar TF, Mellichamp DA, Doyle FJ**. *Process Dynamics and Control*. Hoboken, NJ, USA: Wiley, third edn. 2011. ISBN: 978-0-470-64610-6.

[156] **Sellick CA, Campbell RN, Reece RJ**. Galactose metabolism in yeast—structure and regulation of the Leloir pathway enzymes and the genes encoding them. In: *International Review of Cell and Molecular Biology*, edited by Jeon KW, no. 269 in International Review of Cell and Molecular Biology, 111–150. Amsterdam, Netherlands: Elsevier. 2008. ISBN: 978-0-12-374554-5.

[157] **Semenza GL**. Targeting HIF-1 for cancer therapy. *Nature Reviews Cancer*, 3: 721–732. 2003. doi: 10.1038/nrc1187.

[158] **Sepulchre R, Janković M, Kokotović PV**. *Constructive Nonlinear Control*. Communications and Control Engineering. London, England: Springer. 1997. ISBN: 978-1-4471-1245-7.

[159] **Service RF**. Modified yeast produce opiates from sugar. *Science*, 349: 677. 2015. doi: 10.1126/science.349.6249.677.

[160] **Slotine JJE, Li W**. *Applied Nonlinear Control*. Upper Saddle River, NJ, USA: Prentice Hall. 1991. ISBN: 0-13-040890-5.

[161] **Sontag ED**. Adaptation and regulation with signal detection implies internal model. *Systems & Control Letters*, 50: 119–126. 2003. doi: 10.1016/S0167-6911(03)00136-1.

[162] **Sontag ED**. Molecular systems biology and control. *European Journal of Control*, 11: 396–435. 2005. doi: 10.3166/ejc.11.396-435.

[163] **Stadtman ER**. Symposium on multiple forms of enzymes and control mechanisms. II. Enzyme multiplicity and function in the regulation of divergent metabolic pathways. *Bacteriological Reviews*, 27: 170–181. 1963.

[164] **Steel H, Lillacci G, Khammash M, Papachristodoulou A**. Challenges at the interface of control engineering and synthetic biology. In: *2017 IEEE 56th Annual Conference on Decision and Control (CDC)*, 1014–1023. Piscataway, NJ, USA: IEEE. 2018. doi: 10.1109/CDC.2017.8263791.

[165] **Stein WD**. *Transport and Diffusion across Cell Membranes*. San Diego, CA, USA: Academic Press. 1986. ISBN: 0-12-664661-9.

[166] **Stoltzman CA, Kaadige MR, Peterson CW, Ayer DE**. MondoA senses non-glucose sugars: Regulation of thioredoxin-interacting protein (TXNIP) and the hexose transport curb. *The Journal of Biological Chemistry*, 286: 38027–38034. 2011. doi: 10.1074/jbc.M111.275503.

[167] **Stoltzman CA, Peterson CW, Breen KT, Muoio DM, Billin AN, Ayer DE**. Glucose sensing by MondoA:Mlx complexes: A role for hexokinases and direct regulation of thioredoxin-interacting protein expression. *Proceedings of the National Academy of Sciences of the United States of America*, 105: 6912–6917. 2008. doi: 10.1073/pnas.0712199105.

[168] **Swain PS, Elowitz MB, Siggia ED**. Intrinsic and extrinsic contributions to stochasticity in gene expression. *Proceedings of the National Academy of Sciences of the United States of America*, 99: 12795–12800. 2002. doi: 10.1073/pnas.162041399.

[169] **Szallasi Z, Stelling J, Periwal V**, editors. *System Modeling in Cell Biology: From Concepts to Nuts and Bolts*. Cambridge, MA, USA: The MIT Press. 2006. ISBN: 0-262-19548-8.

[170] **Takakura Y, Kuentzel SL, Raub TJ, Davies A, Baldwin SA, Borchardt RT**. Hexose uptake in primary cultures of bovine brain microvessel endothetial cells. I. Basic characteristics and effects of D-glucose and insulin. *Biochimica et Biophysica Acta (BBA) - Biomembranes*, 1070: 1–10. 1991. doi: 10.1016/0005-2736(91)90139-Y.

[171] **ter Kuile BH, Cook M**. The kinetics of facilitated diffusion followed by enzymatic conversion of the substrate. *Biochimica et Biophysica Acta (BBA) - Biomembranes*, 1193: 235–239. 1994. doi: 10.1016/0005-2736(94)90158-9.

[172] **Thiele DJ, Hamer DH**. Tandemly duplicated upstream control sequences mediate copper-induced transcription of the *Saccharomyces cerevisiae* copper-metallothionein gene. *Molecular and Cellular Biology*, 6: 1158–1163. 1986. doi: 10.1128/MCB.6.4.1158.

[173] **Thomas MK, Rastalsky N, Lee JH, Habener JF**. Hedgehog signaling regulation of insulin production by pancreatic β-cells. *Diabetes*, 49: 2039–2047. 2000. doi: 10.2337/diabetes.49.12.2039.

[174] **Thorens B**. Glucose transporters in the regulation of intestinal, renal, and liver glucose fluxes. *American Journal of Physiology-Gastrointestinal and Liver Physiology*, 270: G541–G553. 1996. doi: 10.1152/ajpgi.1996.270.4.G541.

[175] **Thorens B, Mueckler M**. Glucose transporters in the 21st Century. *American Journal of Physiology-Endocrinology and Metabolism*, 298: E141–E145. 2010. doi: 10.1152/ajpendo.00712.2009.

[176] **Thorsen K**. *Controller Motifs for Homeostatic Regulation and Their Applications in Biological Systems*. PhD Thesis, University of Stavanger, Stavanger, Norway. 2015. ISBN: 978-82-7644-628-9.

[177] **Thorsen K, Agafonov O, Selstø CH, Jolma IW, Ni XY, Drengstig T, Ruoff P**. Robust concentration and frequency control in oscillatory homeostats. *PLoS ONE*, 9: e107766. 2014. doi: 10.1371/journal.pone.0107766.

[178] **Thorsen K, Drengstig T, Ruoff P**. Transepithelial glucose transport and Na^+/K^+ homeostasis in enterocytes: An integrative model. *American Journal of Physiology-Cell Physiology*, 307: C320–C337. 2014. doi: 10.1152/ajpcell.00068.2013.

[179] **Thorsen K, Drengstig T, Ruoff P**. The effect of integral control in oscillatory and chaotic reaction kinetic networks. *Physica D: Nonlinear Phenomena*, 393: 38–46. 2019. doi: 10.1016/j.physd.2019.01.002.

[180] **Thorsen K, Risvoll G, Mazumder M, McMillen DR**. A controller for regulation of intracellular copper in S. cerevisiae. Poster presented at the 17th International Conference on Systems Biology (ICSB2016), Barcelona, Spain. 2016. URL: `https://www.postersessiononline.eu/173580348_eu/congresos/17ICSB/aula/-P-M_77_17ICSB.pdf`.

[181] **Thorsen K, Risvoll GB, Tveit DM, Ruoff P, Drengstig T**. Tuning of physiological controller motifs. In: *Proceedings of the 9th EUROSIM Congress on Modelling and Simulation, EUROSIM 2016, and the 57th SIMS Conference on Simulation and Modelling, SIMS 2016*, edited by Juuso E, Dahlquist E, Leiviskä K, no. 142 in Linköping Electronic Conference Proceedings, 31–37. Linköping, Sweden: Linköping University Electronic Press. 2018. doi: 10.3384/ecp1714231.

[182] **Thorsen K, Ruoff P, Drengstig T**. Control theoretic properties of physiological controller motifs. In: *2013 International Conference on System Science and Engineering (ICSSE)*, 165–170. Piscataway, NJ, USA: IEEE. 2013. doi: 10.1109/ICSSE.2013.6614653.

[183] **Thygesen UH**. *A Survey of Lyapunov Techniques for Stochastic Differential Equations*. IMM Technical Report 18-1997, Department of Mathematical Modeling, Technical University of Denmark, Lyngby, Denmark. 1997. URL: `http://www.imm.dtu.dk/documents/ftp/tr97/tr18_97.abstract.html`.

[184] **Tordjman KM, Leingang KA, Mueckler M**. Differential regulation of the HepG2 and adipocyte/muscle glucose transporters in 3T3L1 adipocytes. Effect of chronic glucose deprivation. *Biochemical Journal*, 271: 201–207. 1990. doi: 10.1042/bj2710201.

[185] **Tveit DM, Fjeld G, Drengstig T, Filipp FV, Ruoff P, Thorsen K**. Exploring mechanisms of glucose uptake regulation and dilution resistance in growing cancer cells. *bioRxiv*, preprint. 2020. doi: 10.1101/2020.01.02.892729.

[186] **Tveit DM, Thorsen K**. Passivity-based analysis of biochemical networks displaying homeostasis. In: *Proceedings of the 58th Conference on Simulation and Modelling (SIMS 58)*, edited by Jonsson MT, no. 138 in Linköping Electronic Conference Proceedings, 108–113. Linköping, Sweden: Linköping University Electronic Press. 2017. doi: 10.3384/ecp17138108.

[187] **Tyson JJ, Othmer HG**. The dynamics of feedback control circuits in biochemical pathways. In: *Progress in Theoretical Biology*, edited by Rosen R, Snell FM, vol. 5, 1–62. New York, NY, USA: Academic Press. 1978. ISBN: 0-12-543105-8.

[188] **Ullmann A**. Catabolite repression: A story without end. *Research in Microbiology*, 147: 455–458. 1996. doi: 10.1016/0923-2508(96)83999-4.

[189] **Umbarger HE**. Evidence for a negative-feedback mechanism in the biosynthesis of isoleucine. *Science*, 123: 848. 1956. doi: 10.1126/science.123.3202.848.

[190] **van Riel NAW**. Dynamic modelling and analysis of biochemical networks: Mechanism-based models and model-based experiments. *Briefings in Bioinformatics*, 7: 364–374. 2006. doi: 10.1093/bib/bbl040.

[191] **Vander Heiden MG, Cantley LC, Thompson CB**. Understanding the Warburg effect: The metabolic requirements of cell proliferation. *Science*, 324: 1029–1033. 2009. doi: 10.1126/science.1160809.

[192] **Vander Heiden MG, DeBerardinis RJ**. Understanding the intersections between metabolism and cancer biology. *Cell*, 168: 657–669. 2017. doi: 10.1016/j.cell.2016.12.039.

[193] **Vazquez A, Liu J, Zhou Y, Oltvai ZN**. Catabolic efficiency of aerobic glycolysis: The Warburg effect revisited. *BMC Systems Biology*, 4: 58. 2010. doi: 10.1186/1752-0509-4-58.

[194] **Vazquez A, Oltvai ZN**. Macromolecular crowding explains overflow metabolism in cells. *Scientific Reports*, 6: 31007. 2016. doi: 10.1038/srep31007.

[195] **Viniegra-Gonzalez G**. Stability properties of metabolic pathways with feedback interactions. In: *Biological and Biochemical Oscillators*, edited by Chance B, Ghosh AK, Pye EK, Hess B, 41–59. New York, NY, USA: Academic Press. 1973. ISBN: 978-0-12-167872-2.

[196] **Vogel HJ**. Control by repression. In: *Control Mechanisms in Cellular Processes*, edited by Bonner DM, 23–65. New York, NY, USA: The Ronald Press Company. 1961.

[197] **Wallden M, Fange D, Lundius EG, Baltekin Ö, Elf J**. The synchronization of replication and division cycles in individual *E. coli* cells. *Cell*, 166: 729–739. 2016. doi: 10.1016/j.cell.2016.06.052.

[198] **Wiener N**. *Cybernetics: Or Control and Communication in the Animal and the Machine*. Cambridge, MA, USA: The MIT Press, second edn. 1961. ISBN: 0-262-23007-0.

[199] **Wilkinson DJ**. Stochastic modelling for quantitative description of heterogeneous biological systems. *Nature Reviews Genetics*, 10: 122–133. 2009. doi: 10.1038/nrg2509.

[200] **Wolkenhauer O**. Systems biology: The reincarnation of systems theory applied in biology? *Briefings in Bioinformatics*, 2: 258–270. 2001. doi: 10.1093/bib/2.3.258.

[201] **Wu N, Zheng B, Shaywitz A, Dagon Y, Tower C, Bellinger G, Shen CH, Wen J, Asara J, McGraw TE, Kahn BB, Cantley LC**. AMPK-dependent degradation of TXNIP upon energy stress leads to enhanced glucose uptake via GLUT1. *Molecular Cell*, 49: 1167–1175. 2013. doi: 10.1016/j.molcel.2013.01.035.

[202] **Wyatt E, Wu R, Rabeh W, Park HW, Ghanefar M, Ardehali H**. Regulation and cytoprotective role of hexokinase III. *PLoS ONE*, 5: e13823. 2010. doi: 10.1371/journal.pone.0013823.

[203] **Xi X, Han J, Zhang JZ**. Stimulation of glucose transport by AMP-activated protein kinase via activation of p38 mitogen-activated protein kinase. *The Journal of Biological Chemistry*, 276: 41029–41034. 2001. doi: 10.1074/jbc.M102824200.

[204] **Yates RA, Pardee AB**. Control of pyrimidine biosynthesis in Escherichia coli by a feed-back mechanism. *The Journal of Biological Chemistry*, 221: 757–770. 1956.

[205] **Yi TM, Huang Y, Simon MI, Doyle J**. Robust perfect adaptation in bacterial chemotaxis through integral feedback control. *Proceedings of the National Academy of Sciences of the United States of America*, 97: 4649–4653. 2000. doi: 10.1073/pnas.97.9.4649.

[206] **Young CD, Nolte EC, Lewis A, Serkova NJ, Anderson SM**. Activated Akt1 accelerates MMTV-c-ErbB2 mammary tumourigenesis in mice without activation of ErbB3. *Breast Cancer Research*, 10: R70. 2008. doi: 10.1186/bcr2132.

[207] **Yu L, Chen X, Sun X, Wang L, Chen S**. The glycolytic switch in tumors: How many players are involved? *Journal of Cancer*, 8: 3430–3440. 2017. doi: 10.7150/jca.21125.

[208] **Zeron ES, Santillán M**. Numerical solution of the chemical master equation: Uniqueness and stability of the stationary distribution for chemical networks, and mRNA bursting in a gene network with negative feedback regulation. In: *Computer Methods, Part C*, edited by Johnson ML, Brand L, no. 487 in Methods in Enzymology, 147–169. San Diego, CA, USA: Academic Press. 2011. ISBN: 978-0-12-381270-4.

Paper 1:
Passivity-based analysis of biochemical networks displaying homeostasis

Passivity-Based Analysis of Biochemical Networks Displaying Homeostasis

Daniel M. Tveit Kristian Thorsen

Department of Electrical Engineering and Computer Science, University of Stavanger, Norway,
{daniel.m.tveit,kristian.thorsen}@uis.no

Abstract

Homeostasis refers to the ability of organisms and cells to maintain a stable internal environment even in the presence of a changing external environment. On the cellular level many compounds such as ions, pH, proteins, and transcription factors have been shown to be tightly regulated, and mathematical models of biochemical networks play a major role in elucidating the mechanisms behind this behaviour. Of particular interest is the control theoretic properties of these models, e.g. stability and robustness. The simplest models consist of two components, a controlled compound and a controller compound. We have previously explored how signalling between these two compounds can be arranged in order for the network to display homeostasis, and have constructed a class of eight two-component reaction kinetic networks with negative feedback that shows set-point tracking and disturbance rejection properties. Here, we take a closer look at the stability and robust control inherent to this class of systems. We show how these systems can be described as negative feedback connections of two nonlinear sub-systems, and show that both sub-systems are output strictly passive and zero-state detectable. Using a passivity-based approach, we show that all eight systems in this class of two-component networks are asymptotically stable.

Keywords: Passivity, homeostasis, adaptation, stability, robust control, integral control, negative feedback

1 Introduction

Control theoretic methods are useful when uncovering the mechanism behind cellular control processes. Especially properties such as stability and robust control are of interest. One structure with these properties is the negative feedback connection, which is employed in several biochemical processes, such as the regulation of enzyme synthesis and activity (Keener and Sneyd, 2009; Tyson and Othmer, 1978). Other more complicated control systems, such as the control of calcium in yeast cells, have also been analysed in this manner (Liu, 2012). We have previously investigated a class of simple two-component biochemical networks displaying homeostasis. These networks have been used in modelling ionic homeostasis in enterocytes (Thorsen et al., 2014), the development of biochemical controllers with robust control to perturbations changing rapidly in time (Fjeld et al., 2017), and developing yeast cells with an increased tolerance to high copper concentrations (Thorsen et al., 2016a). The networks consist of a controlled compound x_1 and a controller compound x_2, and through certain signalling reactions between these two compounds, the systems form negative feedback connections with integral action, giving robust control of x_1. We have identified eight such two-component systems, termed controller motifs (Drengstig et al., 2012). Figure 1 shows the structure of these controller motifs. For the class of two-component systems considered here, x_1 acts on either the synthesis or the degradation of x_2, and x_2 acts on either the synthesis or the degradation of x_1. This gives eight controller motifs with two components, each acting on the other through a single signalling reaction.

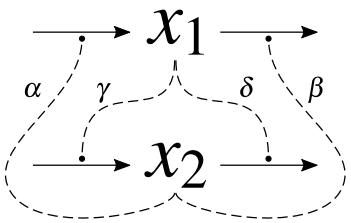

Figure 1. The controller motifs are formed by two compounds, x_1 and x_2, with signalling reactions α, β, γ, δ between them. For each controller motif, there is one signalling reaction from x_1 acting on x_2, and one signalling reaction from x_2 acting on x_1. These signalling reactions form a negative feedback connection with the two compounds. There are in total eight such controller motifs.

In general, the controller motifs take the form

$$\dot{x}_1 = k_{s,1} \cdot \alpha(x_2) - f_{d,1}(x_1) \cdot \beta(x_2) \quad (1)$$

$$\dot{x}_2 = k_{s,2} \cdot \gamma(x_1) - f_{d,2}(x_2) \cdot \delta(x_1) \quad (2)$$

where $k_{s,i}$ are positive rate constants determining the basal synthesis of x_i, the functions $f_{d,i}$ determine the degradation rate of x_i following Michaelis–Menten kinetics (Cornish-Bowden, 2012), and α, β, γ, δ are signalling functions between the two chemical compounds. Only one of the signalling functions α and β, and one of γ and δ, will be non-constant for a given controller motif.

DOI: 10.3384/ecp17138108

The Michaelis–Menten equation models the reaction rate of a compound x_i by an enzyme reaction

$$f_{d,i}(x_i) = \frac{k_{d,i} \cdot x_i}{K_{M,i} + x_i} \tag{3}$$

where $f_{d,i}$ is the reaction rate, $k_{d,i}$ is a positive constant determining the maximal reaction rate, and $K_{M,i}$ is a positive constant called the Michaelis constant (Cornish-Bowden, 2012).

The signalling functions α, β, γ, δ can either be activating or inhibiting. Activating signalling follow the expression for mixed activation (Cornish-Bowden, 2012)

$$f_{act}(x_i) = \frac{x_i}{K_{A,i} + x_i} \tag{4}$$

where the activation of some reaction is determined by the level of x_i, and $K_{A,i}$ is a positive constant for the activation reaction. Inhibiting signalling follow the expression for mixed inhibition (Cornish-Bowden, 2012)

$$f_{inh}(x_i) = \frac{K_{I,i}}{K_{I,i} + x_i} \tag{5}$$

where the amount of inhibition is determined by the level of x_i, and $K_{I,i}$ is a positive constant for the inhibition reaction.

2 Stability

To show asymptotic stability of the controller motifs, we first perform a change of variables, $z_1 = x_1 - x_1^*$ and $z_2 = x_2 - x_2^*$, where (x_1^*, x_2^*) is the equilibrium point of the system. The states x_1 and x_2 represent physical concentrations of compounds. Therefore, a global result corresponds to positive values of the states and the equilibrium point. The change of variables moves the equilibrium point to the origin. Using the fact that $k_{s,1} \cdot \alpha(x_2^*) = f_{d,1}(x_1^*) \cdot \beta(x_2^*)$ and $k_{s,2} \cdot \gamma(x_1^*) = f_{d,2}(x_2^*) \cdot \delta(x_1^*)$, the system is rewritten to the form

$$\dot{z}_1 = -f_1(z_1) + h_{2,\alpha}(z_2) - g_1(z_1) \cdot h_{2,\beta}(z_2) \tag{6}$$
$$\dot{z}_2 = -f_2(z_2) + h_{1,\gamma}(z_1) - g_2(z_2) \cdot h_{1,\delta}(z_1) \tag{7}$$

where these new functions are defined as follows

$$f_1(z_1) = f_{d,1}(z_1 + x_1^*) \cdot \beta(x_2^*) - f_{d,1}(x_1^*) \cdot \beta(x_2^*) \tag{8}$$
$$f_2(z_2) = f_{d,2}(z_2 + x_2^*) \cdot \delta(x_1^*) - f_{d,2}(x_2^*) \cdot \delta(x_1^*) \tag{9}$$
$$g_1(z_1) = f_{d,1}(z_1 + x_1^*) \tag{10}$$
$$g_2(z_2) = f_{d,2}(z_2 + x_2^*) \tag{11}$$
$$h_{1,\gamma}(z_1) = k_{s,2} \cdot \gamma(z_1 + x_1^*) - k_{s,2} \cdot \gamma(x_1^*) \tag{12}$$
$$h_{1,\delta}(z_1) = \delta(z_1 + x_1^*) - \delta(x_1^*) \tag{13}$$
$$h_{2,\alpha}(z_2) = k_{s,1} \cdot \alpha(z_2 + x_2^*) - k_{s,1} \cdot \alpha(x_2^*) \tag{14}$$
$$h_{2,\beta}(z_2) = \beta(z_2 + x_2^*) - \beta(x_2^*) \tag{15}$$

The functions f_i and h_i are strictly increasing and satisfy $f_i(0) = h_i(0) = 0$ for the interval $(-x_i^*, \infty)$. The functions $g_i > 0$ for the same interval. As noted earlier, only one of the signalling functions α and β, and one of γ and δ will be non-constant for a given controller motif. This means that only one of the output functions $h_{2,\alpha}$ and $h_{2,\beta}$, and one of $h_{1,\gamma}$ and $h_{1,\delta}$ will be non-zero. In addition, if the signalling functions $\alpha, \beta, \gamma, \delta$ are inhibiting instead of activating, the corresponding output functions h_i are defined to be negative. For example, the controller motif shown in Figure 2 has non-constant signalling functions β and δ, while $\alpha = \gamma = 1$. Therefore, the corresponding output functions $h_{2,\beta}$ and $h_{1,\delta}$ are non-zero, while $h_{2,\alpha} = h_{1,\gamma} = 0$. In addition, the signalling function δ is inhibiting, and the corresponding output function $h_{1,\delta}$ is defined to be negative.

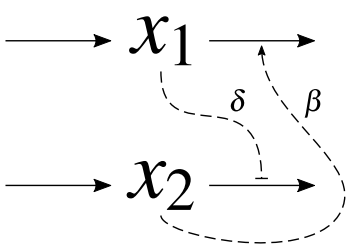

Figure 2. One of eight controller motifs that form a negative feedback connection. In this case, x_1 is acting on x_2 by inhibiting its degradation, and x_2 is acting on x_1 by activating its degradation.

The system equations for this controller motif are given by

$$\dot{x}_1 = k_{s,1} - f_{d,1}(x_1) \cdot \beta(x_2) = k_{s,1} - \frac{k_{d,1} \cdot x_1}{K_{M,1} + x_1} \cdot \frac{x_2}{K_{A,2} + x_2} \tag{16}$$

$$\dot{x}_2 = k_{s,2} - f_{d,2}(x_2) \cdot \delta(x_1) = k_{s,2} - \frac{k_{d,2} \cdot x_2}{K_{M,2} + x_2} \cdot \frac{K_{I,1}}{K_{I,1} + x_1} \tag{17}$$

and the transformed system equations are then

$$\dot{z}_1 = -f_1(z_1) - g_1(z_1) \cdot h_2(z_2) \tag{18}$$
$$\dot{z}_2 = -f_2(z_2) + g_2(z_2) \cdot h_1(z_1) \tag{19}$$

where $h_1 = h_{1,\delta}$ and $h_2 = h_{2,\beta}$.

To show that the controller motifs are asymptotically stable, we think of them as negative feedback connections of two sub-systems. In general, these sub-systems take the form

$$H_1 : \begin{cases} \dot{z}_1 = -f_1(z_1) + g_1(z_1) \cdot u_1 \\ y_1 = h_1(z_1) \end{cases} \tag{20}$$

$$H_2 : \begin{cases} \dot{z}_2 = -f_2(z_2) + g_2(z_2) \cdot u_2 \\ y_2 = h_2(z_2) \end{cases} \tag{21}$$

DOI: 10.3384/ecp17138108

where the negative feedback connection can be formed either by having

$$u_1 = -y_2, \quad u_2 = y_1 \tag{22}$$

or by

$$u_1 = y_2, \quad u_2 = -y_1 \tag{23}$$

This corresponds to which of H_1 and H_2 is in the negative feedback.

2.1 Passivity

The next step is to determine if the two sub-systems are output strictly passive. This is done by using the storage function S_i for sub-system H_i

$$S_i = \int_0^{z_i} \frac{h_i(\sigma)}{g_i(\sigma)} \mathrm{d}\sigma \tag{24}$$

where h_i and g_i are the functions in (20) and (21). The derivative of S along trajectories is then

$$\dot{S}_i = \frac{h_i(z_i)}{g_i(z_i)} \cdot \dot{z}_i = -f_i(z_i) \cdot \frac{h_i(z_i)}{g_i(z_i)} + u_i \cdot y_i \tag{25}$$

The sub-systems are output strictly passive if the following inequality is satisfied (Khalil, 2002; Sepulchre et al., 1997)

$$\dot{S}_i \leq -y_i \cdot \rho_i(y_i) + u_i \cdot y_i \tag{26}$$

where $y_i \cdot \rho_i(y_i) > 0 \; \forall \; y_i \neq 0$. Systems whose stored energy can only increase through the supply of an external source, are passive (Khalil, 2002). For inequality (26), the "energy" absorbed by the system, $u_i \cdot y_i$, is greater than the increase in stored "energy", $\dot{S}_i$. In addition, the system has an "excess" of passivity from the term $y_i \cdot \rho(y_i)$. For the controller motifs, we choose $y_i \cdot \rho_i(y_i) = p_i \cdot y_i^2$, where p_i is a positive constant. Inequality (26) is then satisfied by choosing p_i such that

$$0 < p_i \leq \frac{f_i(z_i)}{h_i(z_i) \cdot g_i(z_i)} \tag{27}$$

for the interval $(-x_i^*, \infty)$. For the same interval, the right-hand side expression can be shown to be greater than zero, and either strictly increasing, or strictly decreasing. Inequality (27) is then satisfied by finding p_i as the lower bound of the right-hand side expression. The lower bound is given by the minimum value of the right-hand side expression at the limits $z_i \to -x_i^*$ and $z_i \to \infty$. Therefore, the value of p_i is determined by

$$p_i = \min \left\{ \lim_{z_i \to -x_i^{*+}} \frac{f_i(z_i)}{h_i(z_i) \cdot g_i(z_i)}, \lim_{z_i \to \infty} \frac{f_i(z_i)}{h_i(z_i) \cdot g_i(z_i)} \right\} \tag{28}$$

Thus, the sub-systems (20) and (21) are output strictly passive.

It has been shown that the negative feedback connection of two output strictly passive systems is asymptotically stable if the sub-systems are zero-state detectable (Sepulchre et al., 1997). To show that H_1 and H_2 are zero-state detectable, we consider the system

$$H : \begin{cases} \dot{z} = f(z,u) \\ y = h(z,u) \end{cases} \tag{29}$$

with $u = 0$. H is said to be zero-state detectable if the origin is asymptotically stable conditionally to Z, where Z is the largest positively invariant set in $\{z \in \mathbb{R}^n \mid y = h(z,0) = 0\}$. For the special case when $Z = \{0\}$, we say that H is zero-state observable (Khalil, 2002; Sepulchre et al., 1997). We now consider the sub-systems $H_1$and H_2, with inputs $u_1 = u_2 = 0$. From the the output functions (12)–(15), it can be seen that

$$y_1 = y_2 = 0 \implies z_1 = z_2 = 0 \tag{30}$$

Therefore, the sub-systems H_1 and H_2 are zero-state observable if the origin is locally asymptotically stable. We verify this by linearisation of the sub-systems at the origin. With $u_i = y_i = 0$, the system equations of (20) and (21) are reduced to $\dot{z}_i = -f_i(z_i)$, and linearisation gives

$$H_1 : \left. \frac{\partial(-f_1)}{\partial z_1} \right|_{z_1=0} = -\frac{k_{d,1} \cdot K_{M,1}}{(K_{M,1} + x_1^*)^2} \cdot \beta(x_2^*) < 0 \tag{31}$$

$$H_2 : \left. \frac{\partial(-f_2)}{\partial z_2} \right|_{z_2=0} = -\frac{k_{d,2} \cdot K_{M,2}}{(K_{M,2} + x_2^*)^2} \cdot \delta(x_1^*) < 0 \tag{32}$$

where f_i are the functions given by (8) and (9).

Finally, to show that the entire system is asymptotically stable, we use the combined storage function

$$S = S_1 + S_2 \tag{33}$$

Because S_1 and S_2 are positive definite, so is S. Since the two sub-systems form a negative feedback connection given by (22) or (23), the derivative of S along trajectories is reduced to

$$\dot{S} = \dot{S}_1 + \dot{S}_2 \leq -p_1 \cdot y_1^2 - p_2 \cdot y_2^2 \tag{34}$$

which is negative definite. This shows that all bounded solutions converge to the set $\{(z_1, z_2) \mid y_1 = y_2 = 0\}$. From (30), we know that this corresponds to the origin. Since the origin has been shown to be locally asymptotically stable by linearisation, we conclude that the controller motifs are asymptotically stable. If the storage functions S_1 and S_2 are radially unbounded, so is S, and the controller motifs are globally asymptotically stable.

3 Integral Control

The system given by equations (1) and (2) can be shown to include integral control. This is done by rewriting equation (2). For example, the controller motif given by equations (16) and (17), shown in Figure 2, can have equation

(17) rewritten to

$$\dot{x}_2 = -\frac{k_{s,2}}{K_{I,1}+x_1}\cdot\left(\frac{x_2}{K_{M,2}+x_2}\cdot\frac{k_{d,2}\cdot K_{I,1}}{k_{s,2}} - K_{I,1} - x_1\right) \tag{35}$$

For $K_{M,2} = 0$, this is reduced to

$$\dot{x}_2 = -\frac{k_{s,2}}{K_{I,1}+x_1}\cdot\left(\frac{k_{d,2}\cdot K_{I,1}}{k_{s,2}} - K_{I,1} - x_1\right) \tag{36}$$

$$= G_i\cdot(x_{1,set} - x_1) \tag{37}$$

which has the form of the integral control law. This means that for $K_{M,2} = 0$, or $K_{M,2} \ll x_2$, the system behaves as an integral controller for x_1 with a set-point given by

$$x_{1,set} = \frac{k_{d,2}\cdot K_{I,1}}{k_{s,2}} - K_{I,1} \tag{38}$$

For the case when $K_{M,2} > 0$, the set-point in (35) is defined as

$$x_{1,set} = \frac{x_2}{K_{M,2}+x_2}\cdot\frac{k_{d,2}\cdot K_{I,1}}{k_{s,2}} - K_{I,1} \tag{39}$$

Thus, there is still integral action, however, the set-point changes with perturbations. The effect of this is shown in Figure 3, where the case with $K_{M,2} = 0$ results in perfect adaptation to perturbations in the synthesis of x_1, and the case with $K_{M,2} > 0$ results in only partial adaptation.

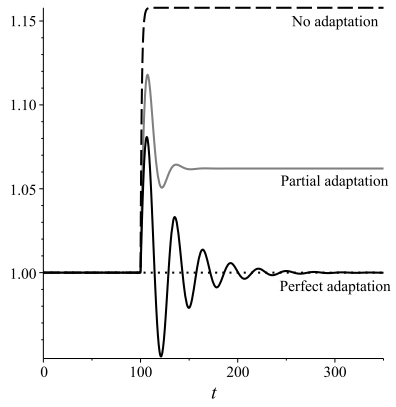

Figure 3. The response to a step-wise perturbation in the synthesis of x_1. Dashed line shows no adaptation, grey line shows partial adaptation, and black line shows perfect adaptation. These three cases correspond to the controller motifs having no integral control (no signalling between x_1 and x_2), integral control with $K_{M,2} > 0$, and integral control with $K_{M,2} = 0$, respectively.

It has previously been shown that the all the controller motifs include integral control (Drengstig et al., 2012; Thorsen et al., 2016b). The system equation of the controller compound x_2 is written to the form of the integral control law

$$\dot{x}_2 = G_i\cdot(x_{1,set} - x_{1,meas}) \tag{40}$$

Where G_i is the controller gain, $x_{1,set}$ is the set point of the controlled compound x_1, and $x_{1,meas}$ is a measurement function of x_1. Just like the system in Figure 2, the other controller motifs show partial or perfect adaptation depending on the value of $K_{M,2}$ (Drengstig et al., 2012).

Because we are able to show that the controller motifs are asymptotically stable, as well as incorporating integral control, they must be robust to all parameter perturbations that do not destroy the stability of the closed-loop system (Khalil, 2002). An implication of asymptotic stability, is that the error $x_{1,set} - x_{1,meas}$ must be zero at the equilibrium point. With any parameter perturbation that does not destroy the stability of the closed-loop system, the equilibrium point may change, however, the error must return to zero. Thus, regulation will be achieved for as long as the perturbed equilibrium point remains asymptotically stable.

4 Example

We demonstrate our approach by considering the controller motif shown in Figure 2, given by the system equations (16) and (17). This system is transformed to the system equations given by (18) and (19). The transformed system can be represented as a negative feedback connection of two sub-systems H_1 and H_2, given by (20) and (21), with

$$u_1 = -y_2 = -h_2(z_2), \quad u_2 = y_1 = h_1(z_1) \tag{41}$$

We use some arbitrary values for the constants $k_{s,1} = 1$, $k_{s,2} = 1$, $k_{d,1} = 3$, $k_{d,2} = 4$, $K_{M,1} = 1.5$, $K_{M,2} = 0.75$, $K_{I,1} = 1.5$, and $K_{A,2} = 2$, such that $x_1^*, x_2^* > 0$. Thereby, the storage function for H_1 is given by

$$S_1 = \int_0^{z_1}\left(0.114 - \frac{0.329}{\sigma + 2.893}\right)\mathrm{d}\sigma \tag{42}$$

and the derivative of S_1 along trajectories satisfy the inequality

$$\dot{S}_1 \leq -p_1\cdot y_1^2 + u_1\cdot y_1 \tag{43}$$

with the constant p_1 determined by

$$0 < p_1 \leq \frac{f_1(z_1)}{h_1(z_1)\cdot g_1(z_1)} = 0.506 + \frac{0.759}{z_1 + 2.893} \tag{44}$$

For the interval $(-x_1^*, \infty)$, the right-hand side is always greater than or equal to 0.506, and so we choose this value for p_1. This is illustrated in Figure 4. Similarly, for subsystem H_2, the inequality

$$0 < p_2 \leq \frac{f_2(z_2)}{h_2(z_2)\cdot g_2(z_2)} = 0.185 + \frac{0.370}{z_2 + 2.050} \tag{45}$$

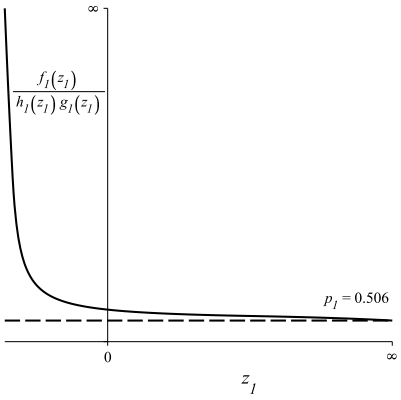

Figure 4. To determine the value of p_1 in inequality (44), we find the lower bound of the right-hand side expression. The figure shows that the lower bound is given by the limit of the right-hand side expression as $z_1 \to \infty$. In this case $p_1 = 0.506$.

is satisfied by choosing $p_2 = 0.185$, such that

$$\dot{S}_2 \leq -p_2 \cdot y_2^2 + u_2 \cdot y_2 \tag{46}$$

where the storage function S_2 is given by

$$S_2 = \int_0^{z_2} \left(0.123 - \frac{0.095}{\sigma + 2.050} - \frac{0.312}{\sigma + 4.050}\right) \mathrm{d}\sigma \tag{47}$$

Thus, the combined storage function $S = S_1 + S_2$ is positive definite and radially unbounded, because S_1 and S_2 are both positive definite and radially unbounded. In addition, the derivative of S along trajectories satisfies

$$\dot{S} \leq -0.506 \cdot y_1^2 - 0.185 \cdot y_2^2 \tag{48}$$

which implies that $\dot{S}$ is negative definite. S and $\dot{S}$ are shown in Figure 5.

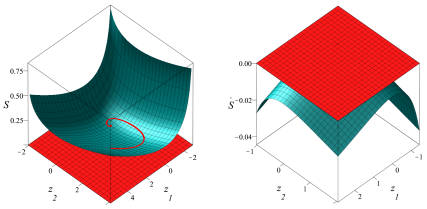

Figure 5. The storage function $S = S_1 + S_2$ is shown to the left, and its derivative along trajectories is shown to the right. The red surfaces are at zero. We see that S is positive definite, and $\dot{S}$ is negative definite. Therefore, all bounded solutions must converge to the set where $y_1 = y_2 = 0$. A trajectory converging to the origin is shown as a red curve within the bowl formed by S in the left figure.

Similarly to Lyapunov functions, we use the combined storage function S, and its derivative along trajectories $\dot{S}$ to draw conclusions about the stability of the system. The difference being that although the combined storage function is positive definite, and its derivative along trajectories negative definite, asymptotic stability is not implied. Instead it merely implies that all bounded solutions converge to the set where the outputs $y_1 = y_2 = 0$. In general, this set could correspond to a number of values (z_1, z_2), however, because the output functions (12)–(15) are strictly increasing and satisfy $h_i(0) = 0$, this set corresponds to the origin. This implies that the sub-systems H_1 and H_2 are zero-state observable if the origin is locally asymptotically stable. This is shown by linearisation at the origin, using equations (31) and (32)

$$H_1 : \left.\frac{\partial(-f_1)}{\partial z_1}\right|_{z_1=0} = -0.118 < 0 \tag{49}$$

$$H_2 : \left.\frac{\partial(-f_2)}{\partial z_2}\right|_{z_2=0} = -0.131 < 0 \tag{50}$$

Thus, the sub-systems are zero-state observable, and the entire system must be asymptotically stable. In addition, as noted earlier, the combined storage function S is radially unbounded, and therefore the system is globally asymptotically stable.

5 Conclusion

In this paper we have shown that a class of eight two-component biochemical networks displaying homeostasis, called controller motifs, are asymptotically stable. We have shown that the general system equations for these networks can be represented as negative feedback connections of two individual sub-systems. Then, these sub-systems are shown to be output strictly passive, and the feedback connection in its entirety is shown to be asymptotically stable. In addition, it is shown that the controller motifs are robust to perturbations because they incorporate integral control.

When modelling cellular processes, it is beneficial to know that uncertainties in parameters do not fundamentally change the behaviour of the model. Because the controller motifs are asymptotically stable with integral action, processes which can be modelled within the framework of the controller motifs will have a qualitative behaviour which aligns well with experimental measurements, even with large uncertainties in parameter values. On the other hand, processes which do not conform well to the controller motifs can have wildly different qualitative responses in the face of parameter uncertainties, and the controller motifs can be excluded as models for such processes. Thus, it is not a matter of parameter tuning. This is a helpful property of the controller motifs, especially in system identification.

Here we have chosen to focus on controller motifs with zero-order synthesis, degradation by an enzyme reaction, and signalling following mixed activation/inhibition.

However, other functions could be used. For example, we could use Hill kinetics for the degradation of the two compounds, or we could use linear activation for the signalling functions. In that case we would have to make sure that the properties assumed still hold.

References

Athel Cornish-Bowden. *Fundamentals of Enzyme Kinetics*. Wiley-Blackwell, fourth edition, 2012. ISBN 978-3-527-33074-4.

T. Drengstig, I. W. Jolma, X. Y. Ni, K. Thorsen, X. M. Xu, and P. Ruoff. A basic set of homeostatic controller motifs. *Biophysical Journal*, 103(9):2000–2010, 2012. ISSN 00063495. doi:10.1016/j.bpj.2012.09.033.

Gunhild Fjeld, Kristian Thorsen, Tormod Drengstig, and Peter Ruoff. The Performance of Homeostatic Controller Motifs Dealing with Perturbations of Rapid Growth and Depletion. *The Journal of Physical Chemistry B*, 2017. ISSN 1520-6106. doi:10.1021/acs.jpcb.7b01989. URL `http://pubs.acs.org/doi/abs/10.1021/acs.jpcb.7b01989`.

James Keener and James Sneyd. *Mathematical Physiology I: Cellular Physiology*. Springer, second edition, 2009. ISBN 978-0-387-75846-6. doi:10.1007/978-0-387-75847-3.

Hassan K. Khalil. *Nonlinear Systems*. Prentice Hall, third edition, 2002. ISBN 0-13-067389-7.

Weijiu Liu. *Introduction to Modeling Biological Cellular Control Systems*. Springer, 2012. ISBN 978-88-470-2489-2. doi:10.1007/978-88-470-2490-8.

Rodolphe Sepulchre, Mrdjan Jankovic, and Petar Kokotovic. *Constructive Nonlinear Control*. Springer, 1997. doi:10.1007/978-1-4471-0967-9.

K. Thorsen, T. Drengstig, and P. Ruoff. Transepithelial glucose transport and Na+/K+ homeostasis in enterocytes: an integrative model. *AJP: Cell Physiology*, 307(4):C320–C337, 2014. ISSN 0363-6143. doi:10.1152/ajpcell.00068.2013. URL `http://ajpcell.physiology.org/content/307/4/C320`.

K. Thorsen, G. Risvoll, M. Mazumder, and D. R. McMillen. A controller for regulation of intracellular copper in S. cerevisiae. In *Poster presented at ICSB2016*, 2016a. doi:10.3252/pso.eu.17ICSB.2016. URL `http://www.postersessiononline.eu/pr/congreso.asp?cod=392299830`.

Kristian Thorsen, Geir B Risvoll, Daniel M Tveit, Peter Ruoff, and Tormod Drengstig. Tuning of Physiological Controller Motifs. In *2016 9th EUROSIM Congress on Modelling and Simulation*, pages 28–33, 2016b. ISBN 9781509041190. doi:10.1109/EUROSIM.2016.174.

John J. Tyson and Hans G. Othmer. The Dynamics of Feedback Control Circuits in Biochemical Pathways. In *Progress in Theoretical Biology Volume 5*, pages 1–62. Academic Press, 1978. ISBN 0-12-543105-8.

Paper 2:
Tuning of physiological controller motifs

Tuning of Physiological Controller Motifs

Kristian Thorsen[1] Geir B. Risvoll[1] Daniel M. Tveit[1] Peter Ruoff[2] Tormod Drengstig[1]

[1]Department of Electrical Engineering and Computer Science, University of Stavanger, Norway,
{kristian.thorsen, geir.risvoll, daniel.m.tveit, tormod.drengstig}@uis.no
[2]Center for Organelle Research, University of Stavanger, Norway, peter.ruoff@uis.no

Abstract

Genetic manipulation is increasingly used to fine tune organisms like bacteria and yeast for production of chemical compounds such as biofuels and pharmaceuticals. The process of creating the optimal organism is difficult as manipulation may destroy adaptation and compensation mechanisms that have been tuned by evolution to keep the organisms fit. The continued progress in synthetic biology depends on our ability to understand, manipulate, and tune these mechanisms. Concepts from control theory and control engineering are very applicable to these challenges. From a control theoretic viewpoint, *disturbances rejection* and *set point tracking* describe how adaptation mechanisms relate to perturbations and to signaling events. In this paper we investigate a set regulatory mechanisms in the form of biochemical reaction schemes, so-called controller motifs. We show how parameters related to the molecular and kinetic mechanisms influence on the dynamical behavior of disturbance rejection and set point tracking of each controller motif. This gives insight into how a molecular controller motif can be tuned to a specified regulatory response.

Keywords: bioengineering, biological systems, adaptation

1 Introduction

1.1 Homeostasis, Disturbance Rejection and Set Point Tracking

Homeostasis is described as the mechanism behind the observed adaptation of an organism in a changing environment (Cannon, 1929; Langley, 1973). From a control theoretic point of view homeostasis can be described by the properties of disturbance rejection and set point tracking.

A physiological example of disturbance rejection is the intravenous/oral glucose tolerance test (IVGTT/OGTT), where the blood glucose concentration is measured at regular intervals after injecting/eating large amounts of glucose (Ackerman et al., 1964). If the blood glucose level is above a predefined level after a certain amount of time, the patient is often diagnosed as diabetic (Ame, 2014). Over the last half century, such disturbance rejection studies are reported in a vast number of publications, see e.g. (Larsen et al., 2003; Steele, 1959), and also a large number of mathematical models are made with the aim to capture the glucose and insulin dynamics, see e.g. the comprehensive review of (Ajmera et al., 2013). Both OGTT and IVGTT represent an impulse (or short time pulse) disturbance perturbation, whereas the chronic infusion of glucose (Topp et al., 2004) represent a stepwise disturbance. Another physiological example of adaptation to a stepwise perturbation change is the adaptation of light sensitivity of the eye, which includes both a compensatory change in pupillary size and an adaptation of the photochemical system in the rods and cones (Guyton and Hall, 2006).

Physiological examples where set point tracking is investigated are relatively rare, although set point determining mechanisms with respect to body temperature and metabolism have beed discussed (Briese, 1998; St Clair Gibson et al., 2005).

Regulatory mechanisms can today be synthetically modified or added to make organism better suitable for a specific job. Still, engineering of biochemical networks has not yet achieved the status and robustness as engineering of electrical and mechanical systems (Ang et al., 2010). From a synthetic biology perspective (Ang and McMillen, 2013; Ang et al., 2013), it is thus of vital importance to have insight into the biochemical mechanisms behind physiological regulatory systems. One possible way to gain such insight is to analyze both the disturbance rejection and set point tracking dynamics of such systems *in vivo*, as well as doing *in silico* studies based on different model candidates. The latter approach is a well known technique used in control engineering. We will in this paper start with the simplest form of biochemical networks with regulatory function and identify by model analysis and simulation how the dynamic response of such networks can be tuned.

1.2 Controller Motifs

A biochemical network with regulatory properties must in its simplest form include at least two components, i.e., state variables, one controlled component and a controller component. The controller component acts on the controlled component in a way that compensates for external disturbances. We have earlier presented a collection of simple two-component regulatory networks (Drengstig et al., 2012; Thorsen et al., 2013), and we have used the name *controller motifs* to describe them. These motifs consist of two chemical species, A and E,

both of them being formed and turned over. A may represent an intracellular compound which is subject to disturbances in the form of e.g. uncontrolled diffusive transport of A in and out of the cell, and E may represent a membrane bound compound such as a transporter protein as shown in Figure 1. Like many cellular compounds which is subject to strict regulation (due to e.g. toxicity if present in large amount), the concentration of A should not exceed or be less than some limits. By connecting the compounds A and E through cellular signaling events such as activation and inhibition, species A becomes the controlled variable, while species E becomes the manipulated variable.

Based on the direction of the E-mediated flow, the motifs fall into two categories termed *inflow* and *outflow* controllers. The complete set of possible inflow and outflow controller motifs are shown in Figure 2, and the *steady state* properties of these controllers were presented in (Drengstig et al., 2012). Based on the *type* of E-mediated inflow or outflow, the controllers are further divided into *activating* (inflow 1/3 and outflow 5/7) or *inhibiting* (inflow 2/4 and outflow 6/8) controller type, indicated by grey and white background in Figure 2, respectively.

In the following we will show how the parameters of the controller motifs, i.e. rate constants, Michaelis-Menten constants, activation constants and inhibition constants, influence on the dynamic performance, and show how it is possible to adjust the system's response similar to the tuning of industrial control systems.

2 Results

2.1 Dynamic Properties of Controller Motifs

The dynamic properties of a two component biochemical system (second order system) can be described in terms of the undamped natural frequency ω_n and the damping ratio ζ. To illustrate how these two parameters relate to the regulatory mechanisms in Figure 2, we use outflow controller 5 as an example. For unique identification, we

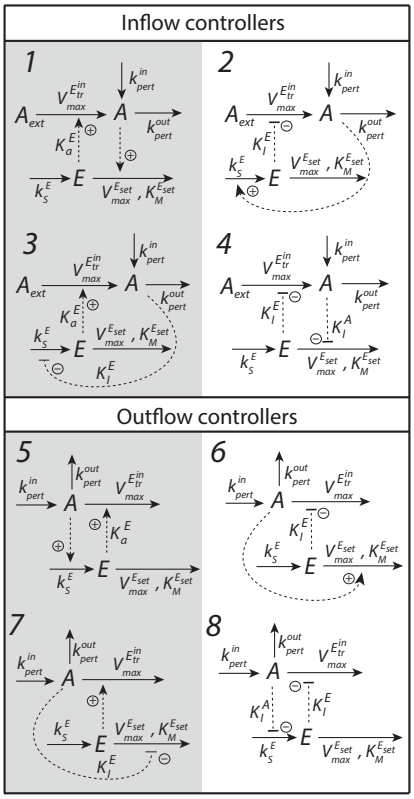

Figure 2. Set of two-component homeostatic controller motifs (Drengstig et al., 2012) classified as inflow and outflow controllers, where grey or white background indicate activating or inhibiting controller types, respectively.

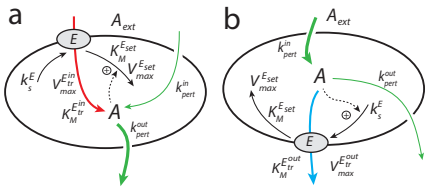

Figure 1. Illustration of a cell with a compound A being under homeostatic control by an inflow controller (panel a) or an outflow controller (panel b). Panel a: An inflow controller compensate for outflow perturbations, k^{out}_{pert} (thick green line), in A by adding more A through an E-mediated inflow (red line). Panel b: An outflow controller compensate for inflow perturbations, k^{in}_{pert} (thick green line), in A by removing excess of A through an E-mediated outflow (blue line).

apply subscript $_5$ on the appropriate parameters and variables, and hence, the nonlinear rate equations for an outflow controller 5 are given as (Drengstig et al., 2012):

$$\dot{A} = k^{in}_{pert} - k^{out}_{pert} \cdot A - V^{E_{tr},5}_{max} \cdot A \cdot \frac{E_5}{\left(K^{E_5}_a + E_5\right)} \tag{1}$$

$$\dot{E_5} = k^{E_5}_s \cdot A - \frac{V^{E_{set},5}_{max} \cdot E_5}{\left(K^{E_{set},5}_M + E_5\right)} \tag{2}$$

As discussed in (Drengstig et al., 2012), the set point $A^{out,5}_{set}$ is found by assuming ideal (theoretical) conditions, i.e. $K^{E_{set},5}_M = 0$ in (2), to give $A^{out,5}_{set} = \frac{V^{E_{set},5}_{max}}{k^{E_5}_s}$. Once the theoretical set point is established, we re-assume realistic conditions and reorganize (2) into the integral control law

equation $\dot{E}_5 = G_{i,5} \cdot (A_{set}^{out,5} - A_{meas})$. This allows us to identify the integral controller gain $G_{i,5}$ and the measurement signal A_{meas} as:

$$\dot{E}_5 = \underbrace{-k_s^{E_5} \cdot \frac{E_5}{K_M^{E_{set,5}} + E_5}}_{G_{i,5}} \cdot \left(\underbrace{\frac{V_{max}^{E_{set,5}}}{k_s^{E_5}}}_{A_{set}^{out,5}} - A \cdot \underbrace{\frac{K_M^{E_{set,5}} + E_5}{E_5}}_{A_{meas}} \right)$$

Note that the measurement signal A_{meas} actually includes information about the control signal E_5 which is not common in industrial control engineering. Note also that as long as $K_M^{E_{set,5}} > 0$, the actual value of A will be less than the theoretical set point $A_{set}^{out,5}$. Nevertheless, the set point tracking properties are good since the control error e, calculated as:

$$e = (A_{set}^{out,5} - A_{meas}) \tag{3}$$

is zero. The difference between the actual level of A and the theoretical set point A_{set} is termed *inaccuracy* (Thorsen, 2015). A general result valid for all controller motifs is that both rate constants for synthesis and degradation of E, i.e. k_s^E and $V_{max}^{E_{set}}$, are a part of the set point A_{set} (Drengstig et al., 2012). At the same time, one of these rate constants is also a part of the integral controller gain G_i.

In order to identify the parameters $\omega_{n,5}$ and ζ_5, we once again assume ideal conditions, i.e. $K_M^{E_{set,5}} = 0$, and continue by linearizing the model in (1) and (2) around an arbitrary working point A_{ss} and $E_{5,ss}$. Since the set point consist of two individual parameters, i.e. k_s^E and $V_{max}^{E_{set}}$, we select $V_{max}^{E_{set}}$ to be our input. We then find the closed looped transfer function from the Laplace transformed input $\Delta V_{max}^{E_{set,5}}(s)$ to the Laplace transformed output $\Delta A(s)$ as:

$$M(s) = \frac{\frac{\left(\left(k_{pert}^{out} + V_{max}^{E_{tr,5}} \right) \cdot V_{max}^{E_{set,5}} - k_{pert}^{in} \cdot k_s^{E_5} \right)^2}{V_{max}^{E_{set,5}} \cdot K_a^{E_5} \cdot V_{max}^{E_{tr,5}} \cdot k_s^{E_5}}}{s^2 + \frac{k_{pert}^{in} \cdot k_s^{E_5}}{V_{max}^{E_{set,5}}} \cdot s + \frac{\left(\left(k_{pert}^{out} + V_{max}^{E_{tr,5}} \right) \cdot V_{max}^{E_{set,5}} - k_{pert}^{in} \cdot k_s^{E_5} \right)^2}{V_{max}^{E_{set,5}} \cdot K_a^{E_5} \cdot V_{max}^{E_{tr,5}}}}$$

Using that $V_{max}^{E_{set,5}} = k_s^{E_5} \cdot A_{set}^{out,5}$, we find $\omega_{n,5}$ and ζ_5 as:

$$\omega_{n,5} = \frac{\sqrt{k_s^{E_5}} \cdot \left(\left(k_{pert}^{out} + V_{max}^{E_{tr,5}} \right) \cdot A_{set}^{out,5} - k_{pert}^{in} \right)}{\sqrt{K_a^{E_5} \cdot V_{max}^{E_{tr,5}} \cdot A_{set}^{out,5}}} \tag{4}$$

$$\zeta_5 = \frac{k_{pert}^{in} \sqrt{K_a^{E_5} \cdot V_{max}^{E_{tr,5}}}}{2 \cdot \sqrt{V_{max}^{E_{set,5}}} \cdot \left(\left(k_{pert}^{out} + V_{max}^{E_{tr,5}} \right) \cdot A_{set}^{out,5} - k_{pert}^{in} \right)} \tag{5}$$

From (4) and (5) we see that, depending on the perturbation levels (inflow versus outflow perturbations), it is possible to obtain negative values for $\omega_{n,5}$ and ζ_5. These negative values correspond to circumstances where the perturbation levels are such that the controller breaks down (Drengstig et al., 2012). Breakdown occurs when the net inflow perturbation is larger than the capacity of the outflow controller, i.e., greater than the maximum of the compensatory flow. In this case there is no stable equilibrium in the system and A integrates towards infinity. Such a state is unwanted and may very likely be toxic for the cell. In this case the values of $\omega_{n,5}$ and ζ_5 are invalid and have no physical meaning. Table 1 gives a summary of ω_n and ζ for the four inflow and four outflow controllers, together with the expression for each set point A_{set}.

Note that there is a close relationship between the expressions for ζ and ω_n for each controller, and thus, it is not possible to specify *both* ζ and ω_n independently.

Since controller 5 is an outflow controller, the inflow perturbation $\Delta k_{pert}^{in}(s)$ is considered the main disturbance, and the transfer function characterizing the disturbance rejection properties is:

$$N(s) = \frac{s}{s^2 + \frac{k_{pert}^{in} \cdot k_s^{E_5}}{V_{max}^{E_{set,5}}} \cdot s + \frac{\left(\left(k_{pert}^{out} + V_{max}^{E_{tr,5}} \right) \cdot V_{max}^{E_{set,5}} - k_{pert}^{in} \cdot k_s^{E_5} \right)^2}{V_{max}^{E_{set,5}} \cdot K_a^{E_5} \cdot V_{max}^{E_{tr,5}}}}$$

As expected, this transfer function has a zero in the origin, implicating homeostatic behavior and perfect adaptation (Drengstig et al., 2008).

2.2 Tuning of Individual Controllers

As shown in (Drengstig et al., 2012), the *steady state* performance of the individual controllers were found to be identical, given a certain set of parameter values. A related issue is to determine whether it is possible to tune the controllers to obtain identical *dynamical* performance using the theoretical design parameters in Table 1. Such tuning will be useful in synthetic biology. Also on a more fundamental level, if such tuning is possible it implies that it is impossible to infer the underlining network structure, i.e., the particular controller motif, responsible for an observed adaptive process by measuring the dynamical properties of the controlled variable alone.

We have selected to use the rate constants of the synthesis and degradation of the controller species, k_s^E and $V_{max}^{E_{set}}$, together with the rate constant of the E-mediated compensatory flow $V_{max}^{E_{tr}}$, as our tunable parameters. These parameters are relatively easy to tune from the perspective of synthetic biology and offer a greater tunable range than the parameters associated with the nonlinearities in the model (K_a^E, K_I^A, and K_I^E). To discuss one of the tunable parameters, the rate constant for synthesis of E, k_s^E, can in practice be modified by altering the promoter of the gene coding for E. One way to do this is a fixed tuning of the promoter itself, e.g. the *Cu*-dependent promoter of the CUP1-gene of *Saccharomyces Cerevisiae* can be modified by mutations to show wide range of different induction ratios (Thiele and Hamer, 1986). Another option is to use a dual mode promoter, a type of promoter who's regulation

Table 1. The set point A_{set}, natural undamped frequency ω_n and damping ratio ζ for controller motifs 1-8 in Figure 2 under theoretical conditions, i.e. $K_M^{E_{set}}$=0. For each controller we have added a subscript to the parameters for unique identification.

$A_{set}^{in,1}=\frac{k_s^{E_1}}{V_{max}^{E_{set,1}}}$	$\omega_{n,1}=\frac{\sqrt{V_{max}^{E_{set,1}}\left(k_{pert}^{in}-k_{pert}^{out}A_{set}^{in,1}+V_{max}^{E_{tr,1}}A_{ext}\right)}}{\sqrt{K_a^{E_1}V_{max}^{E_{tr,1}}A_{ext}}}$	$\zeta_1=\frac{k_{pert}^{out}\sqrt{K_a^{E_1}V_{max}^{E_{tr,1}}A_{ext}}}{2\sqrt{V_{max}^{E_{set,1}}\left(k_{pert}^{in}-k_{pert}^{out}A_{set}^{in,1}+V_{max}^{E_{tr,1}}A_{ext}\right)}}$
$A_{set}^{in,2}=\frac{V_{max}^{E_{set,2}}}{k_s^{E_2}}$	$\omega_{n,2}=\frac{\sqrt{k_s^{E_2}}\left(k_{pert}^{out}A_{set}^{in,2}-k_{pert}^{in}\right)}{\sqrt{K_I^{E_2}V_{max}^{E_{tr,2}}A_{ext}}}$	$\zeta_2=\frac{k_{pert}^{out}\sqrt{K_I^{E_2}V_{max}^{E_{tr,2}}A_{ext}}}{2\sqrt{k_s^{E_2}}\left(k_{pert}^{out}A_{set}^{in,2}-k_{pert}^{in}\right)}$
$A_{set}^{in,3}=\frac{k_s^{E_3}K_I^A}{V_{max}^{E_{set,3}}}-K_I^A$	$\omega_{n,3}=\frac{\sqrt{V_{max}^{E_{set,3}}\left(k_{pert}^{in}-k_{pert}^{out}A_{set}^{in,3}+V_{max}^{E_{tr,3}}A_{ext}\right)}}{\sqrt{\left(K_I^A+A_{set}^{in,3}\right)V_{max}^{E_{tr,3}}K_a^{E_3}A_{ext}}}$	$\zeta_4=\frac{k_{pert}^{out}\sqrt{\left(K_I^A+A_{set}^{in,4}\right)V_{max}^{E_{tr,4}}K_I^{E_4}A_{ext}}}{2\sqrt{k_s^{E_4}}\left(k_{pert}^{out}A_{set}^{in,4}-k_{pert}^{in}\right)}$
$A_{set}^{in,4}=\frac{V_{max}^{E_{set,4}}K_I^A}{k_s^{E_4}}-K_I^A$	$\omega_{n,4}=\frac{\sqrt{k_s^{E_4}\left(k_{pert}^{out}A_{set}^{in,4}-k_{pert}^{in}\right)}}{\sqrt{\left(K_I^A+A_{set}^{in,4}\right)V_{max}^{E_{tr,4}}K_I^{E_4}A_{ext}}}$	$\zeta_3=\frac{k_{pert}^{out}\sqrt{\left(K_I^A+A_{set}^{in,3}\right)V_{max}^{E_{tr,3}}K_a^{E_3}A_{ext}}}{2\sqrt{V_{max}^{E_{set,3}}}\left(k_{pert}^{in}-k_{pert}^{out}A_{set}^{in,3}+V_{max}^{E_{tr,3}}A_{ext}\right)}$
$A_{set}^{out,5}=\frac{V_{max}^{E_{set,5}}}{k_s^{E_5}}$	$\omega_{n,5}=\frac{\sqrt{k_s^{E_5}}\left(\left(k_{pert}^{out}+V_{max}^{E_{tr,5}}\right)A_{set}^{out,5}-k_{pert}^{in}\right)}{\sqrt{K_a^{E_5}V_{max}^{E_{tr,5}}A_{set}^{out,5}}}$	$\zeta_5=\frac{k_{pert}^{in}\sqrt{K_a^{E_5}V_{max}^{E_{tr,5}}}}{2\sqrt{V_{max}^{E_{set,5}}}\left(\left(k_{pert}^{out}+V_{max}^{E_{tr,5}}\right)A_{set}^{out,5}-k_{pert}^{in}\right)}$
$A_{set}^{out,6}=\frac{k_s^{E_6}}{V_{max}^{E_{set,6}}}$	$\omega_{n,6}=\frac{\sqrt{V_{max}^{E_{set,6}}}\left(k_{pert}^{in}-k_{pert}^{out}A_{set}^{out,6}\right)}{\sqrt{K_I^{E_6}V_{max}^{E_{tr,6}}A_{set}^{out,6}}}$	$\zeta_6=\frac{k_{pert}^{in}\sqrt{K_I^{E_6}V_{max}^{E_{tr,6}}}}{2\sqrt{k_s^{E_6}}\left(k_{pert}^{in}-k_{pert}^{out}A_{set}^{out,6}\right)}$
$A_{set}^{out,7}=\frac{V_{max}^{E_{set,7}}K_I^A}{k_s^{E_7}}-K_I^A$	$\omega_{n,7}=\frac{\sqrt{k_s^{E_7}}\left(\left(k_{pert}^{out}+V_{max}^{E_{tr,7}}\right)A_{set}^{out,7}-k_{pert}^{in}\right)}{\sqrt{\left(A_{set}^{out,7}+K_I^A\right)V_{max}^{E_{tr,7}}K_a^{E_7}A_{set}^{out,7}}}$	$\zeta_7=\frac{k_{pert}^{in}\sqrt{\left(A_{set}^{out,7}+K_I^A\right)V_{max}^{E_{tr,7}}K_a^{E_7}}}{2\sqrt{k_s^{E_7}A_{set}^{out,7}}\left(\left(k_{pert}^{out}+V_{max}^{E_{tr,7}}\right)A_{set}^{out,7}-k_{pert}^{in}\right)}$
$A_{set}^{out,8}=\frac{k_s^{E_8}K_I^A}{V_{max}^{E_{set,8}}}-K_I^A$	$\omega_{n,8}=\frac{\sqrt{V_{max}^{E_{set,8}}}\left(k_{pert}^{in}-k_{pert}^{out}A_{set}^{out,8}\right)}{\sqrt{\left(A_{set}^{out,8}+K_I^A\right)V_{max}^{E_{tr,8}}K_I^{E_8}A_{set}^{out,8}}}$	$\zeta_8=\frac{k_{pert}^{in}\sqrt{\left(A_{set}^{out,8}+K_I^A\right)V_{max}^{E_{tr,8}}K_I^{E_8}}}{2\sqrt{V_{max}^{E_{set,8}}A_{set}^{out,8}}\left(k_{pert}^{in}-k_{pert}^{out}A_{set}^{out,8}\right)}$

of protein production depends on two activators. One activator would be the control variable A and another would be a chemical compound that can be meticulously added to the growth medium to achieve a certain level of gene transcription and production of E, represented in the model as the value of k_s^E. One such promoter controlled by Testosterone and IPTG (isopropyl β-D-1-thiogalactopyranoside) has recently been developed (Mazumder and McMillen, 2014).

In order to best tune the parameters we have to know about the operational limits of the system. For this purpose, we define as in (Drengstig et al., 2012) an upper limit for the maximum compensatory flux, $j_{A,max}$=10, corresponding to a maximum level of E_{max}=15 for the activating controllers 1, 3, 5 and 7, and corresponding to E_{min}=0 for the inhibiting controllers 2, 4, 6 and 8. We assume further that the set point of A is A_{set}=1.0, the external concentration is A_{ext}=2. The kinetic constants for activation and inhibition are chosen to avoid saturation effects: K_a^E=2, K_I^A=0.1 and K_I^E=1.0. Moreover, the working point of perturbations is specified as $k_{pert}^{in}=2/k_{pert}^{out}=5$ for inflow controllers and $k_{pert}^{in}=5/k_{pert}^{out}=2$ for outflow controllers. Given these overall system parameters, the tuning procedure of each individual controller motif is based on specifying ζ (or ω_n, but not both) in a similar way as the pole placement method, and determine the last three parameter values of each motif, i.e. $V_{max}^{E_{tr}}$, $V_{max}^{E_{set}}$ and k_s^E.

To illustrate, we specify *two* different dynamical responses in the concentration of A for a step in A_{set}, i.e. one critically damped (ζ=1) and one underdamped (ζ=0.2 corresponding to 50% overshoot) response. A strongly underdamped system overshoots when adapting a change in set point, but shows considerably better disturbance rejection than a critically damped system. Thus, tuning for the latter may be of interest in many biological systems.

We illustrate the procedure in detail by continuing on the outflow controller 5 example, and start by considering the rate expression for the compensatory flux, j_A, from (1):

$$j_A=V_{max}^{E_{tr,5}}\cdot A\cdot\frac{E_5}{\left(K_a^{E_5}+E_5\right)} \tag{6}$$

By setting $j_A=j_{A,max}$=10 and inserting $E_5=E_{5,max}$=15, $A=A_{set}^{out,5}$=1 and $K_a^{E_5}$=2 into (6), gives $V_{max}^{E_{tr,5}}$=11.33. Using the mathematical expressions for $A_{set}^{out,5}$ and ζ_5 tabulated in Table 1, we find $V_{max}^{E_{set,5}}$=2.04 and $k_s^{E_5}$=2.04 for

ζ_5=1 and $V_{max}^{E_{set},5}$=51.0 and $k_s^{E_5}$=51.0 for ζ_5=0.2, see Table 2.

Table 2. The parameters $V_{max}^{E_{tr}}$, $V_{max}^{E_{set}}$, k_s^E and the integral controller gain G_i (in grey) for each controller motif specified for critical damped response ζ=1 and underdamped response ζ=0.2. The other parameters are defined in the main text.

		$V_{max}^{E_{tr}}$	$V_{max}^{E_{set}}$	k_s^E	G_i
Critically damped, ζ=1	Inflow 1	5.67	2.04	2.04	2.04
	Inflow 2	5.00	6.94	6.94	-6.94
	Inflow 3	5.67	2.24	24.68	2.04
	Inflow 4	5.00	84.03	7.64	-6.94
Under-damped, ζ=0.2	Inflow 1	5.67	51.0	51.0	51.0
	Inflow 2	5.00	173.6	173.6	-173.6
	Inflow 3	5.67	56.1	617.1	51.0
	Inflow 4	5.00	2100.7	191.0	-173.6
Critically damped, ζ=1	Outflow 5	11.33	2.04	2.04	-2.04
	Outflow 6	10.00	6.94	6.94	6.94
	Outflow 7	11.33	24.68	2.24	-2.04
	Outflow 8	10.00	7.64	84.03	6.94
Under-damped, ζ=0.2	Outflow 5	11.33	51.0	51.0	-51.0
	Outflow 6	10.00	173.6	173.6	173.6
	Outflow 7	11.33	617.1	56.1	-51.0
	Outflow 8	10.00	191.0	2100.7	173.6

This corresponds to an integral controller gain of $G_{i,5}$=−2.04 and $G_{i,5}$=−51.0, respectively, and a response time of T_r≈0.8 seconds ($\omega_{n,5}$=2.5) and T_r≈0.1 seconds ($\omega_{n,5}$=12.5). The simulation results shown as black curves in panels **c**, and **d** in Figure 3, verify the tuning specifications, both with respect to overshoot and response time.

In order to compare the individual performance of each controller, the above described tuning specifications are applied for all controllers, and the results are shown in Table 2 and verified by simulation in Figure 3.

Note the identical values for G_i (greyed out in Table 2) for all the activating (inflow 1/3 and outflow 5/7) and all the inhibiting (inflow 2/4 and outflow 6/8) controllers, respectively. Note also the opposite signs for activating and inhibiting inflow and outflow controllers, respectively, which is due to the combination of controller type (*activating/inhibiting*) and controller configuration (*inflow/outflow*).

The responses in Figure 3 clusters into two groups, where the first group is the E-activating inflow controllers 1/3 (black and red curves in Figures 3**a** and 3**b**) and the E-inhibiting outflow controllers 6/8 (blue and green curves in Figures 3**c** and 3**d**). The second group is the E-inhibiting inflow controllers 2/4 (blue and green curves in Figures 3**a** and 3**b**) and the E-activating outflow controllers 5/7 (black and red curves in Figures 3**c** and 3**d**). The reason why equally tuned controllers behaves slightly different is due to the nonlinearity of each individual controller combined with a relative large set point step change.

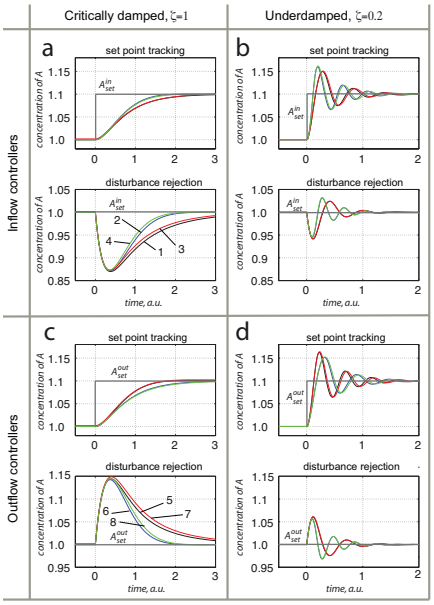

Figure 3. Dynamic properties of inflow and outflow controllers showing the response in concentration of species A. The color codes for the different inflow controller are: 1=black, 2=blue, 3=red and 4=green, and the color codes for the different outflow controllers are: 5=black, 6=blue, 7=red and 8=green. For the *set point tracking* curves, the set point changes from A_{set}=1.0 to A_{set}=1.1 at t=0. For the *disturbance rejection* curves, the disturbance is a unit step change from 5 to 6 at t=0 in k_{pert}^{out} for inflow controllers and in k_{pert}^{in} for outflow controllers. Panels **a** and **b**: Set point tracking (upper) and disturbance rejection (lower) responses for inflow controllers tuned for critically damped (ζ=1) and underdamped (ζ=0.2) responses, using the parameters shown in Table 2. Panels **c** and **d**: Set point tracking (upper) and disturbance rejection (lower) responses for outflow controllers tuned for critically damped (ζ=1) and underdamped (ζ=0.2) responses, using the parameters shown in Table 2.

From Table 1 we see that the inflow and outflow perturbations come into the expressions of ω_n and ζ in different ways. To visualize the effect of varying level of perturbation, Figure 4 shows dynamic responses of inflow controller 3 for k_{pert}^{out}={3,5,7} (Figure 4**a**) and outflow controller 6 for k_{pert}^{in}={5,7,9} (Figure 4**b**). The effect of increased k_{pert}^{out} for inflow controller 3 is slower dynamics with less damped response. On the other hand, outflow controller 6 shows faster dynamics together with more underdamped response at increased k_{pert}^{in} levels.

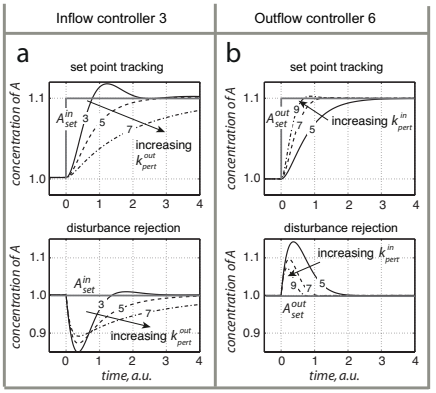

Figure 4. Set point tracking (upper) and disturbance rejection dynamics (lower) of species A using inflow controller 3 (panel **a**) and outflow controller 6 (panel **b**) at different level of outflow and inflow perturbations, respectively. The set point change is a step from A_{set}=1.0 to A_{set}=1.1 at t=0 and the disturbance is a step increase of 1 from original value at t=0. In panel **a** the labeling on the curves corresponds to outflow perturbations of $k^{out}_{pert} \in \{3,5,7\}$. In panel **b** the labeling on the curves corresponds to inflow perturbation of $k^{in}_{pert} \in \{5,7,9\}$.

3 Conclusions

We have shown how a set of homeostatic controller motifs can be tuned, in a similar way as in industrial control systems, to exhibit a specified dynamic response with respect to overshoot δ and response time T_r. We have also shown analytically and through simulations how *i*) the level of inflow/outflow disturbances and *ii*) the values of different rate constants influence on the set point tracking properties. The corresponding disturbance rejection properties is also studied through simulations using a unit step input signal in the disturbance.

An important implication of the fact that all controller motifs can show identical dynamic responses is that one cannot postulate a specific controller motif based on measurement of disturbance rejection and/or set point tracking alone. The motif type, i.e. inflow or outflow, activating or inhibiting, rest on how the molecular mechanisms behind the controller interact and not on the system's ability to show a specific response. The specific response of physiological regulatory system is a result of tuning the system's kinetic parameters and the strength of the perturbation.

There is a great effort going on in both academia and industry to genetically manipulate organisms to produce useful bioproducts. One of the landmark studies published in Science last year was the implementation of the complete biosynthesis of opioids in yeast (Galanie et al., 2015; Service, 2015). Opioids like morphine are the primary drugs used for treatment of severe pain and pain management, and production depends on the cultivation of opium poppies. While the implementation of opioid biosynthesis in yeast is a tremendous achievement, it still requires an improvement in overall yield by a factor of $7 \cdot 10^6$ to compete with poppies (Galanie et al., 2015). Great improvements are expected (Galanie et al., 2015), but this will require an intricate tuning of the different parts of the biosynthesis pathway.

From a synthetic biology point of view, the work in this paper creates a basis one can use to identify which and how properties of a reaction and participating proteins/enzymes contributes to the dynamical response. For instance, the natural undamped frequency ω_n, which is important for the swiftness of a controller motif, will for outflow controller 5 increase if we by some means manage to increase the production of E (increase k^E_s) by e.g. increasing the expression of mRNA coding for E (as shown in Table 1, a change in k^E_s will also change the set point). A related example of such is reported in (Ang et al., 2010), where a two promotor network system is constructed *in silico* from realizable parts within the bacterium *Escherichia coli*. The network includes both basal rates and activated/repressed regulatory inputs, and hence, the network share similarities with inflow controller 2 in Figure 2. Two requirements were used as tuning criteria for the network, i.e. ζ=1 (critically damped) and large ω_n indicating a response time T_r as short as possible. In order to obtain the necessary approximate zero order degradation of the repressor R (corresponding to our species E), two effectors I_1 and I_2 are included in order to force the repressor to work at saturated conditions, i.e. corresponding to the theoretical conditions, $K^{E_{set}}_M$=0, used in this paper.

An alternative approach to tuning is given in (Ang et al., 2013), where the tuning is related to the so-called *response curves*. These are steady state relationships between an input and an output variable, e.g. the molecular concentration of a transcription factor protein and the expressed protein, respectively, and not time dependent tuning as discussed in this paper. However, variations in kinetic parameter values results in different steady state relationships.

References

E. Ackerman, J.W. Rosevear, and W.F. McGuckin. A Mathematical Model of the Glucose-tolerance test. *Physics in Medicine and Biology*, 9(2):203–213, 1964.

I. Ajmera, M. Swat, C. Laibe, N. Le Novère, and V. Chelliah. The impact of mathematical modeling on the understanding of diabetes and related complications. *CPT: Pharmacometrics & Systems Pharmacology*, 2 (7):14, 2013.

Standards of Medical Care in Diabetes–2014. American Diabetes Association, 2014. *Diabetes Care* 37:S14–S80.

J. Ang and D.R. McMillen. Physical Constraints on Biological Integral Control Design for Homeostasis and

Sensory Adaptation. *Biophysical Journal*, 104(2):505–515, 2013.

J. Ang, S. Bagh, B.P. Ingalls, and D.R. McMillen. Considerations for using integral feedback control to construct a perfectly adapting synthetic gene network. *Journal of Theoretical Biology*, 266(4):723–738, 2010.

J. Ang, E. Harris, B.J. Hussey, R. Kil, and D.R. McMillen. Tuning Response Curves for Synthetic Biology. *ACS Synthetic Biology*, 2(10):547–567, 2013.

E. Briese. Normal body temperature of rats: the setpoint controversy. *Neuroscience & Biobehavioral Reviews*, 22(3):427–436, 1998.

W.B. Cannon. Organization for physiological homeostasis. *Physiological reviews*, IX:399–431, 1929.

T. Drengstig, I.W. Jolma, X.Y. Ni, K. Thorsen, X.M. Xu, and P. Ruoff. A Basic Set of Homeostatic Controller Motifs. *Biophysical Journal*, 103:2000–2010, 2012.

T. Drengstig, H.R. Ueda, and P. Ruoff. Predicting Perfect Adaptation Motifs in Reaction Kinetic Networks. *Journal of Physical Chemistry B*, 112(51):16752–16758, 2008.

S. Galanie, K. Thodey, I.J. Trenchard, M.F. Interrante, and C.D. Smolke. Complete biosynthesis of opioids in yeast. *Science*, 349(6252):1095–1100, 2015.

A.C. Guyton and J.E. Hall. *Textbook of Medical Physiology*. Elsevier Saunders, Philadelphia, PA, USA, 11 edition, 2006.

L.L. Langley. *Homeostasis: Origins of the concept*. John Wiley & Sons, 1973.

M.O. Larsen, B. Rolin, M. Wilken, R.D. Carr, and C.F. Gotfredsen. Measurements of insulin secretory capacity and glucose tolerance to predict pancreatic β-cell mass in vivo in the nicotinamide/streptozotocin Göttingen minipig, a model of moderate insulin deficiency and diabetes. *Diabetes*, 52:118–123, 2003.

M. Mazumder and D.R. McMillen. Design and characterization of a dual-mode promoter with activation and repression capability for tuning gene expression in yeast. *Nucleic Acids Research*, 42(14):9514–9522, 2014.

R.F. Service. Modified yeast produce opiates from sugar. *Science*, 349(6249):677–677, 2015.

A. St Clair Gibson, J.H. Goedecke, Y.X. Harley, L.J. Myers, M.I. Lambert, T.D. Noakes, and E.V. Lambert. Metabolic setpoint control mechanisms in different physiological systems at rest and during exercise. *Journal of Theoretical Biology*, 236:60–72, 2005.

R. Steele. Influences of glucose loading and of injected insulin on hepatic glucose output. *Annals of the New York Academy of Sciences*, 82:420–430, 1959.

D.J. Thiele and D.H. Hamer. Tandemly duplicated upstream control sequences mediate copper-induced transcription of the Saccharomyces cerevisiae copper-metallothionein gene. *Molecular and Cellular Biology*, 6(4):1158–1163, 1986.

K. Thorsen. *Controller Motifs for Homeostatic Regulation and Their Applications in Biological Systems*. PhD thesis, University of Stavanger, 2015.

K. Thorsen, P. Ruoff, and T. Drengstig. Control theoretic properties of physiological controller motifs. In *2013 International Conference on System Science and Engineering (ICSSE)*, pages 165–170. IEEE, 2013.

B.G. Topp, M.D. McArthur, and D.T. Finegood. Metabolic adaptations to chronic glucose infusion in rats. *Diabetologia*, 47(9):1602–1610, 2004.

Paper 3:
Homeostatic controllers compensating for growth and perturbations

PLOS ONE

RESEARCH ARTICLE

Homeostatic controllers compensating for growth and perturbations

Peter Ruoff[1]*, **Oleg Agafonov**[1☯¤], **Daniel M. Tveit**[2☯], **Kristian Thorsen**[2], **Tormod Drengstig**[2]

1 Centre for Organelle Research, University of Stavanger, Stavanger, Norway, **2** Department of Electrical Engineering and Computer Science, University of Stavanger, Stavanger, Norway

☯ These authors contributed equally to this work.
¤ Current address: Institute of Cancer Research, Oslo University Hospital, Oslo, Norway
* peter.ruoff@uis.no

Citation: Ruoff P, Agafonov O, Tveit DM, Thorsen K, Drengstig T (2019) Homeostatic controllers compensating for growth and perturbations. PLoS ONE 14(8): e0207831. https://doi.org/10.1371/journal.pone.0207831

Editor: Suzanne Touzeau, INRA, FRANCE

Received: November 1, 2018

Accepted: July 24, 2019

Published: August 12, 2019

Data Availability Statement: All relevant data are within the paper and its Supporting Information files.

Funding: This research was financed in part by Program Area Funds from the University of Stavanger to PR and TD. There was no additional external funding received for this study. The University of Stavanger (funder) had no role in study design, data collection and analysis, decision to publish, or preparation of the manuscript.

Competing interests: The authors have declared that no competing interests exist.

Abstract

Cells and organisms have developed homeostatic mechanisms which protect them against a changing environment. How growth and homeostasis interact is still not well understood, but of increasing interest to the molecular and synthetic biology community to recognize and design control circuits which can oppose the diluting effects of cell growth. In this paper we describe the performance of selected negative feedback controllers in response to different applied growth laws and time dependent outflow perturbations of a controlled variable. The approach taken here is based on deterministic mass action kinetics assuming that cell content is instantaneously mixed. All controllers behave ideal in the sense that they for step-wise perturbations in volume and a controlled compound *A* are able to drive *A* precisely back to the controllers' theoretical set-points. The applied growth kinetics reflect experimentally observed growth laws, which range from surface to volume ratio growth to linear and exponential growth. Our results show that the kinetic implementation of integral control and the structure of the negative feedback loop are two properties which affect controller performance. Best performance is observed for controllers based on derepression kinetics and controllers with an autocatalytic implementation of integral control. Both are able to defend exponential growth and perturbations, although the autocatalytic controller shows an offset from its theoretical set-point. Controllers with activating signaling using zero-order or bimolecular (antithetic) kinetics for integral control behave very similar but less well. Their performance can be improved by implementing negative feedback structures having repression/derepression steps or by increasing controller aggressiveness. Our results provide a guide what type of feedback structures and integral control kinetics are suitable to oppose the dilution effects by different growth laws and time dependent perturbations on a deterministic level.

Introduction

The term *homeostasis* was defined by Walter B. Cannon [1] to describe the coordinated ability of organisms and cells to maintain an internal stability by keeping concentrations of cellular components within certain tolerable limits [2]. Cannon's emphasis on *homeo* indicates that he considered the internal physiological state not as a constant, as suggested earlier by Bernard's concept of a fixed "milieu intérieur" [2, 3], but conceives homeostasis as a dynamic adaptable system which allows variations within certain limits. Dependent on the controlled components, the homeostatic limits in which one or several controllers operate can vary considerably. For example, while the negative feedback regulation of cellular sodium shows an apparently changing and less well-defined set-point [4, 5], the regulation of other metal ions have more strict limits [6–8].

Growth, an essential aspect of all living beings is a highly regulated process. According to Bertalanffy [9, 10], the different observed growth kinetics of organisms can be related to the organisms' metabolism. For example, when respiration is proportional to the surface of the organism linear growth kinetics are obtained. On the other hand, if respiration is proportional to the organism's weight/volume, exponential growth occurs. Growth kinetics of bacteria [11, 12] appear closely related to the bacterial form or shape. Rod-shaped bacteria show exponential growth rates, i.e.

$$\dot{V} = \kappa V; \;\; \kappa > 0 \tag{1}$$

whereas spherical bacteria increase their cellular volume by a rate law related to the surface to volume ratio, i.e.,

$$\dot{V} = \eta \cdot V^{\frac{2}{3}} - \xi \cdot V \tag{2}$$

where η and ξ are constants reflecting anabolism and catabolism, respectively [13].

Although the protective functions of homeostasis need to be in place during growth, the interacting mechanisms between homeostasis and growth are not well understood. In principle, there are two aspects of growth to consider. The first one, which is focused on in this paper is how homeostatic mechanisms can compensate for growth without affecting it. The second aspect, which will be treated in another paper, is how homeostatic mechanisms can influence growth. In this paper we consider growth as an increase of the cellular volume. As a continuous process growth represents a time-dependent perturbation which would lead to the dilution of cellular/cytosolic compounds unless other mechanisms counteract for it.

Integral control is a concept from control engineering [14], which enables robust regulation for step-wise perturbations and has been implicated to occur in a variety of homeostatic regulated systems [5, 15–17]. How different integral controllers will perform under (nonlinear) time-dependent growth is little investigated. Based on a previous study [18] we have chosen four controller motifs, which are shown in Fig 1. The most promising controllers which are able to handle nonlinear time dependent growth are a motif 2 zero-order type of controller based on derepression and a motif 1 first-order controller based on autocatalysis [19–21]. A relatively new discovered integral feedback mechanism, the so-called antithetic motif [22], has also been included. For comparison, we have also included a motif 1 zero-order type of controller. The controllers were investigated with respect to their capabilities to compensate for time-dependent outflow perturbations in A and in the presence of different growth laws (increase in the reaction volume V) according to Bertalanffy's classifications [9, 10]. The growth kinetics that will be considered include linear (constant) as well as saturating and exponential growth laws. We focus here primarily on outflow perturbations, because together with

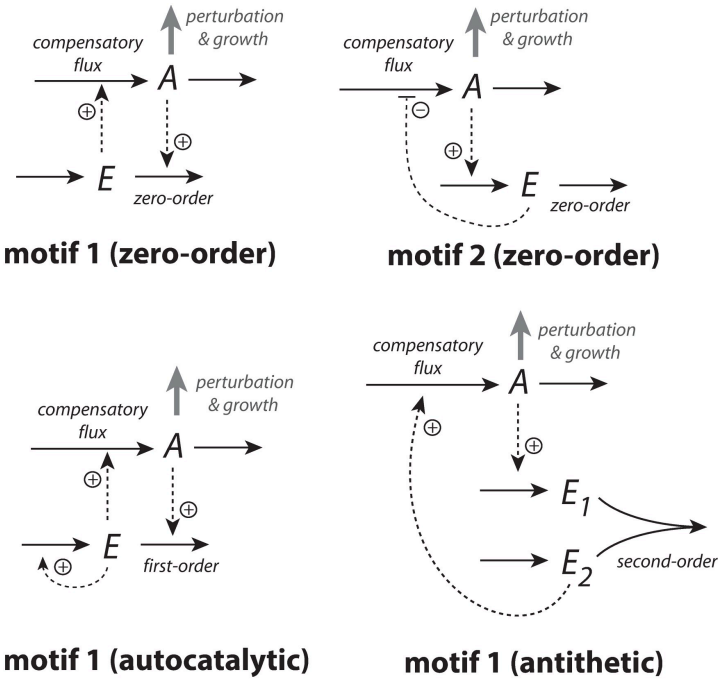

Fig 1. The controllers investigated in this study. Reaction orders are with respect to E. The reaction between E_1 and E_2 in the antithetic controller is an overall second-order process. The controllers behave ideal in the sense that they for step-wise changes in A and/or V, are able to keep A precisely at their defined theoretical set-points A_{set}^{theor}.

https://doi.org/10.1371/journal.pone.0207831.g001

the diluting effects of the different growth laws these perturbations represent the most severe conditions for testing the controllers.

Materials and methods

To arrive at controller candidates which can oppose various dilution and perturbation kinetics a couple of simplifications have been made, which are discussed in more detail below. One is the assumption that compounds in a growing cells undergo instantaneous and ideal mixing, thereby ignoring the spatial organization of the cell. In addition, we ignore stochastic effects due to diffusion or low molecule numbers (however, see Discussion). Deterministic computations were performed by using the Fortran subroutine LSODE [23]. Plots were generated with gnuplot (www.gnuplot.info) and Adobe Illustrator (adobe.com). To make notations simpler, concentrations of compounds are denoted by compound names without square brackets. Time derivatives are generally indicated by the 'dot' notation. Concentrations and rate

parameter values are given in arbitrary units (au). Rate parameters are presented as k_i's (i = 1, 2, 3, . . .) irrespective of their kinetic nature, i.e. whether they represent turnover numbers, Michaelis constants, or inhibition constants. A set of MATLAB (mathworks.com) calculations with instructions are provided in the Supporting Information as a combined zip-file (S1 Matlab).

Overview of treated cases and analytical steady state expressions

The four controller motifs are studied for internal and transporter-based compensatory fluxes, different growth laws, and different removal kinetics of the controlled variable A. In the following we give a brief summary how the paper is structured and under what conditions the four motifs are tested. The paper divides into the following major parts.

In chapter "Reaction kinetics during volume changes" the rate equations during volume changes are derived.

The results are divided into two major cases:

In Case A: "Controllers with transporter-based compensatory fluxes" the behaviors of the four negative feedback motifs are shown when the compensatory fluxes are transporter based and when systems are exposed to linear and exponential growth with corresponding removal kinetics in A during growth. The transporter-based compensatory fluxes consist of an (by controller molecule E activated or derepressed) zero-order inflow of A molecules with respect to the transporter, $\dot{n}_A$, which for each time point is divided by the volume to get the contribution to the concentration of A due to the inflow.

In Case B: "Controllers with cell-internal compensatory fluxes" results are described when the compensatory fluxes are generated cell-internally and when the systems are exposed to linear, exponential, and surface-to-volume ratio related growth. Also here, during growth, A is subject to linear and exponential removal kinetics.

For most of the numerically studied control structures analytical steady state expressions for A are derived in the Supporting Information. The analytical expressions in A_{ss} are derived by writing first down the rate equations for A and E (E_1 and E_2 for the antithetic controller), while treating fluxes coming from precursor species as constants, i.e., rates are zero-order with respect to these species. Then the second time-derivative $\ddot{A}$ is calculated and the rate equation of E (E_2 for the antithetic controller) is inserted into the $\ddot{A}$ equation which is set to zero. This leads to an analytical expression for A_{ss} showing how different parameters influence the steady state.

In "Overview of results" the four motifs are ranked according to their abilities to oppose the different growth laws and outflow perturbations. The motif 2 based controller with repression/derepression kinetics clearly outperforms the other motifs, followed by the autocatalytic motif 1 controller. The performance of the four motifs is discussed in terms of the internal model principle, which reflects the kinetic limits controllers can handle.

We also demonstrate the influence the feedback structure (termed motifs in [7]) has in relationship with the integral controller part. Using an antithetic integral controller together with a motif 2 repression/derepression structure as an example, we show how the motif 2 structure improves controller performance, but also point to the limitations which are caused by the kinetics of the integral controller.

Reaction kinetics during volume changes

To describe concentration changes during cell growth we have to consider the concentration changes due to the increasing reaction volume V. If A denotes the concentration of n_A moles of compound A in volume V, the overall change of concentration A is composed of two terms,

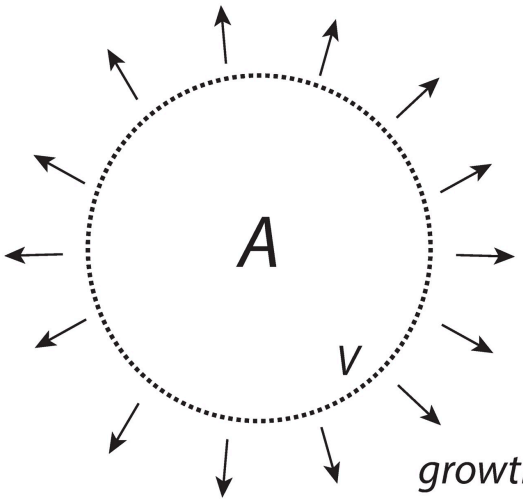

Fig 2. *A* is present inside the cell with a constant amount of n_A moles, while the cellular volume *V* increases with rate $\dot{V}$.

https://doi.org/10.1371/journal.pone.0207831.g002

one that describes the changes of *A* while *V* is kept constant, $(\dot{A})_V$, and of a second term, $A(\dot{V}/V)$, which describes the influence of the volume changes on the concentration of *A*, i.e.,

$$\dot{A} = \frac{\dot{n_A}}{V} - A\left(\frac{\dot{V}}{V}\right) = (\dot{A})_V - A\left(\frac{\dot{V}}{V}\right) \tag{3}$$

Eq 3 will be used as a "template" when formulating the rate equations of cellular compounds in the presence of changing *V*. Before we turn to the actual controller examples we show how growth ($\dot{V}$) affects the concentration of a given species *A* (which will be later our controlled variable) when *A* is unreactive, being produced internally within the cell, or being produced by a transporter-mediated process.

Unreactive *A*

In this example (Fig 2) n_A is kept constant, but the volume *V* increases with rate $\dot{V}$.

As *V* increases the concentration of *A* will decrease, i.e.,

$$A = \frac{n_A}{V} \quad \Rightarrow \quad \dot{A} = \frac{\dot{n_A}}{V} + n_A \cdot \frac{\left(\mathrm{d}\frac{1}{V}\right)}{\mathrm{d}t} = \frac{\dot{n_A}}{V} - n_A \cdot \frac{\dot{V}}{V^2} = \frac{\dot{n_A}}{V} - A \cdot \frac{\dot{V}}{V} \tag{4}$$

Since we assume that n_A is constant, we have that $\dot{n_A} = 0$ and the concentration of *A* decreases according to

$$\dot{A} = -A \cdot \frac{\dot{V}}{V} \quad \Rightarrow \quad \frac{\dot{A}}{A} = -\frac{\dot{V}}{V} \quad \Rightarrow \quad \frac{\mathrm{d}\log(A)}{\mathrm{d}t} = -\frac{\mathrm{d}\log(V)}{\mathrm{d}t} \tag{5}$$

Integrating Eq 5 leads to:

$$\log(A(t)) - \log(A_0) - \left\{\log V(t) - \log V_0\right\} \;\Rightarrow\; \log\left(\frac{A(t)}{A_0}\right) = \log\left(\frac{V_0}{V(t)}\right) \tag{6}$$

which can be rewritten as

$$A(t) = A_0\left(\frac{V_0}{V(t)}\right) \;\Leftrightarrow\; A(t)V(t) = A_0V_0 \tag{7}$$

Eq 7 can also be derived by noting that $A_0 = n_A/V_0$ and $A(t) = n_A/V(t)$. Solving for n_A from one of the equations and inserting it into the other leads to Eq 7.

Cell internal generated *A*

In order to counteract diminishing levels of a controlled compound A compensatory fluxes can be generated by a cell internal compound (assumed here to be homogeneously distributed inside V) or by the help of transporters from stores outside of the cell or from cell-internal (organelle) stores. We will investigate both ways to generate compensatory fluxes.

To achieve a constant level of A from a cell internal source, despite increasing V, we consider first a zero-order enzymatic reaction where enzyme E converts a species S (assumed to be present in sufficiently high amounts) to A, where V is assumed to increase by a constant rate (Fig 3).

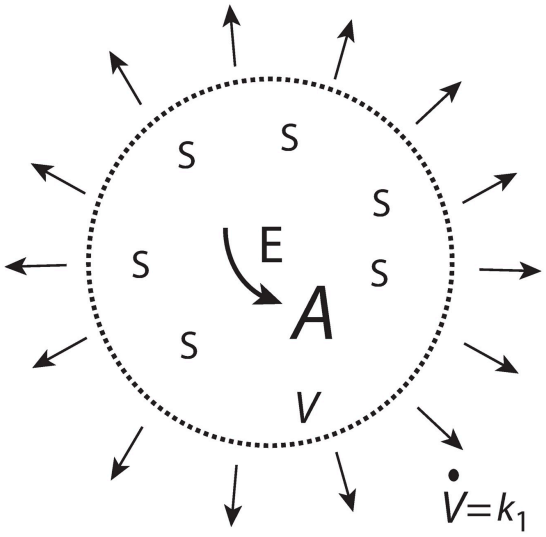

Fig 3. *A* is formed by zero-order kinetics within the cell while the cellular volume increases with a constant rate $\dot{V} = k_1$.

https://doi.org/10.1371/journal.pone.0207831.g003

We assume that E is not subject to any synthesis, but that during the increase of V, E remains always saturated with S and produces A by zero-order kinetics with respect to A. The initial production rate of A at time $t = 0$ is given as

$$\dot{A}_0 = \frac{v_{max,0} \cdot S_0}{K_M + S_0} \tag{8}$$

Since E is considered to be saturated by S at all times we have that $K_M \ll S(t)$ leading to

$$\dot{A}_0 = v_{max,0} = k_2 \cdot E_0 \tag{9}$$

where k_2 is the turnover number of the enzymatic process generating A, and E_0 is the enzyme concentration at time $t = 0$. As volume V increases, the concentrations of E and A are subject to dilution as described by the rate equations

$$\dot{E} = -E \cdot \frac{\dot{V}}{V} \tag{10}$$

$$\dot{A} = k_2 \cdot E - A \cdot \frac{\dot{V}}{V} \tag{11}$$

For $\dot{V} = k_1$ = constant, $E(t)$ and $A(t)$ are described by the equations (S1 Text)

$$E(t) = E_0 \cdot \frac{\alpha}{t + \alpha}\ ; \qquad \alpha = \frac{V_0}{k_1} \tag{12}$$

$$A(t) = k_2 \cdot E_0 \cdot \alpha - (k_2 \cdot E_0 \cdot \alpha - A_0) \cdot \frac{\alpha}{t + \alpha} \tag{13}$$

From Eq 13 we see that A will approach a final concentration $A_{\text{final}} = k_2 \cdot E_0 \cdot \alpha$ even when V continues to grow. The time needed of A to approach A_{final} is determined by the term $\alpha/(t+\alpha)$.

Fig 4 shows that A_{final} is independent of the initial values of A. However, the system is not stable against perturbations which remove A. In such a case A will go to zero (S1 Text).

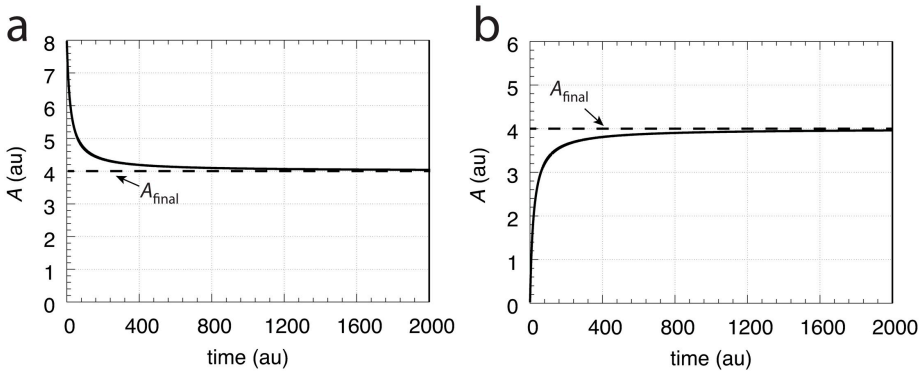

Fig 4. A approaches A_{final} independent of the initial concentration of A. (a) $A_0 = 8.0$; (b) $A_0 = 0.0$. All other rate parameters are: $k_1 = \dot{V} = 1.0$, $k_2 = 2.0$, $E_0 = 0.1$, $V_0 = 20.0$.

https://doi.org/10.1371/journal.pone.0207831.g004

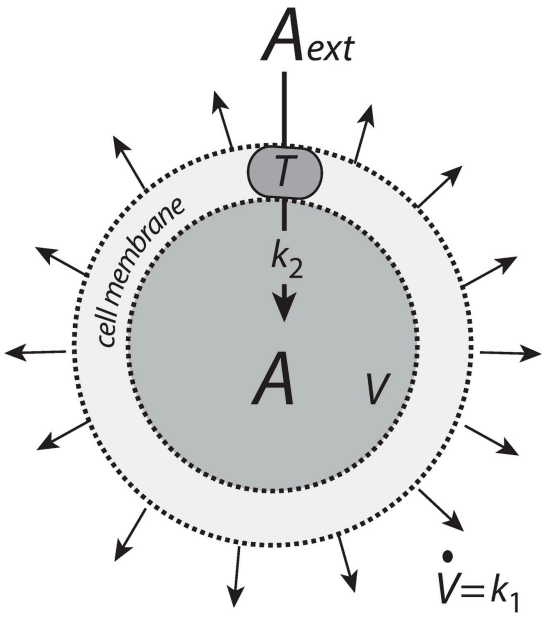

Fig 5. *A* is imported into the cell by transporter *T*.

https://doi.org/10.1371/journal.pone.0207831.g005

Transporter generated *A*

Alternatively, A may be imported into the cell by a transporter T (Fig 5).

Also here we consider that the transporter works under saturation (zero-order) conditions adding $\dot{n_A}$ moles of A per time unit into the cellular volume V

$$\dot{n_A} = \frac{k_2 \cdot T \cdot A_{ext}}{K_M^T + A_{ext}} \simeq k_2 \cdot T \tag{14}$$

where T denotes the (surface/membrane) concentration of the transporter, K_M^T is a dissociation constant between external A (A_{ext}) and T, and k_2 is the turnover number of the transporter-mediated uptake of A.

The change in the concentration of A inside an expanding cell is given by (see Eq 3)

$$\dot{A} = \frac{\dot{n_A}}{V} - A\left(\frac{\dot{V}}{V}\right) = \frac{k_2 \cdot T}{V} - A\left(\frac{\dot{V}}{V}\right) \tag{15}$$

For constant $\dot{V}$, k_2, and T the steady state of A ($\dot{A} = 0$) is $k_2 T/\dot{V}$ independent of the initial concentration of A. However, also in the transporter-based inflow of A, the steady state in A is not stable against perturbations removing A. Any reaction within the cell removing A while

growth occurs will drive A to zero (S2 Text). To get a steady state that is stable against perturbations a negative feedback controller needs to be included.

Case A.1: Controllers with transporter-based compensatory fluxes and linear time-dependent perturbations

In this section the four controller motifs (Fig 1) are tested using a transporter-based compensatory flux with respect to constant growth, $\dot{V} = k_1$. In addition, an outflow perturbation with a time-dependent rate parameter k_3 is invoked, which removes A as a first-order reaction with respect to A.

Motif 1 zero-order controller

Fig 6 shows the motif 1 controller with zero-order implementation of integral control [7]. A is the controlled compound and E is the controller molecule which concentration (in the ideal controller case) is proportional to the integrated error between A and A_{set}^{theor}. M is considered as a store/precursor into which "consumed" E is recycled to. M is included to make it explicit

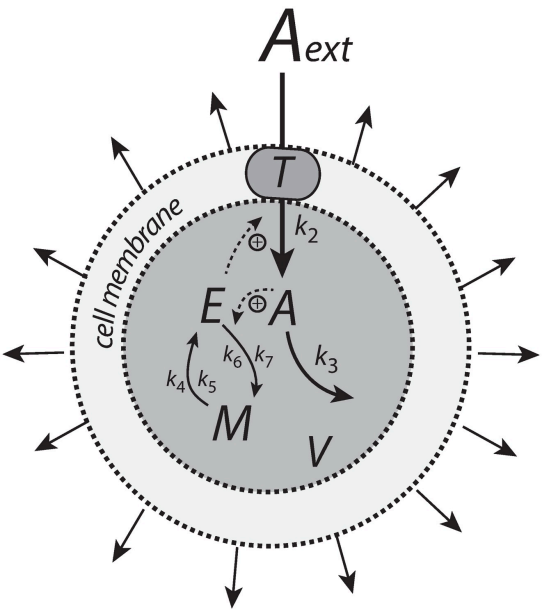

Fig 6. Motif 1 based zero-order integral controller with a transporter (T) generated compensatory flux. The controller species E is produced by an enzymatic zero-order process from compound M. E is recycled by another zero-order process (with respect to E) but the rate of E-removal is proportional to the concentration of A. Outflow perturbations are represented by the rate $r_3 = k_3 \cdot A$, where k_3 is either constant or increases linearly with time.

https://doi.org/10.1371/journal.pone.0207831.g006

that even under recycling conditions the increasing demand for E under growth and other time-dependent perturbations leads to a continuous reduction in M. This may lead to controller breakdown once all M is consumed. A situation when this occurs will be shown below for the motif 1 autocatalytic controller.

The rate equations for this system are:

$$\dot{A} = \frac{\dot{n_A}}{V} - k_3 \cdot A - A\left(\frac{\dot{V}}{V}\right) = \frac{k_2 \cdot E \cdot T}{V}\left(\frac{A_{ext}}{K_M^T + A_{ext}}\right) - k_3 \cdot A - A\left(\frac{\dot{V}}{V}\right) \tag{16}$$

$$\dot{E} = \frac{k_4 \cdot M}{k_5 + M} - \left(\frac{k_6 \cdot E}{k_7 + E}\right)A - E\left(\frac{\dot{V}}{V}\right) \tag{17}$$

$$\dot{M} = -\frac{k_4 \cdot M}{k_5 + M} + \left(\frac{k_6 \cdot E}{k_7 + E}\right)A - M\left(\frac{\dot{V}}{V}\right) \tag{18}$$

For simplicity, T and $A_{ext}/(K_M^T + A_{ext})$ are set to 1 leading to an inflow rate in A of k_2E/V. When $\dot{k_3} = \dot{V} = 0$, the set-point of the controller is (Ref. [7], S3 Text)

$$A_{set}^{theor} = \frac{k_4}{k_6} \tag{19}$$

independent of the inflow rate constant k_2 and the time-dependent outflow perturbation parameter k_3.

When $\dot{V}$ = constant the zero-order controller maintains a steady state below A_{set}^{theor} (S3 Text):

$$A_{ss} = \frac{k_4}{k_6 + \frac{2\dot{V}k_3}{k_2}} \tag{20}$$

which is dependent of $\dot{V}$, and the rate constants k_2 and k_3.

In testing the performance of this controller we consider three phases (see Fig 7). During the first phase the volume and the perturbation k_3 are kept constant. The controller is able to compensate for the perturbation rate $k_3 \cdot A$ and keeps A at its theoretical set-point A_{set}^{theor}. In the second phase the volume increases linearly with time, while k_3 remains constant. The zero-order controller is now no longer able to maintain homeostasis at $A_{set}^{theor} = k_4/k_6$, but shows a $\dot{V}$-dependent offset below A_{set}^{theor} as described by Eq 20. When k_3 increases linearly during phase 3 along the increase in V the controller breaks down and A goes to zero.

Motif 1 antithetic controller

The antithetic controller [22] uses two controller molecules, E_1 and E_2 (Fig 8). Compound E_1 is activated by A but is removed by compound E_2 by a second-order process. E_2 is formed by a zero-order process which acts as a constant reference rate. In addition, E_2 also acts as a signaling molecule, which closes the negative feedback loop by activating the transporter-based compensatory inflow of A.

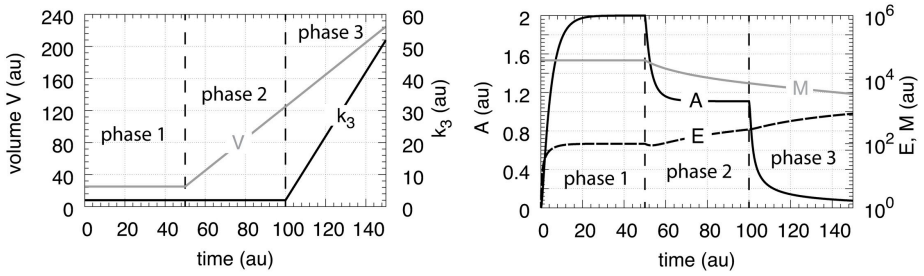

Fig 7. Performance of the motif 1 zero-order controller with transporter mediated compensatory flux (Eqs 16–18). Phase 1: constant volume V and constant k_3. Initial concentrations and rate constant values: $V_0 = 25.0$, $\dot{V} = 0.0$, $A_0 = 0.0$, $E_0 = 0.0$, $M_0 = 4 \times 10^4$, $k_2 = 1.0$, $k_3 = 2.0$, $\dot{k_3} = 0.0$, $k_4 = 20.0$, $k_5 = 1 \times 10^{-6}$, $k_6 = 10.0$, $k_7 = 1 \times 10^{-6}$. The controller keeps A at its theoretical set-point, $A_{set}^{theor} = k_4/k_6 = 2.0$ (Eq 19). Phase 2: rate constants remain the same as in phase 1, but V increases linearly with $\dot{V} = 2.0$, while k_3 remains constant at $k_3 = 2.0$. In agreement with Eq 20, the controller shows an offset below A_{set}^{theor} with $A_{ss} = 1.11$. Phase 3: V continues to increase with the same speed while k_3 starts to increase linearly with $\dot{k_3} = 1.0$. As indicated by Eq 20 the controller now breaks down and A goes to zero as V and k_3 increase.

https://doi.org/10.1371/journal.pone.0207831.g007

Assuming, as in the previous two examples that T and $A_{ext}/(K_M^T + A_{ext})$ are both 1, the rate equations are

$$\dot{A} = \frac{n_A^{\cdot}}{V} - k_3 \cdot A - A \cdot \frac{\dot{V}}{V} = \frac{k_2 \cdot E_2}{V} - k_3 \cdot A - A\left(\frac{\dot{V}}{V}\right) \tag{21}$$

$$\dot{E_1} = A\left(\frac{k_4 \cdot M}{k_5 + M}\right) - k_6 \cdot E_1 \cdot E_2 - E_1\left(\frac{\dot{V}}{V}\right) \tag{22}$$

$$\dot{E_2} = \frac{k_8 \cdot O}{k_9 + O} - k_6 \cdot E_1 \cdot E_2 - E_2\left(\frac{\dot{V}}{V}\right) \tag{23}$$

$$\dot{M} = -A\left(\frac{k_4 \cdot M}{k_5 + M}\right) - M\left(\frac{\dot{V}}{V}\right) \tag{24}$$

$$\dot{O} = -\frac{k_8 \cdot O}{k_9 + O} - O\left(\frac{\dot{V}}{V}\right) \tag{25}$$

$$\dot{Q} = k_3 \cdot A - Q\left(\frac{\dot{V}}{V}\right) \tag{26}$$

$$\dot{P} = k_6 \cdot E_1 \cdot E_2 - P\left(\frac{\dot{V}}{V}\right) \tag{27}$$

where $k_5 \ll M$ and $k_9 \ll O$ such that the generation of E_1 and E_2 are zero-order processes with respect to M and O.

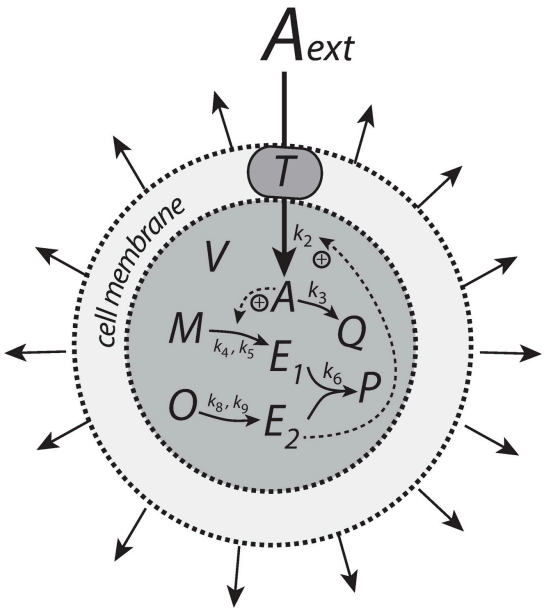

Fig 8. Motif 1 based controller with second-order (antithetic) integral control. The controller species E_2 is produced by an enzymatic zero-order process from compound O. E_2 activates the transporter-based compensatory flux of A and is removed by E_1 using second-order kinetics forming P.

https://doi.org/10.1371/journal.pone.0207831.g008

In case $\dot{V} = 0$ and $\dot{k_3} = 0$ the set-point of the controller is given by setting Eqs 22 and 23 to zero. Eliminating the second-order term $k_6 \cdot E_1 \cdot E_2$ leads to

$$A_{set}^{theor} = \frac{k_8}{k_4} = 2.0 \tag{28}$$

which is shown in phase 1 of Fig 9. In phase 2 the volume increases linearly with $\dot{V} = 2.0$ (Fig 9, left panel) while k_3 remains to be constant at $k_3 = 2.0$. The controller is no longer able to keep A at its theoretical set-point (Eq 28). When $\dot{V}$ and k_3 are constant an analytical expression of A_{ss} can be derived in good agreement with the numerical calculations (S4 Text):

$$A_{ss} = \frac{k_2 k_8}{k_2 k_4 + 2 k_3 \dot{V}} \tag{29}$$

which is analogous to the A_{ss} expression of the motif 1 zero-order controller (Eq 20). Finally, in phase 3 k_3 increases linearly with $\dot{k_3} = 1$ together with $\dot{V} = 2.0$. As indicated by Eq 29 and shown by the numerical calculations (Fig 9) the antithetic controller, like the zero-order controller, breaks down and A goes to zero (S4 Text).

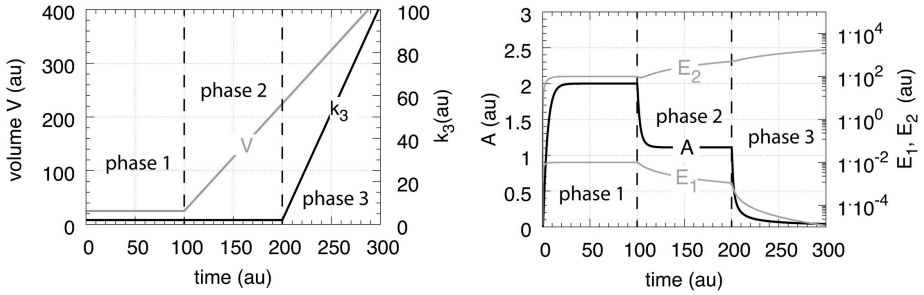

Fig 9. Performance of the antithetic controller with transporter mediated compensatory flux (Eqs 21–27). Phase 1: constant volume V and constant k_3. Initial concentrations and rate constant values: $V_0 = 25.0$, $\dot{V} = 0.0$, $A_0 = 0.0$, $E_{1,0} = 0.0$, $E_{2,0} = 0.0$, $M_0 = 1 \times 10^5$, $O_0 = 1 \times 10^5$, $k_2 = 1.0$, $k_3 = 2.0$, $\dot{k}_3 = 0.0$, $k_4 = 10.0$, $k_5 = 1 \times 10^{-6}$, $k_6 = 20.0$, k_7 not used, $k_8 = 20.0$, $k_9 = 1 \times 10^{-6}$. The controller keeps A at its theoretical set-point at $A_{set}^{theor} = k_8/k_4 = 2.0$ (Eq 28). Phase 2: rate constants remain the same as in phase 1, but V increases linearly with $\dot{V} = 2.0$, while k_3 remains constant at $k_3 = 2.0$. The controller shows an offset below A_{set}^{theor} with $A_{ss} = 1.11$ in agreement with Eq 29. Phase 3: V continues to increase while k_3 increases linearly with $\dot{k}_3 = 1.0$. As indicated by Eq 29 the controller breaks down and A goes to zero.

https://doi.org/10.1371/journal.pone.0207831.g009

Although not shown explicitly here, the following mass balances are obeyed:

$$n_{M,0} = n_M(t) + n_{E_1}(t) + n_P(t) \tag{30}$$

$$n_{O,0} = n_O(t) + n_{E_2}(t) + n_P(t) \tag{31}$$

where $n_{i,0}$ and n_i are respectively the initial number of moles and the number of moles at time t of compound i.

As described above, when using a transporter mediated compensation in A the antithetic and the motif 1 zero-order controllers have to increase their controller variables E_2 or E in order to keep A_{ss} constant, as indicated by the equation

$$\dot{A} = 0 \;\Rightarrow\; \frac{k_2 \cdot E_{(2)}(t)}{V(t)} = k_3 \cdot A_{ss} \tag{32}$$

where $E_{(2)}$ represents E_2 or E and $(\dot{V}/V)A_{ss}$ becomes negligible.

Motif 1 autocatalytic controller

Similar to controllers based on double integral action [24] an autocatalytic design [19] is able to keep the controlled species at its set-point even when perturbations become linearly time dependent and rapid [18]. However, in contrast to double integral action the autocatalytic controller is able to compensate for time-dependent perturbations of the form $a \cdot t^n$ where n is larger than 1.

Fig 10 shows the reaction scheme. The controller compound E is produced autocatalytically, i.e., its rate is proportionally to the concentration of E, while M, present in relative large amounts, produces E by an enzyme-catalyzed reaction which is zero-order with respect to M. E increases the activity of transporter T and leads to an increased import of external A into the cell. The negative feedback is closed by an A-induced recycling of E to M. Rate constant k_3 represents a perturbation which removes A by a first-order process with respect to A. The rate

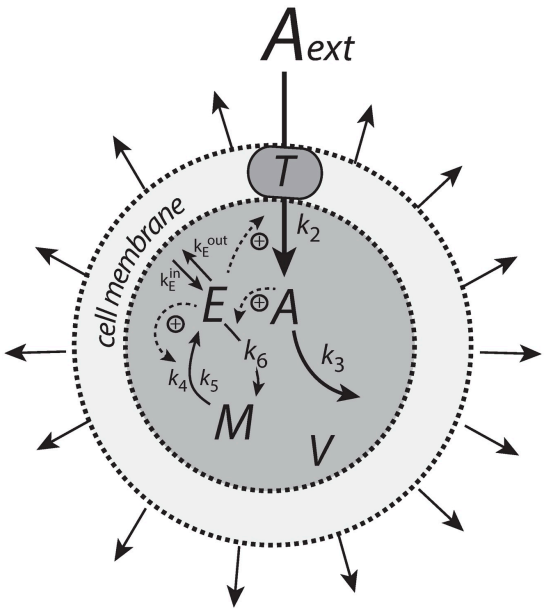

Fig 10. Motif 1 autocatalytic integral controller. The controller species E is produced by an enzymatic zero-order process from compound M, but E activates its own production and the transporter-based compensatory flux. The negative feedback is due to the inflow activation of A by E through transporter T, while A activates the (first-order) recycling of E to M. Outflow perturbation in A is described by the rate $k_3 \cdot A$, where k_3 is either a constant or increases linearly with time. k_E^{in} and k_E^{out} represent background reactions creating and removing E.

https://doi.org/10.1371/journal.pone.0207831.g010

equations are:

$$\dot{A} = \frac{\dot{n_A}}{V} - k_3 \cdot A - A\left(\frac{\dot{V}}{V}\right) = \frac{k_2 \cdot E \cdot T}{V}\left(\frac{A_{ext}}{K_M^T + A_{ext}}\right) - k_3 \cdot A - A\left(\frac{\dot{V}}{V}\right) \tag{33}$$

$$\dot{E} = E\left(\frac{k_4 \cdot M}{k_5 + M}\right) - k_6 \cdot E \cdot A - E\left(\frac{\dot{V}}{V}\right) + k_E^{in} - k_E^{out} \cdot E \tag{34}$$

$$\dot{M} = -E\left(\frac{k_4 \cdot M}{k_5 + M}\right) + k_6 \cdot E \cdot A - M\left(\frac{\dot{V}}{V}\right) \tag{35}$$

As in the previous cases, in Eq 33, the term $T \cdot A_{ext}/(K_M^T + A_{ext})$ is set to 1. The last two terms in Eq 34, $k_E^{in} - k_E^{out} \cdot E$, represent required background reactions to keep E at a sufficiently high level such that the autocatalysis in E can start at low/zero initial E concentrations (see also Ref. [18] and Discussion there). In the calculations presented here, k_E^{in} and k_E^{out} are set

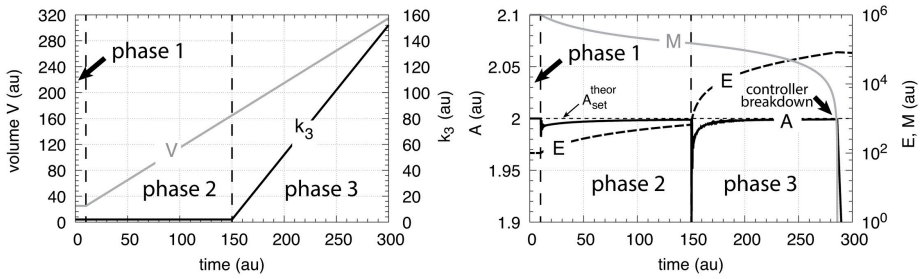

Fig 11. Performance of the motif 1 autocatalytic controller (Eqs 33–35). Phase 1: constant volume V and constant k_3. Initial concentrations and rate constant values (at the controller's steady state): $V_0 = 25.0$, $\dot{V} = 0.0$, $A_0 = 2.0$, $E_0 = 100.0$, $M_0 = 1 \times 10^6$, $k_2 = 1.0$, $k_3 = 2.0$, $\dot{k_3} = 0.0$, $k_4 = 20.0$, $k_5 = 1 \times 10^{-6}$, $k_6 = 10.0$, $k_E^{in} = k_E^{out} = 1 \times 10^{-5}$. The controller keeps A at its set-point at $A_{set}^{theor} = k_4/k_6 = 2.0$. Phase 2: rate constants remain the same as in phase 1, but V increases linearly with $\dot{V} = 1.0$. Phase 3: V continues to increase with the same rate and k_3 increases with rate $\dot{k_3} = 1.0$. The controller moves A towards A_{set}^{theor} in both phase 2 and phase 3, but breaks down when no additional E becomes available through M (indicated by the arrow in the right panel).

https://doi.org/10.1371/journal.pone.0207831.g011

to $1{\times}10^{-5}$. To show that in this case the controller can start from initial concentration $E_0 = 0$, see the corresponding calculation later in the paper when using a cell-internal compensatory flux, or test it using S1 Matlab for Fig 11. When E_0 is larger than 10^{-5} the $k_E^{in} - k_E^{out} \cdot E$ term is not needed, but its presence will not affect controller dynamics or set-point as long as k_E^{in} and k_E^{out} are kept low. In case the k_E^{in} and k_E^{out} values are higher, a change/reduction in the set-point is observed, which the controller still defends (see later in this chapter).

To determine the controller's set-point at constant V and k_3 we set Eq 34 to zero. Neglecting the $k_E^{in} - k_E^{out} \cdot E$ term and setting $\dot{V} = 0$, we can solve for the steady state value of A, which defines the controller's theoretical set-point A_{set}^{theor}:

$$\dot{E} = E_{ss}\left(\frac{k_4 \cdot M}{k_5 + M}\right) - k_6 \cdot E_{ss} \cdot A_{ss} = E_{ss}\left[\left(\frac{k_4 \cdot M}{k_5 + M}\right) - k_6 \cdot A_{ss}\right] = 0 \tag{36}$$

Since $M/(k_5 + M) = 1$ (ideal zero-order conditions), we get from Eq 36

$$k_4 - k_6 \cdot A_{ss} = 0 \quad \Rightarrow \quad A_{ss} = A_{set}^{theor} = \frac{k_4}{k_6} \tag{37}$$

For constant $\dot{V}$ and $\dot{k_3}$ values the set-point is calculated to be (S5 Text)

$$A_{ss} = \frac{k_4}{k_6} - \frac{\dot{k_3}}{k_6 \cdot k_3} \rightarrow \frac{k_4}{k_6} = A_{set}^{theor} \quad \text{as} \quad t \rightarrow \infty \tag{38}$$

According to previous findings on the autocatalytic controller [18], any time-dependent function $k_3(t) = k_{3,0} + a{\cdot}t^n$ where a, $n > 0$ will lead to the set-point conditions described by Eq 38 (S5 Text).

The recycling scheme between E and M implies that E and M obey a mass balance of the form

$$n_E(t) + n_M(t) = n_{E,0} + n_{M,0} \tag{39}$$

with $n_E(t) = E(t){\cdot}V(t)$, $n_M(t) = M(t){\cdot}V(t)$, and where $n_{E,0}$ and $n_{M,0}$ are the initial number of

moles of respectively E and M. The rates how n_E and n_M change at a given time t are given as (S5 Text)

$$\dot{n_E} = \left[\dot{E} + E\left(\frac{\dot{V}}{V}\right)\right] \cdot V = -\dot{n_M} = -\left[\dot{M} + M\left(\frac{\dot{V}}{V}\right)\right] \cdot V \tag{40}$$

Fig 11 shows the results. During the first phase no volume change occurs and k_3 is a constant. The controller keeps A at $A_{set}^{theor} = 2.0$ as described by Eq 37. During the second phase both V and k_3 increase linearly and the controller still keeps A at $A_{set}^{theor} = 2.0$ according to Eq 38. To keep A at its set-point during increasing V and/or k_3 the concentration of E has to increase in order to maintain the steady state condition given by Eq 33 when $\dot{A} = 0$ and $\dot{V}/V \to 0$, i.e.,

$$E(t) = \frac{k_3(t) \cdot V(t) \cdot A_{ss}}{k_2} \tag{41}$$

From the initial conditions (see legend of Fig 11) we have that $n_E(t) + n_M(t) = V_0 \cdot M_0 = 2.5 \times 10^7$.

When k_E^{in} and k_E^{out} are significantly higher than 10^{-5}, then the set-point of the controller changes to the following steady state value in A:

$$A_{ss} \approx \frac{k_4 - k_E^{out}}{k_6} \tag{42}$$

The new set-point is defended by the controller for step-wise changes and for linearly increasing values of k_3 and V (for details, see S5 Text).

Motif 2 zero-order controller

The reaction scheme of this controller is shown in Fig 12. The transporter-based compensatory flux is regulated by E through repression or derepression by E. E is removed by a zero-order reaction creating M, which then is recycled in a A-dependent manner.

The rate equations are

$$\dot{A} = \frac{\dot{n_A}}{V} - k_3 \cdot A - A\left(\frac{\dot{V}}{V}\right) = \frac{k_2 k_4}{k_4 + E}\left(\frac{T \cdot A_{ext}}{K_M^T + A_{ext}}\right) \cdot \frac{1}{V} - k_3 \cdot A - A\left(\frac{\dot{V}}{V}\right) \tag{43}$$

$$\dot{E} = \left(\frac{k_8 \cdot M}{k_{11} + M}\right) \cdot A - \frac{k_9 \cdot E}{k_{10} + E} - E\left(\frac{\dot{V}}{V}\right) \tag{44}$$

$$\dot{M} = -\left(\frac{k_8 \cdot M}{k_{11} + M}\right) \cdot A + \frac{k_9 \cdot E}{k_{10} + E} - M\left(\frac{\dot{V}}{V}\right) \tag{45}$$

$$\dot{P} = k_3 \cdot A - P\left(\frac{\dot{V}}{V}\right) \tag{46}$$

Also here, we keep for the sake of simplicity, $T \cdot A_{ext}/(K_M^T + A_{ext}) = 1$. In presence of growing V and k_3 the motif 2 zero-order controller successfully defends its theoretical set-point given by (S6 Text)

$$A_{set}^{theor} = \frac{k_9}{k_8} \tag{47}$$

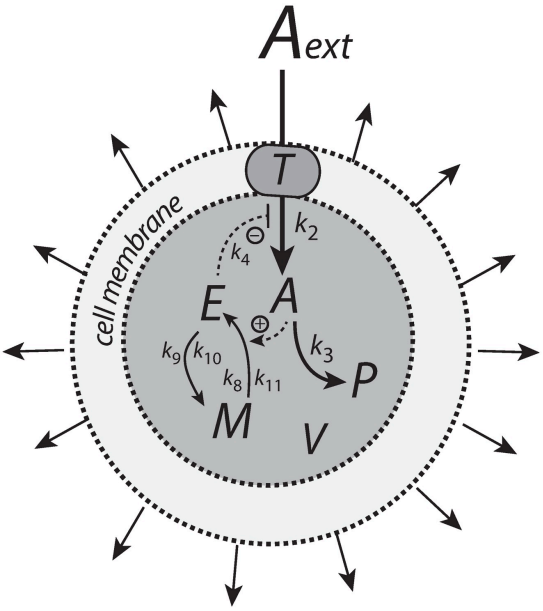

Fig 12. Motif 2 based controller with zero-order integral control. An increase of the compensatory flux occurs by a decrease of E (derepression of the compensatory flux).

https://doi.org/10.1371/journal.pone.0207831.g012

However, since an increase of the compensatory flux is based on derepression by E (decreasing E), the controller will break down when $E \ll k_4$ or $k_4/(k_4+E) \approx 1$. Neglecting the $A \cdot \dot{V} / V$ term, the point when the breakdown occurs can be estimated by setting Eq 43 to zero

$$\dot{A} = \frac{k_2}{V} - k_3 \cdot A_{set}^{theor} = 0 \quad \Rightarrow \quad k_3 \cdot V = \frac{k_2}{A_{set}^{theor}} \tag{48}$$

Fig 13 shows that the motif 2 based controller is able to defend successfully against linear growth in both V and k_3 and keeping A at A_{set}^{theor}. Prolonged time intervals with increasing V and k_3 will lead to controller breakdown when the condition of Eq 48 is met. The condition $k_4/(k_4+E) \approx 1$ also indicates that the capacity limit of the controller has been reached, because the compensatory flux $k_2\, k_4/(k_4+E)$ (Eq 43) has reached its maximum value k_2 and can no longer be increased.

Case A.2: Controllers with transporter-based compensatory fluxes and exponential time-dependent perturbations

Here we describe the performance of the four controller motifs (Fig 1) with transporter-based compensatory fluxes when exposed to exponential growth, $\dot{V} = \kappa \cdot V$, and an exponential increase in the outflow perturbation rate parameter k_3 (Fig 14).

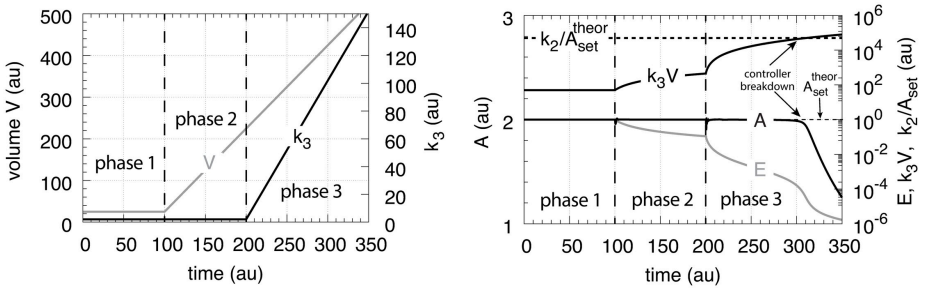

Fig 13. Performance of the motif 2 zero-order based controller with respect to linear increases in V and k_3. The controller is able to defend A_{set}^{theor} successfully, but breaks down when k_3V reaches k_2/A_{set}^{theor} (Eq 48). Rate parameters: $k_2 = 1 \times 10^5$, $k_4 = 1 \times 10^{-3}$, $k_8 = 1.0$, $k_9 = 2.0$, $k_{10} = k_{11} = 1 \times 10^{-6}$. Initial conditions: $A_0 = A_{set}^{theor} = 2.0$, $E_0 = 1.0$, $M_0 = 1 \times 10^6$, $P_0 = 0.0$, $V_0 = 25.0$, $k_{3,0} = 2.0$. $\dot{V} = 2.0$ (phase 2 and phase 3), $\dot{k}_3 = 1.0$ (phase 3).

https://doi.org/10.1371/journal.pone.0207831.g013

There are three phases the controllers are exposed to. During the first phase the controllers are at their steady states and V and k_3 are kept constant at respectively 25.0 and 2.0. During the second phase V increases exponentially according to $\dot{V} = \kappa V$ ($\kappa = 0.1$), while k_3 is kept constant at 2.0. During phase 3, V continues to grow exponentially and k_3 starts to increase

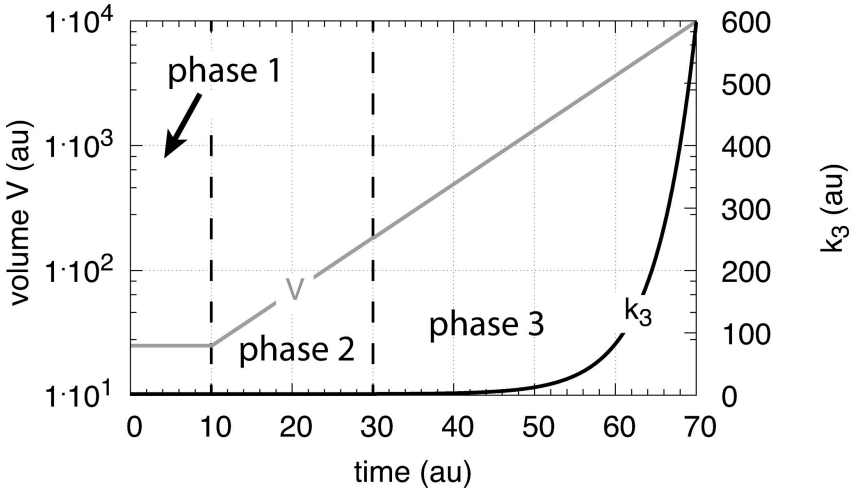

Fig 14. The perturbation profile with exponential growth of V and k_3. Due to presentation reasons V is plotted semi-logarithmically while the k_3 scale is linear.

https://doi.org/10.1371/journal.pone.0207831.g014

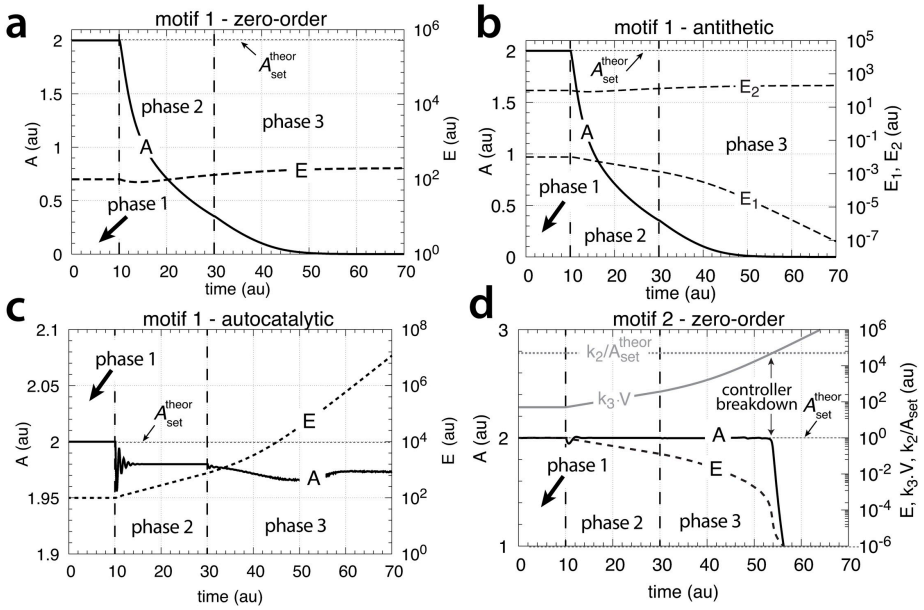

Fig 15. Performance of the (a) motif 1-zero-order, (b) -antithetic, (c) -autocatalytic, and (d) motif 2 zero-order controllers with transporter-based compensatory fluxes in relation to the perturbation profile of Fig 14. For rate equations of the individual controllers, see the descriptions in the previous sections dealing with linear time-dependent perturbations. Rate parameters and initial conditions: (a) see legend of Fig 7, (b) see Fig 9, (c) see Fig 11, but using $M_0 = 1{\times}10^{10}$, and (d) see Fig 13.

https://doi.org/10.1371/journal.pone.0207831.g015

according to

$$k_3(t) = k_{3,p3} + 0.2\left(e^{0.2(t-t_{p3})} - 1\right) \tag{49}$$

where $k_{3,p3}$ and t_{p3} are the values of respectively k_3 and time t at the beginning of phase 3.

Fig 15 shows that only the motif 2 based controller with derepression kinetics (panel d) is able to counteract both exponential increases in V and k_3. However, due to the derepression kinetics and due to the transporter based kinetics (see Eq 48) the controller breaks down when the product of the perturbations, $k_3 V$ reaches k_6/A_{set}^{theor}. The motif 1 autocatalytic controller (panel c) shows slight constant offsets below A_{set}^{theor}, as expected [18], both for the single exponential increase of V during phase 2 and when both V and k_3 increase exponentially in phase 3. These offsets increase when the values of k_E^{in} and k_E^{out} are large and cannot be neglected (S5 Text). Since E increases with increasing perturbation strengths the controller is limited by the supply for E via M as indicated in Fig 11. Neither the motif 1 based zero-order controller (panel a) nor the antithetic controller based on motif 1 (panel b) are able to compensate for exponentially increasing perturbation strengths. They behave very similar, as already seen in Figs 7 and 9 for linear time-dependent perturbations.

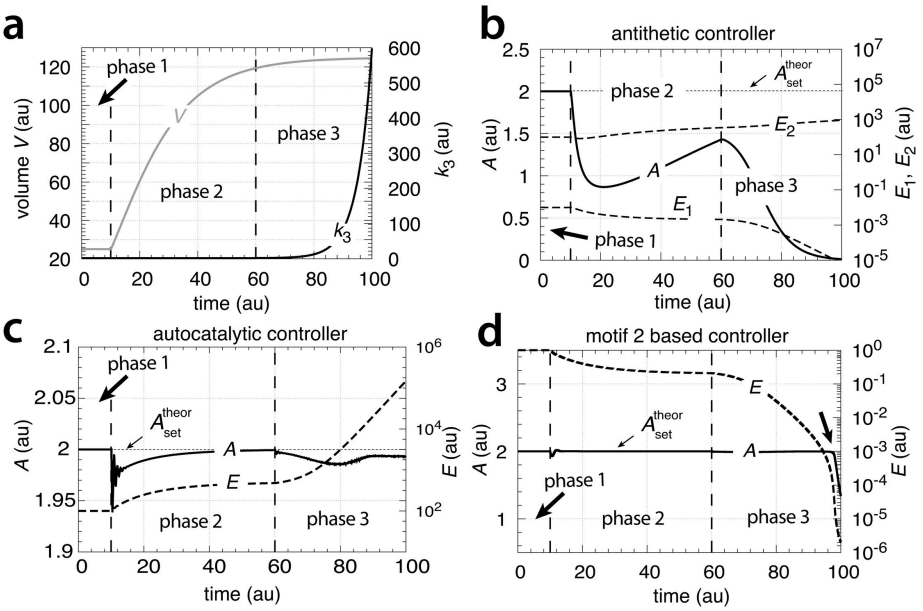

Fig 16. Performance of the motif 1 antithetic, motif 1 autocatalytic and motif 2 zero-order controllers with respect to surface to volume ratio related growth and an exponential increase of k_3. (a) Perturbation profile. Phase 1: constant V (25.0) and k_3 (2.0); phase 2: V increases according to Eq 2 ($\eta = 1$ and $\xi = 0.2$) and k_3 remains constant; phase 3: V continues to increase and k_3 starts to increase exponentially as described by Eq 49. (b) Behavior of the antithetic controller (Eqs 21–27). Rate constant values as in Fig 9. Initial concentrations: $A_0 = 2.0$, $E_{1,0} = 0.01$, $E_{2,0} = 100$, $M_0 = O_0 = 1 \times 10^6$. (c) Behavior of the autocatalytic controller (Eqs 33–35). Rate constant values as in Fig 11. Initial concentrations: $A_0 = 2.0$, $E_0 = 0.01$, $M_0 = 1 \times 10^6$. (d) Behavior of the motif 2 zero-order controller (Eqs 43–46). Initial concentrations: $A_0 = 2.0$, $E_0 = 1.0$, $M_0 = 1 \times 10^3$. Note the breakdown of the controller at the very end of phase 3 due to low E (arrow).

https://doi.org/10.1371/journal.pone.0207831.g016

Growth related to surface to volume ratio and controllers with transporter-based compensatory fluxes

We have investigated how the controllers with transporter-based compensatory fluxes behave with respect to the growth law described by Eq 2 ($\eta = 1$ and $\xi = 0.2$) when k_3 increases exponentially in phase 3 according to Eq 49 (Fig 16a).

Fig 16b–16d show the results of the antithetic, motif 1 autocatalytic and motif 2 zero-order controllers. The motif 1 zero-order controller's behavior of A is identical to that of the antithetic controller and only the result of the antithetic controller is shown. Typically for this type of growth law is that the motif 1 based controllers gain successively control during phase 2 when $\dot{V}$ decreases and approaches zero. During phase 3, when k_3 increases exponentially, only the motif 2 based is able to defend its theoretical set-point, but breaks down when E become too low. The autocatalytic controller shows a constant offset below A^{theor}_{set}. Both the antithetic and the motif 1 zero-order controllers break down during phase 3 and A goes to zero.

Case B.1: Controllers with cell-internal compensatory fluxes and linear time-dependent perturbations

We consider here the four controllers, but the compensatory fluxes are now generated from cell-internal and homogeneously distributed sources.

Motif 1 zero-order controller

Fig 17 shows the motif 1 zero-order controller using a cell-internal compensatory flux. The homogenously distributed compound N serves as a source for A, which is activated by E. Compound M serves as a source for E, while by the activation of A, M is recycled from E.

The rate equations are

$$\dot{A} = k_2 \cdot E\left(\frac{N}{k_7 + N}\right) - k_3 \cdot A - A\left(\frac{\dot{V}}{V}\right) \tag{50}$$

$$\dot{E} = \frac{k_4 \cdot M}{k_5 + M} - \left(\frac{k_6 \cdot E}{k_8 + E}\right)A - E\left(\frac{\dot{V}}{V}\right) \tag{51}$$

$$\dot{M} = -\frac{k_4 \cdot M}{k_5 + M} + \left(\frac{k_6 \cdot E}{k_8 + E}\right)A - M\left(\frac{\dot{V}}{V}\right) \tag{52}$$

$$\dot{N} = -\left(\frac{k_2 \cdot N}{k_7 + N}\right)E - N\left(\frac{\dot{V}}{V}\right) \tag{53}$$

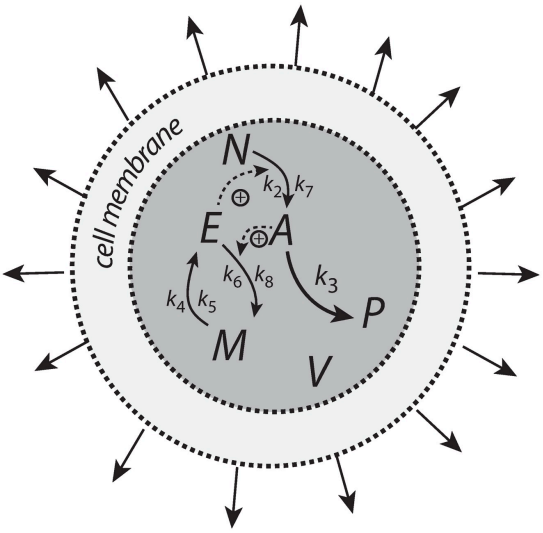

Fig 17. Motif 1 zero-order controller with a cell-internal compensatory flux.

https://doi.org/10.1371/journal.pone.0207831.g017

$$\dot{P} = -k_3 \cdot A - P\left(\frac{\dot{V}}{V}\right) \tag{54}$$

The steady state of A when both $\dot{V}$ and $\dot{k_3}$ are constant is given by the following expression (S3 Text)

$$A_{ss} = \frac{k_2 k_4}{k_2 k_6 + \dot{k_3}} \tag{55}$$

When $\dot{k_3} = 0$ and $\dot{V}$ = constant A_{ss} becomes $A_{set}^{theor} = k_4/k_6$ and the motif 1 zero-order controller is able to compensate for a constant growth rate (Fig 18, phases 1 and 2). However, when k_3 increases linearly, A_{ss} is below A_{set}^{theor} and remains constant as long as sufficient M and N are present (Fig 18, phase 3). Thus, in comparison with a transporter-mediated compensatory fluxes, the motif 1 zero-order controller with an internally generated compensatory flux shows an improved performance by being able to compensate for a constant growth rate in the absence of other outflow perturbations in A.

Motif 1 antithetic controller

When the antithetic integral controller is equipped with an internally generated compensatory flux (Fig 19) its performance towards constant growth and linearly increasing outflow perturbations k_3 is significantly improved in comparison with a controller having a transporter generated compensatory flux (Fig 9). The rate equation for A is now changed to

$$\dot{A} = \left(\frac{k_2 \cdot N}{k_7 + N}\right) E_2 - k_3 \cdot A - A\left(\frac{\dot{V}}{V}\right) \tag{56}$$

while the other rate equations (Eqs 22–27) remain the same.

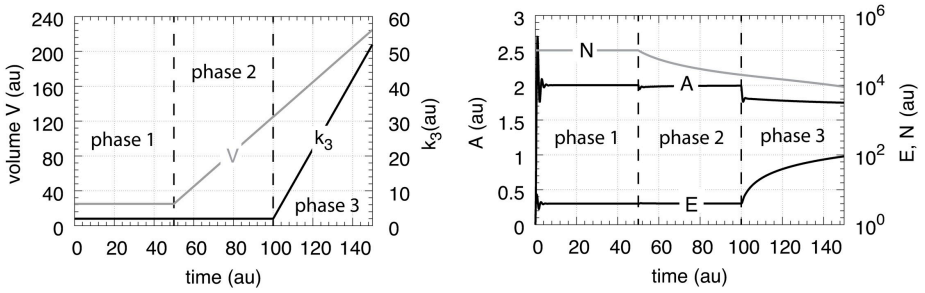

Fig 18. Performance of the motif 1 zero-order controller with internally generated compensatory flux (Fig 17; Eqs 50–54). Phase 1: constant volume V and constant k_3. Initial volume, concentrations, and rate constants: $V_0 = 25.0$, $\dot{V} = 0.0$, $A_0 = 0.0$, $E_0 = 0.0$, $M_0 = 4 \times 10^4$, $N_0 = 1 \times 10^5$, $P_0 = 0.0$, $k_2 = 1.0$, $k_3 = 2.0$, $\dot{k_3} = 0.0$, $k_4 = 20.0$, $k_5 = 1 \times 10^{-6}$, $k_6 = 10.0$, $k_7 = 1 \times 10^{-6}$, $k_8 = 1 \times 10^{-6}$. The controller moves A to its set-point at $A_{set}^{theor} = (k_4/k_6) = 2.0$ (Eq 55). Phase 2: rate constants remain the same as in phase 1, but V increases linearly with $\dot{V} = 2.0$, while k_3 remains constant at $k_3 = 2.0$. The controller is able to keep A at $A_{set}^{theor} = (k_4/k_6) = 2.0$ in agreement with Eq 55. Phase 3: V continues to increase with the same speed while k_3 now linearly increases with $\dot{k_3} = 1.0$. As indicated by Eq 55 A_{ss} leads to a constant offset below A_{set}^{theor}.

https://doi.org/10.1371/journal.pone.0207831.g018

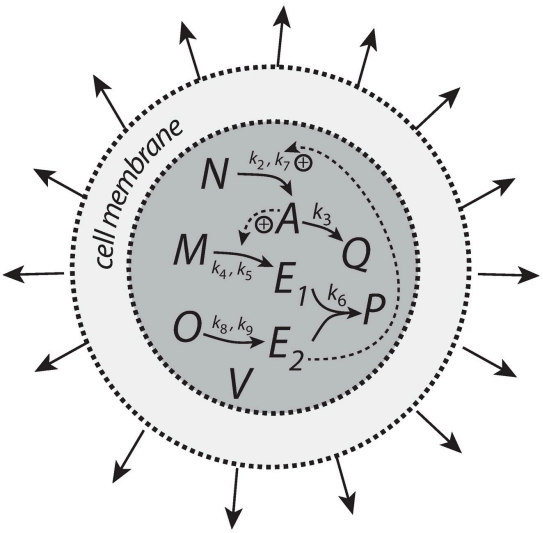

Fig 19. The antithetic controller with an internal generated compensatory flux.

https://doi.org/10.1371/journal.pone.0207831.g019

When $\dot{V}$ is constant A_{ss} becomes (S4 Text)

$$A_{ss} = \frac{k_2 k_8}{k_2 k_4 + \dot{k}_3} \tag{57}$$

As indicated by Eq 57 numerical results show (Fig 20, phase 2) that the antithetic controller is now able to compensate for linear volume increases by moving A to $A_{set}^{theor} = (k_8/k_4)$. However, an offset in A_{ss} below A_{set}^{theor} is observed when, in addition, k_3 increases linearly with time, i.e., when $\dot{k}_3$ is constant.

Although not explicitly shown here, during the volume increase, the mass (mole) balances described by Eqs 30 and 31 are obeyed in addition to the mass balance connecting N, A, and Q

$$n_{N,0} = n_N(t) + n_A(t) + n_Q(t) \tag{58}$$

where $n_{N,0}$ is the number of moles of initial N at $t = 0$ with $n_{A,0} = n_{Q,0} = 0$.

Motif 1 autocatalytic controller

Fig 21 shows the autocatalytic controller but now with an internally generated compensatory flux. As for the motif 1 zero-order controller (Fig 17) the compensatory flux originates from compound N and is activated by E. N is present in high concentration and forms A by a zero-order process with respect to N.

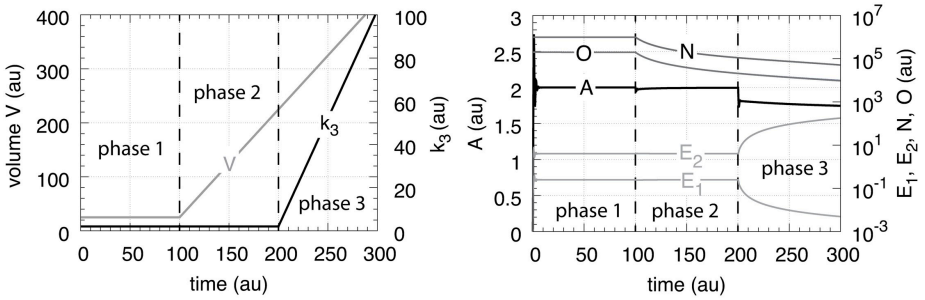

Fig 20. Performance of the antithetic controller when the compensatory flux is homogeneously generated within the cellular volume (Eqs 56 and 22–27). Phase 1: constant volume V and constant k_3. Initial concentrations and rate constant values: $V_0 = 25.0$, $\dot{V} = 0.0$, $A_0 = 0.0$, $E_{1,0} = 0.0$, $E_{2,0} = 0.0$, $M_0 = 2 \times 10^5$, $N_0 = 1 \times 10^6$, $O_0 = 2 \times 10^5$, $k_2 = 1.0$, $k_3 = 2.0$, $\dot{k_3} = 0.0$, $k_4 = 10.0$, $k_5 = 1 \times 10^{-6}$, $k_6 = 20.0$, $k_7 = 1 \times 10^{-5}$, $k_8 = 20.0$, $k_9 = 1 \times 10^{-5}$. The controller moves A to $A_{set}^{theor} = (k_8/k_4) = 2.0$ (Eq 57 when $\dot{k_3} = 0$). Phase 2: rate constants remain the same as in phase 1, but V increases linearly with $\dot{V} = 2.0$, while k_3 remains constant at $k_3 = 2.0$. The controller is able to maintain A at $A_{set}^{theor} = k_4/k_6 = 2.0$ in agreement with Eq 57. Phase 3: V continues to increase with the same speed while k_3 now linearly increases with $\dot{k_3} = 1.0$. As indicated by Eq 57 the controller is no longer able to keep A at A_{set}^{theor} but shows a constant steady state value below its theoretical set-point.

https://doi.org/10.1371/journal.pone.0207831.g020

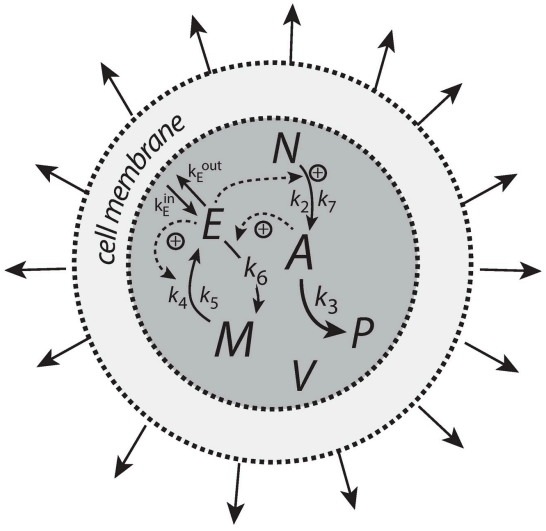

Fig 21. Scheme of autocatalytic controller with an internally generated compensatory flux from compound *N*. Otherwise the controller has the same structure as shown in Fig 10.

https://doi.org/10.1371/journal.pone.0207831.g021

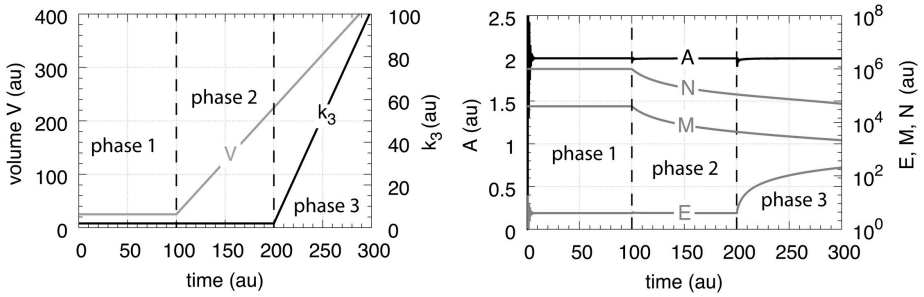

Fig 22. Performance of the autocatalytic controller when the compensatory flux is generated within the cellular volume (Eqs 34, 35, 59 and 60). Phase 1: constant volume V and constant k_3. Initial concentrations and rate constant values: $V_0 = 25.0$, $\dot{V} = 0.0$, $A_0 = 0.0$, $E_0 = 0.0$, $M_0 = 4 \times 10^4$, $N_0 = 1 \times 10^6$, $k_2 = 1.0$, $k_3 = 2.0$, $\dot{k}_3 = 0.0$, $k_4 = 20.0$, $k_5 = 1 \times 10^{-6}$, $k_6 = 10.0$, $k_7 = 1 \times 10^{-6}$, $k_E^{in} = k_E^{out} = 1 \times 10^{-5}$. The controller moves A to its theoretical set-point at $A_{set}^{theor} = (k_4/k_6) = 2.0$ (Eq 37). Phase 2: rate constants remain the same as in phase 1, but V increases linearly with $\dot{V} = 2.0$, while k_3 remains constant at $k_3 = 2.0$. The controller is able to maintain A at A_{set}^{theor} in agreement with Eq 37. Phase 3: V continues to increase with the same speed while k_3 now linearly increases with $\dot{k}_3 = 1.0$. As indicated by Eq 38 the controller keeps A at A_{set}^{theor} as k_3 increases.

https://doi.org/10.1371/journal.pone.0207831.g022

The rate equation for the controlled variable A is

$$\dot{A} = k_2 \cdot E\left(\frac{N}{k_7 + N}\right) - k_3 \cdot A - A\left(\frac{\dot{V}}{V}\right) \tag{59}$$

while the rate equations for E and M remain the same as Eqs 34 and 35. Species P is included with the rate equation

$$\dot{P} = k_3 \cdot A - P\left(\frac{\dot{V}}{V}\right) \tag{60}$$

to test that the mass (mole) balance between N, A, and P is preserved.

The controller's steady state in A is also in this case described by Eq 38 (S5 Text). In contrast to the other controllers, even when $\dot{V}$ and $\dot{k}_3$ are constant, the autocatalytic controller is able to move A to $A_{set}^{theor} = (k_4/k_6)$ (Fig 22).

When k_E^{in} and k_E^{out} are large and cannot be neglected the steady state in A is described by the quadratic equation (S5 Text)

$$A_{ss}^2 - A_{ss}\left(\frac{k_4 - k_E^{out}}{k_6} - \frac{\dot{k}_3}{k_3 k_6}\right) - \frac{k_2 k_E^{in}}{k_3 k_6} = 0 \tag{61}$$

In case only V increases linearly A_{ss} is given by the solution of Eq 61, independent of V's growth rate. On the other hand, if k_3 increases linearly, the terms $\dot{k}_3/k_3k_6$ and $k_2k_E^{in}/k_3k_5$ go to zero for large k_3 and A_{ss} is given by $(k_4 - k_E^{out})/k_6$ as described by Eq 42 for the transporter-based compensatory flux.

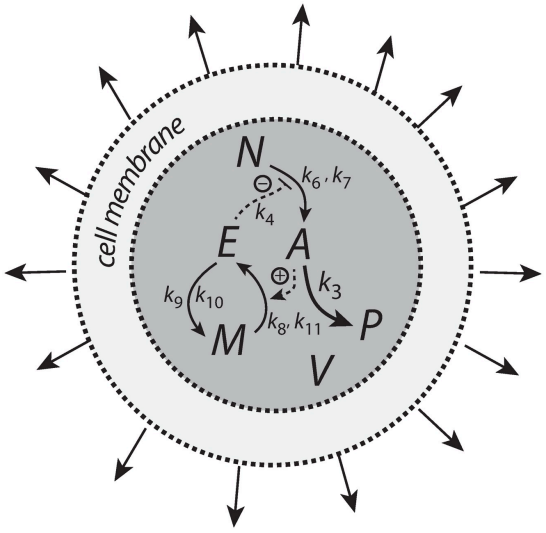

Fig 23. Motif 2 type controller with integral control based on zero-order kinetics and a cell-internally generated compensatory flux from compound *N*.

https://doi.org/10.1371/journal.pone.0207831.g023

Motif 2 zero-order controller

The rate equations for the motif 2 controller using a cell-internal compensatory flux are (Fig 23):

$$\dot{A} = \left(\frac{k_4 \cdot k_6}{k_4 + E}\right) \cdot \left(\frac{N}{k_7 + N}\right) - k_3 \cdot A - A\left(\frac{\dot{V}}{V}\right) \tag{62}$$

$$\dot{E} = \left(\frac{k_8 \cdot M}{k_{11} + M}\right) \cdot A - \frac{k_9 \cdot E}{k_{10} + E} - E\left(\frac{\dot{V}}{V}\right) \tag{63}$$

$$\dot{M} = -\left(\frac{k_8 \cdot M}{k_{11} + M}\right) \cdot A + \frac{k_9 \cdot E}{k_{10} + E} - M\left(\frac{\dot{V}}{V}\right) \tag{64}$$

$$\dot{N} = -\left(\frac{k_4 \cdot k_6}{k_4 + E}\right) \cdot \left(\frac{N}{k_7 + N}\right) - N\left(\frac{\dot{V}}{V}\right) \tag{65}$$

$$\dot{P} = k_3 \cdot A - P\left(\frac{\dot{V}}{V}\right) \tag{66}$$

Fig 24 shows the performance of the motif 2 feedback structure with zero-order integral control. The controller is able to defend successfully A_{set}^{theor} against a linear increase in V (phase 2) as well

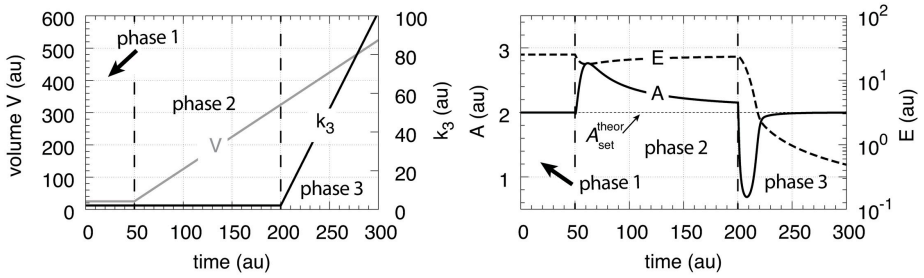

Fig 24. Performance of the motif 2 feedback scheme with zero-order based integral control and a cell-internal compensatory flux. Rate constants and initial conditions: $k_3 = 2.0$, $k_4 = 1 \times 10^{-3}$, $k_6 = 1 \times 10^5$, $k_7 = 1 \times 10^{-6}$, $k_8 = 1.0$, $k_9 = 2.0$, $k_{10} = k_{11} = 1 \times 10^{-6}$, $A_0 = 2.0$, $E_0 = V_0 = 25.0$, $M_0 = 1 \times 10^6$, $N_0 = 3 \times 10^6$. Phase 1: V and k_3 remain unchanged. Phase 2: V increases linearly with $\dot{V} = 2.0$, while k_3 remains constant. Phase 3: V continues to increase and k_3 increases linearly with $\dot{k}_3 = 1.0$.

https://doi.org/10.1371/journal.pone.0207831.g024

as against linear increase in V and a simultaneous linear increase in k_3 (phase 3). For both cases the controller will move A precisely to $A_{set}^{theor} = k_9/k_8$ without any offset (see S6 Text for details).

Case B.2: Controllers with cell-internal compensatory fluxes and exponential time-dependent perturbations

The controllers are exposed to the same exponential perturbation profiles as in Fig 14. The exponential growth of V is written as $\dot{V} = \kappa \cdot V$, where κ (>0) is a constant and related to the doubling time of V given by ln 2/κ.

Fig 25a shows the performance of the motif 1 zero-order controller while Fig 25b shows the responses of the motif 1 antithetic controller. During exponential growth and constant k_3 the motif 1 zero-order and the antithetic controller show slight offsets from the theoretical set-point A_{set}^{theor}, while during phase 3 when both V and k_3 increase exponentially, both controllers break down. Besides their different kinetic implementation of integral control both the motif 1 zero-order and the motif 1 antithetic controller have analogous responses (for details, see S3 and S4 Texts).

Fig 25c shows the response of the autocatalytic controller when $k_E^{in} = k_E^{out} = 1 \times 10^{-5}$. The controller is able to keep A at A_{set}^{theor} during exponential growth while k_3 is kept constant. Only when V and k_3 both increase exponentially then there is an offset from A_{set}^{theor}, which can be estimated as:

$$A_{ss} = \frac{k_4}{k_6} - \frac{\kappa}{k_6} - \frac{\zeta}{k_6} \tag{67}$$

where the theoretical set-point $A_{set}^{theor} = k_4/k_6$ and κ and ζ describe the doubling times ln 2/κ and ln 2/ζ of the exponential increases for V and k_3, respectively (see S5 Text).

In case k_E^{in} and k_E^{out} are large Eq 67 changes to (S5 Text):

$$A_{ss} = \frac{k_4}{k_6} - \frac{\kappa}{k_6} - \frac{\zeta}{k_6} - \frac{k_E^{out}}{k_6} \tag{68}$$

The motif 2 based controller shows in phase 2 a significant overcompensation from A_{set}^{theor} when exposed to exponential growth only. The overcompensated steady state in A at constant

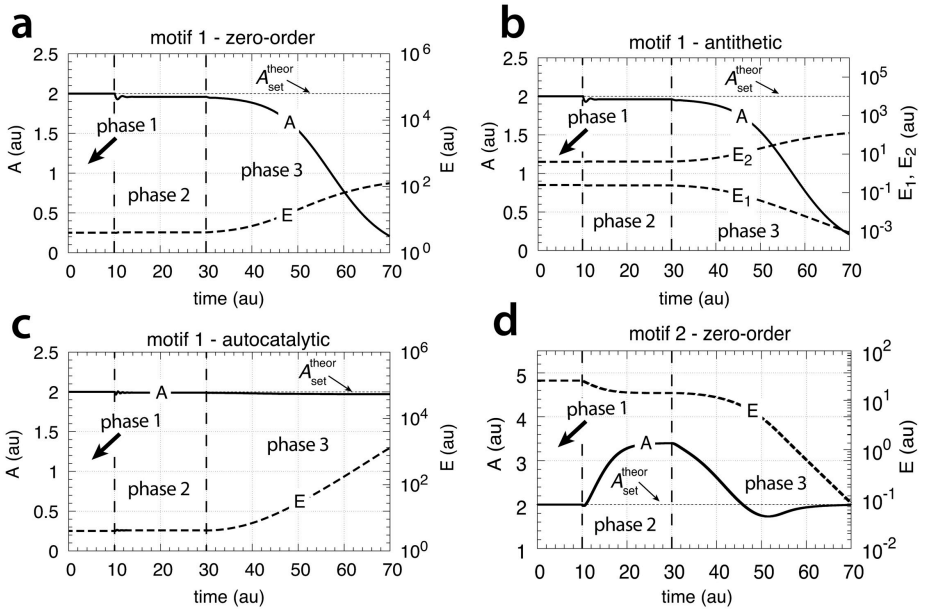

Fig 25. Behaviors of the motif 1 zero-order, antithetic, autocatalytic and motif 2 zero-order controllers with internal compensatory fluxes in response to an exponential increase in V and k_3. Time/perturbation profiles of V and k_3 are the same as in Fig 14. (a) Behavior of the motif 1 zero-order controller. Rate constant values as in Fig 18. Initial concentrations: $A_0 = 2.0$, $E_0 = 4.0$, $V_0 = 25.0$, $M_0 = 4 \times 10^9$, $N_0 = 1 \times 10^6$. (b) Behavior of the antithetic controller. Rate constants as in Fig 20. Initial concentrations: $A_0 = 2.0$, $E_{1,0} = 0.25$, $E_{2,0} = 4.0$, $V_0 = 25.0$, $M_0 = N_0 = O_0 = 1 \times 10^6$, $Q_0 = P_0 = 0.0$. During phase 2 the controller shows a slight but constant offset below A_{set}^{theor}. During phase 3 the controller breaks down when both V and k_3 increase exponentially. (c) Behavior of the autocatalytic controller. Rate constants are as described in Fig 22. Initial concentrations: $A_0 = 2.0$, $E_0 = 4.0$, $V_0 = 25.0$, $M_0 = 4 \times 10^9$, $N_0 = 1 \times 10^7$. During autocatalytic growth only (phase 2) the autocatalytic controller is able to move A_{ss} precisely to A_{set}^{theor}, but shows an offset from A_{set}^{theor} when both k_3 and V increase exponentially). (d) Behavior of the motif 2 based controller (Eqs 62–66). Rate constants and initial conditions as in Fig 24. Note the significant overcompensation (offset above A_{set}^{theor}) during phase 2, but the return to A_{set}^{theor} ($=k_9/k_8$) when k_3 starts to grow exponentially.

https://doi.org/10.1371/journal.pone.0207831.g025

k_3 and exponential growth can be expressed as

$$A_{ss} = A_{set}^{theor} + \frac{\kappa}{k_8} E_{ss} \tag{69}$$

where $A_{set}^{theor} = k_9/k_8$ and $(\kappa/k_8)E_{ss}$ is the overcompensated offset (S6 Text).

The response kinetics of the motif 2 based controller is mostly determined by k_4, which reflects the derepression property by E. For large k_4 the derepression by E is observed to be slow and less effective.

Remarkably, when both k_3 and V increase exponentially in phase 3 the controller is able to move A close to A_{set}^{theor}. For this case A_{ss} can be written as (S6 Text)

$$A_{ss} = \left(\frac{\gamma_0}{1+\gamma_0}\right) A_{set}^{app} \tag{70}$$

where

$$\gamma_0 = \frac{k_4 k_6 k_8}{\dot{k_3}(k_4 + E(t))^2} \tag{71}$$

and

$$A_{set}^{app} = A_{set}^{theor} + \frac{\kappa}{k_8} E(t) \tag{72}$$

Note that during phase 3 E is not in a steady state, but decreases due to the controller's derepression, while $\dot{k_3}$ increases exponentially. However, the derepression kinetics by E are faster than the exponential increase of $\dot{k_3}$ (Eq 71), such that γ_0 increases and A_{set}^{app} and A_{ss} approach A_{set}^{theor} (S6 Text).

Growth related to the surface to volume ratio and controllers with cell-internal compensatory fluxes

Here we show how the four controllers having cell internal compensatory fluxes perform with respect to a surface to volume ratio related growth law as found for spherical bacteria ([9, 10, 13], Eq 2). We consider again three phases as in the previous sections, but with the difference that V now grows according to Eq 2 with $\eta = 1$ and $\xi = 0.2$ (Fig 26a). The values of η and ξ are arbitrarily chosen. The outflow perturbation, described by k_3, is kept constant during phases 1 and 2, but increases exponentially during phase 3 (Eq 49). The response behaviors of the controllers towards increasing volume (when k_3 is kept constant) is initially very similar to that when V increases linearly. However, the motifs gain more and more control as $\dot{V}$ decreases, provided that there is sufficient material in the cell to generate enough E's (for the motif 1 controllers) or that there is still sufficient E left (for the motif 2 controller) to keep the negative feedback loop operating.

As an example, Fig 26 shows the behavior of the motif 1 antithetic and autocatalytic controllers and the motif 2 zero-order controller when k_3 in phase 3 increases exponentially as described by Fig 14 and compensatory fluxes are generated cell internally. The motif 1 zero-order controller's behavior (not shown) is again very similar in comparison with the motif 1 antithetic controller.

Overview of results

Tables 1 and 2 gives an overview of controller performances by dividing perturbations into (i) linear V only, (ii) linear V and k_3, (iii) exponential V only, and (iv) exponential V and k_3. Controller performances are described by the four categories *perfect adaptation*, *partial adaptation*, *over-adaptation*, and *breakdown*. Perfect adaptation means that the controller is able to keep A at A_{set}^{theor}. A controller with partial adaptation can maintain a constant A value during an applied outflow perturbation, but below A_{set}^{theor}. A controller showing over-adaptation keeps A above A_{set}^{theor} even when the perturbation leads to a decrease in A. Controller breakdown means that the controller is unable to withstand the perturbation and A goes to zero.

Concerning the results with respect to surface/volume related growth we group this growth law together with the category of linear growth, because controllers behave initially quite similar towards these two growth laws (compare phases 2 in Fig 16b–16d with respective phase 2 behaviors of Figs 9, 11 and 13 and phases 2 in Fig 26b–26d with the phase 2 behaviors of Figs 20, 22 and 24, respectively).

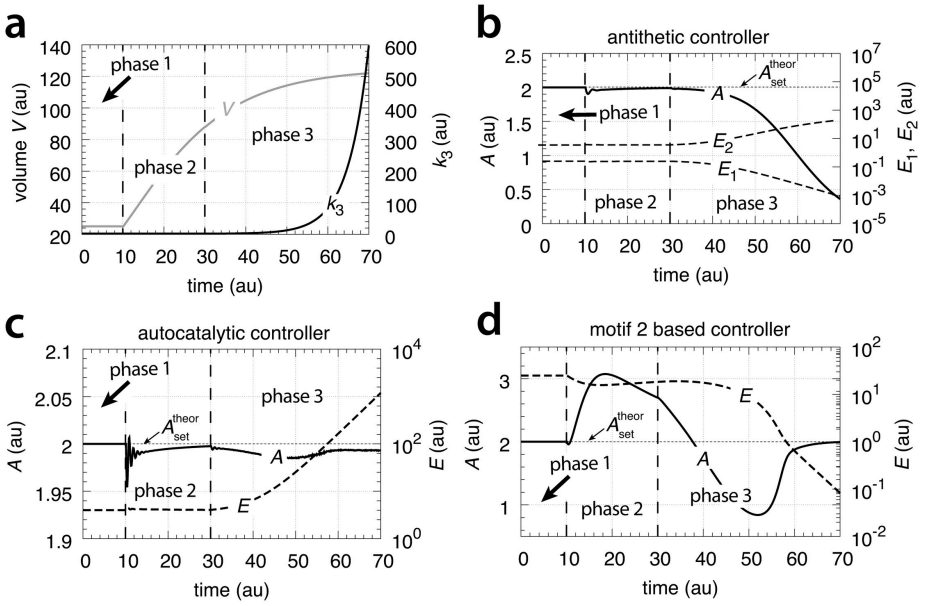

Fig 26. Performance of the antithetic, autocatalytic and motif 2 based controllers towards surface/volume related growth in V and exponentially increasing outflow perturbation k_3 with cell-internal compensatory flux. Rate constant values and initial conditions as in Fig 25.

https://doi.org/10.1371/journal.pone.0207831.g026

Clearly, motif 1 controllers based on zero-order or on antithetic integral control, cannot oppose an exponential volume increase or when an additional exponential increase in k_3 is applied. When exponentially increasing perturbations are applied the motif 1 autocatalytic controller shows good performances with a stable offset in A below A^{theor}_{set}, but requires the presence of sufficient controller species E to maintain autocatalysis. The motif 2 controller using zero-order based integral control shows best performance, and is able to keep A at A^{theor}_{set}, even when both V and k_3 increase exponentially. However, the drawback of controllers based on derepression, like motif 2, is that controller breakdown occurs when concentrations of the derepressing control species is getting too low.

Table 1. Performance of controllers based on internal generated compensatory fluxes.

controller type	linear V only	linear V and k_3	exponential V only	exponential V and k_3
m1—zero-order	perfect adaptation	partial adaptation	breakdown	breakdown
m1—antithetic	perfect adaptation	partial adaptation	breakdown	breakdown
m1—autocatalytic	perfect adaptation	perfect adaptation	perfect adaptation	partial adaptation
m2—zero-order	perfect adaptation	perfect adaptation	over-adaptation	perfect adaptation

https://doi.org/10.1371/journal.pone.0207831.t001

Table 2. Performance of controllers based on transporter based compensatory fluxes.

controller type	linear V only	linear V and k_3	exponential V only	exponential V and k_3
m1—zero-order	partial adaptation	breakdown	breakdown	breakdown
m1—antithetic	partial adaptation	breakdown	breakdown	breakdown
m1—autocatalytic	perfect adaptation	perfect adaptation	partial adaptation	partial adaptation
m2—zero-order	perfect adaptation	perfect adaptation	perfect adaptation	perfect adaptation

https://doi.org/10.1371/journal.pone.0207831.t002

Discussion

Internal model principle and the kinetic limit of controllers

From Tables 1 and 2 it is seen that the motif 2 controller outperforms the other controllers. The derepression kinetics of the motif 2 controller is described by the term (Eqs 43 and 62):

$$f_{inhib}(E) = \frac{k_4}{k_4 + E} \tag{73}$$

which is an essential part in generating the compensatory flux in A. For decreasing (derepressing) $E\,f_{inhib}(E)$ increases with hyperbolic response kinetics, i.e. having exponentially increasing doubling times. The motif 2 controller is therefore able, as observed [18], to counteract hyperbolically decreasing concentrations in A. The balancing between a perturbation and the by the perturbation induced compensatory flux reflects the *Internal Model Principle* [25–27], which states that if a controller is able to oppose a perturbation, then the controller has the capability to generate that kind of perturbation internally. For the motif 2 controller the hyperbolic response kinetics represents the upper kinetic limit which the controller can handle. In addition, the motif 2 controller will handle any perturbing rate laws with doubling times lower than an exponential (constant doubling times relate to an exponential rate law), although overcompensation may occur as seen in Fig 25d.

Thus, as indicated in Tables 1 and 2 controllers group according to their kinetic limits, where the motif 2 controller with hyperbolic response kinetics performs better than controllers based on exponential/autocatalytic or linear responses.

Repression/derepression kinetics are ubiquitously used in homeostatic mechanisms (see Supplementary Material in [7]), in gene on/off regulations [28–30] and as rhythm generators [31, 32]. The fast response of derepression is also used in signaling [33], but may be needed to be kept under additional control as indicated in a study of the nitrogenase switch [30] to avoid overenhanced/overcompensated responses.

Breakdown of the motif 2 controller occurs when the compensatory flux has reached its maximum value (described by rate constant k_2 in Figs 12 and 23).

A somewhat surprising behavior of the motif 2 controller is its overcompensation when growth increases exponentially at constant k_3 (see phase 2 in Fig 25d). The overcompensation can be described analytically (Eq 69). Its origin is due to the fact that with a cell-internal compensatory flux an exponetial increase in V at constant k_3 allows for steady states in A and E, independent of V, where A_{ss} is *larger* than A_{set}^{theor} (S6 Text).

Performance improvement by increased controller aggressiveness

Although the motif 1 zero-order and the antithetic controllers break down when exposed to exponential growth and perturbations (Figs 15a and 15b and 25a and 25b), their performance can be significantly improved at constant $\dot{V}$ by increasing of what can be described as the

controllers' aggressiveness. By aggressiveness of a controller we mean loosely the controller's response to a perturbation in terms of (mainly) quickness and precision. Increasing the aggressiveness of a controller will generally lead to a quicker controller response and an improved controller precision.

The aggressiveness of an integral controller can be varied by the controller's gain. The gain is a factor in front of the error integral. For an ideal motif 1 zero-order integral controller (working at constant V and k_3) $\dot{E}$ is proportional to the error $e = (A_{set}^{theor} - A)$ [7], i.e.,

$$\dot{E} = k_6\left(\frac{k_4}{k_6} - A\right) \tag{74}$$

where k_6 is the controller gain and k_4/k_6 is the controller's theoretical set-point, A_{set}^{theor}. As indicated by Eq 74 the concentration of E is proportional to the integrated error with respect to time. By increasing k_6 and k_4 such that A_{set}^{theor} remains unchanged the gain of the controller is increased and the controller becomes more aggressive.

For constant $\dot{V}$ and k_3 the steady state of A for the motif 1 zero-order controller is given by Eq 20

$$A_{ss} = \frac{k_4}{k_6 + \frac{2\dot{V}k_3}{k_2}} \tag{20}$$

where the offset in A_{ss} below A_{set}^{theor} is due to the term $2\dot{V}k_3/k_2$. This term indicates that for increasing $\dot{V}$ and/or increasing k_3 values the controller will break down and A will go to zero as observed in Fig 15a. There are two ways the controller's aggressiveness can be increased. One way, as indicated above, is by increasing k_4 and k_6 such that $A_{set}^{theor} = k_4/k_6$ is preserved with k_6 becoming much larger than $2\dot{V}k_3/k_2$. As a result the controller's response kinetics become quicker and A_{ss} moves closer to $A_{set}^{theor} = k_4/k_6$. The other way is to increase k_2, which means to increase the activity of the transporter. In a synthetic biology context this could be done by over-expressing the genes which code for the transporter. On the other hand, "normal" cells may already have optimized controller aggressiveness or may change it in response to environmental conditions.

Similar arguments apply also for the antithetic controller. Qian et al. [34] have shown that when the controller dynamics become faster than growth this leads to an improved controller performance.

Fig 27 shows the results of increasing the aggressiveness of the motif 1 zero-order and antithetic controllers by increasing k_2 from 1.0 to 1×10^3. The perturbation is divided into three phases. During the first phase the volume V is kept constant at 25.0 and the controllers are at their set-points. In phase 2 the volume increases with a constant rate ($\dot{V} = 1.0$). Finally, in phase 3 V continues to grow with $\dot{V} = 1.0$ but k_2 is increased to 1×10^3. Both controllers show improved precisions, but show different kinetics in their way to reach A_{set}^{theor}.

Similar is the situation when the compensatory flux is internally generated. Eq 55 shows the steady state in A for the motif 1 zero-order controller. Also here increasing k_2 values will move A_{ss} towards the theoretical set-point $A_{set}^{theor} = k_4/k_6$.

Aggressiveness can also be increased for the autocatalytic controller by increasing k_4 and k_6 such that the k_4/k_6 ratio is maintained. This will move the steady state in A closer to its theoretical set-point as offsets become smaller (Eqs S14 and S20 in S5 Text).

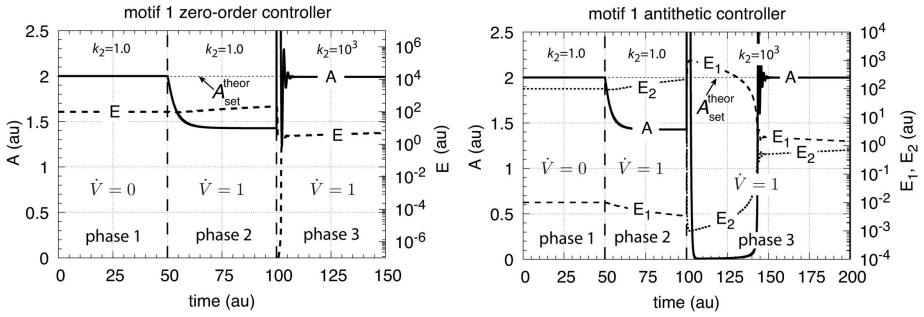

Fig 27. Increased transporter activity (k_2 values) lead to increased aggressiveness and improved controller precision for transporter-based motif 1 zero-order controller (left panel) and motif 1 antithetic controller (right panel) during constant growth (see Figs 6 and 8). Phase 1: controllers are at their steady state, no growth, $k_2 = 1.0$. Phase 2: constant growth ($\dot{V} = 1.0$) and $k_2 = 1.0$. Both controllers show an offset in A_{ss} below A_{set}^{theor}. Phase 3: constant growth continues but k_2 is increased to 1×10^3. Both controllers show improved precision and have their A_{ss} close to A_{set}^{theor}, but show different adaptation kinetics during the transition from phase 2 to phase 3. Rate parameters and initial concentrations, zero-order controller: $k_3 = 2.0$, $k_4 = 20.0$, $k_5 = 1 \times 10^{-6}$, $k_6 = 10.0$, $k_7 = 1 \times 10^{-6}$, $A_0 = 2.0$, $E_0 = 100.0$, $V_0 = 25.0$, $M_0 = 1 \times 10^7$. Rate parameters and initial concentrations, antithetic controller: $k_3 = 2.0$, $k_4 = 10.0$, $k_5 = 1 \times 10^{-6}$, $k_6 = 10.0$, $k_8 = 20.0$, $k_9 = 1 \times 10^{-6}$, $A_0 = 2.0$, $E_{1,0} = 1 \times 10^{-2}$, $E_{2,0} = 1 \times 10^2$, $V_0 = 25.0$, $M_0 = O_0 = 1 \times 10^8$.

https://doi.org/10.1371/journal.pone.0207831.g027

Roles of kinetic implementations of integral control and negative feedback structures

For the transporter-based cases the increased aggressiveness of the motif 1 zero-order and antithetic controllers allows them to defend their theoretical set-points as long as (see Eqs 20 and 29)

$$k_6 \text{ (or } k_4) \gg 2\dot{V}\left(\frac{k_3}{k_2}\right) \tag{75}$$

However, for exponentially increasing V and $\dot{V}$ this can be achieved only for a certain (often short) time period. The motif 1 zero-order controller will break down when Eq 75 is no longer fulfilled. On the other hand, as shown above, the autocatalytic motif 1 controller is able to maintain a stable steady state in A, although with an offset from A_{set}^{theor}, when V and k_3 increase exponentially (but also here dependent on the controller's aggressiveness). As Eq 38 (for the transporter-based compensatory flux) indicates, any time-dependent perturbation of the type $k_3(t) = k_{3,0} + a{\cdot}t^n$ ($a, n > 0$) will be successfully defended by the autocatalytic controller, because $\dot{k_3}/k_3 \to 0$ (S5 Text) and thereby restoring the controller's theoretical set-point. However, breakdown may occur if no sufficient supply of E (for example via M, Fig 11) can be maintained.

The sudden breakdown of a fully adapted controller due to capacity limits or exhaustion of the controller variables E or E_1/E_2 has an interesting analogy in physiology described by Selye's *General Adaptation Syndrome* (GAS) [35]. When an animal is exposed to constant but severe stress (for example cold temperatures) the animal can stay, after an alarm reaction, in a stage of resistance, where the animal appears perfectly adapted to its environment. However, after a certain time there appears the stage of exhaustion and the animal dies, despite of sufficient food supplies. To understand the sudden and unexpected breakdown of adaptation, Selye introduced the concept of *adaptation energy* [36]. In our analogous examples here, the

adaptation energy can be associated with the amounts of precursors M, N, and O, and with the maximum controller capacity, described by the maximum rate a compensatory flux can deliver. Although our single loop controllers are a far cry from a physiologically regulated system, the analogy to Selye's GAS is thought-provoking.

Our results indicate that the type of kinetics realizing integral control and the structure of the negative feedback loop play essential roles in how a controller will perform. The antithetic integral controller has in the literature [22, 37, 38] so far only been considered in a motif 1 setting based on activation (Fig 1). However, its second-order integral controller part can be embedded into other feedback structures (S7 Text). Although the intension of this work was not to consider novel implementations of the antithetic integral controller, it is illustrative to see the controller's improvement and limitations when considering the antithetic controller in a motif 2 background. Fig 28 shows two such implementations, one with a transporter based compensatory flux and the other with a cell internal one.

When merging the motif 2 structure with the antithetic integral controller, we keep the antithetic controller's rate constant values, but change the k_2 and the inhibition constant (k_{10}) values to those used in the motif 2 controller calculations. For the transporter based motif 2 antithetic controller Eq 21 is now replaced by

$$\dot{A} = \frac{k_2 \cdot k_{10}}{k_{10} + E_1} \cdot \frac{1}{V} - k_3 \cdot A - A\left(\frac{\dot{V}}{V}\right) \tag{76}$$

while for the controller with a cell internal compensatory flux, Eq 56 is replaced by

$$\dot{A} = \left(\frac{N}{k_7 + N}\right) \cdot \left(\frac{k_2 k_{10}}{k_{10} + E_1}\right) - k_3 \cdot A - A\left(\frac{\dot{V}}{V}\right) \tag{77}$$

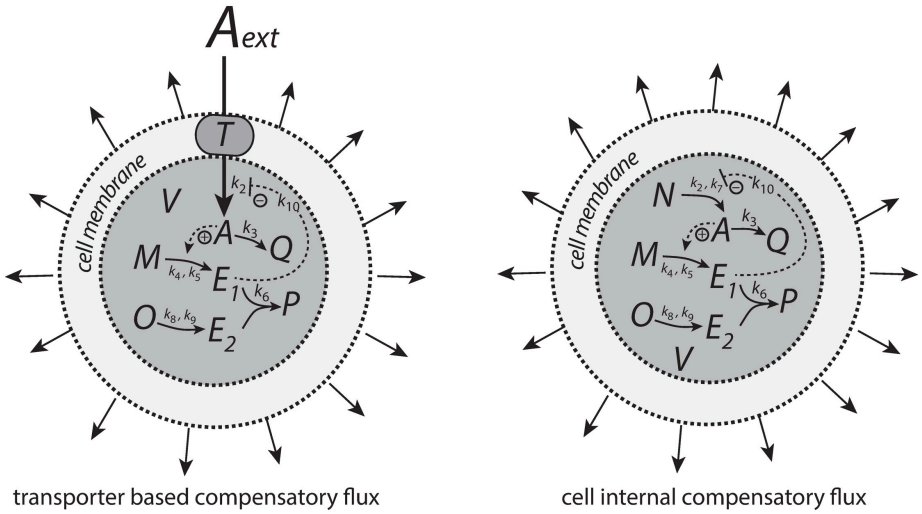

Fig 28. Antithetic integral controllers with motif 2 feedback structure and transporter based and cell internal compensatory fluxes.

https://doi.org/10.1371/journal.pone.0207831.g028

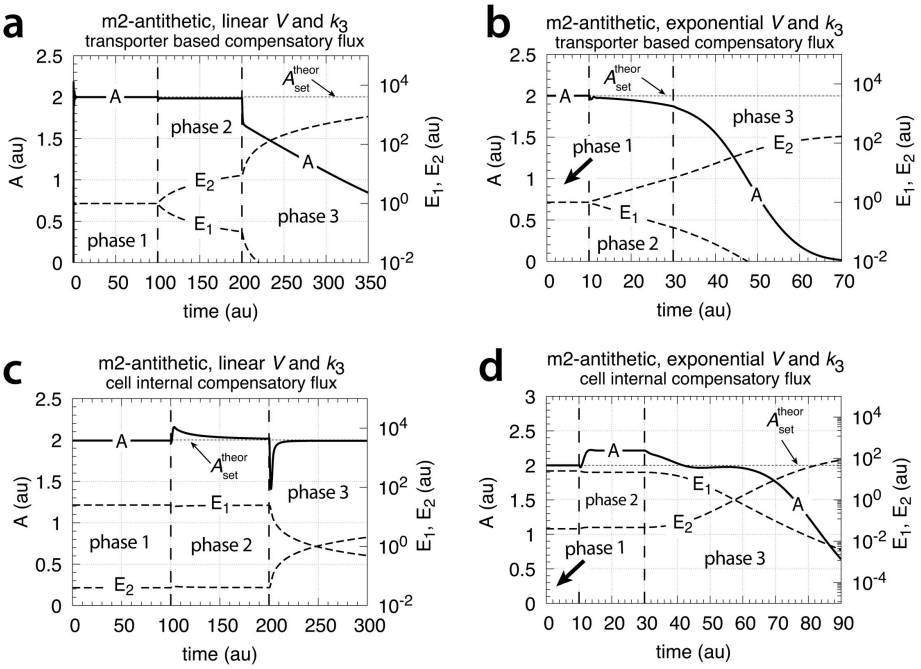

Fig 29. Performance of the antithetic controller in a motif 2 (m2) structural background (Fig 28). (a) The controller has a transporter mediated compensatory flux and is exposed to linear growth and increase in k_3 as in Fig 9a. Same rate constants and initial concentrations as in Fig 9 with the exception that $k_2 = 1 \times 10^5$, and $k_{10} = 1 \times 10^{-3}$. Note the minor offset in A during phase 2. (b) Same controller with rate constants as in (a), but exposed to exponential volume and k_3 increases as in Fig 14. Initial concentrations: $A_0 = 2.0$, $E_{1,0} = E_{2,0} = 1.0$, $M_0 = O_0 = 1 \times 10^5$. The controller is not able to oppose exponential growth. (c) Controller with a cell internal compensatory flux (Fig 28) and exposed to the conditions as in Fig 20. Same rate constants as in (a). Initial concentrations: $A_0 = 2.0$, $E_{1,0} = E_{2,0} = 25.0$, $M_0 = O_0 = 2 \times 10^5$, $N_0 = O_0 = 1 \times 10^6$. The controller is fully capable to oppose linear growth together with a linear increase in k_3. (d) Same controller with rate constants as in (c), but exposed to exponential volume and k_3 increases as in Fig 14. Initial concentrations as in (c), but to avoid depletion of M and O initial concentrations of these compounds were raised to 1×10^6. Note also here the overcompensation in the case growth occurs exponentially in phase 2. Despite the larger consumption rates of M and O in comparison with (c) the controller is not able to counteract both exponential increases in V and k_3. See S7 Text for more details.

https://doi.org/10.1371/journal.pone.0207831.g029

The other rate equations (Eqs 22–27) remain unchanged. Fig 29 shows the results when linear and exponential growth and k_3 changes (see Figs 9a and 14) are applied to the controllers in Fig 28.

In comparison with the motif 1 antithetic structure, the usage of the motif 2 negative feedback shows a clear improvement in the antithetic controllers' performance (compare Fig 29a, 29b, 29c and 29d with Figs 9, 15, 20 and 25, respectively). The feedback design based on a cell internal compensatory flux shows again a better performance in comparison when the compensatory flux is transporter based. On the other hand, when both V and k_3 increase exponentially both motif 2 antithetic controllers are not able to keep A at a constant steady state. The

reason for this is that the rate of derepression/removal in E_1 is limited by its reaction with E_2 and thereby is slower than the E removal in the motif 2 zero-order case.

From a biochemical perspective one may question how realistic a second-order removal of E_1 and E_2 is. Since practically all physiological reactions within a cell are catalyzed by enzymes, it appears to be an interesting alternative to study the performance of controllers when an enzyme uses E_1 and E_2 as substrates.

With respect to the autocatalytic implementation to achieve integral control [19–21], the occurrence of autocatalysis and positive feedback loops are becoming more and more recognized in signaling and homeostatic regulation [39–41]. As an illustration, in cortisol homeostasis ACTH signaling from the brain-pituitary system to the cortisol producing adrenals occurs by autocatalysis/positive feedback [42]. In blood sugar homeostasis insulin secretion is activated by several positive feedback/autocatalytic signaling pathways [43–45] to ensure an effective regulation in glucose concentration. These examples indicate the importance of additional "helper kinetics" (such as autocatalysis/positive feedback) to obtain a homeostatic regulation with optimum response and precision properties. For synthetic biology this means that knowledge about controller structure and their inherent kinetics are important aspects in the design and implementation of artificial regulatory units when trying to oppose the dilution effects of growth or other time-dependent perturbations.

Outlook

The approach taken here is based on ordinary mass action kinetics and thereby is purely deterministic. In addition, we made the assumption that the cellular volume is well-mixed and homogenous. Both assumptions are subject to certain criticism, when applied to biochemical reactions within a cell. While in many cases a chemically reacting system can be treated as a continuous deterministic process, in other cases, in particular when the number of reacting molecules becomes low, reactions may better be described as discrete stochastic processes [46–48]. However, many, if not most of the stochastic approaches to describe cellular processes still treat (and require) that systems are treated as homogenous, thereby neglecting "recruiting" or "funneling" mechanisms which occur, for example, on the surface of cellular membranes, involve multiprotein complexes ("antenna") in photon harvesting [49], or use substrate channeling ("tunnels") in enzyme-catalyzed reactions [50].

Ignoring these spatial aspects, it may be mentioned, that the controller motifs 1 and 2 (Fig 1) based on zero-order and first-order autocatalysis are well-described by the Gillespie algorithm [46] and show an excellent correspondence between the stochastic and deterministic approach (P. Ruoff, unpublished results). The motif 1 antithetic controller has been shown to work well under stochastic conditions by exploiting noise, and achieves regulation where a similar deterministic approach apparently fails [21]. How these controllers behave under time-dependent perturbations and stochastic conditions is an interesting aspect which we would like to investigate in a later work.

Nevertheless, we feel that the deterministic calculations presented here give a first ranking between the various integral controllers when exposed to different growth laws and dilution kinetics.

Supporting information

S1 Matlab. A set of Matlab files showing the results of Figs 4, 7, 9, 11, 13, 15, 18, 20, 22, 24, 25, 26 and 27.
(ZIP)

S1 Text. Steady state of cell-internal-generated compound *A* without negative feedback.
(PDF)

S2 Text. Steady state of transporter-generated compound *A* without negative feedback.
(PDF)

S3 Text. Steady states and theoretical set-point for motif 1 zero-order controller.
(PDF)

S4 Text. Steady states and theoretical set-point for motif 1 second-order (antithetic) controller.
(PDF)

S5 Text. Steady states and theoretical set-point for motif 1 autocatalytic controller.
(PDF)

S6 Text. Steady states and theoretical set-point for motif 2 zero-order controller.
(PDF)

S7 Text. Novel antithetic integral controller arrangements and steady states in a motif 2 background.
(PDF)

Author Contributions

Conceptualization: Peter Ruoff, Oleg Agafonov.

Formal analysis: Peter Ruoff, Oleg Agafonov, Kristian Thorsen, Tormod Drengstig.

Investigation: Peter Ruoff, Oleg Agafonov, Tormod Drengstig.

Methodology: Peter Ruoff.

Project administration: Peter Ruoff.

Software: Peter Ruoff, Daniel M. Tveit, Tormod Drengstig.

Validation: Peter Ruoff, Oleg Agafonov, Daniel M. Tveit, Tormod Drengstig.

Visualization: Peter Ruoff.

Writing – original draft: Peter Ruoff.

References

1. Cannon W. Organization for Physiological Homeostatics. Physiol Rev. 1929; 9:399–431. https://doi.org/10.1152/physrev.1929.9.3.399
2. Langley LL, editor. Homeostasis. Origins of the Concept. Stroudsbourg, Pennsylvania: Dowden, Hutchinson & Ross, Inc.; 1973.
3. Bernard C. An Introduction to the Study of Experimental Medicine. English translation of the 1865 French edition by Henry Copley Greene. Dover: Macmillan & Co., Ltd; 1957.
4. Mrosovsky N. Rheostasis. The Physiology of Change. New York: Oxford University Press; 1990.
5. Risvoll GB, Thorsen K, Ruoff P, Drengstig T. Variable setpoint as a relaxing component in physiological control. Physiological Reports. 2017; 5(17):e13408. https://doi.org/10.14814/phy2.13408 PMID: 28904081
6. Ni XY, Drengstig T, Ruoff P. The control of the controller: Molecular mechanisms for robust perfect adaptation and temperature compensation. Biophys J. 2009;p. https://doi.org/10.1016/j.bpj.2009.06.030 PMID: 19720012
7. Drengstig T, Jolma I, Ni X, Thorsen K, Xu X, Ruoff P. A basic set of homeostatic controller motifs. Biophys J. 2012; 103(9):2000–2010. https://doi.org/10.1016/j.bpj.2012.09.033 PMID: 23199928

8. Thorsen K, Agafonov O, Selstø CH, Jolma IW, Ni XY, Drengstig T, et al. Robust Concentration and Frequency Control in Oscillatory Homeostats. PLOS ONE. 2014; 9(9):e107766. https://doi.org/10.1371/journal.pone.0107766 PMID: 25238410
9. von Bertalanffy L. Metabolic types and growth types. The American Naturalist. 1951; 85(821):111–117. https://doi.org/10.1086/281659
10. von Bertalanffy L. Quantitative laws in metabolism and growth. The Quarterly Review of Biology. 1957; 32(3):217–231. https://doi.org/10.1086/401873 PMID: 13485376
11. Smith JH. On the early growth rate of the individual fungus hypha. New Phytologist. 1924; 23(2):65–78. https://doi.org/10.1111/j.1469-8137.1924.tb06621.x
12. Schmalhausen I, Bordzilowskaja N. Das Wachstum niederer Organismen. I. Das Individuelle Wachstum der Bakterien und Hefe. Wilhelm Roux' Archiv für Entwicklungsmechanik der Organismen. 1930; 121(4):726–754.
13. von Bertalanffy L. Principles and Theory of Growth. In: Nowinski WW, editor. Fundamental Aspects of Normal and Malignant Growth. Elsevier; 1960. p. 137–259.
14. Wilkie J, Johnson M, Reza K. Control Engineering. An Introductory Course. New York: Palgrave; 2002.
15. Yi TM, Huang Y, Simon MI, Doyle J. Robust perfect adaptation in bacterial chemotaxis through integral feedback control. PNAS. 2000; 97(9):4649–53. https://doi.org/10.1073/pnas.97.9.4649 PMID: 10781070
16. El-Samad H, Goff JP, Khammash M. Calcium homeostasis and parturient hypocalcemia: an integral feedback perspective. J Theor Biol. 2002; 214(1):17–29. https://doi.org/10.1006/jtbi.2001.2422 PMID: 11786029
17. Kitano H. Towards a theory of biological robustness. Mol Sys Biol. 2007; 3:1–7.
18. Fjeld G, Thorsen K, Drengstig T, Ruoff P. The Performance of Homeostatic Controller Motifs Dealing with Perturbations of Rapid Growth and Depletion. The Journal of Physical Chemistry B. 2017; 121:6097–6107. https://doi.org/10.1021/acs.jpcb.7b01989 PMID: 28571313
19. Drengstig T, Ni XY, Thorsen K, Jolma IW, Ruoff P. Robust Adaptation and Homeostasis by Autocatalysis. J Phys Chem B. 2012; 116:5355–5363. https://doi.org/10.1021/jp3004568 PMID: 22506960
20. Shoval O, Goentoro L, Hart Y, Mayo A, Sontag E, Alon U. Fold-change detection and scalar symmetry of sensory input fields. PNAS. 2010;p. 201002352. https://doi.org/10.1073/pnas.1002352107 PMID: 20729472
21. Briat C, Zechner C, Khammash M. Design of a synthetic integral feedback circuit: dynamic analysis and DNA implementation. ACS Synthetic Biology. 2016; 5(10):1108–1116. https://doi.org/10.1021/acssynbio.6b00014 PMID: 27345033
22. Briat C, Gupta A, Khammash M. Antithetic integral feedback ensures robust perfect adaptation in noisy biomolecular networks. Cell Systems. 2016; 2(1):15–26. https://doi.org/10.1016/j.cels.2016.01.004 PMID: 27136686
23. Radhakrishnan K, Hindmarsh AC. Description and Use of LSODE, the Livermore Solver for Ordinary Differential Equations. NASA Reference Publication 1327, Lawrence Livermore National Laboratory Report UCRL-ID-113855. Cleveland, OH 44135-3191: National Aeronautics and Space Administration, Lewis Research Center; 1993.
24. Thorsen K, Ruoff P, Drengstig T. Antagonistic regulation with a unique setpoint, integral and double integral action. bioRxiv. 2018;p. 248682.
25. Francis BA, Wonham WM. The Internal Model Principle of Control Theory. Automatica. 1976; 12 (5):457–465. https://doi.org/10.1016/0005-1098(76)90006-6
26. Isidori A, Byrnes CI. Output Regulation of Nonlinear Systems. IEEE Transactions on Automatic Control. 1990; 35(2):131–140. https://doi.org/10.1109/9.45168
27. Sontag ED. Adaptation and regulation with signal detection implies internal model. Systems & Control Letters. 2003; 50(2):119–126. https://doi.org/10.1016/S0167-6911(03)00136-1
28. Jacob F, Monod J. On the regulation of gene activity. In: Cold Spring Harbor Symposia on Quantitative Biology. vol. 26. Cold Spring Harbor Laboratory Press; 1961. p. 193–211.
29. Umbarger HE. Feedback control by endproduct inhibition. In: Cold Spring Harbor symposia on quantitative biology. vol. 26. Cold Spring Harbor Laboratory Press; 1961. p. 301–312.
30. Poza-Carrión C, Jiménez-Vicente E, Navarro-Rodríguez M, Echavarri-Erasun C, Rubio LM. Kinetics of nif gene expression in a nitrogen-fixing bacterium. Journal of Bacteriology. 2014; 196(3):595–603. https://doi.org/10.1128/JB.00942-13 PMID: 24244007
31. Goodwin BC. Temporal Organization in Cells. Academic Press; 1963.

32. Forger DB. Biological Clocks, Rhythms, and Oscillations: The Theory of Biological Timekeeping. MIT Press; 2017.
33. Lim B, Samper N, Lu H, Rushlow C, Jiménez G, Shvartsman SY. Kinetics of gene derepression by ERK signaling. PNAS. 2013; 110(25):10330–10335. https://doi.org/10.1073/pnas.1303635110 PMID: 23733957
34. Qian Y, Del Vecchio D. Realizing 'integral control' in living cells: how to overcome leaky integration due to dilution? Journal of The Royal Society Interface. 2018; 15(139):20170902. https://doi.org/10.1098/rsif.2017.0902
35. Selye H. The Stress of Life. Revised Edition. New York: McGraw-Hill; 1975.
36. Selye H. Experimental evidence supporting the conception of "adaptation energy". American Journal of Physiology. 1938; 123(3):758–765. https://doi.org/10.1152/ajplegacy.1938.123.3.758
37. Ferrell JE Jr. Perfect and near-perfect adaptation in cell signaling. Cell Systems. 2016; 2(2):62–67. https://doi.org/10.1016/j.cels.2016.02.006 PMID: 27135159
38. Gómez-Schiavon M, El-Samad H. Complexity-aware simple modeling. Current Opinion in Microbiology. 2018; 45:47–52. https://doi.org/10.1016/j.mib.2018.01.004 PMID: 29494832
39. DeAngelis DL, Post WM, Travis CC. Positive Feedback in Natural Systems. Springer Science & Business Media; 1980.
40. Becskei A, Séraphin B, Serrano L. Positive feedback in eukaryotic gene networks: cell differentiation by graded to binary response conversion. The EMBO Journal. 2001; 20(10):2528–2535. https://doi.org/10.1093/emboj/20.10.2528 PMID: 11350942
41. Angeli D, Ferrell JE, Sontag ED. Detection of multistability, bifurcations, and hysteresis in a large class of biological positive-feedback systems. PNAS. 2004; 101(7):1822–1827. https://doi.org/10.1073/pnas.0308265100 PMID: 14766974
42. Peters A, Conrad M, Hubold C, Schweiger U, Fischer B, Fehm HL. The principle of homeostasis in the hypothalamus-pituitary-adrenal system: new insight from positive feedback. American Journal of Physiology-Regulatory, Integrative and Comparative Physiology. 2007; 293(1):R83–R98. https://doi.org/10.1152/ajpregu.00907.2006 PMID: 17459911
43. Thomas MK, Rastalsky N, Lee JH, Habener JF. Hedgehog signaling regulation of insulin production by pancreatic beta-cells. Diabetes. 2000; 49(12):2039–2047. https://doi.org/10.2337/diabetes.49.12.2039 PMID: 11118005
44. Leibiger IB, Leibiger B, Berggren PO. Insulin feedback action on pancreatic β-cell function. FEBS Letters. 2002; 532(1-2):1–6. https://doi.org/10.1016/s0014-5793(02)03627-x PMID: 12459452
45. Jacques-Silva MC, Correa-Medina M, Cabrera O, Rodriguez-Diaz R, Makeeva N, Fachado A, et al. ATP-gated P2X3 receptors constitute a positive autocrine signal for insulin release in the human pancreatic β cell. PNAS. 2010; 107(14):6465–6470. https://doi.org/10.1073/pnas.0908935107 PMID: 20308565
46. Gillespie DT. Exact stochastic simulation of coupled chemical reactions. The Journal of Physical Chemistry. 1977; 81(25):2340–2361. https://doi.org/10.1021/j100540a008
47. Gillespie DT. A rigorous derivation of the chemical master equation. Physica A. 1992; 188(1-3):404–425. https://doi.org/10.1016/0378-4371(92)90283-V
48. Wilkinson DJ. Stochastic Modelling for Systems Biology. Chapman and Hall/CRC; 2006.
49. Fromme P. Photosynthetic protein complexes: a structural approach. John Wiley & Sons; 2008.
50. Huang X, Holden HM, Raushel FM. Channeling of substrates and intermediates in enzyme-catalyzed reactions. Annual Review of Biochemistry. 2001; 70(1):149–180. https://doi.org/10.1146/annurev.biochem.70.1.149 PMID: 11395405

Supporting Material, File S1 Text

Homeostatic Controllers Compensating for Growth and Perturbations

P. Ruoff[1*], O. Agafonov[1], D. M. Tveit[2], K. Thorsen[2], T. Drengstig[2]
[1]Centre for Organelle Research
[2]Department of Electrical Engineering and Computer Science,
University of Stavanger, Stavanger, Norway

[*]Corresponding author. Address: Centre for Organelle Research, University of Stavanger, N-4036 Stavanger, Norway, Tel.: (47) 5183-1887, Fax: (47) 5183-1750, E-mail: peter.ruoff@uis.no

Steady state of cell-internal-generated compound A without negative feedback

Integrating $\dot{V}{=}k_1$ from V_0 to $V(t)$ and from time zero to time t gives

$$V(t) = k_1 t + V_0 \tag{S1}$$

Inserting Eq. S1 into the equation $\dot{E} = -E\dot{V}/V$ (Eq. 10), we get

$$\dot{E} = -E\left(\frac{k_1}{k_1 t{+}V_0}\right) = -E\left(\frac{1}{t{+}\alpha}\right) \tag{S2}$$

where $\alpha = V_0/k_1$. Separation of variables gives

$$\frac{\mathrm{d}E}{E} = \frac{\mathrm{d}t}{t{+}\alpha} \tag{S3}$$

Integrating from time zero to t and from E_0 to $E(t)$ we get

$$\ln\left(\frac{E}{E_0}\right) = \ln\left(\frac{\alpha}{\alpha{+}t}\right) \quad \Rightarrow \quad E = E_0\left(\frac{\alpha}{\alpha{+}t}\right) \tag{S4}$$

Inserting E from Eq. S4 into the rate equation for A (Eq. 11)

$$\dot{A} = k_2{\cdot}E - A{\cdot}\frac{\dot{V}}{V} = k_2{\cdot}E - A{\cdot}\frac{k_1}{V_0{+}k_1{\cdot}t} = k_2{\cdot}E - A{\cdot}\frac{1}{\alpha{+}t} \tag{S5}$$

we get the following rate equation for A

$$\dot{A} + \frac{A}{\alpha{+}t} = k_2 E_0\left(\frac{\alpha}{\alpha{+}t}\right) \tag{S6}$$

The solution of Eq. S6 is given by Eq. 11, i.e.,

$$A(t) = k_2 E_0 \alpha + (A_0 - k_2 E_0 \alpha)\left(\frac{\alpha}{\alpha{+}t}\right) \tag{S7}$$

Supporting Material, File S2 Text

Homeostatic Controllers Compensating for Growth and Perturbations

P. Ruoff[1*], O. Agafonov[1], D. M. Tveit[2], K. Thorsen[2], T. Drengstig[2]
[1]Centre for Organelle Research
[2]Department of Electrical Engineering and Computer Science,
University of Stavanger, Stavanger, Norway

[*]Corresponding author. Address: Centre for Organelle Research, University of Stavanger, N-4036 Stavanger, Norway, Tel.: (47) 5183-1887, Fax: (47) 5183-1750, E-mail: peter.ruoff@uis.no

Steady state of transporter-generated compound A without negative feedback

We start with Eq. 15 where transporter T pumps external A (A_{ext}) into a constantly growing cell ($\dot{V}$=constant)

$$\dot{A} = \frac{k_2 \cdot T}{V} - A\left(\frac{\dot{V}}{V}\right) \tag{S1}$$

We assume that the surface concentration of T is constant and that the pump rate is zero-order with respect to the external A concentration.

The steady state of A is given by setting Eq. S1 to zero, which gives

$$\dot{A} = \frac{k_2 \cdot T}{V} - A\left(\frac{\dot{V}}{V}\right) = 0 \quad \Rightarrow \quad A_{ss} = \frac{k_2 \cdot T}{\dot{V}} \tag{S2}$$

independent of the initial concentration of A.

In case there is a first-order removal of cellular A with respect to A the rate equation becomes

$$\dot{A} = \frac{k_2 \cdot T}{V} - k_3 \cdot A - A\left(\frac{\dot{V}}{V}\right) = 0 \tag{S3}$$

Setting Eq. S3 to zero leads to

$$A_{ss} = \frac{k_2 \cdot T}{k_3 V + \dot{V}} \;\rightarrow\; 0 \quad \text{as} \quad \mathrm{V} \rightarrow \infty \tag{S4}$$

In case the removal of cellular A is zero-order with respect to A (for example by an enzyme removing A at maximum velocity V_{max}), then in this case the steady state condition

$$\dot{A} = \frac{k_2 \cdot T}{V} - V_{max} - A\left(\frac{\dot{V}}{V}\right) = 0 \tag{S5}$$

gives

$$A_{ss} = \frac{1}{\dot{V}} \left(k_2 \cdot T - V_{max} \cdot V \right) \tag{S6}$$

As the volume V grows there will be a critical volume V_{crit}=$k_2 T / V_{max}$ at which A_{ss} becomes zero.

Supporting Material, File S3 Text

Homeostatic Controllers Compensating for Growth and Perturbations

P. Ruoff[1]*, O. Agafonov[1], D. M. Tveit[2], K. Thorsen[2], T. Drengstig[2]
[1]Centre for Organelle Research
[2]Department of Electrical Engineering and Computer Science,
University of Stavanger, Stavanger, Norway

*Corresponding author. Address: Centre for Organelle Research, University of Stavanger, N-4036 Stavanger, Norway, Tel.: (47) 5183-1887, Fax: (47) 5183-1750, E-mail: peter.ruoff@uis.no

Steady states and theoretical set-point for motif 1 zero-order controller

Transporter-based compensatory flux with constant values of $\dot{V}$ and $\dot{k_3}$

The rate equations for A and E when the compensatory flux is transporter based, are

$$\dot{A} = \frac{k_2 E}{V} - k_3 \cdot A - A\left(\frac{\dot{V}}{V}\right) \tag{S1}$$

$$\dot{E} = k_4 - k_6 \cdot A - E\left(\frac{\dot{V}}{V}\right) \tag{S2}$$

with $\frac{M}{k_5+M}=\frac{E}{k_7+E}=1$ (see Eq. 16). For constant V ($\dot{V}=0$) and k_3 ($\dot{k_3}=0$), Eq. S2 defines the theoretical set-point, i.e.

$$\dot{E} = k_4 - k_6 \cdot A - A\left(\frac{\dot{V}}{V}\right) = 0 \quad \Rightarrow \quad A_{ss} = A_{set}^{theor} = \frac{k_4}{k_6} \tag{S3}$$

As long as $\frac{E}{k_7+E}=1$ the controller will for any step-wise perturbation in k_3 or V move A_{ss} to A_{set}^{theor}.
However, for constant $\dot{V}$ and $\dot{k_3}$, Eq. S3 is no longer valid. In case the volume V increases linearly, E needs to increase in order to oppose the dilution of A. To get an estimate of A_{ss} for constant $\dot{V}$ and $\dot{k_3}$, we take the double time derivative of A, and set $\ddot{A}$ and $\dot{A}$ to zero

$$\ddot{A} = \frac{k_2 \dot{E}}{V} - \frac{k_2 E \dot{V}}{V^2} - \dot{k_3} A + A\left(\frac{\dot{V}}{V}\right)^2 = 0 \tag{S4}$$

Inserting Eq. S2 into Eq. S4 gives

$$\frac{k_2}{V}\left[k_4 - k_6 \cdot A - E\left(\frac{\dot{V}}{V}\right)\right] - k_2 \cdot E\left(\frac{\dot{V}}{V^2}\right) - \dot{k_3} A + A\left(\frac{\dot{V}}{V}\right)^2 = 0 \tag{S5}$$

Multiplying Eq. S5 with V leads to

$$k_2k_4 - k_2k_6{\cdot}A - 2k_2E\left(\frac{\dot{V}}{V}\right) - \dot{k_3}A{\cdot}V + \underbrace{A\left(\frac{\dot{V}^2}{V}\right)}_{\to 0} = 0 \tag{S6}$$

Assuming steady state conditions in Eq. S1 and neglecting there the $A\dot{V}/V$ term we can approximately write

$$\dot{A} = \frac{k_2E}{V} - k_3{\cdot}A - A\left(\frac{\dot{V}}{V}\right) = 0 \quad \Rightarrow \quad \frac{k_2E}{V} = k_3{\cdot}A_{ss} \tag{S7}$$

with E and V increasing. Inserting the right-hand side of Eq. S7 into Eq. S6 gives

$$k_2k_4 - k_2k_6{\cdot}A_{ss} - 2k_3A_{ss}\dot{V} - \dot{k_3}A_{ss}{\cdot}V = 0 \tag{S8}$$

Solving for A_{ss}, we get

$$A_{ss} = \frac{k_2k_4}{k_2k_6{+}2k_3\dot{V}{+}\dot{k_3}V} \tag{S9}$$

In phase 2 of Fig. 7 we have $\dot{k_3}$=0. For k_2=2.0, k_3=2.0, k_4=20.0, k_4=10.0, and $\dot{V}$=2.0, A_{ss} is calculated after Eq. S9 to be 1.25, while the numerical value of A_{ss} is 1.11. When in phase 3 (Fig. 7) $\dot{k_3}$=1.0, Eq. S9 indicates, as observed, that A_{ss} will go to zero as V increases.

Cell-internal compensatory flux with constant values of $\dot{V}$ and $\dot{k_3}$

Rate equations for A and E (Eqs. 50 and 51) are written as

$$\dot{A} = k_3{\cdot}E - k_3{\cdot}A - A\left(\frac{\dot{V}}{V}\right) \tag{S10}$$

$$\dot{E} = k_4 - k_6{\cdot}A - E\left(\frac{\dot{V}}{V}\right) \tag{S11}$$

by using $N/(k_7{+}N){=}M/(k_5{+}M){=}1$. In addition, $E/(k_8{+}E){=}1$ giving the controller ideal behavior/precision for step-wise perturbations in k_3 and V. Calculating $\ddot{A}$ and setting $\ddot{A}$ and $\dot{A}$ to zero, gives

$$\ddot{A}{=}k_2{\cdot}\dot{E}{-}\dot{k_3}A{+}A\left(\frac{\dot{V}}{V}\right)^2{=}k_2\left[k_4{-}k_6{\cdot}A{-}E\left(\frac{\dot{V}}{V}\right)\right]{-}\dot{k_3}A{+}A\left(\frac{\dot{V}}{V}\right)^2=0 \tag{S12}$$

Neglecting the $\dot{V}/V$ terms (steady state when time t and volume V become large) leads to Eq. 53

$$k_2k_4 = k_2k_6A_{ss} + \dot{k_3}A_{ss} \quad \Rightarrow \quad A_{ss} = \frac{k_2k_4}{k_2k_6{+}\dot{k_3}} \tag{S13}$$

Model calculations at the end of phase 3 in Fig. 18 (k_2=1.0, k_4=20.0, k_6=10.0, and $\dot{k_3}$=1.0) show an A_{ss}=1.75, while the estimated value from Eq. S13 gives a value of 1.82.

Supporting Material, File S4 Text

Homeostatic Controllers Compensating for Growth and Perturbations

P. Ruoff[1]*, O. Agafonov[1], D. M. Tveit[2], K. Thorsen[2], T. Drengstig[2]
[1]Centre for Organelle Research
[2]Department of Electrical Engineering and Computer Science,
University of Stavanger, Stavanger, Norway

*Corresponding author. Address: Centre for Organelle Research, University of Stavanger, N-4036 Stavanger, Norway, Tel.: (47) 5183-1887, Fax: (47) 5183-1750, E-mail: peter.ruoff@uis.no

Steady states and theoretical set-point for motif 1 second-order (antithetic) controller

Transporter-based compensatory flux with constant values of $\dot{V}$ and $\dot{k_3}$

The rate equations (Eqs. 21-23) are written as

$$\dot{A} = \frac{k_2 E_2}{V} - k_3 \cdot A - A\left(\frac{\dot{V}}{V}\right) \tag{S1}$$

$$\dot{E_1} = k_4 \cdot A - k_6 \cdot E_1 \cdot E_2 - E_1\left(\frac{\dot{V}}{V}\right) \quad \text{with} \quad \frac{M}{k_5 + M} = 1 \tag{S2}$$

$$\dot{E_2} = k_8 - k_6 \cdot E_1 \cdot E_2 - E_2\left(\frac{\dot{V}}{V}\right) \quad \text{with} \quad \frac{O}{k_9 + O} = 1 \tag{S3}$$

By setting $\dot{E_1}$=0 and neglecting the dilution term (considering $V \gg \dot{V}$) steady state conditions require

$$k_4 \cdot A = k_6 \cdot E_1 \cdot E_2 \tag{S4}$$

Calculating the double time derivative of A and setting it and $\dot{A}$ to zero gives

$$\ddot{A} = \frac{k_2 \dot{E_2}}{V} - \frac{k_2 E_2 \dot{V}}{V^2} - \dot{k_3} \cdot A + A\left(\frac{\dot{V}}{V}\right)^2 = 0 \tag{S5}$$

Inserting $\dot{E_2}$ from Eq. S3 into Eq. S5

$$\ddot{A} = \frac{k_2}{V}\left[k_8 - \underbrace{k_6 \cdot E_1 \cdot E_2}_{k_4 \cdot A} - E_2\left(\frac{\dot{V}}{V}\right)\right] - \frac{k_2 E_2 \dot{V}}{V^2} - \dot{k_3} \cdot A + A\left(\frac{\dot{V}}{V}\right)^2 = 0 \tag{S6}$$

Multiplying Eq. S6 by V yields

$$\ddot{A} = k_2 \left[k_8 - k_4 \cdot A - E_2 \left(\frac{\dot{V}}{V} \right) \right] - \frac{k_2 E_2}{V} \cdot \dot{V} - \dot{k_3} \cdot A \cdot V + \underbrace{A \left(\frac{\dot{V}^2}{V} \right)}_{\approx 0} = 0 \quad \text{(S7)}$$

giving

$$k_2 k_8 - k_2 k_4 \cdot A_{ss} - 2 \cdot \underbrace{\frac{k_2 E_2}{V}}_{k_3 \cdot A_{ss}} \cdot \dot{V} - \dot{k_3} \cdot A_{ss} \cdot V = 0 \quad \text{(S8)}$$

using the steady state condition from Eq. S1 that $k_2 E_2 / V = k_3 A_{ss}$. Solving for A_{ss} gives

$$A_{ss} = \frac{k_2 k_8}{k_2 k_4 + 2 k_3 \dot{V} + \dot{k_3} V} \quad \text{(S9)}$$

which is analogous to the A_{ss} expression for the motif 1 zero-order controller (see S3 Text, Eq. S9). As for the motif 1 zero-order controller A_{ss} will go to zero for the antithetic controller when $\dot{k_3} \neq 0$ (Fig. 9, phase 3).

Cell-internal-based compensatory flux with constant values of $\dot{V}$ and $\dot{k_3}$

The rate equation for A with an cell internal compensatory flux is given by

$$\dot{A} = k_2 E_2 - k_3 \cdot A - A \left(\frac{\dot{V}}{V} \right) \quad \text{(S10)}$$

where in Eq. 56 $N/(k_7+N)$ is set to 1.0. The rate equations for E_1 and E_2 are as given by Eqs. S2 and S3, respectively.

Calculating $\ddot{A}$ from Eq. S10 gives

$$\ddot{A} = k_2 \dot{E_2} - \dot{k_3} \cdot A + A \left(\frac{\dot{V}}{V} \right)^2 = 0 \quad \text{(S11)}$$

Inserting $\dot{E}_2$ from Eq. S3 into Eq. S11 gives

$$k_2 \left[k_8 - \underbrace{k_6 \cdot E_1 \cdot E_2}_{k_4 \cdot A_{ss}} - E_2 \left(\underbrace{\frac{\dot{V}}{V}}_{\to 0} \right) \right] - \dot{k_3} \cdot A_{ss} + A_{ss} \left(\underbrace{\frac{\dot{V}}{V}}_{\to 0} \right)^2 = 0 \qquad \text{(S12)}$$

Collecting the A_{ss} terms and observing that $\dot{V}/V \to 0$, we get

$$k_2 k_8 = k_2 k_4 \cdot A_{ss} + \dot{k_3} A_{ss} \quad \Rightarrow \quad A_{ss} = \frac{k_2 k_8}{k_2 k_4 + \dot{k_3}} \qquad \text{(S13)}$$

Note, that also in case of a cell-internal generated compensatory flux the steady state expressions for A for the motif 1 zero-order and the antithetic controllers show the same behaviors (compare S3 Text Eq. S13) with Eq. S13 above.

Supporting Material, File S5 Text

Homeostatic Controllers Compensating for Growth and Perturbations

P. Ruoff[1]*, O. Agafonov[1], D. M. Tveit[2], K. Thorsen[2], T. Drengstig[2]
[1]Centre for Organelle Research
[2]Department of Electrical Engineering and Computer Science,
University of Stavanger, Stavanger, Norway

*Corresponding author. Address: Centre for Organelle Research, University of Stavanger, N-4036 Stavanger, Norway, Tel.: (47) 5183-1887, Fax: (47) 5183-1750, E-mail: peter.ruoff@uis.no

Steady states and theoretical set-point for motif 1 autocatalytic controller

Transporter-based compensatory flux with constant values of $\dot{V}$ and $\dot{k_3}$ (k_E^{in}=k_E^{out}=1×10^{-5})

The rate equations Eqs. 33-34 are rewritten in the following form

$$\dot{A} = \frac{k_2 E}{V} - k_3 \cdot A - A\left(\frac{\dot{V}}{V}\right) \tag{S1}$$

$$\dot{E} = k_4 \cdot E - k_6 \cdot A \cdot E - E\left(\frac{\dot{V}}{V}\right) \tag{S2}$$

where in Eq. 34 $M/(k_5+M)$=1.0 and the term $k_E^{in}-k_E^{out}\cdot E$ is neglected. In addition, sufficent M is present to avoid a controller breakdown as shown in phase 3 of Fig. 11.

Calculating $\ddot{A}$ from Eq. S1 gives

$$\ddot{A} = \frac{k_2 \dot{E}}{V} - \frac{k_2 E \dot{V}}{V^2} - \dot{k_3} \cdot A + A\left(\frac{\dot{V}}{V}\right)^2 = 0 \tag{S3}$$

Note that $\ddot{V}$=0 since $\dot{V}$=constant. In addition we assume steady state in A such that $\dot{A}$=0.

Inserting Eq. S2 into Eq. S3 gives

$$\frac{k_2}{V}\left[k_4 E - k_6 \cdot E \cdot A - E\left(\frac{\dot{V}}{V}\right)\right] - \frac{k_2 E \dot{V}}{V^2} - \dot{k_3} A + A\left(\frac{\dot{V}}{V}\right)^2 = 0 \tag{S4}$$

Collecting terms gives

$$\underbrace{\frac{k_2 E}{V}}_{k_3 A_{ss}} \cdot k_4 - \underbrace{\frac{k_2 E}{V}}_{k_3 A_{ss}} \cdot k_6 \cdot A_{ss} - \frac{2E}{V}\left(\underbrace{\frac{\dot{V}}{V}}_{\to 0}\right) - \dot{k_3} A_{ss} + A_{ss}\left(\underbrace{\frac{\dot{V}}{V}}_{\to 0}\right)^2 = 0 \quad \text{(S5)}$$

Rearranged we get

$$k_3 k_4 A_{ss} - k_3 k_6 A_{ss}^2 - \dot{k_3} A_{ss} = 0 \quad \Rightarrow \quad A_{ss} = \frac{k_3 k_4 - \dot{k_3}}{k_3 k_6} = A_{set}^{theor} - \frac{\dot{k_3}}{k_3 k_6} \quad \text{(S6)}$$

where A_{set}^{theor}=k_4/k_6 for step-wise perturbations.
To show that the autocatalytic controller can manage a k_3 perturbation of the form

$$k_3(t) = k_{3,0} + a \cdot t^n \quad \text{(S7)}$$

we note that the ratio $\dot{k_3}/k_3 \to 0$ as $t \to \infty$, i.e.

$$\lim_{t\to\infty}\left\{\frac{\dot{k_3}}{k_3}\right\} = \lim_{t\to\infty}\left\{\frac{n \cdot a t^{n-1}}{k_{3,0}+at^n}\right\} \overset{\text{L'Hôpital}}{=} n(n-1)\lim_{t\to\infty}\left\{\frac{1}{t}\right\} = 0 \quad \text{(S8)}$$

such that the term $\dot{k_3}/(k_3 k_6)$ in Eq. S6 goes to zero.

Transporter-based compensatory flux with constant values of $\dot{V}$ and $\dot{k_3}$ and non-negligible k_E^{in} and k_E^{out} terms (k_E^{in}=k_E^{out}=10.0)

Starting with rate equation 34 (now S9):

$$\dot{E} = k_4 \cdot E - k_6 \cdot A \cdot E + k_E^{in} - k_E^{out} \cdot E - E\left(\frac{\dot{V}}{V}\right) \quad \text{(S9)}$$

Inserting Eq. S9 into Eq. S3 gives:

$$\ddot{A} = \frac{k_2}{V}\left[k_4 E - k_6 \cdot E \cdot A + k_E^{in} - k_E^{out} \cdot E - E\left(\frac{\dot{V}}{V}\right)\right] - \frac{k_2 E \dot{V}}{V^2} - \dot{k_3} A + A\left(\frac{\dot{V}}{V}\right)^2 \quad \text{(S10)}$$

Looking for the steady state when V and k_3 increase linearly ($\dot{V}$ and $\dot{k_3}$ are constant), the $\dot{V}/V$ and $\dot{V}/V^2$ terms are neglected by assuming that $\dot{V} \ll V$. For $\dot{A}$ this leads to

$$\dot{A} = \frac{k_2 E}{V} - k_3 \cdot A - A\left(\frac{\dot{V}}{V}\right) \approx \frac{k_2 E}{V} - k_3 \cdot A \tag{S11}$$

which, when setting Eq. S11 to zero, gives the relationship between the steady state in A, A_{ss}, and the changing E, V, and k_3 values, i.e.,

$$E = \left(\frac{k_3}{k_2}\right) \cdot V \cdot A_{ss} \tag{S12}$$

Setting Eq. S10 to zero, neglecting the $\dot{V}/V$ and $\dot{V}/V^2$ terms and inserting E from Eq. S12 into Eq. S10, results in the expression for A_{ss}

$$A_{ss}^2 - A_{ss}\left(\frac{k_4}{k_6} - \frac{k_E^{out}}{k_6} - \frac{\dot{k_3}}{k_3 k_6} + \frac{k_2 k_E^{in}}{V}\right) = 0 \tag{S13}$$

For increasing k_3 and V the terms $\dot{k_3}/k_3 k_6$ and $k_2 k_E^{in}/V$ become small in comparison with $(k_4 - k_E^{out})/k_6$ such that the new set-point is approximately

$$A_{ss} \approx \frac{k_4 - k_E^{out}}{k_6} \tag{S14}$$

Fig. S1 illustrates the change in set-point for k_E^{in}=k_E^{out}=10.0, using the rate constant values from Fig. 11. During the first phase the system is as in Fig. 11, with k_E^{in}=k_E^{out}=1×10^{-5}. In phases 2 and 3 the values of k_E^{in} and k_E^{out} are changed 10.0. Eq. S14 predicts a set-point of 1.0. In phase 2 of Fig. S1 the numerically calculated A_{ss} is 1.001, while in phase 3 this value is 0.9996, indicating that Eq. S14 describes the new set-point quite well.

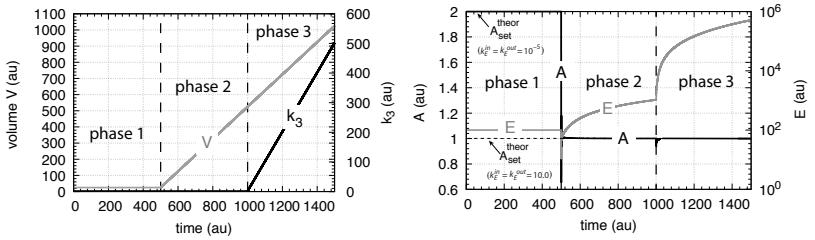

Figure S1. Performance of the motif 1 autocatalytic controller (Eqs. 33-35). Phase 1: constant volume V and constant k_3. Initial concentrations and rate constant values (at steady state) as in Fig. 11: V_0=25.0, $\dot{V}$=0.0, A_0=2.0, E_0=100.0, M_0=1 × 10^{12}, k_2=1.0, k_3=2.0, $\dot{k_3}$=0.0, k_4=20.0, k_5=1 × 10^{-6}, k_6=10.0, and k_E^{in}=k_E^{out}=1×10^{-5}. The controller keeps A at its set-point at A_{set}^{theor}=k_4/k_6=2.0. Phase 2: rate constants remain the same as in phase 1, but k_E^{in}=k_E^{out}=10.0 and V increases linearly with $\dot{V}$=1.0. Phase 3: V continues to increase with the same rate and k_3 increases with rate $\dot{k_3}$=1.0. The controller moves A towards the new set-point A_{set}^{theor}=$(k_4-k_E^{out})/k_6$=1.0 in both phase 2 and phase 3. In comparison to Fig. 11 no breakdown in phase 3 occurs due to a high initial M concentration.

The set-point (Eq. S14) is also defended for step-wise perturbations in V or k_3. For k_E^{in}=k_E^{out}=10.0 a change of k_3 from 2.0 to 8.0 (V kept constant at 25.0 and other rate constants remain as in Fig. S1) shows a numerical A_{ss} value of 1.005, while the same A_{ss} value is observed for a step-wise change of V from 25.0 to 100.0, while k_3 is kept constant at 2.0.

Transporter-based compensatory flux with exponentially increasing values of $\dot{V}$ and $\dot{k_3}$ and non-negligible k_E^{in} and k_E^{out} terms (k_E^{in}=k_E^{out}=10.0)

The autocatalytic rate of V is described by the equation

$$\dot{V} = \kappa V \tag{S15}$$

where κ is a constant (=0.1) and related to the doubling time of V by $\ln 2/\kappa$. Similarly, the autocatalytic increase of k_3 is described by

$$\dot{k_3} = \zeta k_3 \tag{S16}$$

where $\ln 2/\zeta$ is the doubling time of k_3. In accordance with Eq. 48, ζ=0.2.

The rate equations for A and E take the form (assuming again that sufficient M is always present and $M/(k_5{+}M)$=1.0):

$$\dot{A} = \frac{k_2 E}{V} - k_3 \cdot A - \kappa \cdot A \tag{S17}$$

$$\dot{E} = k_4 \cdot E - k_6 \cdot A \cdot E + k_E^{in} - k_E^{out} \cdot E - \kappa \cdot E \tag{S18}$$

Setting $\dot{A}$=0 and calculating $\ddot{A}$=0 gives

$$\ddot{A} = \frac{k_2 \dot{E}}{V} - \frac{k_2 \dot{V}}{V^2} - \dot{k_3} A_{ss} - \underbrace{\kappa \dot{A_{ss}}}_{=0} = 0 \tag{S19}$$

Inserting Eq. S18 into Eq. S19, and substituting the relationship between growing E, V, k_3 and the steady state in A (A_{ss} from Eq. S17),

$$E = \frac{V}{k_2}(k_3 + \kappa) A_{ss} \ , \tag{S20}$$

into the equation of $\ddot{A}$, we get:

$$\ddot{A} = k_4(k_3{+}\kappa)A_{ss} - k_6(k_3{+}\kappa)A_{ss}^2 + \frac{k_2 k_9}{V} - k_E^{out}(k_3{+}\kappa)A_{ss} - \kappa(k_3{+}\kappa)A_{ss} - \zeta k_3 A_{ss} - \frac{k_2 \kappa}{V} = 0 \tag{S21}$$

Rearranging leads to a quadratic equation in A_{ss}

$$A_{ss}^2 - \left(\frac{k_4}{k_6} - \frac{k_E^{out}}{k_6} - \frac{\kappa}{k_6} - \underbrace{\frac{\zeta k_3}{k_6(k_3{+}\kappa)}}_{\to \zeta/k_6} \right) A_{ss} - \underbrace{\frac{k_2}{V}(k_9{-}\kappa)}_{\to 0} = 0 \tag{S22}$$

For increasing k_3 the term $\zeta k_3/(k_6(k_3{+}\kappa))$ approaches ζ/k_6, while for increasing large V the last term in Eq. S22 vanishes.

When both V and k_3 increase exponentially the set-point becomes

$$A_{ss} \approx \frac{k_4 - k_E^{out} - \kappa - \zeta}{k_6} \tag{S23}$$

In comparison with linear growth (Eq. S14) exponential growth gives additional offsets in the set-point, which depend on κ and ζ, i.e., on how fast the exponential growth in V or k_3 occurs. This is shown in Fig. S2 where the perturbation profile of Fig. 14 and the rate constant values from Fig. 11 (Fig. 15c) are applied, except that k_E^{in} and k_E^{out} are changed in phases 2 and 3 from 1×10^{-5} to 10.0.

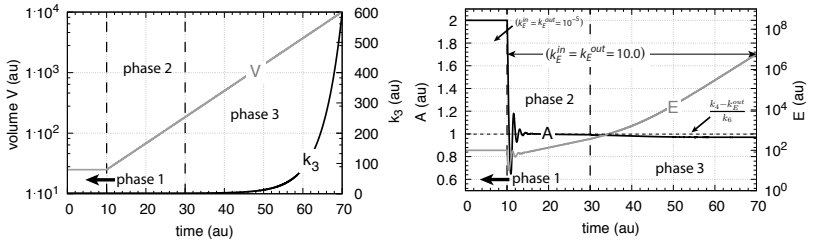

Figure S2. Performance of the motif 1 autocatalytic controller (Eqs. 33-35) with transporter based compensatory flux applying the perturbation profile from Fig. 14. Phase 1: constant volume V and constant k_3. Initial concentrations and rate constant values (at steady state) as in Fig. 11: V_0=25.0, $\dot{V}$=0.0, A_0=2.0, E_0=100.0, M_0=1×10^{12}, k_2=1.0, k_3=2.0, $\dot{k_3}$=0.0, k_4=20.0, k_5=1×10^{-6}, k_6=10.0, and k_E^{in}=k_E^{out}=1×10^{-5}. The controller keeps A at its set-point at A_{set}^{theor}=k_4/k_6=2.0. Phase 2: rate constants remain the same as in phase 1, but k_E^{in}=k_E^{out} are both changed to 10.0 and V increases exponentially with $\dot{V}$=κV ($\kappa = 0.1$). Phase 3: V continues to increase exponentially and k_3 starts to increase exponentially with the rate law $\dot{k_3}$=ζk_3 ($\zeta = 0.2$). The controller moves A towards a new steady state dependent on κ and/or ζ as outlined by Eq. S23. For comparison the set-point $k_4 - k_E^{out}/k_6$ (=1.0) for linear growth is indicated as a dashed line showing the offset from $k_4 - k_E^{out}/k_6$ due to exponential growth.

Cell-internal compensatory flux with constant values of $\dot{V}$ and $\dot{k_3}$ (k_E^{in}=k_E^{out}=1×10^{-5})

Assuming that N and M are sufficiently high to avoid controller breakdown by low N and M values, the rate equations for A and E are in this case (neglecting the k_E^{in}−k_E^{out}·E term with $k_E^{in} = k_E^{out} = 1\times10^{-5}$):

$$\dot{A} = k_2 \cdot E - k_3 \cdot A - A\left(\frac{\dot{V}}{V}\right) \tag{S24}$$

$$\dot{E} = k_4 \cdot E - k_6 \cdot A \cdot E - E\left(\frac{\dot{V}}{V}\right) \tag{S25}$$

Calculating $\ddot{A}$ and setting it to zero gives

$$\ddot{A} = k_2\dot{E} - \dot{k_3}A + A\left(\frac{\dot{V}}{V}\right)^2 = 0 \tag{S26}$$

Inserting Eq. S25 into Eq S26

$$\ddot{A} = k_2\left[k_4 \underbrace{E}_{k_3A_{ss}/k_2} - k_6 \cdot A \cdot \underbrace{E}_{k_3A_{ss}/k_2} - \underbrace{E}_{k_3A_{ss}/k_2}\left(\frac{\dot{V}}{V}\right)\right] - \dot{k_3}A_{ss} + A_{ss}\left(\frac{\dot{V}}{V}\right)^2 = 0 \tag{S27}$$

From the steady state condition of Eq. S24, we use approximately (for large V) $E = k_3A_{ss}/k_2$. Collecting terms in Eq. S27

$$k_3k_4A_{ss} - k_3k_6A_{ss}^2 - \dot{k_3}A_{ss} = 0 \tag{S28}$$

Dividing by A_{ss} gives

$$A_{ss} = \frac{k_4}{k_6} - \frac{\dot{k_3}}{k_3k_6} \tag{S29}$$

where k_4/k_6=A_{set}^{theor}.

Cell-internal compensatory flux with linearly increasing values of $\dot{V}$ and $\dot{k_3}$ and non-negligible k_E^{in} and k_E^{out} terms (k_E^{in}=k_E^{out}=10.0)

The rate equation for A is described by Eq. S24, while the rate equation for E now includes the $k_E^{in}-k_E^{out}\cdot E$ term:

$$\dot{E} = k_4\cdot E - k_6\cdot A\cdot E + k_E^{in}-k_E^{out}\cdot E - E\left(\frac{\dot{V}}{V}\right) \tag{S30}$$

Inserting Eq. S30 into the expression for $\ddot{A}$ (Eq. S26) gives:

$$\ddot{A} = k_2\left[k_4 E - k_6\cdot A\cdot E + k_E^{in}-k_E^{out}\cdot E - E\left(\frac{\dot{V}}{V}\right)\right] - \dot{k_3}A_{ss} + A_{ss}\left(\frac{\dot{V}}{V}\right)^2 = 0 \tag{S31}$$

Setting $\dot{A}$=0 (Eq. S24), neglecting the $A\dot{V}/V$ term, we get the (approximate, for large V) relationship between increasing E and k_3 while A is kept at its steady state, i.e.,

$$E = \left(\frac{k_3}{k_2}\right)A_{ss} \tag{S32}$$

Inserting E from Eq. S32 into Eq. S31, neglecting the terms containing $\dot{V}/V$ gives

$$k_3k_4A_{ss} - k_3k_6A_{ss}^2 + k_2k_E^{in} - k_3k_E^{out}A_{ss} - \dot{k_3}A_{ss} = 0 \tag{S33}$$

Rearranging Eq. S33 gives Eq. 61:

$$A_{ss}^2 - A_{ss}\left(\frac{k_4-k_E^{out}}{k_6}-\frac{\dot{k_3}}{k_3k_6}\right) - \frac{k_2k_E^{in}}{k_3k_6} = 0 \tag{S34}$$

Fig. S3 shows the behavior for linearly increasing V and k_3. When only V increases in phase 2 the controller moves A to the A_{ss} value described by the solution of Eq. S34. Although this steady state in A is dependent on the value of k_3, it is independent of how fast V grows. Finally, in phase 3 k_3 starts to grow and the controller moves A_{ss} to the set-point $(k_4 - k_E^{out})/k_6$ independent of the (linear) growth rate of k_3 (see, however, the chapter below when V and k_3 grow exponentially and k_E^{in}=k_E^{out}=10.0).

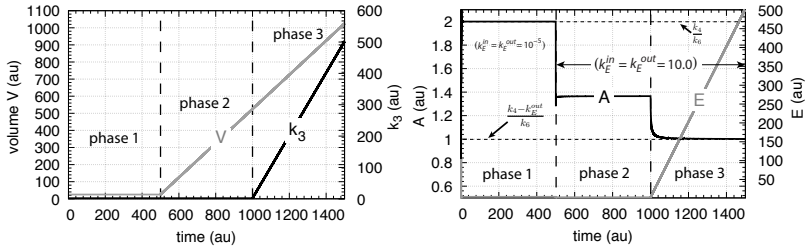

Figure S3. Performance of the motif 1 autocatalytic controller (Eq. 59 and Eqs. 34-35). Phase 1: constant volume V and constant k_3. Initial concentrations and rate constant values: V_0=25.0, $\dot{V}$=0.0, A_0=2.0, E_0=100.0, N_0=M_0=1×10^{12}, k_2=1.0, k_3=2.0, $\dot{k_3}$=0.0, k_4=20.0, k_5=1×10^{-6}, k_6=10.0, and k_E^{in}=k_E^{out}=1×10^{-5}. The controller keeps A at its set-point at A_{set}^{theor}=k_4/k_6=2.0. Phase 2: rate constants remain the same as in phase 1, but k_E^{in}=k_E^{out}=10.0 and V increases linearly with $\dot{V}$=1.0. The numerical value of A_{ss} is 1.3656 and independent of how fast V grows. This value is in excellent agreement with the solution of the quadratic equation (1.3660). Phase 3: V continues to increase with the same rate and k_3 starts to grow with rate $\dot{k_3}$=1.0. The controller moves A now towards the new set-point $(k_4-k_E^{out})/k_6$=1.0.

Cell-internal compensatory flux with exponential increase of $\dot{V}$ and $\dot{k_3}$ (k_E^{in}=k_E^{out}=1×10^{-5})

We have the same rate equations as above (Eqs. S24-S25) with k_E^{in}=k_E^{out}=1×10^{-5} (which we neglect in the analytical approach here). Since V and k_3 both grow exponentially we can write

$$\dot{V} = \kappa V \quad \& \quad \dot{k_3} = \zeta k_3 \tag{S35}$$

where κ and ζ are constants. The rate equations are (assuming sufficient amounts of N and M, and, for the sake of simplicity, we set $N/(k_7 + N)$=$M/(k_5 + M)$=1.0)

$$\dot{A} = k_2 \cdot E - k_3 \cdot A - \kappa A \tag{S36}$$

$$\dot{E} = k_4 \cdot E - k_6 \cdot A \cdot E - \kappa E \tag{S37}$$

Assuming steady state in A ($\dot{A}$=0) we can write from Eq. S36

$$E = \left(\frac{k_3 + \kappa}{k_2} \right) A_{ss} \tag{S38}$$

where E increases in relationship with k_3 in order to keep A at its steady state.

Calculating $\ddot{A}$ and noting that $\dot{A}$=0 and that ζ and κ are constants, gives

$$\ddot{A} = k_2 \dot{E} - \dot{k_3} A_{ss} = k_2 \left[k_4 E - k_6 \cdot A_{ss} \cdot E - E \cdot \kappa \right] - \dot{k_3} A_{ss} = 0 \tag{S39}$$

Inserting the expression for E_{ss} from Eq. S38 into Eq. S39 and collecting terms gives

$$A_{ss} = \frac{k_4}{k_6} - \frac{\kappa}{k_6} - \frac{\dot{k_3}}{k_6(k_3+\kappa)} \tag{S40}$$

In Eq. S40 k_4/k_6 is the theoretical set-point A_{set}^{theor} the controller defends when step-wise perturbations are applied. The term κ/k_6 is the offset from A_{set}^{theor} due to the exponential increase of V, while the term $\dot{k_3}/(k_6(k_3+\kappa))$ is the offset due to the exponential increase of k_3. This last term can be reduced to the ratio ζ/k_6 by using $\dot{k_3}$=ζk_3 and observing that

$$\lim_{k_3 \to \infty} \frac{\dot{k_3}}{k_6(k_3+\kappa)} = \lim_{k_3 \to \infty} \frac{\zeta k_3}{k_6(k_3+\kappa)} \overset{\text{L'Hôpital}}{=} \frac{\zeta}{k_6} \tag{S41}$$

Referring to Fig. 25c, the numerical steady state is calculated at the end of phase 2 to be 1.99. The same offset of 0.01 is obtained for κ/k_6 from Eq. S40 (rate constant values are found in Fig. 22). At the end of phase 3 in Fig. 25c the numerical A_{ss} value is 1.971, while the overall calculated offset from Eq. S40 is 1.97 which includes the exponential increase of k_3 (Eq. 48) with a ζ of 0.2.

Cell-internal compensatory flux with exponentially increasing values of $\dot{V}$ and $\dot{k_3}$ and non-negligible k_E^{in} and k_E^{out} terms (k_E^{in}=k_E^{out}=10.0)

The rate equations and conditions are the same as in the previous section, except that $\dot{E}$ now includes the term $k_E^{in}-k_E^{out}\cdot E$, i.e.,

$$\dot{A} = k_2\cdot E - k_3\cdot A - \kappa A \tag{S36}$$

$$\dot{E} = k_4\cdot E - k_6\cdot A\cdot E + k_E^{in} - k_E^{out}\cdot E - \kappa E \tag{S42}$$

We calculate $\ddot{A}$, set $\dot{A}$ and $\ddot{A}$ to zero, and then insert Eq. S37 into the $\ddot{A}$-expression. Then all E's are substituted with the expression from Eq. S38, which gives the equation for $\ddot{A}$ and A_{ss}:

$$\begin{aligned}
\ddot{A} =& k_2\dot{E} - \dot{k_3}A_{ss} = k_2\left[k_4E - k_6\cdot A_{ss}\cdot E + k_E^{in} - k_E^{out}\cdot E - E\cdot\kappa\right] - \dot{k_3}A_{ss} \\
&= k_2\left[k_4\left(\frac{k_3+\kappa}{k_2}\right)A_{ss} - k_6\cdot A_{ss}\cdot\left(\frac{k_3+\kappa}{k_2}\right)A_{ss} + k_E^{in} - k_E^{out}\cdot\left(\frac{k_3+\kappa}{k_2}\right)A_{ss} - \kappa\left(\frac{k_3+\kappa}{k_2}\right)A_{ss}\right] \\
&- \dot{k_3}A_{ss} \\
&= k_4(k_3+\kappa)A_{ss} - k_6(k_3+\kappa)A_{ss}^2 + k_2k_E^{in} - k_E^{out}(k_3+\kappa)A_{ss} - \kappa(k_3+\kappa)A_{ss} - \dot{k_3}A_{ss} \\
&= -k_6(k_3+\kappa)A_{ss}^2 + A_{ss}\left[k_4(k_3+\kappa) - k_E^{out}(k_3+\kappa) - \kappa(k_3+\kappa) - \dot{k_3}\right] + k_2k_E^{in} \\
&= 0
\end{aligned} \tag{S43}$$

Dividing the last expression in Eq. S43 by $-k_6(k_3+\kappa)$ gives

$$A_{ss}^2 - A_{ss}\left[\frac{k_4}{k_6} - \frac{k_E^{out}}{k_6} - \frac{\kappa}{k_6} - \frac{\zeta k_3}{k_6(k_3+\kappa)}\right] - \frac{k_2k_E^{in}}{k_6(k_3+\kappa)} = 0 \tag{S44}$$

where $\dot{k_3}$ has been substituted by ζk_3 (see Eq. S35). When k_3 becomes large the term $k_3/(k_3+\kappa)$ goes to 1 and $k_2k_E^{in}/k_6(k_3+\kappa)$ goes to 0, such that Eq. S44 can be written as:

$$A_{ss}^2 - A_{ss}\left[\frac{k_4}{k_6} - \frac{k_E^{out}}{k_6} - \frac{\kappa}{k_6} - \frac{\zeta}{k_6}\right] = 0 \tag{S45}$$

and A_{ss} becomes:

$$A_{ss} = \frac{k_4}{k_6} - \frac{\kappa}{k_6} - \frac{\zeta}{k_6} - \frac{k_E^{out}}{k_6} \tag{S46}$$

Supporting Material, File S6 Text

Homeostatic Controllers Compensating for Growth and Perturbations

P. Ruoff[1]*, O. Agafonov[1], D. M. Tveit[2], K. Thorsen[2], T. Drengstig[2]
[1]Centre for Organelle Research
[2]Department of Electrical Engineering and Computer Science,
University of Stavanger, Stavanger, Norway

*Corresponding author. Address: Centre for Organelle Research, University of Stavanger, N-4036 Stavanger, Norway, Tel.: (47) 5183-1887, Fax: (47) 5183-1750, E-mail: peter.ruoff@uis.no

Steady states and theoretical set-point for motif 2 zero-order controller

Transporter-based compensatory flux with constant values of $\dot{V}$ and $\dot{k_3}$

We refer to the rate equations for A and E (Eqs. 43-44), which are written in the following form:

$$\dot{A} = \frac{k_2 k_4}{k_4+E} \cdot \frac{1}{V} - k_3 \cdot A - A\left(\frac{\dot{V}}{V}\right) \tag{S1}$$

$$\dot{E} = k_8 \cdot A - k_9 - E\left(\frac{\dot{V}}{V}\right) \tag{S2}$$

by setting in Eq. 44 $M/(k_{11}+M)=E/(k_{10}+E)=1$.

Calculating $\ddot{A}$ gives

$$\ddot{A} = -\frac{k_2 k_4}{(k_4+E)^2} \cdot \frac{\dot{E}}{V} - \left(\frac{k_2 k_4}{k_4+E}\right)\frac{\dot{V}}{V^2} - \dot{k_3}A + A\left(\frac{\dot{V}}{V}\right)^2 \tag{S3}$$

Inserting Eq. S2 into Eq. S3 leads to

$$\ddot{A} = -\frac{k_2 k_4}{(k_4+E)^2} \cdot \frac{1}{V}\left[k_8 \cdot A - k_9 - E\left(\frac{\dot{V}}{V}\right)\right] - \left(\frac{k_2 k_4}{k_4+E}\right)\frac{\dot{V}}{V^2} - \dot{k_3}A + A\left(\frac{\dot{V}}{V}\right)^2 \tag{S4}$$

Multiplying Eq. S4 by $V(k_4+E)^2/(k_2 k_4)$ gives

$$\ddot{A} = -k_8 A + k_9 + E\left(\frac{\dot{V}}{V}\right) - (k_4+E)\left(\frac{\dot{V}}{V}\right) - \dot{k_3}A \cdot \frac{V(k_4+E)^2}{k_2 k_4} + A\left(\frac{\dot{V}}{V}\right)^2 \cdot \frac{V(k_4+E)^2}{k_2 k_4} \tag{S5}$$

Setting the $\dot{V}/V$ terms in Eq. S5 to zero we get

$$\ddot{A} = -k_8 A + k_9 - \dot{k_3} A \cdot \frac{V(k_4{+}E)^2}{k_2 k_4} \tag{S6}$$

Setting Eq. S1 to zero and neglecting the $\dot{V}/V$ terms gives the relationship between decreasing E and increasing V and k_3 to keep A at a constant steady state A_{ss}, i.e.

$$\frac{k_2 k_4}{(k_4{+}E)\cdot V} = k_3 A_{ss} \quad \Rightarrow \quad (k_4{+}E)^2 = \frac{(k_2 k_4)^2}{k_3^2 A_{ss}^2 V^2} \tag{S7}$$

Inserting $(k_2 k_4)^2$ from Eq. S7 into Eq. S6 and setting $\ddot{A}$=0 gives

$$A_{ss} = \underbrace{\frac{k_9}{k_8}}_{A_{set}^{theor}} - \underbrace{\frac{\dot{k_3} k_2 k_4}{k_3^2 A_{ss} V}}_{\text{offset}} \tag{S8}$$

For constant $\dot{k_3}$ and increasing values of V and k_3 the offset term $\dot{k_3} k_2 k_4 / k_3^2 A_{ss} V$ goes to zero and A_{ss} is kept by the controller at its theoretical set-point A_{set}^{theor}=k_9/k_8 as clearly seen in Fig. 13. Since a constant A_{ss} level by this controller type is maintained by decreasing E values the negative feedback loop will break when E becomes low and the controller reaches its capacity limits (Eq. 48).

Cell-internal compensatory flux with constant values of $\dot{V}$ and and $\dot{k_3}$

In this case the rate equations (Eqs. 62-63) are written as

$$\dot{A} = \frac{k_4 k_6}{k_4{+}E} - k_3 \cdot A - A\left(\frac{\dot{V}}{V}\right) \tag{S9}$$

$$\dot{E} = k_8 \cdot A - k_9 - E\left(\frac{\dot{V}}{V}\right) \tag{S10}$$

by setting $N/(k_7+N)=E/(k_{10}+E)=M/(k_{11}+M)=1$. Taking the second-time derivative $\ddot{A}$ gives

$$\ddot{A} = -\frac{k_4 k_6}{(k_4+E)^2}\dot{E} - \dot{k_3}A + A\left(\frac{\dot{V}}{V}\right)^2 \tag{S11}$$

Inserting $\dot{E}$ from Eq. S10 into Eq. S11

$$\ddot{A} = -\frac{k_4 k_6}{(k_4+E)^2}\left[k_8 \cdot A - k_9 - E\left(\frac{\dot{V}}{V}\right)\right] - \dot{k_3}A + A\left(\frac{\dot{V}}{V}\right)^2 \tag{S12}$$

Setting Eq. S9 to zero and neglecting the $\dot{V}/V$ term, we have the condition how E has to decrease for increasing k_3 to keep A constant at A_{ss}, i.e.,

$$\frac{k_4 k_6}{(k_4+E)} = k_3 A_{ss} \quad \Rightarrow \quad (k_4+E)^2 = \frac{(k_4 k_6)^2}{k_3^2 A_{ss}^2} \tag{S13}$$

Substituting $(k_4+E)^2$ in Eq. S11 by $(k_4 k_6)^2/k_3^2 A_{ss}^2$, setting the resulting equation to zero, and neglecting the $\dot{V}/V$ terms, leads to

$$A_{ss} = \frac{k_9}{k_8} - \frac{\dot{k_3} k_4 k_6}{k_3^2 k_8 A_{ss}} \tag{S14}$$

where $A_{set}^{theor}=k_9/k_8$ and the offset term is zero for $\dot{k_3}=0$, and goes to zero when $\dot{k_3}$ is constant and k_3 increases.

Cell-internal compensatory flux with exponential increase of $\dot{V}$ and $\dot{k_3}$

i) Exponential increase in V and constant k_3 (phase 2). We start again with the rate equations

$$\dot{A} = \frac{k_4 k_6}{k_4+E} - k_3 \cdot A - A\left(\frac{\dot{V}}{V}\right) \tag{S9}$$

$$\dot{E} = k_8 \cdot A - k_9 - E\left(\frac{\dot{V}}{V}\right) \tag{S2}$$

In the case $\dot{k_3}$=0, but V increases exponentially, say $\dot{V}$=κV, A_{ss} and E_{ss} show constant value, where A_{ss} shows an offset above A_{set}^{theor} (overcompensation). The steady state in A can be calculated by setting Eq. S2 to zero, i.e.,

$$A_{ss} = \underbrace{\frac{k_9}{k_8}}_{A_{set}^{theor}} + \underbrace{\frac{\kappa}{k_8}E_{ss}}_{\text{overcompensated offset}} \tag{S15}$$

ii) Exponential increase in V and k_3 (phase 3). Assuming that $\dot{V}$=κV and $\dot{k_3}$=ζk_3 with κ and ζ constants, we can calculate $\ddot{A}$

$$\ddot{A} = -\frac{k_4 k_6}{(k_4+E)^2}\dot{E} - \dot{k_3}A \tag{S16}$$

assuming that $\dot{A}$=0. Inserting Eq. S2 (note that $\dot{V}/V$=κ) into Eq. S16 and setting Eq. S16 to zero gives the expression for the steady state of A, A_{ss},

$$-\frac{k_4 k_6}{(k_4+E)^2}\left[k_8 \cdot A_{ss} - k_9 - \kappa \cdot E\right] - \dot{k_3}A_{ss} = 0 \tag{S17}$$

leading to

$$A_{ss} = -\frac{k_4 k_6}{\dot{k_3}(k_4+E)^2}\left[k_8 \cdot A_{ss} - k_9 - \kappa \cdot E\right] \tag{S18}$$

Note, that while A is in a steady state, E is decreasing (derepressing) in order to increase the compensatory flux. Eq. S18 can be rewritten as

$$A_{ss} = -\underbrace{\frac{k_4 k_6 k_8}{\dot{k_3}(k_4+E)^2}}_{\gamma_0}\left[A_{ss} - \overbrace{\underbrace{\frac{k_9}{k_8}}_{A_{set}^{theor}} - \underbrace{\frac{\kappa}{k_8}E}_{\text{overcompensated offset}}}^{A_{set}^{app}}\right] \tag{S19}$$

where $A_{set}^{apparent}$ is an "apparent set-point". Thus, Eq. S19 can be written as

$$A_{ss} = -\gamma_0(A_{ss} - A_{set}^{app}) \quad \Rightarrow \quad A_{ss} = \left(\frac{\gamma_0}{1+\gamma_0}\right) A_{set}^{app} \tag{S20}$$

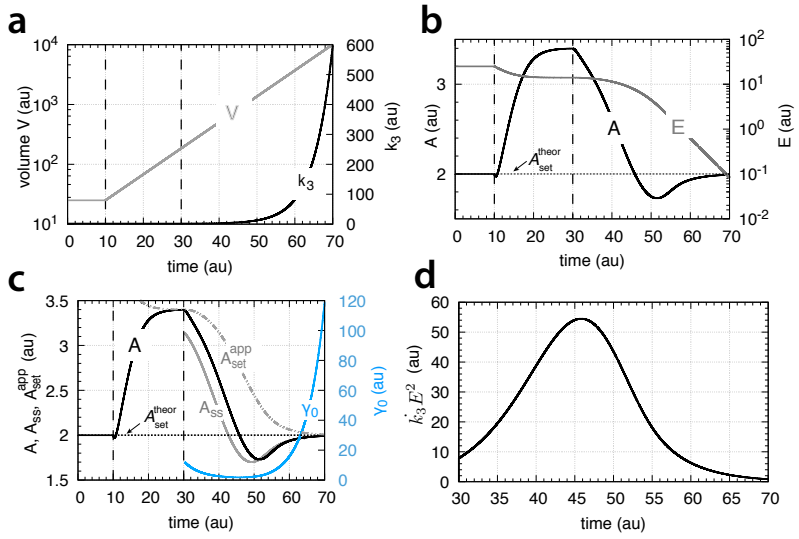

Figure S1. (a) Perturbation profile of V and k_3 (same figure as Fig. 14). (b) Response of controller (same results as in Fig. 25d). (c) Behaviors of A_{ss} and A_{set}^{app} as a function of time (Eq. S20). (d) By the end of phase 3 E^2 decreases more rapidly than the exponential increase of $\dot{k_3}$, which is indicated by the product $\dot{k_3}E^2$ going to zero.

Fig. S1c shows how γ_0 and A_{set}^{app} changes with respect to the controller's behavior when exposed to exponential increase in V and k_3 with the response shown in Fig. 25d. For convenience the perturbation profile and the controller's response are repeated in Figs. S1a and b. The derepression by decreasing E leads to an increase in γ_0 (Fig. S1c, curve outlined in blue). The increase in γ_0 is the result of E^2 decreasing more rapidly than the exponential increase of $\dot{k_3}$. This is indicated in Fig. S1 where the product $\dot{k_3}E^2$ during phase 3 decreases and $A_{ss} \rightarrow A_{set}^{theor}$.

Supporting Material, File S7 Text

Homeostatic Controllers Compensating for Growth and Perturbations

P. Ruoff[1*], O. Agafonov[1], D. M. Tveit[2], K. Thorsen[2], T. Drengstig[2]
[1]Centre for Organelle Research
[2]Department of Electrical Engineering and Computer Science,
University of Stavanger, Stavanger, Norway

*Corresponding author. Address: Centre for Organelle Research, University of Stavanger, N-4036 Stavanger, Norway, Tel.: (47) 5183-1887, Fax: (47) 5183-1750, E-mail: peter.ruoff@uis.no

Novel antithetic integral controller arrangements and steady states in a motif 2 background

Novel antithetic integral controller arrangements

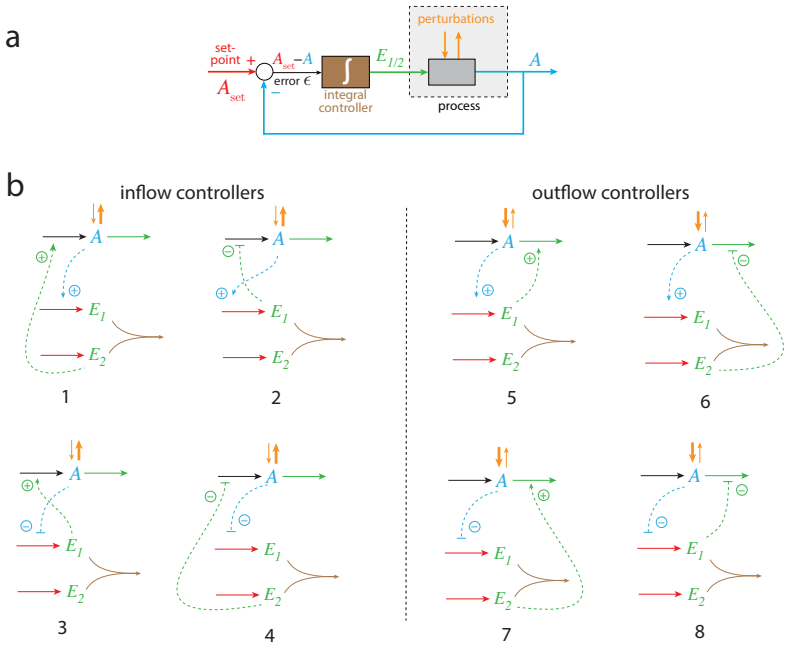

Figure S1. (a) Color-coded representation of a negative feedback loop containing an integral controller. (b) Molecular feedback schemes where the antithetic integral controller (outlined in brown) is embedded within different structural feedback loops which relate to the basic feedback motifs described in Ref. (1). Colors indicate how the different kinetic and signaling processes relate to the parts in the feedback loop in (a). Numbers define the different motifs.

Fig. S1a shows a generalized feedback loop containing an integral controller outlined in brown color. In Fig. S1b eight basic molecular feedback arrangements are shown in corresponding color code. The antithetic integral controller (also outlined in brown) is due to the removal of E_1 and E_2 by second-order kinetics. Activating and inhibitory signaling is shown by the dashed lines. In the following we describe some of the steady state behaviors in relation to the motif 2 antithetic controller.

Steady states and theoretical set-point for motif 2 antithetic controller

Transporter-based compensatory flux with constant values of $\dot{V}$ and k_3

The rate equations (Eqs. 76, 22, and 23) are

$$\dot{A} = \frac{k_2 \cdot k_{10}}{k_{10}+E_1} \cdot \frac{1}{V} - k_3 \cdot A - A\left(\frac{\dot{V}}{V}\right) \tag{S1}$$

$$\dot{E}_1 = A\left(\frac{k_4 \cdot M}{k_5+M}\right) - k_6 \cdot E_1 \cdot E_2 - E_1\left(\frac{\dot{V}}{V}\right) \tag{S2}$$

$$\dot{E}_2 = \frac{k_8 \cdot O}{k_9+O} - k_6 \cdot E_1 \cdot E_2 - E_2\left(\frac{\dot{V}}{V}\right) \tag{S3}$$

In deriving an expression for the steady state in A, we assume that precursors M and O are in sufficient amounts such that

$$\frac{M}{k_5+M} = \frac{O}{k_9+O} = 1$$

We can get an expression for A directly when inspecting Eq. S2. Rewriting Eq. S2 gives

$$k_4 \cdot A = \dot{E_1} + k_6 \cdot E_1 \cdot E_2 + E_1 \left(\frac{\dot{V}}{V} \right) \tag{S4}$$

During the first phase in Fig. 29a, when $\dot{V}$=$\dot{k_3}$=0, and A, E_1, and E_2 are in a steady state, we get

$$A_{ss} = \frac{k_6}{k_4} E_1 \cdot E_2 = \frac{k_8}{k_4} = A_{set}^{theor} \tag{S5}$$

showing that $E_1 \cdot E_2$ is constant. In case V and k_3 are linearly increasing the $E_1 \dot{V}/V$ term in Eq. S4 can be neglected, as E_1 is getting low and the $\dot{V}/V$ term goes to zero. $\dot{E_1}$ is negative, but low. Ignoring $\dot{E_1}$ shows that A can be described in term of $E_1 E_2$

$$A = \frac{k_6}{k_4} E_1 \cdot E_2 \tag{S6}$$

In fact, A and $k_6 E_1 E_2 / k_4$ follow each other very closely (Fig. S2), even when the controller is no longer able to cope with the linear increase of V and k_3

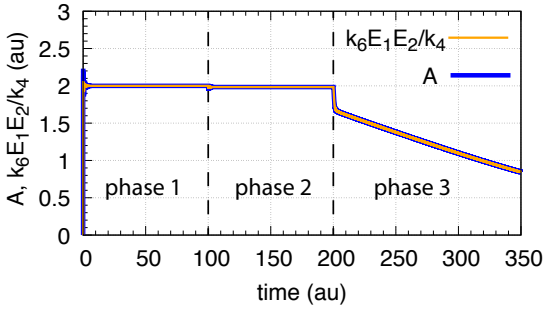

Figure S2. Same system as in Fig. 29a with $k_6 E_1 E_2 / k_4$ (orange curve) overlayed on A (blue curve), showing that $k_6 E_1 E_2 / k_4$ describes the behavior of A closely.

Fig. S2 shows that in phase 3 the product E_1E_2 can no longer be kept constant. Subtracting Eq. S2 from Eq. S3 and solving for A gives

$$A = \underbrace{\frac{k_8}{k_4}}_{A_{set}^{theor}} - \frac{\mathrm{d}(E_2 - E_1)}{\mathrm{d}t} - (E_2 - E_1)\left(\frac{\dot{V}}{V}\right) \tag{S7}$$

indicating that the increase in E_2 (Fig. 29a) cannot be matched by the derepressing/decreasing E_1, resulting in the decrease of A and the breakdown of the controller.

Transporter-based compensatory flux with exponential increase of $\dot{V}$ and $\dot{k}_3$

In case V and k_3 increase exponentially $k_6E_1E_2/k_4$ still describes the behavior of A, but the controller is not able (in comparison with a linear increase in V and k_3) to keep E_1E_2 constant (see Fig. S3).

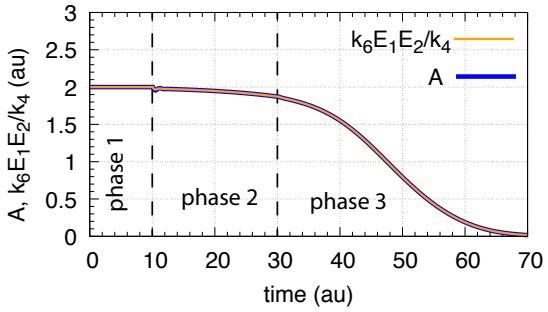

Figure S3. Same system as in Fig. 29b with $k_6E_1E_2/k_4$ (orange curve) overlayed on A (blue curve).

The increasing E_2 values cannot be balanced by the decreasing E_1 concentration leading to controller breakdown.

Cell-internal compensatory flux with constant values of $\dot{V}$ and and $\dot{k_3}$

When the compensatory flux is cell internal the rate equation for A (Eq. 76 with $N/(k_7+N) = 1$) becomes

$$\dot{A} = \frac{k_2 \cdot k_{10}}{k_{10}+E_1} - k_3 \cdot A - A\left(\frac{\dot{V}}{V}\right) \tag{S8}$$

while the rate equations for E_1 and E_2 remain as described by Eqs. S2 and S3. Calculating $\ddot{A}$ and setting it to zero leads to the following expression

$$\ddot{A} = -\frac{k_2 \cdot k_{10}}{(k_{10}+E_1)^2}\dot{E_1} - \dot{k_3} \cdot A - k_3 \cdot \dot{A} + A\left(\frac{\dot{V}}{V}\right)^2 = 0 \tag{S9}$$

Considering first the case that k_3 is kept constant ($\dot{k_3}$=0), while V increases linearly, we observe (phase 2, Fig. 29c) that A attains a stable steady state with $\dot{A}$=0. Considering further that $\dot{V}/V \rightarrow 0$, we arrive at the condition that $\dot{E_1}$=0, i.e.

$$\ddot{A} = -\frac{k_2 \cdot k_{10}}{(k_{10}+E_1)^2}\dot{E_1} = 0 \tag{S10}$$

Since $\dot{A} = \dot{E_1} = \dot{V}/V = 0$, we arrive at Eq. S5 showing that in case of a cell-internal compensatory flux the m2-antithetic controller is able to keep A at A_{set}^{theor} as long as there is sufficient supply for A, E_1, and E_2 and that the maximum compensatory flux k_2 has not been reached.

When k_3 increases linearly, the term $\dot{k_3} \cdot A$ in Eq. S9 cannot be ignored. Inserting Eq. S2 into Eq. S9, observing from the numerical calculation that

$\dot{A}$=0, and approximating $\dot{V}/V = 0$, Eq. S9 is written as

$$\left[k_4 A_{ss} - k_8 - \underbrace{E_1 \left(\frac{\dot{V}}{V} \right)}_{\to 0} \right] = -\frac{\dot{k_3}(k_{10}+E_1)^2}{k_2 k_{10}} A_{ss} \tag{S11}$$

Dividing the left- and right-hand side of Eq. S11 by k_4, observing that k_8/k_4=A_{set}^{theor}, and rearranging the equation, gives

$$A_{ss} \left(1 + \frac{\dot{k_3}(k_{10}+E_1)^2}{k_2 k_4 k_{10}} \right) = A_{set}^{theor} \tag{S12}$$

or

$$A_{ss} = \frac{A_{set}^{theor}}{1 + \frac{\dot{k_3}(k_{10}+E_1)^2}{k_2 k_4 k_{10}}} \tag{S13}$$

Eq. S13 indicates that when both V and k_3 increase linearly there should be an offset in A_{ss} below A_{set}^{theor}, but the "offset term"

$$\frac{\dot{k_3}(k_{10}+E_1)^2}{k_2 k_4 k_{10}}$$

is generally low, because k_2 represents the maximum compensatory flux, which in the calculations is 1×10^5. The "offset term" can further be reduced by increasing the aggressiveness of the controller when increasing k_4 and k_8 values, but maintaining the k_8/k_4 ratio, i.e., keeping A_{set}^{theor} constant.

Cell-internal compensatory flux with exponential increase of $\dot{V}$ and and $\dot{k_3}$

Fig. 29d shows that when only V increases exponentially during phase 2 with $\dot{V}$=κV (κ being a constant), and k_3 is kept constant ($\dot{k_3} = 0$), the controller is able to maintain a constant steady state in A, as well as in E_1 and E_2. The rate equations in this case are

$$\dot{A} = \frac{k_2 \cdot k_{10}}{k_{10} + E_1} - k_3 \cdot A - \kappa A \tag{S14}$$

$$\dot{E}_1 = k_4 A - k_6 \cdot E_1 \cdot E_2 - \kappa E_1 \tag{S15}$$

$$\dot{E}_2 = k_8 - k_6 \cdot E_1 \cdot E_2 - \kappa E_2 \tag{S16}$$

Since A, E_1, and E_2 are during phase 2 in a steady state (Fig. 29d) we get an expression for A_{ss}, by setting Eq. S15 to zero and solving for A_{ss}

$$A_{ss} = \frac{k_6}{k_4} E_1 \cdot E_2 + \frac{\kappa}{k_4} E_1 \tag{S17}$$

Another expression for A_{ss} can be found by calculating $\dot{E}_1 - \dot{E}_2$ and setting the resulting expression to zero (E_1 and E_2 are in a steady state)

$$\dot{E}_1 - \dot{E}_2 = k_4 \cdot A_{ss} - k_8 + \kappa(E_2 - E_1) = 0 \tag{S18}$$

which gives

$$A_{ss} = \underbrace{\frac{k_8}{k_4}}_{A_{set}^{theor}} + \underbrace{\frac{\kappa(E_1 - E_2)}{k_4}}_{\text{overcompensation part}} \tag{S19}$$

which identifies the factors leading to the overcompensation. Interestingly, increasing the controller aggressiveness by increasing k_8 and k_4, but keeping their ratio (A_{set}^{theor}) constant, the overcompensation can be reduced and A_{ss} will approach A_{set}^{theor}.

Setting Eqs. S19 and S17 equal, and solving for $k_6 E_1 E_2 / k_4$ leads to the relationship

$$\frac{k_6}{k_4} E_1 \cdot E_2 = A_{set}^{theor} - \frac{\kappa E_2}{k_4} \tag{S20}$$

showing that $k_6E_1E_2/k_4$ lies (under steady state conditions) slightly below A_{set}^{theor}.

When in phase 3 k_3 increases exponentially, E_1 decreases. The resulting derepression by E_1 moves A_{ss} towards A_{set}^{theor}, but when the E_1 concentration becomes too low due to the increasing E_2 (which removes E_1) homeostasis is lost once E_2 exceeds E_1. For low E_1 values $\dot{E}_1$ is also low, and, as Eq. S15 indicates, the decreasing A concentrations is quite well described by $k_6E_1E_2/k_4$ (Fig. S4).

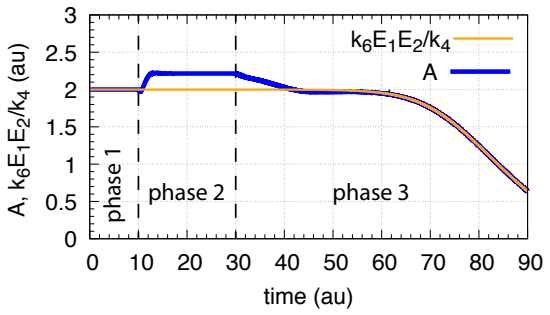

Figure S4. Same system as in Fig. 29d with $k_6E_1E_2/k_4$ (orange curve) overlayed on A (blue curve).

References

[1] Drengstig, T.; Jolma, I.; Ni, X.; Thorsen, K.; Xu, X.; Ruoff, P. *Biophys J* **2012**, *103*(9), 2000–2010.

Paper 4:
Exploring mechanisms of glucose uptake regulation and dilution resistance in growing cancer cells

Manuscript submitted to **Biophysical** *Journal*
Article

Exploring Mechanisms of Glucose Uptake Regulation and Dilution Resistance in Growing Cancer Cells

Daniel M. Tveit[1], Gunhild Fjeld[2], Tormod Drengstig[1], Fabian V. Filipp[3], Peter Ruoff[2], and Kristian Thorsen[1,*]

[1]Department of Electrical Engineering and Computer Science, University of Stavanger, Stavanger, Norway
[2]Centre for Organelle Research, University of Stavanger, Stavanger, Norway
[3]Systems Biology and Cancer Metabolism, Program for Quantitative Systems Biology, University of California Merced, Merced, CA, USA
[*]Correspondence: kristian.thorsen@uis.no

ABSTRACT Most cancer cells rely on aerobic glycolysis and increased glucose uptake for the production of biosynthetic precursors needed to support rapid proliferation. Increased glucose uptake and glycolytic activity may result in intracellular acidosis and increase of osmotically active substances, leading to cell swelling. This causes dilution of cellular constituents, which can markedly influence cellular reactions and the function of proteins, and hence, control mechanisms used by cancer cells to maintain a highly glycolytic phenotype must be robust to dilution. In this paper, we review the literature on cancer cell metabolism and glucose uptake, and employ mathematical modeling to examine control mechanisms in cancer cell metabolism that show robust homeostatic control in the presence of dilution. Using differential gene expression data from the Expression Atlas database, we identify the key components of glucose uptake in cancer, in order to guide the construction of a mathematical model. By simulations of this model we show that while negative feedback from downstream glycolytic metabolites to glucose transporters is sufficient for homeostatic control of glycolysis in a constant cellular volume, it is necessary to control intermediate glycolytic enzymes in order to achieve homeostatic control during growth. With a focus on glucose uptake in cancer, we demonstrate a systems biology approach to the identification, reduction, and analysis of complex regulatory systems.

SIGNIFICANCE Rapid proliferation and increased glycolytic activity in cancer cells lead to dilution of cellular constituents, which can markedly influence cellular reactions and the function of proteins. Therefore, control mechanisms used by cancer cells to maintain a highly glycolytic phenotype must be robust to dilution. We construct a mathematical model of glucose uptake in cancer, and using a systems biology approach to the analysis of regulatory networks, identify the presence of integral control motifs as a means for achieving dilution resistance. Furthermore, we show that while negative feedback from downstream glycolytic metabolites to glucose transporters is sufficient for homeostatic control of glycolysis in a constant cellular volume, it is necessary to control intermediate glycolytic enzymes to achieve homeostatic control during growth.

INTRODUCTION

It is well established that cell swelling and shrinkage affect important cellular functions, in part by dilution and concentration of cellular compounds (1–4). Such changes in concentration can markedly influence the function of intracellular proteins (1). This has been demonstrated in studies on the effect of volume change on enzyme reactions in solitary vesicles, showing that there is a significant impact on the dynamical and steady state behavior of these reactions (5). The significance of dilution due to growth is emphasized by the cell-size control mechanism employed in budding-yeast. In these cells, the concentration of a cell cycle activator maintained at a constant level during growth relative to a growth diluted inhibitor provides a measurement of cell volume and a molecular mechanism for cell-size control (6, 7). Although most proteins are maintained at constant concentrations in growing cells, owing to mRNA amounts and number of ribosomes increasing with cell size, we lack an understanding of the molecular mechanisms that coordinate biosynthesis to achieve constant protein concentrations during growth (7, 8). Investigations into the performance of so-called integral control motifs (ICMs) have revealed mechanisms by which robustness to dilution can be achieved (9, 10). In this paper, we look into homeostatic mechanisms regulating glucose uptake in rapidly growing cancer cells. We identify the presence of ICMs as part of glucose uptake in cancer, and investigate how homeostatic control of metabolite and protein concentrations is achieved in the presence of dilution due to growth.

Most cancer cells show an increased uptake and metabolism of glucose, a phenotype that can be detected by ^{18}fluoro-deoxyglucose positron emission tomography (FDG-PET) (11–13). This growth mode relies on a balanced production of cellular components to avoid molecular crowding and solvent capacity constraints (14, 15). The cell represents a tiny reagent reservoir and is reliant on a balanced influx and efflux of compounds to support growth rates corresponding to that seen in cancer. Thus, as the cell expands, its constituents need to increase at the same rate to meet the growth requirements, meaning a proportional increase in nucleic acids, polysaccharides, proteins, and lipids (16). Aside from biomass formation for the purpose of growth, metabolism also affects cell volume through uptake of nutrients, by creation of osmotically active substances, developing intracellular acidosis, and by depletion of available ATP (1, 17, 18). In fact, increased cellular volume appears to be required for proliferation, and hypertonic shrinkage inhibits cell proliferation, whereas slight osmotic swelling has the opposite effect (1). In contrast, differentiation is followed by cell shrinkage in a number of cells (1).

In the following, we take a look at some key elements of the rewiring of glycolysis that produce the increased glycolytic activity seen in cancer. Next, we look at the various control mechanisms in place that maintain this increased glucose uptake and metabolic activity. We then focus our attention to glucose uptake, and show that differential gene expression of cancer and normal cells corroborate the reported rewiring in cancer. With this information, we construct a mathematical model of glucose uptake in cancer, formulated as a system of ordinary differential equations (ODEs). We construct the model in a stepwise manner, where each step adds a layer of regulation to the model. This is done in order to investigate the role each control mechanism serve. We show how dilution is incorporated into the model, and run simulations for each step of model construction. Finally, we show how control mechanisms of glucose uptake in cancer form ICMs, and how this enables robust homeostatic control of glycolysis, even in the presence of dilution.

Rewiring of Glycolysis in Cancer

Cancer cells show an increased reliance on glycolysis and lactic acid fermentation, even in the presence of oxygen, and a more glycolytic phenotype is persistent with a more aggressive cancer cell type (12, 19, 20). This is known as the Warburg effect, or aerobic glycolysis, and is necessary in order to meet the increased demands of rapid proliferation (11). In cancer cells, the Warburg effect is in supplement to oxidative phosphorylation rather than a replacement (21). This is in contrast to normal cells that maintain a high rate of glycolysis at the expense of oxidative phosphorylation; a phenomenon known as the Crabtree effect (21). However, in the hypoxic tumor microenvironment, cancer cells naturally show a decreased reliance on oxidative phosphorylation (21, 22). The increased glycolytic flux in cancer supplies biosynthetic pathways with precursors, meets the increased bioenergetic demand of proliferation, and contributes to tumor invasion through the excretion of lactate and consequent acidification of the tumor microenvironment (11, 12, 21, 23, 24). The mechanisms that reprogram metabolism in cancer are often cancer-specific, nevertheless, there are common hallmarks, notably a shift towards protein isoforms that promote biosynthesis and proliferation (11, 21).

In the first step of glycolysis, glucose is transported into the cell. The GLUT (gene symbol *SLC2A*) family of glucose transporters are membrane-spanning proteins facilitating the transport of sugars across biological membranes along the concentration gradient (25, 26). GLUT1 is one of 14 currently identified GLUT proteins expressed in humans, and is expressed in almost every tissue (27–30). Together with its high affinity for glucose, this gives GLUT1 a clear role in the basal glucose uptake of most tissues (25, 28, 29). Elevated expression of GLUT1 has been reported in most cancers, and the expression level correlates reciprocally with the survival of cancer patients (12, 23, 30). Hypoxia-inducible factor-1 (HIF-1), a dimer of HIF-1α and HIF-1β, is one of the factors responsible for upregulating GLUT1 in tumor cells (12, 21, 30, 31). HIF-1β is constitutively expressed, whereas HIF-1α is regulated through oxygen-dependent and oxygen-independent mechanisms (31). GLUT1 expression is upregulated through hypoxia-response elements on the GLUT1 promoter that bind HIF-1 (30). HIF-1α has increased levels in most cancers, which provides a mechanism by which cancer cells overexpress GLUT1 (12, 30, 31). Other factors known to cause overexpression and translocation of GLUT1 to the cell membrane in cancer include the oncoprotein c-Myc, protein kinase Akt/PKB, and oncogenic KRAS and BRAF (12, 21, 30).

Glycolysis consists of several reversible reactions and three (essentially) irreversible reactions (see Figure 1). Because they are irreversible, these three reactions represent committed steps of glycolysis, and the enzymes that drive these reactions function as gatekeepers of glycolysis and have a key role in regulating the glycolytic flux (21). In the first irreversible reaction of glycolysis, glucose is phosphorylated to glucose 6-phosphate (G6P) by hexokinase, coupled to the dephosphorylation of ATP (13, 32, 33). Hexokinase 2 (HK2) is one of four isoforms of hexokinase found in mammalian tissue (13). HK2 has a very high affinity for glucose, with a Michaelis constant (K_M value) of 0.02–0.03 mM (13, 32). To support increased glucose uptake in cancer, HK2 is overexpressed and bound to the outer mitochondrial membrane protein voltage-dependent anion channel (VDAC) (13, 21, 32). VDAC supplies HK2 with ATP by recruiting help from ATP synthase and adenine nucleotide translocator, resulting in a mechanism that rapidly converts glucose to G6P (13). HK2 is product inhibited by G6P, however, it is likely that this inhibition is minimal due to rapid utilization of G6P in cancer cells (21, 32).

The second irreversible reaction of glycolysis is catalyzed by phosphorfructokinase 1 (PFK1), and is the phosphorylation of fructose 6-phosphate (F6P) to fructose 1,6-bisphosphate (F1,6BP) with the concomitant dephosphorylation of ATP (21, 33, 34). PFK1 is a tetrameric enzyme that exists in liver (PFKL), muscle (PFKM), and platelet (PFKP) isoforms in mammalian cells (21, 34, 35). PFK1 expression is upregulated in cancer cells, and increased expression of the PFKP isoform is a characteristic feature of cancer (34, 35). Krüppel-like factor 4 (KLF4), which has elevated levels in certain cancer types, has been shown to activate transcription of the *PFKP* gene by directly binding to its promoter (34). In addition, PFK1 is allosterically activated by fructose 2,6-bisphosphate (F2,6BP), which shows increased generation associated with overexpression of the phosphofructokinase 2 (PFK2) isoform PFKFB3 in cancer (21).

The third irreversible reaction of glycolysis is the conversion of phosphoenolpyruvate (PEP) to pyruvate by the transfer of a phosphoryl group to ADP (21, 33). Cancer cells control this reaction by expressing the low-affinity M2 isoform of pyruvate kinase (PKM2) (11, 21). The PKM2 tetramer is allosterically regulated by various metabolites and responds to nutritional and stress signals, whereas the normal M1 isoform of pyruvate kinase (PKM1) is a constitutively active tetramer (21, 36). The regulation of PKM2 enables cancer cells to dictate the flow of carbon into biosynthetic pathways and adapt to different conditions of nutrient availability and anabolic demands (11, 21, 36). Additionally, PKM2 is regulated between its metabolically active tetrameric form and metabolically inactive dimeric form, where the PKM2 dimer is imported into the nucleus and stimulates transcription of glycolytic genes (36).

In addition to the key regulatory enzymes of glycolysis described above, other important glycolytic enzymes are also upregulated in cancer. For example, of the lactate dehydrogenases (LDHs), LDHA is the predominantly expressed isozyme in cancer (21). LDHA has a high affinity for pyruvate, and favors the conversion of pyruvate to lactate (21). Enolase 1 (ENO1) is induced in cancer cells through HIF-1α overexpression (30, 31). Aldolase A (ALDOA) is the predominant aldolase isoform expressed in hepatoma and gastric cancer tissues, and favors the cleaving of F1,6BP (21, 37). Taken together, the glycolytic isoforms expressed in cancer show a concerted effort to increase glycolytic activity and promote production of biosynthetic precursors. A schematic of glycolysis is shown in Figure 1, highlighting some of the key isoforms that are commonly overexpressed in cancer.

Regulation of Glucose Uptake in Cancer

We now focus our attention to glucose uptake and the initial steps of glycolysis, and discuss the control mechanisms that regulate glucose uptake in cancer. Although key glycolytic enzymes are upregulated in cancer, they are still involved in metabolic regulation and respond to signals such as nutritional and oxidative stress, however, this regulation changes to favor proliferation (11, 21, 36, 38). Regulation of nutrient transporters by the availability of nutrients is a phenomenon observed in bacteria and yeast, and similarly, an inhibitory effect of glucose on GLUT1 expression has been observed in several mammalian cell lines (39, 40). To study the effect of glucose on GLUT1 expression, cells have been subjected to glucose deprivation experiments, with the common result that GLUT1 content at the cell surface is increased (39, 41–45). This is achieved by different mechanisms, including increased GLUT1 mRNA transcription and stability, increased protein synthesis or decreased protein degradation, and translocation of the transporter to the cell membrane (39).

Extracellular glucose supply directly affects the intracellular glucose level (46). Thus, it is possible that GLUT1 content at the cell surface is regulated in some way by the intracellular level of glucose, as has been previously suggested (41, 47). In fact, comparisons of mammary tumors and normal mammary tissue in mice have shown that increased GLUT1 level correlates with decreased intracellular glucose level and increased glycolytic activity (38). One way in which intracellular glucose affects GLUT1 expression is via AMP-activated protein kinase (AMPK) (48). AMPK is comprised of one catalytic α-subunit, and two regulatory subunits, β and γ (48, 49). Intracellular glucose regulates AMPK activity in a few different ways: An abundance of glucose will quickly be phosphorylated to G6P by HK2. G6P is then used to supply glycolysis, lowering the AMP/ATP and ADP/ATP ratios, keeping AMPK from being activated by the binding of AMP and ADP (48). High glucose levels and increased biomass generation also reduce the NAD^+/NADH ratio, which indirectly inhibits AMPK through silent information regulator T1 (SIRT1) and serine-threonine liver kinase B1 (LKB1) (21, 48, 50, 51). Downstream of G6P, the accumulation of diacylglycerol (DAG) and glycogen both lead to inhibition of AMPK. DAG inhibits AMPK by activating protein kinase C (PKC), which in turn induces the inhibitory phosphorylation of the AMPK α-subunit, while glycogen inhibits AMPK by binding to the β-subunit (48). In addition, activation of protein phosphatase 2A (PP2A) as a result of high glucose levels inhibits AMPK (48, 52, 53).

AMPK in turn has been shown to affect GLUT1 expression (54). One mechanism by which this happens is by increasing the degradation of thioredoxin interacting protein (TXNIP). TXNIP can bind directly to GLUT1 and induce internalization, as well as reduce GLUT1 mRNA level (48, 55). Another suggested mechanism is that downstream of AMPK, p38 mitogen-activated protein kinase (MAPK) activation leads to enhancement of GLUT1 mediated glucose transport (56).

Another important aspect of glucose uptake is the regulation of HK2, as it drives the first committed step of glycolysis and maintains a high concentration gradient of glucose across the cell membrane, thereby driving the facilitated diffusion

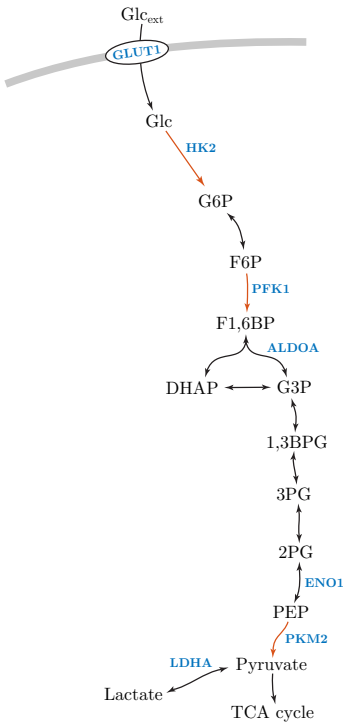

Figure 1: Schematic of glycolysis with some of the commonly overexpressed isoforms in cancer highlighted in blue. Reactions highlighted in red indicate the committed steps of glycolysis. Abbreviations: Extracellular glucose (Glc_{ext}), glucose transporter 1 (GLUT1), glucose (Glc), hexokinase 2 (HK2), glucose 6-phosphate (G6P), fructose 6-phosphate (F6P), phosphofructokinase 1 (PFK1), fructose 1,6-bisphosphate (F1,6BP), aldolase A (ALDOA), dihydroxyacetone phosphate (DHAP), glyceraldehyde 3-phosphate (G3P), 1,3-bisphosphoglycerate (1,3BPG), 3-phosphoglycerate (3PG), 2-phosphoglycerate (2PG), enolase 1 (ENO1), phosphoenolpyruvate (PEP), pyruvate kinase M2 (PKM2), lactate dehydrogenase A (LDHA), tricarboxylic acid cycle (TCA cycle).

of glucose by GLUT1 (21, 57, 58). Activators of the HK2 promoter include glucose, insulin, glucagon, p53, cAMP, and hypoxic conditions (13, 32, 59). Interestingly, it is glucose rather than downstream glycolytic metabolites that activate the HK2 promoter (13, 32, 59–61). Together with the fact that HK2 phosphorylates glucose to G6P in a reaction that is essentially irreversible, these two compounds form a stabilizing feedback connection (13, 62). Additionally, the binding of HK2 to the outer mitochondrial membrane via VDAC helps prevent apoptosis in cancer cells (13, 32). Together with the diminished inhibition (or possibly saturated inhibition) of HK2 by G6P that is associated with mitochondrial bound HK2, this gives a clear role for HK2 in promoting a malignant phenotype (32, 63–65).

The control mechanisms discussed above are summarized in Figure 2A. Here, glucose uptake and supply to metabolism includes regulatory pathways that inhibit GLUT1 mediated glucose uptake via AMPK, as well as the stabilizing feedback connection formed by glucose and HK2. The mechanisms that affect AMPK depend on the production of G6P, and therefore, G6P represents the potential for these mechanisms to ultimately affect GLUT1 mediated glucose uptake. Before we can construct a mathematical model of the system in Figure 2A, activating and inhibiting pathways need to be translated into reactions that

can be described by reaction kinetic equations. To this end, parallel pathways with similar overall effects are grouped together, shown in Figure 2B. These combined pathways are then turned into activating or inhibiting reactions affecting generation or removal reactions of the compounds considered, shown in Figure 2C. The conversion of the system in Figure 2B to the system in Figure 2C preserves the effect one compound has on another, however, this conversion is not unique. For example, a negative effect of G6P on GLUT1 content at the cell surface could also be achieved if G6P activates the degradation or internalization of GLUT1 (62). Additionally, the activating and inhibiting reactions of Figure 2C do not need to represent the same molecular mechanisms. For example, the generation of G6P is driven by the phosphorylation of glucose by HK2, whereas glucose induces HK2 generation by activating the HK2 promoter. We use the system in Figure 2C as a simplified representation of glucose uptake in cancer, and as a basis for our mathematical model.

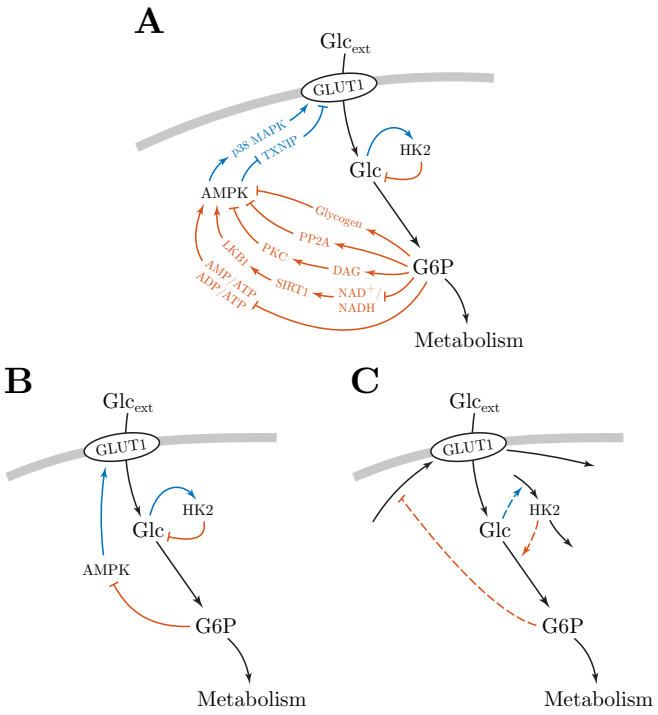

Figure 2: Panel A summarizes the control mechanisms of glucose uptake in cancer reported in the literature. Line marker-ends indicate the effect one compound has on another, arrowhead for positive and flat head for negative. Colored pathways indicate the overall effect of that pathway, blue for positive and red for negative. Black lines represent the flow of glucose to metabolism. Panel B shows colored pathways grouped together based on similar overall effects. Panel C shows the system in panel B translated into a form where activating and inhibiting effects act on reactions generating and turning over compounds. This allows for the system to be described by a simplified mathematical model using reaction kinetic equations.

METHODS

Differential Gene Expression

Expression Atlas was used to collect differential gene expression data comparing cancer cells with normal (i.e. non-cancerous) cells, across a variety of tissues and cell types. Expression Atlas is an open science resource providing information on gene and protein expression in animal and plant samples of different cell types, organism parts, developmental stages, diseases, and other conditions (66). Expression Atlas contains thousands of selected microarray and RNA-sequencing datasets that are manually curated, annotated, checked for high quality, and processed using standardized analysis methods (66). For genes of interest, users can view baseline expression in tissues, and differential expression for biologically meaningful pairwise comparisons (66).

Differential expression data of the *SLC2A* gene family, *HK1-3*, *GCK*, *PFKM*, *PFKP*, *PKM*, and *PKLR* genes in human was gathered from the Expression Atlas database. We curated the data to ensure only experiments comparing cancer cells with normal cells were included. Differential gene expression experiments with drug treatments were removed. Expression Atlas reports experiment results as $\log_2$-fold changes. In this paper, we report the arithmetic mean of $\log_2$-fold changes (i.e. $\log_2$ of the geometric mean fold change) for each gene across all experiments. Additional genes were analyzed, but due to low number of experiments (less than 5), are not included in the main results (see Section S1 in the Supporting Material).

Computational Methods

Systems of ODEs are solved numerically in initial value problems using Matlab R2018a and the `ode45` ODE solver, based on the Dormand-Prince (4, 5) pair (67). Initial values and parameters for all simulations are provided in the Supporting Material. Simulation results are given in arbitrary units (arb. unit). Reaction rates are expressed as concentrations per unit of time.

RESULTS AND DISCUSSION

Corroborating the Reported Rewiring of Glycolysis in Cancer

Average $\log_2$-fold changes for key genes associated with glucose uptake and glycolysis, across a variety of tissues and cell types, are shown in Figure 3. The differential gene expression data largely corroborates the reported rewiring of glycolysis in cancer discussed above. Namely, a shift towards GLUT1 (*SLC2A1* gene) mediated glucose uptake, predominant expression of the PKM2 (PKM1 and PKM2 are different splicing products of the *PKM* gene (21)) isoform, and overexpression of HK2. We also found a slight upregulation of the *PFKP* gene in cancer, consistent with previous studies (34). Hence, the model proposed in Figure 2C appears to include the key components of glucose uptake in cancer, and provides a good basis for mathematical modeling.

The results also shows an increased *HK3* transcript abundance in cancer. This is not surprising, since it has been shown that HK3 is upregulated by hypoxia, partially through HIF dependent signaling (68). Whereas HK2 bind to the outer mitochondrial membrane, HK3 does not (13, 68). A consequence of mitochondrial bound HK2 is the prevention of cell death by inhibiting formation of the mitochondrial permeability transition pore (MPTP) complex (13, 68). On the other hand, HK3 overexpression promotes cell survival in response to oxidative stress, decreases the production of reactive oxygen species (ROS), perserves mitochondrial membrane potential, and promotes mitochondrial biogenesis (68). Therefore, it is likely that HK2 and HK3 serve different, but complementary, roles in maintaining a highly glycolytic phenotype and promoting cancer cell survival. Notably, inhibition of glucose or G6P binding to the regulatory half of HK3 (N-terminal domain) impairs catalysis in the catalytic half (C-terminal domain), suggesting a cooperative effect of glucose binding in the regulatory half to subsequent binding in the catalytic half (68). Hence, it appears that HK3 interacts with glucose in a similar way to that of HK2 in Figure 2. As a result, we will only consider HK2 in the following mathematical modeling, but note that HK2 can be thought of as a pool of both HK2 and HK3.

Modeling Rate Expressions in a Changing Volume

When modeling rate expressions in a changing volume, care must be taken so that concentrations are handled in the correct way. As an example we show how this is done for a simple enzyme reaction. The Michaelis–Menten equation describes the rate of an enzyme reaction, assuming steady state for the substrate-enzyme complex (69)

$$v = \frac{k_{\text{cat}} \cdot c_{\text{E}} \cdot c_{\text{S}}}{K_{\text{M}} + c_{\text{S}}} \tag{1}$$

where v is the reaction rate, k_{cat} is the catalytic constant (or turnover number), K_{M} is the Michaelis constant, c_{E} is the (total) concentration of enzyme, and c_{S} is the concentration of substrate. We start by considering some compound x in a changing

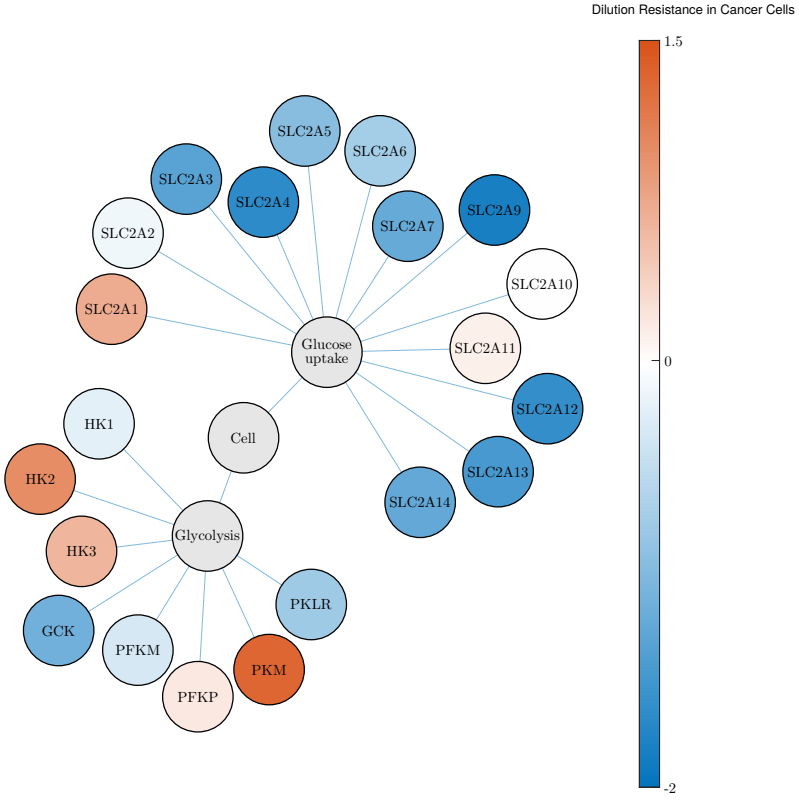

Figure 3: Differential gene expression of key genes associated with glucose uptake and glycolysis. The differential gene expression compares cancer cells with normal cells, across a variety of tissues and cell types, reported as the average $\log_2$-fold change of several experiments. Upregulation in cancer cells is indicated by red, and downregulation by blue. White indicates no change. The differential gene expression corroborates the reported rewiring of glycolysis in cancer. Namely, a shift towards GLUT1 (*SLC2A1* gene) mediated glucose uptake, overexpression of HK2, and a predominant reliance on PKM2 (PKM1 and PKM2 are different splicing products of the *PKM* gene (21)). We also found upregulation of the *HK3* and *PFKP* genes. See Section S1 in the Supporting Material for information on the individual differential gene expression experiments.

volume. Using the product rule, we express the change in concentration of x as

$$n_x(t) = c_x(t) \cdot V(t) \tag{2}$$

$$\dot{n}_x(t) = \dot{c}_x(t) \cdot V(t) + c_x(t) \cdot \dot{V}(t) \tag{3}$$

$$\dot{c}_x(t) = \frac{\dot{n}_x(t)}{V(t)} - c_x(t) \cdot \frac{\dot{V}(t)}{V(t)} \tag{4}$$

where n_x is the amount of compound, c_x is the concentration of compound, and V is the volume. We use dot notation to indicate time derivative. The first term of Eq. 4 is identical to the time derivative of c_x in a constant volume, while the second term represents the dilution of c_x (10). We will call this the *dilution term*. Using Eq. 1, we express the differential equation of a

product P being formed by an enzyme reaction in a changing volume by introducing the dilution term from Eq. 4 (5)

$$\dot{c}_{\mathrm{P}}(t) = \frac{k_{\mathrm{cat}} \cdot c_{\mathrm{E}}(t) \cdot c_{\mathrm{S}}(t)}{K_{\mathrm{M}} + c_{\mathrm{S}}(t)} - c_{\mathrm{P}}(t) \cdot \frac{\dot{V}(t)}{V(t)} \tag{5}$$

It is important to note that all constituents of the enzyme reaction, i.e. product, enzyme, and substrate, are diluted as the volume increases. This means that even if an enzyme is present in constant amount, a large enough volume increase can effectively stop the enzyme reaction by dilution of the enzyme concentration (5).

Modeling Glucose Uptake in Cancer

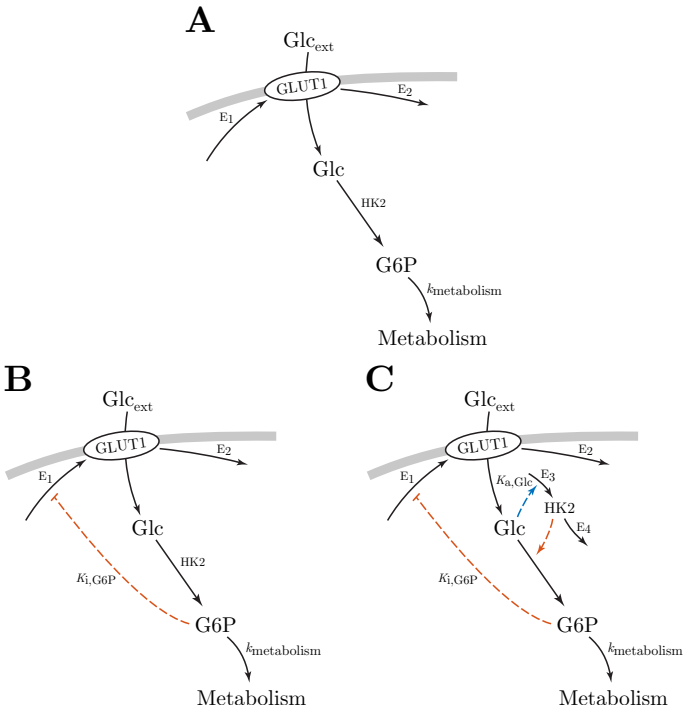

Figure 4: The mathematical model of glucose uptake is constructed in three steps. Panel A shows the first step, with only the uptake and supply of glucose to metabolism. The second step is shown in panel B, which includes feedback inhibition from G6P to GLUT1 mediated glucose uptake. Panel C shows the final step, where the model also includes the stabilizing feedback connection formed by HK2 and intracellular glucose.

We construct the mathematical model of glucose uptake in three steps, starting with glucose uptake and supply to metabolism without any of the control mechanisms discussed above. This system is shown in Figure 4A. Assuming low intracellular concentration of glucose due to rapid conversion by HK2, facilitated diffusion of glucose by GLUT1 can be approximated by the Michaelis–Menten equation (57, 58). In this first step of model construction, we assume that HK2 is not being generated and turned over (and therefore, HK2 synthesis is not activated by intracellular glucose), and that the concentration of HK2 simply dilutes as the cellular volume increases. The phosphorylation of glucose to G6P is modeled by the Michaelis–Menten equation,

and the sink reaction to metabolism is modeled by a first order reaction with rate constant $k_{\text{metabolism}}$. GLUT1 is assumed to be generated and turned over in reactions driven by enzymes E_1 and E_2, respectively, but feedback inhibition from G6P is omitted for the time being. The enzymes E_1 and E_2 are themselves present in constant amounts only (i.e. their concentrations simply dilute with increasing volume). We assume the production of GLUT1 is proportional to the concentration of E_1, and that the degradation of GLUT1 by E_2 is given by a Michaelis–Menten-type process. We are considering a growing cell, which introduces the dilution term from Eq. 4. The dynamical model is given by the following system of ODEs

$$\dot{c}_{\text{Glc}}(t) = \frac{k_{\text{cat,GLUT1}} \cdot c_{\text{GLUT1}}(t) \cdot c_{\text{Glc,ext}}(t)}{K_{\text{M,GLUT1}} + c_{\text{Glc,ext}}(t)} \cdot \frac{A(t)}{V(t)} - \frac{k_{\text{cat,HK2}} \cdot c_{\text{HK2}}(t) \cdot c_{\text{Glc}}(t)}{K_{\text{M,HK2}} + c_{\text{Glc}}(t)} - c_{\text{Glc}}(t) \cdot \frac{\dot{V}(t)}{V(t)} \tag{6}$$

$$\dot{c}_{\text{G6P}}(t) = \frac{k_{\text{cat,HK2}} \cdot c_{\text{HK2}}(t) \cdot c_{\text{Glc}}(t)}{K_{\text{M,HK2}} + c_{\text{Glc}}(t)} - k_{\text{metabolism}} \cdot c_{\text{G6P}}(t) - c_{\text{G6P}}(t) \cdot \frac{\dot{V}(t)}{V(t)} \tag{7}$$

$$\dot{c}_{\text{GLUT1}}(t) = k_{\text{cat,1}} \cdot c_{E,1}(t) \cdot \frac{V(t)}{A(t)} - \frac{k_{\text{cat,2}} \cdot c_{\text{E,2}}(t) \cdot c_{\text{GLUT1}}(t)}{K_{\text{M,2}} + c_{\text{GLUT1}}(t)} \cdot \frac{V(t)}{A(t)} - c_{\text{GLUT1}}(t) \cdot \frac{\dot{A}(t)}{A(t)} \tag{8}$$

where c_{Glc} and c_{G6P} are concentrations in the cellular volume V, whereas c_{GLUT1} is a concentration at the cell surface A. As a consequence, the import of glucose is converted by the factor $\frac{A}{V}$ to a flux given with respect to the cellular volume. Similarly, the generation and degradation of GLUT1 are converted by the factor $\frac{V}{A}$ to fluxes with respect to the cell surface area, since the enzymes generating and turning over GLUT1 are situated inside the cell. HK2, E_1, and E_2 are not assumed to be generated and turned over, and their concentrations dilute from some initial concentrations as the cellular volume increases. These concentrations are given by $c_{\text{x}}(t) = n_{\text{x}}/V(t)$ (x = HK2, E_1, E_2), where n_{x} is the amount of compound x (constant quantities).

We call the system of ODEs given by Eqs. 6–8 *model A*, corresponding to the system shown in Figure 4A. This model only describes the uptake of glucose and supply to metabolism, without any control mechanisms in place. To examine the regulatory mechanisms of glucose uptake, we build on this model, and add feedback inhibition from G6P to GLUT1 production. This feedback is based on the many pathways that regulate GLUT1 mediated glucose uptake via AMPK, summarized in Figure 2A. This way, a reduction in G6P level will reduce inhibition of GLUT1 production, thereby increasing GLUT1 mediated glucose uptake. We model this feedback by allosteric inhibition (specifically, a special case of mixed inhibition) of the reaction producing GLUT1 (69, 70). The model is shown in Figure 4B, and given by Eqs. 6–7, and the additional ODE

$$\dot{c}_{\text{GLUT1}}(t) = k_{\text{cat,1}} \cdot c_{E,1}(t) \cdot \frac{K_{\text{i,G6P}}}{K_{\text{i,G6P}} + c_{\text{G6P}}(t)} \cdot \frac{V(t)}{A(t)} - \frac{k_{\text{cat,2}} \cdot c_{\text{E,2}}(t) \cdot c_{\text{GLUT1}}(t)}{K_{\text{M,2}} + c_{\text{GLUT1}}(t)} \cdot \frac{V(t)}{A(t)} - c_{\text{GLUT1}}(t) \cdot \frac{\dot{A}(t)}{A(t)} \tag{9}$$

where $K_{\text{i,G6P}}$ is the inhibition constant for the allosteric inhibition of GLUT1 production by G6P. We call this *model B*.

We simulate models A and B in three phases (Figure 5): In the first phase (white area, $t = [0, 50]$), the cellular volume is kept constant. In the second phase (light gray area, $t = [50, 100]$), we still maintain a constant cellular volume, and probe the regulatory function of the feedback inhibition in model B by reducing the extracellular glucose concentration by 75% at the start of the phase. In the third phase (dark gray area, $t = [100, 150]$), we investigate the effect of dilution on the two models by increasing the cellular volume linearly. The simulation results are shown in Figure 5, with initial values and parameters provided in Table S1 in the Supporting Material. Dashed red lines show the dynamical response of model A, and solid blue lines show model B. The bottom right plot of cellular volume (solid black line) and surface area (dashed black line) is the same for both simulations. In the first phase (white area), the cellular volume is constant and both systems have settled at steady state, producing a constant glycolytic flux (represented by the phosphorylation of glucose). At the start of the second phase (light gray area), extracellular glucose concentration is reduced while the cellular volume remains constant. Comparing the two models, we see that model A shows no adaptation to such a perturbation in glucose supply, resulting in reduced metabolite levels (intracellular glucose and G6P) and glycolytic flux. Model B, however, is able to fully compensate for the reduction in glucose supply. This is achieved by increasing the surface concentration of GLUT1, thereby increasing GLUT1 mediated glucose uptake to match the previous uptake rate of the system. In the final phase of the simulations (dark gray area), cellular volume starts to increase linearly. Although neither of the models are able to compensate for dilution, in the case of model B, GLUT1 production is increased in an attempt to mitigate the effect of dilution. However, this compensatory response is not being effectuated as the level of HK2 is not being maintained, resulting in reduced glycolytic flux as the concentration of HK2 dilutes. The simulation results show that feedback inhibition from downstream glycolytic metabolites to glucose transporters is sufficient for homeostatic control of glycolysis in a constant volume, consistent with principles of metabolic regulation by negative feedback (71, 72). The regulation of glucose transporters by feedback inhibition is, however, not sufficient to maintain a constant glycolytic flux during growth. It appears that control of HK2 may be necessary for homeostatic control during growth.

In order to compensate for dilution, we extend model B, and add activation of HK2 synthesis by intracellular glucose. As mentioned earlier, this forms a stabilizing feedback connection together with the phosphorylation of glucose to G6P (62). This

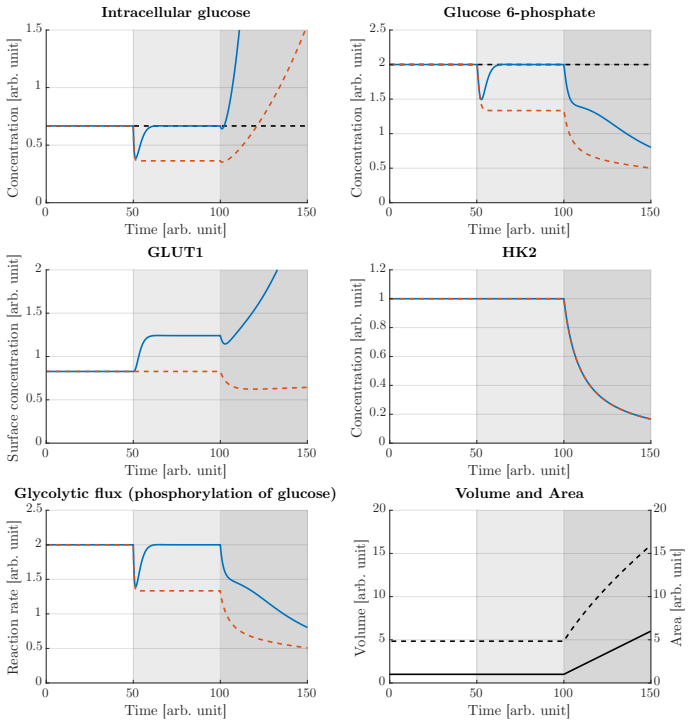

Figure 5: Simulation results of model A (dashed red lines) and model B (solid blue lines). The bottom right plot of volume (solid black line) and surface area (dashed black line) is the same for the two simulations. Initially, the cellular volume is kept constant and the systems have settled at steady state (white area, $t = [0, 50]$). At the start of the second phase (light gray area, $t = [50, 100]$), extracellular glucose concentration is reduced by 75%. Whereas model A shows no adaptation in this phase, model B is able to regulate intracellular glucose and G6P levels back to pre-perturbed values (dashed black lines), and maintain homeostatic control of glycolysis (regulation of the glycolytic flux). In the last phase (dark gray area, $t = [100, 150]$), the cellular volume starts to increase linearly. Neither of the models are able to compensate for dilution, however, GLUT1 mediated glucose uptake is increased in model B, but due to dilution of HK2 this compensatory response is not being effectuated. Note that due to dilution of HK2, intracellular glucose accumulates in the final phase. Such an accumulation can not go on forever, and as the concentration of intracellular glucose approaches that of extracellular glucose, our assumption of GLUT1 mediated glucose uptake following the Michaelis–Menten equation will break down. A similar limit for the surface concentration of GLUT1 will also likely be approached. Nevertheless, the simulation results are able to show that models A and B do not achieve homeostatic control of glysolysis in the presence of dilution. Initial values and parameters are provided in Table S1 in the Supporting Material.

feedback connection stabilizes the level of HK2 in the presence of dilution, such that the concentration of HK2 remains more or less constant during growth, providing robustness to dilution in the first irreversible step of glycolysis. In turn, this robustness allows GLUT1 mediated glucose uptake to regulate the glycolytic flux during growth. With this addition it is necessary to add reactions generating and turning over HK2, so that activation by intracellular glucose can be mediated through these reactions. The activation of HK2 synthesis is modeled by allosteric activation (specifically, a special case of mixed activation) (69, 70).

We assume the synthesis and degradation of HK2 are driven by enzymes E_3 and E_4, respectively, where the synthesis is proportional to the level of E_3, and the degradation by E_4 follows a Michaelis–Menten-type process. The model is shown in Figure 4C and given by Eqs. 6–7, 9, and the following ODE describing the change in HK2 concentration

$$\dot{c}_{\mathrm{HK2}}(t) = k_{\mathrm{cat},3} \cdot c_{\mathrm{E},3}(t) \cdot \frac{c_{\mathrm{Glc}}(t)}{K_{\mathrm{a,Glc}} + c_{\mathrm{Glc}}(t)} - \frac{k_{\mathrm{cat},4} \cdot c_{\mathrm{E},4}(t) \cdot c_{\mathrm{HK2}}(t)}{K_{\mathrm{M},4} + c_{\mathrm{HK2}}(t)} - c_{\mathrm{HK2}}(t) \cdot \frac{\dot{V}(t)}{V(t)} \tag{10}$$

where $K_{\mathrm{a,Glc}}$ is the activation constant for the allosteric activation of HK2 synthesis by intracellular glucose. The enzymes E_i ($i = 1, 2, 3, 4$) are not assumed to be generated and turned over, and their concentrations dilute as the volume increases. These concentrations are given by $c_{\mathrm{E,i}}(t) = n_{\mathrm{E,i}}/V(t)$ ($i = 1, 2, 3, 4$), where $n_{\mathrm{E,i}}$ (the amount of E_i) are constant quantities. We call this *model C*.

We simulate model C in four phases (Figure 6): In the first phase (white area, $t = [0, 400]$), the volume is kept constant. In the second phase (light gray area, $t = [400, 800]$), we increase the volume linearly to investigate whether model C is able to maintain homeostatic control of glycolysis during growth. While the volume is still increasing, extracellular glucose concentration is increased 4-fold at the start of the third phase (dark gray area, $t = [800, 1200]$). Finally, in the last phase (white area, $t = [1200, 1600]$), volume increase is stopped. The simulation results are shown in Figure 6, with initial values and parameters provided in Table S2 in the Supporting Material. The bottom right plot shows volume (solid black line) and surface area (dashed black line) during the simulation. In the first phase (white area), the system has settled at steady state, producing a constant glycolytic flux. In the second phase (light gray area), we see that model C is able to compensate for dilution and produce a constant glycolytic flux, however, steady state values are shifted compared to steady state values without growth (dashed black lines in intracellular glucose and G6P plots). These growth associated offsets could indicate the inability of the control mechanisms to fully compensate for dilution. However, they could also represent set-point changes during the growth phase. To investigate the cause of the growth associated offsets, we increase extracellular glucose concentration as the cellular volume is growing. This is done at the start of the third phase (dark gray area). Due to the subsequent increase in glucose uptake, a sudden reduction in the surface concentration of GLUT1 follows. Nevertheless, the surface concentration of GLUT1 continues to increase throughout this phase in order to compensate for dilution. Interestingly, it seems that the control mechanisms attempt to bring the system back to steady state values associated with growth, not steady state values associated with constant volume. If the latter were true, we would not expect to see the regulatory action in Figure 6 bringing intracellular glucose and G6P levels away from steady state values associated with constant volume (dashed black lines). This suggests that the growth associated offsets may be caused by set-point changes, rather than the inability to maintain the glycolytic flux during growth. Finally, the first phase is repeated and the volume is kept constant again, but is now much larger (white area). In this phase, we see that metabolite levels and the glycolytic flux return to steady state values associated with constant volume. This is achieved by the increase of surface concentration of GLUT1 during the growth phase, which is made possible due to the relationship between cellular volume and cell surface area (see Section S2 in the Supporting Material). Thus, the growth associated offsets appears to be dependent on the rate of volume increase, not the total volume.

Taken together, the simulation results of models A, B, and C in Figure 5 and Figure 6 show that while negative feedback from downstream metabolites to nutrient transporters is sufficient for homeostatic control in a constant volume, it is necessary to stabilize the concentrations of intermediate enzymes in order to achieve homeostatic control during growth. The simulations also demonstrate that during the growth phase, growth associated offsets from steady state values associated with constant volume are observed, and that these offsets appears to be caused by set-point changes that are dependent on the growth rate. Importantly, investigations into control mechanisms similar to the ones identified in this paper, have shown that growth associated offsets become negligible if the kinetics of the controller species behave on a timescale much faster than cell growth (9, 10, 73–75). These control mechanisms, called ICMs, achieve robust homeostatic control due to a negative feedback structure that includes integral action. In the following, we take a closer look at the function of such ICMs and show how the control mechanisms discussed above realize integral action and dilution resistance.

A Closer Look at Integral Control Motifs

Asymptotic regulation is the notion that a regulation error approaches zero, i.e. the output perfectly reaches a desired reference, as time tends to infinity (76). If asymptotic regulation is achieved in the presence of disturbances, asymptotic disturbance rejection (also called robustness) is achieved (76). In the case of constant reference signal, or set-point, and constant disturbance, asymptotic regulation and disturbance rejection can be achieved by integral action (76). A block diagram of negative feedback with integral action is shown in Figure 7. For a system subject to disturbance w, the output y is to be regulated to a set-point r. This is achieved by comparing the system output to the set-point, giving the regulation error $e = r - y$. The integral controller integrates the regulation error, producing the control action input u to the system. Thus, when the system output deviates from the set-point, the regulation error is non-zero, which produces a change in the control action. Because the feedback is negative,

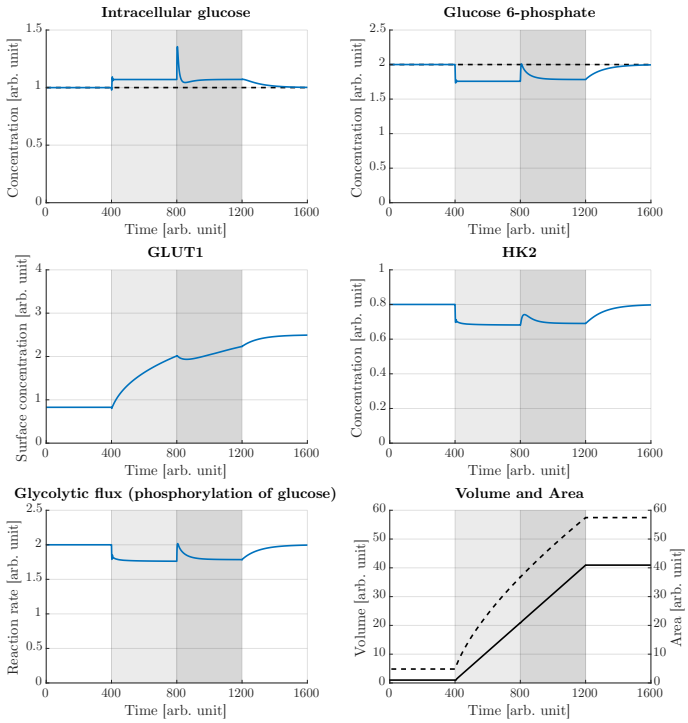

Figure 6: Simulation results of model C. The bottom right plot shows volume (solid black line) and surface area (dashed black line) during the simulation. Initially, the cellular volume is kept constant, and the system has settled at steady state (white area, $t = [0, 400]$). In the second phase (light gray area, $t = [400, 800]$), the cellular volume increases linearly. During this phase, metabolite levels and the glycolytic flux are maintained at constant levels, however, with offsets from steady state values associated with constant volume (dashed black lines in intracellular glucose and G6P plots). At the start of the third phase (dark gray area, $t = [800, 1200]$), as the volume is still increasing, the concentration of extracellular glucose is increased 4-fold. Interestingly, the system is regulated back to steady state values associated with growth, and away from steady state values associated with constant volume. This suggests that the growth associated offsets are caused by set-point changes. Finally, the first phase is repeated, and the volume is kept constant (white area, $t = [1200, 1600]$). In this phase we see that metabolite levels and the glycolytic flux return to steady state values associated with constant volume. This indicates that the growth associated offsets are dependent on the growth rate, rather than the total volume. Initial values and parameters are provided in Table S2 in the Supporting Material.

this change in control action counteracts the deviation of the system output from the set-point. Importantly, when the system output reaches the desired set-point, the output is maintained exactly at the set-point, as the "memory" element of the integral controller stores the accumulated regulation error (9). The block diagram in Figure 7 suggests a constant integral gain G_i, though this gain can be variable, often referred to as gain scheduling (62, 76). The mathematical description of the integral controller, called the integral control law, is given by

$$\dot{u}(t) = G_i \cdot (r - y(t)) \tag{11}$$

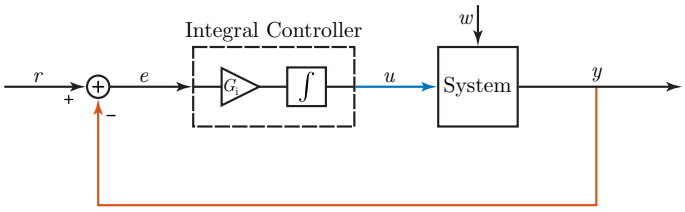

Figure 7: Block diagram of negative feedback with integral action. The system output y is fed back (red output feedback) and compared to the reference signal r to produce the regulation error $e = r - y$. The regulation error is multiplied by an integral gain G_i and integrated over time to produce the control action u (blue system input). In the presence of an uncontrolled disturbance w (black disturbance input), a deviation in system output from the reference will cause a non-zero regulation error. This produces a change in the control action, and since the feedback is negative, this control action functions to contract the deviation in system output from the reference.

Investigations into robust homeostatic systems have revealed several motifs that include negative feedback with integral action (9, 62, 77, 78). The control mechanisms considered in this paper correspond to a class of ICMs called homeostatic controller motifs (62). It has been shown that these homeostatic controller motifs are robust to all parameter perturbations that do not destroy the stability of the system (79). For example, feedback inhibition from G6P to GLUT1 generation produces the same structure as that of Figure 7. Red output feedback corresponds to the inhibition of GLUT1 generation by G6P, the integral controller block corresponds to GLUT1 level, blue system input corresponds to GLUT1 mediated glucose uptake, and the system block corresponds to the level of G6P. The black disturbance input corresponds to perturbations made in extracellular glucose and cellular volume. By manipulating Eq. 9, we show that GLUT1 functions as an integral controller for G6P level

$$\dot{c}_{\mathrm{GLUT1}}(t) = k_{\mathrm{cat},1} \cdot c_{E,1}(t) \cdot \frac{K_{\mathrm{i,G6P}}}{K_{\mathrm{i,G6P}} + c_{\mathrm{G6P}}(t)} \cdot \frac{V(t)}{A(t)} - \frac{k_{\mathrm{cat},2} \cdot c_{\mathrm{E},2}(t) \cdot c_{\mathrm{GLUT1}}(t)}{K_{\mathrm{M},2} + c_{\mathrm{GLUT1}}(t)} \cdot \frac{V(t)}{A(t)} - c_{\mathrm{GLUT1}}(t) \cdot \frac{\dot{A}(t)}{A(t)} \tag{12}$$

$$\approx k_{\mathrm{cat},1} \cdot c_{\mathrm{E},1}(t) \cdot \frac{K_{\mathrm{i,G6P}}}{K_{\mathrm{i,G6P}} + c_{\mathrm{G6P}}(t)} \cdot \frac{V(t)}{A(t)} - k_{\mathrm{cat},2} \cdot c_{\mathrm{E},2}(t) \cdot \frac{V(t)}{A(t)} - c_{\mathrm{GLUT1}}(t) \cdot \frac{\dot{A}(t)}{A(t)} \tag{13}$$

$$= G_{\mathrm{i}}(t) \cdot \left(c_{\mathrm{G6P,set}} - \dot{A}(t) \cdot o_{\mathrm{G6P}}(t) - c_{\mathrm{G6P}}(t)\right) \tag{14}$$

where we make the simplification $K_{\mathrm{M},2} \ll c_{\mathrm{GLUT1}}$. The following definitions are made

$$G_{\mathrm{i}}(t) = \frac{1}{A(t)} \cdot \frac{k_{\mathrm{cat},2} \cdot n_{\mathrm{E},2}}{K_{\mathrm{i,G6P}} + c_{\mathrm{G6P}}(t)} \tag{15}$$

$$c_{\mathrm{G6P,set}} = \frac{k_{\mathrm{cat},1} \cdot n_{\mathrm{E},1} - k_{\mathrm{cat},2} \cdot n_{\mathrm{E},2}}{k_{\mathrm{cat},2} \cdot n_{\mathrm{E},2}} \cdot K_{\mathrm{i,G6P}} \tag{16}$$

$$o_{\mathrm{G6P}}(t) = \frac{K_{\mathrm{i,G6P}} + c_{\mathrm{G6P}}(t)}{k_{\mathrm{cat},2} \cdot n_{\mathrm{E},2}} \cdot c_{\mathrm{GLUT1}}(t) \tag{17}$$

The set-point for G6P level, $c_{\mathrm{G6P,set}}$, is given entirely by parameters associated with GLUT1 generation and degradation. This means that perturbations in G6P are fully compensated for, as the set-point remains unchanged for such perturbations (73). In the case without growth, $\dot{A} = 0$, Eq. 14 is reduced to the same form as the integral control law in Eq. 11. In the case with growth, a growth associated offset, $\dot{A} \cdot o_{\mathrm{G6P}}$, is introduced. However, if the reaction rates for the generation and degradation of GLUT1 behave on a timescale much faster than the rate of dilution, o_{G6P} is small, and the growth associated offset becomes negligible. ICMs with controller reactions much faster than the rate of dilution are called quasi-ICMs, and characteristically show small growth associated offsets (9). One mechanism of regulating GLUT1 and HK2 activity is through translocation between biological membranes and the cytosol, indicating that the activity of these species can respond quickly, and that regulation of glucose uptake in cancer may achieve dilution resistance through the formation of quasi-ICMs (39, 55, 80). Similar to GLUT1, it is possible to show that HK2 functions as an integral controller for the level of intracellular glucose (See Section S3 in the Supporting Material).

CONCLUSION

In this paper, we have constructed a mathematical model of glucose uptake based on the reported rewiring of glycolysis in cancer and differential gene expression of cancer and normal cells. With basis in the literature, we added control mechanisms to the model in a stepwise manner, in order to investigate the role each regulatory mechanism serve. Expectedly, we found that feedback inhibition from downstream glycolytic metabolites to glucose transporters is sufficient for homeostatic control of glycolysis in a constant volume. However, in a growing volume, we found that regulation of intermediate glycolytic enzymes is needed for homeostatic control of glycolysis. Cancer cells show a shift towards GLUT1 mediated glucose uptake and a reliance on HK2. We found that these species form regulatory mechanisms for glycolysis through their interactions with glycolytic metabolites. These regulatory mechanisms are a class of ICMs known as homeostatic controller motifs, and achieve robust homeostatic control by negative feedback with integral action (9, 62). Our simulation results show that during growth, offsets from steady state values associated with constant volume are observed. These growth associated offsets can be interpreted as set-point changes, and are dependent on the growth rate of the cell, not the total volume. In his definition of homeostasis, Cannon emphasized that homeostasis does not imply perfect adaptation to disturbances, but allows for some variability in steady state (81). Similarly, rheostasis is defined as systems that show homeostatic control at any one instant, but over the span of time show change in the regulated level (82). Living organisms are not necessarily concerned with perfect regulation, but rather with the presence of some level of regulation. Thus, it is likely that sufficient regulation can be achieved even if the growth associated offsets are fairly large. This variability in steady state can then be viewed as a relaxing condition on the control mechanisms employed (83).

Investigations into ICMs have shown that growth associated offsets becomes negligible if the rates of the controller reactions, i.e. the generation and degradation of GLUT1 and HK2, are much faster compared to the rate of dilution (9, 10, 73–75). In our model, enzymes responsible for generating and removing the controller species (E_i, $i = 1, 2, 3, 4$) are present in constant amounts only, meaning that their concentrations simply dilute with increasing volume. This is a worst-case scenario in which regulation in the presence of dilution is possible. In this scenario, we found that model C is able to compensate for dilution in a linearly increasing volume. However, most protein and mRNA concentrations are independent of cell size, and therefore it is likely that the concentrations $c_{E,i}$ ($i = 1, 2, 3, 4$) should be considered constant (7). In this case, it has been shown that regulation is possible even in the presence of dilution in an exponentially increasing cell volume (9, 10).

Taking a closer look at feedback inhibition from downstream glycolytic metabolites to GLUT1 mediated glucose uptake, we have shown how this control mechanism realizes integral action to regulate glycolysis. We have also shown how dilution affects this ICM, and related the growth associated offset in G6P to a term dependent on the growth rate of the cell. In recent years, ICMs have garnered much attention (9, 10, 62, 75, 77, 78). This paper uses glucose uptake in cancer to demonstrate a systems biology approach to the analysis of complex regulatory systems, where control mechanisms are reduced into their essential components, which can then be represented by ICMs. A benefit of this approach is simplifying the mathematical description of the complex system, while retaining the essential behavior, such that a more manageable system can be considered and an in-depth analysis of its function can be done.

AUTHOR CONTRIBUTIONS

DT, TD, KT, FF, and PR conceived and designed the research. DT and TD performed simulations. DT, TD, KT, and FF analyzed the data. DT and GF wrote the manuscript with contributions from all coauthors.

REFERENCES

1. Lang, F., G. L. Busch, M. Ritter, H. Völkl, S. Waldegger, E. Gulbins, and D. Häussinger, 1998. Functional Significance of Cell Volume Regulatory Mechanisms. *Physiological Reviews* 78:247–306.

2. Clegg, J. S., S. A. Jackson, and K. Fendl, 1990. Effects of Reduced Cell Volume and Water Content on Glycolysis in L-929 Cells. *Journal of Cellular Physiology* 142:386–391.

3. Peak, M., M. al-Habori, and L. Agius, 1992. Regulation of Glycogen Synthesis and Glycolysis by Insulin, pH and Cell Volume. Interactions between Swelling and Alkalinization in Mediating the Effects of Insulin. *Biochemical Journal* 282:797–805.

4. Häussinger, D., W. Newsome, S. vom Dahl, B. Stoll, B. Noe, R. Schreiber, M. Wettstein, and F. Lang, 1994. Control of Liver Cell Function by the Hydration State. *Biochemical Society Transactions* 22:497–502.

5. Lizana, L., B. Bauer, and O. Orwar, 2008. Controlling the Rates of Biochemical Reactions and Signaling Networks by Shape and Volume Changes. *Proceedings of the National Academy of Sciences of the United States of America* 105:4099–4104.

6. Schmoller, K. M., J. J. Turner, M. Kõivomägi, and J. M. Skotheim, 2015. Dilution of the Cell Cycle Inhibitor Whi5 Controls Budding-Yeast Cell Size. *Nature* 526:268–272.

7. Schmoller, K. M., and J. M. Skotheim, 2015. The Biosynthetic Basis of Cell Size Control. *Trends in Cell Biology* 25:793–802.

8. Saint, M., F. Bertaux, W. Tang, X.-M. Sun, L. Game, A. Köferle, J. Bähler, V. Shahrezaei, and S. Marguerat, 2019. Single-Cell Imaging and RNA Sequencing Reveal Patterns of Gene Expression Heterogeneity during Fission Yeast Growth and Adaptation. *Nature Microbiology* 4:480–491.

9. Qian, Y., and D. Del Vecchio, 2018. Realizing 'Integral Control' in Living Cells: How to Overcome Leaky Integration Due to Dilution? *Journal of the Royal Society Interface* 15:20170902.

10. Ruoff, P., O. Agafonov, D. M. Tveit, K. Thorsen, and T. Drengstig, 2019. Homeostatic Controllers Compensating for Growth and Perturbations. *PLoS ONE* 14:e0207831.

11. Vander Heiden, M. G., L. C. Cantley, and C. B. Thompson, 2009. Understanding the Warburg Effect: The Metabolic Requirements of Cell Proliferation. *Science* 324:1029–1033.

12. Gatenby, R. A., and R. J. Gillies, 2004. Why Do Cancers Have High Aerobic Glycolysis? *Nature Reviews Cancer* 4:891–899.

13. Mathupala, S. P., Y. H. Ko, and P. L. Pedersen, 2006. Hexokinase II: Cancer's Double-Edged Sword Acting as Both Facilitator and Gatekeeper of Malignancy When Bound to Mitochondria. *Oncogene* 25:4777–4786.

14. Vazquez, A., and Z. N. Oltvai, 2016. Macromolecular Crowding Explains Overflow Metabolism in Cells. *Scientific Reports* 6:31007.

15. Vazquez, A., J. Liu, Y. Zhou, and Z. N. Oltvai, 2010. Catabolic Efficiency of Aerobic Glycolysis: The Warburg Effect Revisited. *BMC Systems Biology* 4:58.

16. Guertin, D. A., and D. M. Sabatini, 2008. Chapter 12: Cell Growth. *In* The Molecular Basis of Cancer, Saunders, Philadelphia, PA, 169–175. 3 edition.

17. Furlong, T. J., and K. R. Spring, 1990. Mechanisms Underlying Volume Regulatory Decrease by Necturus Gallbladder Epithelium. *American Journal of Physiology-Cell Physiology* 258:C1016–C1024.

18. Natarajan, R., N. Gonzales, L. Xu, and J. L. Nadler, 1992. Vascular Smooth Muscle Cells Exhibit Increased Growth in Response to Elevated Glucose. *Biochemical and Biophysical Research Communications* 187:552–560.

19. Di Chiro, G., J. Hatazawa, D. A. Katz, H. V. Rizzoli, and D. J. De Michele, 1987. Glucose Utilization by Intracranial Meningiomas as an Index of Tumor Aggressivity and Probability of Recurrence: A PET Study. *Radiology* 164:521–526.

20. Sánchez-Aragó, M., M. Chamorro, and J. M. Cuezva, 2010. Selection of Cancer Cells with Repressed Mitochondria Triggers Colon Cancer Progression. *Carcinogenesis* 31:567–576.

21. Hay, N., 2016. Reprogramming Glucose Metabolism in Cancer: Can It Be Exploited for Cancer Therapy? *Nature Reviews Cancer* 16:635–649.

22. Hsu, P. P., and D. M. Sabatini, 2008. Cancer Cell Metabolism: Warburg and Beyond. *Cell* 134:703–707.

23. Hanahan, D., and R. A. Weinberg, 2011. Hallmarks of Cancer: The next Generation. *Cell* 144:646–674.

24. DeBerardinis, R. J., J. J. Lum, G. Hatzivassiliou, and C. B. Thompson, 2008. The Biology of Cancer: Metabolic Reprogramming Fuels Cell Growth and Proliferation. *Cell Metabolism* 7:11–20.

25. Carruthers, A., J. DeZutter, A. Ganguly, and S. U. Devaskar, 2009. Will the Original Glucose Transporter Isoform Please Stand Up! *American Journal of Physiology-Endocrinology and Metabolism* 297:E836–E848.

26. Joost, H.-G., G. I. Bell, J. D. Best, M. J. Birnbaum, M. J. Charron, Y. T. Chen, H. Doege, D. E. James, H. F. Lodish, K. H. Moley, J. F. Moley, M. Mueckler, S. Rogers, A. Schürmann, S. Seino, and B. Thorens, 2002. Nomenclature of the GLUT/SLC2A Family of Sugar/Polyol Transport Facilitators. *American Journal of Physiology-Endocrinology and Metabolism* 282:E974–E976.

27. Thorens, B., and M. Mueckler, 2010. Glucose Transporters in the 21st Century. *American Journal of Physiology-Endocrinology and Metabolism* 298:E141–E145.

28. Bell, G. I., T. Kayano, J. B. Buse, C. F. Burant, J. Takeda, D. Lin, H. Fukumoto, and S. Seino, 1990. Molecular Biology of Mammalian Glucose Transporters. *Diabetes Care* 13:198–208.

29. Thorens, B., 1996. Glucose Transporters in the Regulation of Intestinal, Renal, and Liver Glucose Fluxes. *American Journal of Physiology-Gastrointestinal and Liver Physiology* 270:G541–G553.

30. Ganapathy, V., M. Thangaraju, and P. D. Prasad, 2009. Nutrient Transporters in Cancer: Relevance to Warburg Hypothesis and Beyond. *Pharmacology & Therapeutics* 121:29–40.

31. Semenza, G. L., 2003. Targeting HIF-1 for Cancer Therapy. *Nature Reviews Cancer* 3:721–732.

32. Pedersen, P. L., S. Mathupala, A. Rempel, J. Geschwind, and Y. H. Ko, 2002. Mitochondrial Bound Type II Hexokinase: A Key Player in the Growth and Survival of Many Cancers and an Ideal Prospect for Therapeutic Intervention. *Biochimica et Biophysica Acta (BBA) - Bioenergetics* 1555:14–20.

33. Berg, J. M., J. L. Tymoczko, G. J. Gatto, Jr., and L. Stryer, 2015. Biochemistry. W. H. Freeman & Company, New York, NY, 8 edition.

34. Moon, J.-S., H. E. Kim, E. Koh, S. H. Park, W.-J. Jin, B.-W. Park, S. W. Park, and K.-S. Kim, 2011. Krüppel-like Factor 4 (KLF4) Activates the Transcription of the Gene for the Platelet Isoform of Phosphofructokinase (PFKP) in Breast Cancer. *Journal of Biological Chemistry* 286:23808–23816.

35. Kim, N. H., Y. H. Cha, J. Lee, S.-H. Lee, J. H. Yang, J. S. Yun, E. S. Cho, X. Zhang, M. Nam, N. Kim, Y.-S. Yuk, S. Y. Cha, Y. Lee, J. K. Ryu, S. Park, J.-H. Cheong, S. W. Kang, S.-Y. Kim, G.-S. Hwang, J. I. Yook, and H. S. Kim, 2017. Snail Reprograms Glucose Metabolism by Repressing Phosphofructokinase PFKP Allowing Cancer Cell Survival under Metabolic Stress. *Nature Communications* 8:14374.

36. Filipp, F. V., 2013. Cancer Metabolism Meets Systems Biology: Pyruvate Kinase Isoform PKM2 Is a Metabolic Master Regulator. *Journal of Carcinogenesis* 12:14.

37. Asaka, M., T. Kimura, T. Meguro, M. Kato, M. Kudo, T. Miyazaki, and E. Alpert, 1994. Alteration of Aldolase Isozymes in Serum and Tissues of Patients with Cancer and Other Diseases. *Journal of Clinical Laboratory Analysis* 8:144–148.

38. Young, C. D., E. C. Nolte, A. Lewis, N. J. Serkova, and S. M. Anderson, 2008. Activated Akt1 Accelerates MMTV-c-ErbB2 Mammary Tumourigenesis in Mice without Activation of ErbB3. *Breast Cancer Research* 10:R70.

39. Klip, A., T. Tsakiridis, A. Marette, and P. A. Ortiz, 1994. Regulation of Expression of Glucose Transporters by Glucose: A Review of Studies in Vivo and in Cell Cultures. *The FASEB Journal* 8:43–53.

40. Celenza, J. L., L. Marshall-Carlson, and M. Carlson, 1988. The Yeast SNF3 Gene Encodes a Glucose Transporter Homologous to the Mammalian Protein. *Proceedings of the National Academy of Sciences of the United States of America* 85:2130–2134.

41. Haspel, H. C., D. C. Mynarcik, P. A. Ortiz, R. A. Honkanen, and M. G. Rosenfeld, 1991. Glucose Deprivation Induces the Selective Accumulation of Hexose Transporter Protein GLUT-1 in the Plasma Membrane of Normal Rat Kidney Cells. *Molecular Endocrinology* 5:61–72.

42. Haspel, H. C., E. W. Wilk, M. J. Birnbaum, S. W. Cushman, and O. M. Rosen, 1986. Glucose Deprivation and Hexose Transporter Polypeptides of Murine Fibroblasts. *Journal of Biological Chemistry* 261:6778–6789.

43. Takakura, Y., S. L. Kuentzel, T. J. Raub, A. Davies, S. A. Baldwin, and R. T. Borchardt, 1991. Hexose Uptake in Primary Cultures of Bovine Brain Microvessel Endothelial Cells. I. Basic Characteristics and Effects of D-Glucose and Insulin. *Biochimica et Biophysica Acta (BBA) - Biomembranes* 1070:1–10.

44. Boado, R. J., and W. M. Pardridge, 1993. Glucose Deprivation Causes Posttranscriptional Enhancement of Brain Capillary Endothelial Glucose Transporter Gene Expression via GLUT1 mRNA Stabilization. *Journal of Neurochemistry* 60:2290–2296.

45. Tordjman, K. M., K. A. Leingang, and M. Mueckler, 1990. Differential Regulation of the HepG2 and Adipocyte/Muscle Glucose Transporters in 3T3L1 Adipocytes. Effect of Chronic Glucose Deprivation. *Biochemical Journal* 271:201–207.

46. John, S. A., M. Ottolia, J. N. Weiss, and B. Ribalet, 2008. Dynamic Modulation of Intracellular Glucose Imaged in Single Cells Using a FRET-Based Glucose Nanosensor. *Pflügers Archiv - European Journal of Physiology* 456:307–322.

47. Macheda, M. L., S. Rogers, and J. D. Best, 2005. Molecular and Cellular Regulation of Glucose Transporter (GLUT) Proteins in Cancer. *Journal of Cellular Physiology* 202:654–662.

48. Jeon, S.-M., 2016. Regulation and Function of AMPK in Physiology and Diseases. *Experimental & Molecular Medicine* 48:e245.

49. Davies, S. P., S. A. Hawley, A. Woods, D. Carling, T. A. J. Haystead, and D. G. Hardie, 1994. Purification of the AMP-activated Protein Kinase on ATP-γ-Sepharose and Analysis of Its Subunit Structure. *European Journal of Biochemistry* 223:351–357.

50. Ruderman, N. B., X. J. Xu, L. Nelson, J. M. Cacicedo, A. K. Saha, F. Lan, and Y. Ido, 2010. AMPK and SIRT1: A Long-Standing Partnership? *American Journal of Physiology-Endocrinology and Metabolism* 298:E751–E760.

51. Vander Heiden, M. G., and R. J. DeBerardinis, 2017. Understanding the Intersections between Metabolism and Cancer Biology. *Cell* 168:657–669.

52. Galbo, T., R. J. Perry, E. Nishimura, V. T. Samuel, B. Quistorff, and G. I. Shulman, 2013. PP2A Inhibition Results in Hepatic Insulin Resistance despite Akt2 Activation. *Aging* 5:770–781.

53. Kabashima, T., T. Kawaguchi, B. E. Wadzinski, and K. Uyeda, 2003. Xylulose 5-Phosphate Mediates Glucose-Induced Lipogenesis by Xylulose 5-Phosphate-Activated Protein Phosphatase in Rat Liver. *Proceedings of the National Academy of Sciences of the United States of America* 100:5107–5112.

54. Barnes, K., J. C. Ingram, O. H. Porras, L. F. Barros, E. R. Hudson, L. G. D. Fryer, F. Foufelle, D. Carling, D. G. Hardie, and S. A. Baldwin, 2002. Activation of GLUT1 by Metabolic and Osmotic Stress: Potential Involvement of AMP-Activated Protein Kinase (AMPK). *Journal of Cell Science* 115:2433–2442.

55. Wu, N., B. Zheng, A. Shaywitz, Y. Dagon, C. Tower, G. Bellinger, C.-H. Shen, J. Wen, J. Asara, T. E. McGraw, B. B. Kahn, and L. C. Cantley, 2013. AMPK-Dependent Degradation of TXNIP upon Energy Stress Leads to Enhanced Glucose Uptake via GLUT1. *Molecular Cell* 49:1167–1175.

56. Xi, X., J. Han, and J.-Z. Zhang, 2001. Stimulation of Glucose Transport by AMP-Activated Protein Kinase via Activation of P38 Mitogen-Activated Protein Kinase. *Journal of Biological Chemistry* 276:41029–41034.

57. ter Kuile, B. H., and M. Cook, 1994. The Kinetics of Facilitated Diffusion Followed by Enzymatic Conversion of the Substrate. *Biochimica et Biophysica Acta (BBA) - Biomembranes* 1193:235–239.

58. Stein, W. D., and W. R. Lieb, 1986. Transport and Diffusion across Cell Membranes. Academic Press, San Diego, California.

59. Lee, M. G., and P. L. Pedersen, 2003. Glucose Metabolism in Cancer: Importance of Transcription Factor-DNA Interactions within a Short Segment of the Proximal Region Og the Type II Hexokinase Promoter. *Journal of Biological Chemistry* 278:41047–41058.

60. Mathupala, S. P., A. Rempel, and P. L. Pedersen, 1995. Glucose Catabolism in Cancer Cells. Isolation, Sequence, and Activity of the Promoter for Type II Hexokinase. *Journal of Biological Chemistry* 270:16918–16925.

61. Rempel, A., S. P. Mathupala, and P. L. Pedersen, 1996. Glucose Catabolism in Cancer Cells: Regulation of the Type II Hexokinase Promoter by Glucose and Cyclic AMP. *FEBS Letters* 385:233–237.

62. Drengstig, T., I. Jolma, X. Ni, K. Thorsen, X. Xu, and P. Ruoff, 2012. A Basic Set of Homeostatic Controller Motifs. *Biophysical Journal* 103:2000–2010.

63. Bustamante, E., and P. L. Pedersen, 1977. High Aerobic Glycolysis of Rat Hepatoma Cells in Culture: Role of Mitochondrial Hexokinase. *Proceedings of the National Academy of Sciences of the United States of America* 74:3735–3739.

64. Nakashima, R. A., M. G. Paggi, L. J. Scott, and P. L. Pedersen, 1988. Purification and Characterization of a Bindable Form of Mitochondrial Bound Hexokinase from the Highly Glycolytic AS-30D Rat Hepatoma Cell Line. *Cancer Research* 48:913–919.

65. Marín-Hernández, A., S. Rodríguez-Enríquez, P. A. Vital-González, F. L. Flores-Rodríguez, M. Macías-Silva, M. Sosa-Garrocho, and R. Moreno-Sánchez, 2006. Determining and Understanding the Control of Glycolysis in Fast-Growth Tumor Cells. Flux Control by an over-Expressed but Strongly Product-Inhibited Hexokinase. *The FEBS Journal* 273:1975–1988.

66. Petryszak, R., M. Keays, Y. A. Tang, N. A. Fonseca, E. Barrera, T. Burdett, A. Füllgrabe, A. M.-P. Fuentes, S. Jupp, S. Koskinen, O. Mannion, L. Huerta, K. Megy, C. Snow, E. Williams, M. Barzine, E. Hastings, H. Weisser, J. Wright, P. Jaiswal, W. Huber, J. Choudhary, H. E. Parkinson, and A. Brazma, 2016. Expression Atlas Update—an Integrated Database of Gene and Protein Expression in Humans, Animals and Plants. *Nucleic Acids Research* 44:D746–D752.

67. Shampine, L. F., and M. W. Reichelt, 1997. The MATLAB ODE Suite. *SIAM Journal on Scientific Computing* 18:1–22.

68. Wyatt, E., R. Wu, W. Rabeh, H.-W. Park, M. Ghanefar, and H. Ardehali, 2010. Regulation and Cytoprotective Role of Hexokinase III. *PLoS ONE* 5:e13823.

69. Cornish-Bowden, A., 2012. Fundamentals of Enzyme Kinetics. Wiley-Blackwell, Weinheim, Germany, 4 edition.

70. Keener, J., and J. Sneyd, 2009. Mathematical Physiology I: Cellular Physiology, volume 8/1 of *Interdisciplinary Applied Mathematics*. Springer, New York, NY, 2 edition.

71. Stadtman, E. R., 1963. Symptosium on Multiple Forms of Enzymes and Control Mechanisms. II. Enzyme Multiplicity and Function in the Regulation of Divergent Metabolic Pathways. *Bacteriological Reviews* 27:170–181.

72. Cohen, G. N., 1965. Regulation of Enzyme Activity in Microorganisms. *Annual Review of Microbiology* 19:105–126.

73. Ang, J., and D. R. McMillen, 2013. Physical Constraints on Biological Integral Control Design for Homeostasis and Sensory Adaptation. *Biophysical Journal* 104:505–515.

74. Ang, J., S. Bagh, B. P. Ingalls, and D. R. McMillen, 2010. Considerations for Using Integral Feedback Control to Construct a Perfectly Adapting Synthetic Gene Network. *Journal of Theoretical Biology* 266:723–738.

75. Aoki, S. K., G. Lillacci, A. Gupta, A. Baumschlager, D. Schweingruber, and M. Khammash, 2019. A Universal Biomolecular Integral Feedback Controller for Robust Perfect Adaptation. *Nature* 570:533–537.

76. Khalil, H. K., 2002. Nonlinear Systems. Prentice Hall, Upper Saddle River, New Jersey, 3 edition.

77. Briat, C., A. Gupta, and M. Khammash, 2016. Antithetic Integral Feedback Ensures Robust Perfect Adaptation in Noisy Biomolecular Networks. *Cell Systems* 2:15–26.

78. Drengstig, T., X. Y. Ni, K. Thorsen, I. W. Jolma, and P. Ruoff, 2012. Robust Adaptation and Homeostasis by Autocatalysis. *The Journal of Physical Chemistry B* 116:5355–5363.

79. Tveit, D. M., and K. Thorsen, 2017. Passivity-Based Analysis of Biochemical Networks Displaying Homeostasis. *In* Proceedings of the 58th Conference on Simulation and Modelling (SIMS 58) Reykjavik, Iceland, September 25th – 27th, 2017. Linköping University Electronic Press, Linköpings universitet, Reykjavik, Iceland, Linköping Electronic Conference Proceedings, 108–113.

80. John, S., J. N. Weiss, and B. Ribalet, 2011. Subcellular Localization of Hexokinases I and II Directs the Metabolic Fate of Glucose. *PLoS ONE* 6:e17674.

81. Cannon, W. B., 1929. Organization for Physiological Homeostasis. *Physiological Reviews* 9:399–431.

82. Mrosovsky, N., 1990. Rheostasis: The Physiology of Change. Oxford University Press, New York.

83. Risvoll, G. B., K. Thorsen, P. Ruoff, and T. Drengstig, 2017. Variable Setpoint as a Relaxing Component in Physiological Control. *Physiological Reports* 5:e13408.

Supporting Material

Exploring Mechanisms of Glucose Uptake Regulation and Dilution Resistance in Growing Cancer Cells

Daniel M. Tveit[1], Gunhild Fjeld[2], Tormod Drengstig[1], Fabian V. Filipp[3], Peter Ruoff[2], and Kristian Thorsen[1]

[1]Department of Electrical Engineering and Computer Science, University of Stavanger, Stavanger, Norway
[2]Centre for Organelle Research, University of Stavanger, Stavanger, Norway
[3]Systems Biology and Cancer Metabolism, Program for Quantitative Systems Biology, University of California Merced, Merced, CA, USA

S1 Differential Gene Expression

Differential gene expression data collected from the Expression Atlas[1] database are provided in the file `Differential expression.xlsx`. The first sheet shows mean $\log_2$-fold change for the genes considered, along with the number of experiments used to calculate the mean. The following sheets show $\log_2$-fold change for each individual experiment, indicating the type of cells compared.

S2 Note on Cellular Volume and Surface Area

Assuming spherical cells, the surface area A and its rate of change $\dot{A}$ are calculated from the cellular volume V and change in cellular volume $\dot{V}$ as follows

$$A(t) = 4\pi \left(\frac{3V(t)}{4\pi}\right)^{\frac{2}{3}} \tag{1}$$

$$\dot{A}(t) = \frac{2\dot{V}(t)}{\left(\frac{3V(t)}{4\pi}\right)^{\frac{1}{3}}} \tag{2}$$

This gives the relationship

$$\frac{\dot{V}(t)}{V(t)} = \frac{3}{2} \cdot \frac{\dot{A}(t)}{A(t)} \tag{3}$$

which expresses the difference in dilution between concentrations in the cellular volume and at the cell surface. This is the reason the surface concentration of GLUT1 does not settle at a constant level during growth (see Figure 6 in the main paper). In Eq. 14 in the main paper, the offset $\dot{A} \cdot o_{\text{G6P}}$ does not fully account for the difference in G6P set-point and observed level during growth. In fact, the offset is off by a factor $\frac{3}{2}$, due to this difference in dilution of components. The same is not true for the negative feedback connection formed by HK2 and intracellular glucose, as both components are concentrations with respect to the cellular volume.

[1]`https://www.ebi.ac.uk/gxa/home` (see also reference (66) in the main paper)

S3 Integral Control of Intracellular Glucose

Similar to how GLUT1 functions as an integral controller for G6P, HK2 functions as an integral controller for intracellular glucose

$$\dot{c}_{\mathrm{HK2}}(t) = k_{\mathrm{cat},3} \cdot c_{\mathrm{E},3}(t) \cdot \frac{c_{\mathrm{Glc}}(t)}{K_{\mathrm{a,Glc}} + c_{\mathrm{Glc}}(t)} - \frac{k_{\mathrm{cat},4} \cdot c_{\mathrm{E},4}(t) \cdot c_{\mathrm{HK2}}(t)}{K_{\mathrm{M},4} + c_{\mathrm{HK2}}(t)} - c_{\mathrm{HK2}}(t) \cdot \frac{\dot{V}(t)}{V(t)} \tag{4}$$

$$\approx k_{\mathrm{cat},3} \cdot c_{\mathrm{E},3}(t) \cdot \frac{c_{\mathrm{Glc}}(t)}{K_{\mathrm{a,Glc}} + c_{\mathrm{Glc}}(t)} - k_{\mathrm{cat},4} \cdot c_{\mathrm{E},4}(t) - c_{\mathrm{HK2}}(t) \cdot \frac{\dot{V}(t)}{V(t)} \tag{5}$$

$$= G_{\mathrm{i}}(t) \cdot \Big(c_{\mathrm{Glc,set}} - \dot{V}(t) \cdot o_{\mathrm{Glc}}(t) - c_{\mathrm{Glc}}(t) \Big) \tag{6}$$

where the simplification $K_{\mathrm{M},4} \ll c_{\mathrm{HK2}}$ is made. The following definitions are made

$$G_{\mathrm{i}}(t) = \frac{1}{V(t)} \cdot \frac{k_{\mathrm{cat},4} \cdot n_{\mathrm{E},4} - k_{\mathrm{cat},3} \cdot n_{\mathrm{E},3}}{K_{\mathrm{a,Glc}} + c_{\mathrm{Glc}}(t)} \tag{7}$$

$$c_{\mathrm{Glc,set}} = \frac{k_{\mathrm{cat},4} \cdot n_{\mathrm{E},4}}{k_{\mathrm{cat},3} \cdot n_{\mathrm{E},3} - k_{\mathrm{cat},4} \cdot n_{\mathrm{E},4}} \cdot K_{\mathrm{a,Glc}} \tag{8}$$

$$o_{\mathrm{Glc}}(t) = \frac{K_{\mathrm{a,Glc}} + c_{\mathrm{Glc}}(t)}{k_{\mathrm{cat},4} \cdot n_{\mathrm{E},4} - k_{\mathrm{cat},3} \cdot n_{\mathrm{E},3}} \cdot c_{\mathrm{HK2}(t)} \tag{9}$$

S4 Initial Values and Parameters

Initial Values		
Name	Model A	Model B
c_{Glc}	0.6669	0.6669
c_{G6P}	2.0004	2.0004
c_{GLUT1}	0.8273	0.8273
Parameters		
n_{HK2}	1.0000	1.0000
V	$f(t) = 1.0000 + \dot{V} \cdot t$	$f(t) = 1.0000 + \dot{V} \cdot t$
$\dot{V}$	$f(t) = \begin{cases} 0, & t < 100 \\ 0.1000 & t \geq 100 \end{cases}$	$f(t) = \begin{cases} 0, & t < 100 \\ 0.1000 & t \geq 100 \end{cases}$
$c_{\mathrm{Glc,ext}}$	$f(t) = \begin{cases} 5.0000, & t < 50 \\ 1.2500, & t \geq 50 \end{cases}$	$f(t) = \begin{cases} 5.0000, & t < 50 \\ 1.2500, & t \geq 50 \end{cases}$
$k_{\mathrm{cat,GLUT1}}$	0.6000	0.6000
$K_{\mathrm{M,GLUT1}}$	1.0000	1.0000
$k_{\mathrm{cat,HK2}}$	5.0000	5.0000
$K_{\mathrm{M,HK2}}$	1.0000	1.0000
$k_{\mathrm{metabolism}}$	1.0000	1.0000
$k_{\mathrm{cat},1}$	1.0000	6.0000
$n_{\mathrm{E},1}$	1.0000	1.0000
$k_{\mathrm{cat},2}$	2.0000	2.0000
$K_{\mathrm{M},2}$	0.8273	0.0001
$n_{\mathrm{E},2}$	1.0000	1.0000
$K_{\mathrm{i,G6P}}$	–	1.0000

Table S1: Initial values and parameters for the simulations of model A and B in Figure 5.

Initial Values	
Name	Model C
c_{Glc}	0.9997
c_{G6P}	2.0004
c_{GLUT1}	0.8273
c_{HK2}	0.8002
Parameters	
V	$f(t) = 1.0000 + \dot{V} \cdot t$
$\dot{V}$	$f(t) = \begin{cases} 0.0500, & 400 \leq t < 1200 \\ 0, & \text{otherwise} \end{cases}$
$c_{\mathrm{Glc,ext}}$	$f(t) = \begin{cases} 5.0000, & t < 800 \\ 20.0000, & t \geq 800 \end{cases}$
$k_{\mathrm{cat,GLUT1}}$	0.6000
$K_{\mathrm{M,GLUT1}}$	1.0000
$k_{\mathrm{cat,HK2}}$	5.0000
$K_{\mathrm{M,HK2}}$	1.0000
$k_{\mathrm{metabolism}}$	1.0000
$k_{\mathrm{cat,1}}$	6.0000
$n_{\mathrm{E,1}}$	1.0000
$k_{\mathrm{cat,2}}$	2.0000
$K_{\mathrm{M,2}}$	0.0001
$n_{\mathrm{E,2}}$	1.0000
$k_{\mathrm{cat,3}}$	2.0000
$n_{\mathrm{E,3}}$	1.0000
$k_{\mathrm{cat,4}}$	1.0000
$K_{\mathrm{M,4}}$	0.0001
$n_{\mathrm{E,4}}$	1.0000
$K_{\mathrm{i,G6P}}$	1.0000
$K_{\mathrm{a,Glc}}$	1.0000

Table S2: Initial values and parameters for the simulation of model C in Figure 6.